RATIONAL DESIGN OF MULTI-FUNCTIONAL NANOMATERIALS

EDITED BY: Carlos Lodeiro, José Luis Capelo and Hugo Miguel Santos
PUBLISHED IN: Frontiers in Chemistry

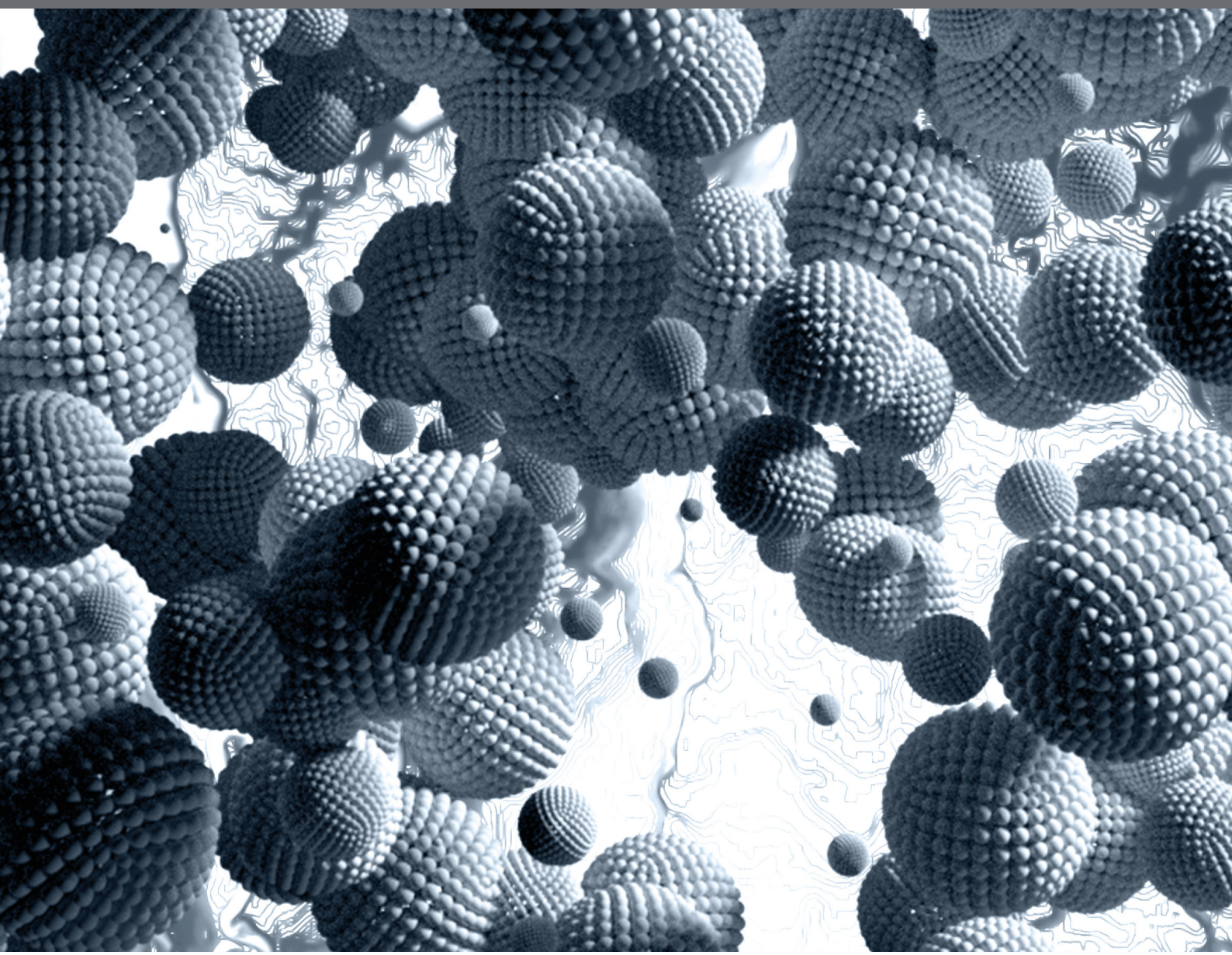

frontiers Research Topics

ISSN 1664-8714
ISBN 978-2-88945-987-2
DOI 10.3389/978-2-88945-987-2

About Frontiers

Frontiers is more than just an open-access publisher of scholarly articles: it is a pioneering approach to the world of academia, radically improving the way scholarly research is managed. The grand vision of Frontiers is a world where all people have an equal opportunity to seek, share and generate knowledge. Frontiers provides immediate and permanent online open access to all its publications, but this alone is not enough to realize our grand goals.

Frontiers Journal Series

The Frontiers Journal Series is a multi-tier and interdisciplinary set of open-access, online journals, promising a paradigm shift from the current review, selection and dissemination processes in academic publishing. All Frontiers journals are driven by researchers for researchers; therefore, they constitute a service to the scholarly community. At the same time, the Frontiers Journal Series operates on a revolutionary invention, the tiered publishing system, initially addressing specific communities of scholars, and gradually climbing up to broader public understanding, thus serving the interests of the lay society, too.

Dedication to Quality

Each Frontiers article is a landmark of the highest quality, thanks to genuinely collaborative interactions between authors and review editors, who include some of the world's best academicians. Research must be certified by peers before entering a stream of knowledge that may eventually reach the public - and shape society; therefore, Frontiers only applies the most rigorous and unbiased reviews.
Frontiers revolutionizes research publishing by freely delivering the most outstanding research, evaluated with no bias from both the academic and social point of view. By applying the most advanced information technologies, Frontiers is catapulting scholarly publishing into a new generation.

What are Frontiers Research Topics?

Frontiers Research Topics are very popular trademarks of the Frontiers Journals Series: they are collections of at least ten articles, all centered on a particular subject. With their unique mix of varied contributions from Original Research to Review Articles, Frontiers Research Topics unify the most influential researchers, the latest key findings and historical advances in a hot research area! Find out more on how to host your own Frontiers Research Topic or contribute to one as an author by contacting the Frontiers Editorial Office: researchtopics@frontiersin.org

RATIONAL DESIGN OF MULTI-FUNCTIONAL NANOMATERIALS

Topic Editors:
Carlos Lodeiro, NOVA University of Lisbon, PROTEOMASS Scientific Society, Portugal
José Luis Capelo, NOVA University of Lisbon, PROTEOMASS Scientific Society, Portugal
Hugo Miguel Santos, NOVA University of Lisbon, PROTEOMASS Scientific Society, Portugal

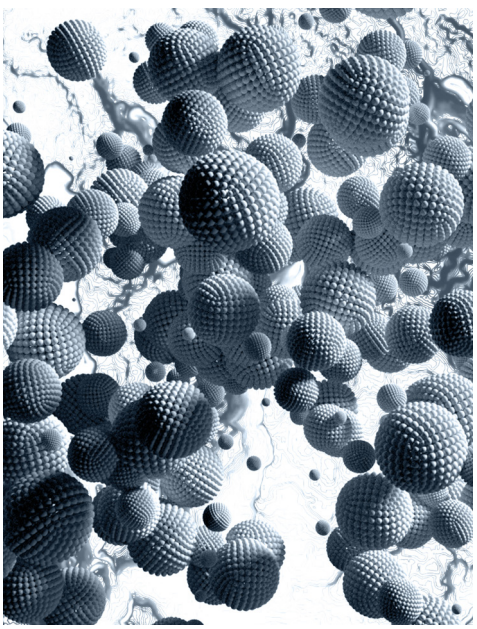

Image: GiroScience/Shutterstock.com

One of the most important issues, when a nanomaterial is designed, is to control the synthetic pathways to ensure the final desired product. A combination of dry and wet procedures, as well as chemical and physical methodologies, it is possible to successfully prepare new multifunctional nanomaterials, often as a result of multidisciplinary cooperation between chemists, physics, biologist, physicians, material engineers, etc. Drug delivery, environmental detection of contaminants, and many industrial applications directly rely on properties such as water solubility, permeability, cell penetration, shape control, and size of the monodispersed nanoparticle, among others.

Functionalized nanomaterials play a crucial role in modern research areas because of their unique physical and chemical properties, explored in many different fields including medicine and biology, new materials, pharmacology as drug delivery systems, and in environmental analysis for sensing new contaminants, among other technical and industrial applications.

For future technological applications, the rational design of these multifunctional nanomaterials is critical, and often depends on the excellent control of the organic and inorganic chemical reactions involved during production. The success of their applications relies directly on the photophysical properties created in the final material, including the emission of light or colorimetric responses, water solubility, selectivity, sensitivity, stability, etc. For example, from an analytical point of view, the detection and quantification of emerging analytes is directly dependent on the selectivity and sensitivity showed by the material in a complex media.

Citation: Lodeiro, C., Capelo, J. L., Santos, H. M., eds. (2019). Rational Design of Multi-Functional Nanomaterials. Lausanne: Frontiers Media.
doi: 10.3389/978-2-88945-987-2

Table of Contents

TITANIUM NANOMATERIALS AND CATALYSIS

GRAPHENE AND METALLIC NANOMATERIALS

frontiers in Chemistry

EDITORIAL
published: 24 May 2019
doi: 10.3389/fchem.2019.00358

Editorial: Rational Design of Multi-Functional Nanomaterials

Carlos Lodeiro[1,2]*, *José Luis Capelo*[1,2] *and Hugo M. Santos*[1,2]

[1] BIOSCOPE Group, LAQV-REQUIMTE Research Unit, Chemistry Department, Faculty of Science and Technology, University NOVA of Lisbon, Caparica, Portugal, [2] PROTEOMASS Scientific Society, Caparica, Portugal

Keywords: nanomaterials, nanoparticles, structural control, rational functionalization, detection, delivery, advanced multifunctional nanomaterials

Editorial on the Research Topic

Rational Design of Multi-Functional Nanomaterials

At the beginning of 2018, and after closing the international symposium on Nanoparticles, Nanomaterials and Applications[1] (3rd ISN2A) held in Costa de Caparica (Portugal), we encourage different research groups working at the nanoscale field to submit their latest scientific findings or revisions, to a new Research Topic devoted to "Rational Design of Multi-Functional Nanomaterials." Two important keywords appear in the title: Rational-Design and Multi-functional Applications.

Concerning the first term, Rational Design, one of the most important subjects when a nanomaterial is designed, is to control the synthetic pathways to ensure the final desired product. A combination of dry and wet synthetic techniques, in conjunction with the adequate chemical and physical characterization methodologies, it is possible to prepare new nanomaterials successfully. This complex issue frequently is a result of multidisciplinary cooperation between chemists, physics, biologist, physicians, material engineers, among other disciplines. The second statement, Multifunctional applications, deals with the use of nanomaterials in fields some time collaboratives, such as drug delivery, cell and tissue imaging, as new antibiotic tools, in environmental detection and removing of contaminants, catalysis, and many industrial applications directly rely on properties such as water solubility, permeability, photostability, cell penetration, magnetic properties, related shape, and size control among others. Nowadays, functionalized nanomaterials play a crucial role in modern research areas because of their unique physical and chemical properties arise from their size and shape.

In the international year of the Periodic Table, we can highlight in this collection of papers the use of gold, silver, iron, platinum, molybdenum, titanium, and cobalt as metal precursors among the use of organic@inorganic polymers, and Silica as the chemical protagonist in this collection of papers.

Sixty-eight researchers from Portugal, Spain, Italy, Germany, Switzerland, Hungary, Russia, United States of America, Saudi Arabia, South Korea, Taiwan, and Indonesia, submitted 10 original and review articles covering all the aspects highlighted in the title. Related to the contributions in the field of biomedical sciences and applications, Caponetti et al. in Italy reported an elegant paper on Fluorescent Nanoparticles for bioimaging; The use of Gold Nanoparticles for Photothermal therapy was studied by Vines et al. in South Korea and the USA, and also Gold Based Organometallic nanocomposites for Antitumoral activity studies were reported by Dalmases et al. in a collaborative paper including researchers from Spain and Germany, and finally iron was

[1]The International Caparica Symposium on Nanoparticles and Nanomaterials and Applications (ISN2A), is celebrated biannually in Caparica-(Portugal), is a high-quality forum to share innovative solutions to the many challenges created by human activity using and producing nanomaterials.

OPEN ACCESS

Edited by:
Fan Zhang,
Fudan University, China

Reviewed by:
Xiaoji Xie,
Nanjing Tech University, China

***Correspondence:**
Carlos Lodeiro
cle@fct.unl.pt

Specialty section:
This article was submitted to Nanoscience, a section of the journal Frontiers in Chemistry

Received: *13 March 2019*
Accepted: *30 April 2019*
Published: *24 May 2019*

Citation:
Lodeiro C, Capelo JL and Santos HM (2019) Editorial: Rational Design of Multi-Functional Nanomaterials. Front. Chem. 7:358. doi: 10.3389/fchem.2019.00358

present as Magnetic Nanoparticles for drug delivery applications reviewed by Price et al. including researchers from the United States of America, Saudi Arabia, and Russia. The actually topic of antibiotic resistance and new antibiotic studies was covered using silver nanomaterials by Djafari et al. in Portugal with a manuscript about Silver Nanotriangles as antibacterial tools, and Nuti et al. with the contribution of researchers in Portugal, Spain, and Italy with the synthesis of Mesoporous Silver nanoparticles for antibiotic delivery.

Catalysis and industrial applications were represented by the contributions of Sahroni et al. from Taiwan and Indonesia with Hybrid Nanomaterials for reversible lithium storage based on MoS2, Szabó et al. from Hungary and Switzerland present a paper on Titanium based nanomaterials for catalysis applications, Martinez et al. studied several Pt-Co Nanoparticles for CO oxidation, and finally the use of TiO2/Au nanoparticles for hydrogen generation via photocatalysis was explored by May-Masnou et al. from Spain.

In summary, this Research Topic have explored the state-of-the-art and beyond in the rational design of nanoparticles and nanocomposites, based on metallic, polymeric, or soft raw materials, as well as their different applications in medicine, imaging, drug delivery, catalysis, energy storage, or sensing.

For all future technological applications, the rational design of these multifunctional nanomaterials is critical, and in many cases will be controlled by the organic and inorganic chemical reactions involved during the production. The success of their applications relies directly on the photophysical and chemical properties created in the final material, including the emission of light or colourimetric responses, water solubility, selectivity, sensitivity, stability, thermal stability, functionalization, etc.

AUTHOR CONTRIBUTIONS

All authors listed have made a substantial, direct and intellectual contribution to the work, and approved it for publication.

ACKNOWLEDGMENTS

The guest editors thanks to PROTEOMASS Scientific Society (Portugal), Laboratorio Associado de Química Verde, LAQV/REQUIMTE, The Faculty of Science and Technology-University NOVA of Lisbon and the companies Paralab, LaborSpirit, TransTejo, Bruker, Almada Municipality, Portuguese Society of Chemistry, MPDI editorial, and Tourism of Portugal for their help in the organization of the 3rd ISN^{2}A conference (www.isn2a2018.com).

The authors thank the project MultiNANO@Tox, financed by national funds from FCT/MEC (UID/Multi/04378/2013 - UID/QUI/50006/2013) and the FCT-MEC project PTDC/QEQ-MED/2118/2014. HS thanks to the FCT-MEC for the researcher IF contract. All guest editors thank the support to the PROTEOMASS Scientific Society, and special thanks to the editorial Frontiers in, Inorganic Chemistry and Nanoscience sessions for their support and allow the Guest Editors to organize this fantastic Collection of Papers.

Conflict of Interest Statement: The authors declare that the research was conducted in the absence of any commercial or financial relationships that could be construed as a potential conflict of interest.

frontiers in Chemistry

REVIEW
published: 05 April 2019
doi: 10.3389/fchem.2019.00167

Gold Nanoparticles for Photothermal Cancer Therapy

Jeremy B. Vines[1], Jee-Hyun Yoon[2], Na-Eun Ryu[3], Dong-Jin Lim[4] and Hansoo Park[3]**

[1] Casinbio USA, Birmingham, AL, United States, [2] Department of Herbology, College of Korean Medicine, Woosuk University, Jeonju, South Korea, [3] School of Integrative Engineering, Chung-Ang University, Seoul, South Korea, [4] Otolaryngology Head and Neck Surgery, University of Alabama at Birmingham, Birmingham, AL, United States

Gold is a multifunctional material that has been utilized in medicinal applications for centuries because it has been recognized for its bacteriostatic, anticorrosive, and antioxidative properties. Modern medicine makes routine, conventional use of gold and has even developed more advanced applications by taking advantage of its ability to be manufactured at the nanoscale and functionalized because of the presence of thiol and amine groups, allowing for the conjugation of various functional groups such as targeted antibodies or drug products. It has been shown that colloidal gold exhibits localized plasmon surface resonance (LPSR), meaning that gold nanoparticles can absorb light at specific wavelengths, resulting in photoacoustic and photothermal properties, making them potentially useful for hyperthermic cancer treatments and medical imaging applications. Modifying gold nanoparticle shape and size can change their LPSR photochemical activities, thereby also altering their photothermal and photoacoustic properties, allowing for the utilization of different wavelengths of light, such as light in the near-infrared spectrum. By manufacturing gold in a nanoscale format, it is possible to passively distribute the material through the body, where it can localize in tumors (which are characterized by leaky blood vessels) and be safely excreted through the urinary system. In this paper, we give a quick review of the structure, applications, recent advancements, and potential future directions for the utilization of gold nanoparticles in cancer therapeutics.

Keywords: gold, photo-active property, hyperthermia, nanoparticles, cancer therapeutics

OPEN ACCESS

Edited by:
José Luis Capelo, Universidade Nova de Lisboa, Portugal

Reviewed by:
Huaibin Shen, Henan University, China
Amitava Adhikary, Oakland University, United States

****Correspondence:***
Dong-Jin Lim
daniel.djlim@gmail.com
Hansoo Park
heyshoo@cau.ac.kr

Specialty section:
This article was submitted to Nanoscience, a section of the journal Frontiers in Chemistry

Received: *26 October 2018*
Accepted: *05 March 2019*
Published: *05 April 2019*

Citation:
Vines JB, Yoon J-H, Ryu N-E, Lim D-J and Park H (2019) Gold Nanoparticles for Photothermal Cancer Therapy. Front. Chem. 7:167. doi: 10.3389/fchem.2019.00167

INTRODUCTION

Current Limitations in Conventional Cancer Therapies

In 2017, cancer was the second-most common cause of death in the United States, comprising 22.5% of the total number of deaths; 591,699 people died from complications related to cancer in 2017 (Heron, 2018). Unfortunately, owing to the heterogeneous nature of cancer, there are currently no fully comprehensive approaches for treatment; options are mainly limited to chemotherapy, radiotherapy, immunotherapy, and surgery. Although these approaches provide some therapeutic efficacy, they are limited by their risk to normal, healthy cells, their potential to destroy the immune system, or by conferring an increased risk for the development of secondary cancers (Nolsoe et al., 1993; Vogel and Venugopalan, 2003; Kievit and Zhang, 2011). For this reason, a large body of cancer therapy research focuses on finding effective therapies that can complement or even replace current therapies by improving efficacy and reducing inadvertent side effects.

Hyperthermia as a Cancer Treatment Modality

In the pursuit of therapies capable of reducing undesired side effects and enhancing efficacy, there has been growing interest in utilizing hyperthermia to achieve these goals. Hyperthermic cancer therapy was originally developed based on historical examples in which cancer patients infected by erysipelas had high fevers that either reduced cancer symptoms or resulted in the complete regression of tumors (Moyer and Delman, 2008). Since the original study pioneered by Coley in 1893, additional studies have been performed in which hyperthermia was carefully applied to general regions of cancerous tumor growth to maintain tissue temperatures of around 42 to 45°C (Luk et al., 1980). In practical settings, however, the ability to precisely manage heating surrounding the tumor area would be critical to improve and adapt this alternative modality on cancer treatment. Additionally, other cancer treatment modalities such as radiation and chemotherapy can be utilized together for successful cancer treatment. In this regard, not only does hyperthermia cause apoptosis of cancer cells, but can also improve therapeutic efficacy when used in concert with radiation or chemotherapy (Kampinga, 2006). In the presence of thermal stress, tumors become radiosensitized, making them more likely to respond to radiotherapy, resulting in improved cancer survival rates. This fact has been demonstrated in studies of metastatic head and neck squamous cell cancers, where radical radiation treatment with hyperthermia resulted in improved outcomes without increasing toxicity (Moyer and Delman, 2008; Kaur et al., 2011). A similar sensitization is further seen with chemotherapeutics when used in combination with hyperthermia. When clinically-relevant drugs for malignant melanoma are combined with low or high grade hyperthermia (43 and 45°C, respectively), intrinsic or extrinsic ER-mediated apoptosis can be induced (Mantso et al., 2018).

Many preclinical studies have been performed to demonstrate that both radio and chemotherapy can be enhanced by simultaneously incorporating hyperthermic therapy (Peeken et al., 2017). Unfortunately, traditional hyperthermia techniques are not ideal due to the fact that they are not minimally invasive, and result in the non-specific generation of heat throughout the body (Kaur et al., 2016). As a result, substantial undesirable side effects are created. For example, whole-body hyperthermia may cause cardiovascular side effects and gastrointestinal symptoms (Chatterjee et al., 2011). Regarding this, a more promising modality for cancer treatment would involve a targeted, nanoparticle-mediated localized hyperthermia One treatment modality that continues to gain attention and is currently under investigation for potential widespread use is photothermal therapy (PTT) (Bardhan et al., 2011; Melancon et al., 2011). Photothermal therapy is based on the conversion of light energy (usually in the near-infrared region) into heat energy to induce subsequent cellular necrosis or apoptosis (Ray et al., 2012).

Compared with other methods, light is an ideal external stimulus as it is easily regulated, focused, and remotely controlled. This ease of focus and control enable better targeted treatments that lead to less damage to healthy tissues (Yang X. et al., 2012; Khaletskaya et al., 2013; Zhu et al., 2014). Unfortunately, traditional photodynamic therapy (PDT) of tissues mediated by laser or visible light is limited by insufficient depth of penetration, limiting its usefulness for deep tumor therapy (Ochsner, 1997; Wilson and Patterson, 2008; Benov, 2015). However, near-infrared (NIR) light (in the wavelength range of 800–1,200 nm) has much greater body transparency, making it preferable for PTT. In contrast to traditional PDT, which relies on the presence of oxygen to generate reactive oxygen species, and is considerably limited in application due to its limited depth of penetration (Wilson and Patterson, 2008), PTT mainly exerts effects by increasing the local temperature within tumors (Wang and Qiu, 2016). Regarding this, it has been demonstrated that in order to completely destroy cancer cells *in vitro*, a threshold temperature ranging between 70 and 80°C is required (Huang et al., 2006). Furthermore, at temperatures ranging from 55 to 95°C, tumorigenic damage is evident *in vivo* conditions (Thomsen, 1991).

Hyperthermic Nanoparticle Systems and Limitations

Some current nanoparticle technologies for hyperthermic therapy include ferromagnetic nanoparticles such as iron oxide (van Landeghem et al., 2009; Wang et al., 2010; Cassim et al., 2011; Maier-Hauff et al., 2011), doped iron oxide (Lee et al., 2011; Fantechi et al., 2014; Gordon et al., 2014) and super-paramagnetic iron oxide nanoparticles (SPION) (Le Renard et al., 2010; Kruse et al., 2014; Zheng et al., 2014) as well as carbon nanotube (CNT) technologies including single walled carbon nanotubes (SWCNTs) and multi-walled carbon nanotubes (MWCNTs) (Burke et al., 2009; Huang et al., 2010) in addition to various polymer-based technologies (Kaur et al., 2016).

Ferromagnetic nanoparticles including SPION, iron oxide, and doped iron oxide are typically stimulated under the presence of alternating magnetic fields (AMFs) during which materials are induced to rapidly magnetize and demagnetize. When these materials are manufactured as nanoparticles, their magnetization rapidly fluctuates generating a net field of zero (superparamagnetism). When superparamagnetic nanoparticles are stimulated with magnetic fields they behave like paramagnets with a single magnetic domain and enhanced magnetic susceptibility. Upon the application of an AMF, superparamagnetic nanoparticles can be reasonably excited to generate heat sufficient for thermal therapy. The main limitation of the magnetic nanoparticle approach is the fact that it is difficult to generate fine-tuned and precise treatment of tumors due to the fact that AMF fields are generally targeted toward the whole body in contrast to the tumor specifically as seen with photothermal approaches (Dennis et al., 2008).

CNTs are nanomaterials that are composed of sheets of carbon atoms arranged into the shape of a honeycomb-like lattice that are rolled into the shape of a tube only a few nanometers in diameter but with lengths anywhere on the scale of hundreds of nanometers to microns (Kaur et al., 2016). SWCNTs are made up of one CNT while MWCNTs are comprised of

multiple tubes stacked within each other. CNTs are capable of responding to light across a broad-spectrum including light in both the visible and NIR spectrums. Previous studies have shown the successful utilization of SWCNTs for the treatment of squamous cell carcinoma tumor xenografts in mice using NIR illumination (Huang et al., 2010) and the successful utilization of MWCNTs in concert with short pulses of low-power laser illumination for the treatment of renal cancer xenografts (Burke et al., 2009). However, one of the main limitations associated with CNTs is the fact that granulomas resembling asbestos associated mesothelioma in the mesothelial and pleural linings have occasionally presented in mice, raising concerns regarding their long-term biocompatibility (Poland et al., 2008).

There are also currently many polymeric materials geared toward applications in PTT. To date, polypyrrole, poly-(3,4-ethylenedioxythiophene):poly(4-styrenesulfonate) (PEDOT:PSS), dopamine-melanin (polydopamine), and polyaniline nanoparticles are some of the most commonly used materials that have been reported to show photothermal effects (Chen et al., 2012; Cheng et al., 2012; Yang K. et al., 2012; Liu et al., 2013; Vines et al., 2018).

Perhaps one of the oldest conducting polymers employed for PTT is known as Polyaniline (Zhou et al., 2013). Its low cost, mechanical flexibility, and excellent conductivity has provided this material with considerable recognition (Li et al., 2009). In addition, polyaniline has historical use as an electroactive tissue for studying cellular proliferation prior to its utilization in PTT due to its excellent biocompatibility (Heeger, 2001). Another of the most commonly used base materials for use in PTT cancer treatments is Polypyrrole (PPy) (Wang, 2016; Manivasagan et al., 2017). PPy, which was originally known as "pyrrole black" due to its composition as a black precipitate from acidic pyrrole/ H_2O_2 aqueous solutions was first synthesized in the early 20th century. PPy has recently found popularity as an electro-responsive material in biomedical engineering applications (Ateh et al., 2006; Svirskis et al., 2010; Balint et al., 2014) as it is generally regarded as biocompatible, with little or no adverse effects on health (George et al., 2005; Fahlgren et al., 2015).

Poly(3,4-ethylenedioxythiophene):poly(4-styrenesulfonate) (PEDOT:PSS) is another class of polymer-based nanoparticles commonly used for NIR-mediated hyperthermic therapy. In perhaps the first documented study of this material for photothermal cancer therapy, PEGylated PEDOT:PSS nanoparticles (PDOT:PSS-PEG) were synthesized via a layer-by-layer approach, creating nanoparticles of ∼80 nm in diameter (Cheng et al., 2012). Polydopamine, another commonly utilized polymer for PTT, was first explored as a potential PTT agent by Liu et al. (2013). In this study, dopamine-melanin colloidal nanospheres were fabricated via the oxidation and self-polymerization of dopamine in a mixture containing water, ethanol, and ammonia at room temperature.

While these polymer based nanoparticle systems show some promise, many polymer based systems such as polydopamine hold less than ideal mass extinction coefficients (Dong et al., 2016). In addition to sometimes holding weaker photothermal efficiencies, the degradation profiles of many of these polymers is not fully understood, creating questions as to their long-term biocompatibility (Cheng et al., 2014). For this reason, it may be beneficial to utilize nanomaterials with longer documented historical utilization in clinical practice.

Gold in Medicine and Hyperthermic Cancer Therapeutics

Gold (Au), one of the noble metals, has been characterized by its resistance to corrosion and oxidation. These properties have been known for centuries, as evidenced by gold's long-documented use in medicinal applications. Colloidal Au was documented in the Middle Ages as a substance for treatment and diagnosis of diseases (Pricker, 1996). Inspired by the early discovery of the bacteriostatic properties of $K[Au(CN)_2]$ (Shaw, 1999), gold compounds were eventually utilized for modern medical treatments. Recent advancements in nanomedicine have recognized the use of Au in the therapeutic delivery of drugs or as a therapeutic modality in itself. For example, colloidal Au is covalently linked onto adenoviral vectors for selective cancer targeting and induces hyperthermia by application of near-infrared (NIR) laser light (Everts et al., 2006).

Recent advancements in the multi-functional design of gold nanoparticles allow for the generation of localized heat in the proximity of cancer tissues and additionally allow the delivery of multiple desired drugs in a controlled and targeted manner. Gold nanoparticles have many benefits that make them suitable for the photothermal treatment of cancer such as: (1) they can be administered into the local tumor area while minimizing non-specific distribution, (2) they can be activated via near-infrared (NIR) laser light, creating the ability to penetrate deep into biological tissues, and (3) they can be modulated to create multifaceted cancer PTT and drug delivery systems (Kennedy et al., 2011).

Gold's Localized Surface Plasmon Resonance (LSPR) as a Distinctive Photo-Active Property

Colloidal Au exhibits a unique localized surface plasmon resonance (LSPR) when a specific wavelength of light meets electrons on the surface of gold. LSPR is defined as an optical phenomenon where interactions occur between the incident light and surface electrons in a conduction band (Petryayeva and Krull, 2011). The light causes a collective coherent oscillation of conduction band electrons, leading to the subsequent extinction of light. Scattering and absorption of the light depends not only on the physical dimensions of the gold nanoparticle but also on the medium of the colloidal Au (El-Sayed, 2001; Kelly et al., 2003). Small colloidal Au absorbs the blue-green portion of the visible spectrum and visible light in the red portion of the visible light spectrum. However, in large colloidal Au, the LSPR results in the absorption of longer wavelengths of light along the red portion of the VLS, resulting in the reflection of light in the blue spectrum. A study of the LSPR spectra of different colloidal Au also indicates a shift toward the red spectrum. For example, 22 nm of colloidal Au in water exhibited a maximum absorption spectrum at 517 nm. However, when 99 mm of colloidal Au is present, there is a significant shift toward the red end of the

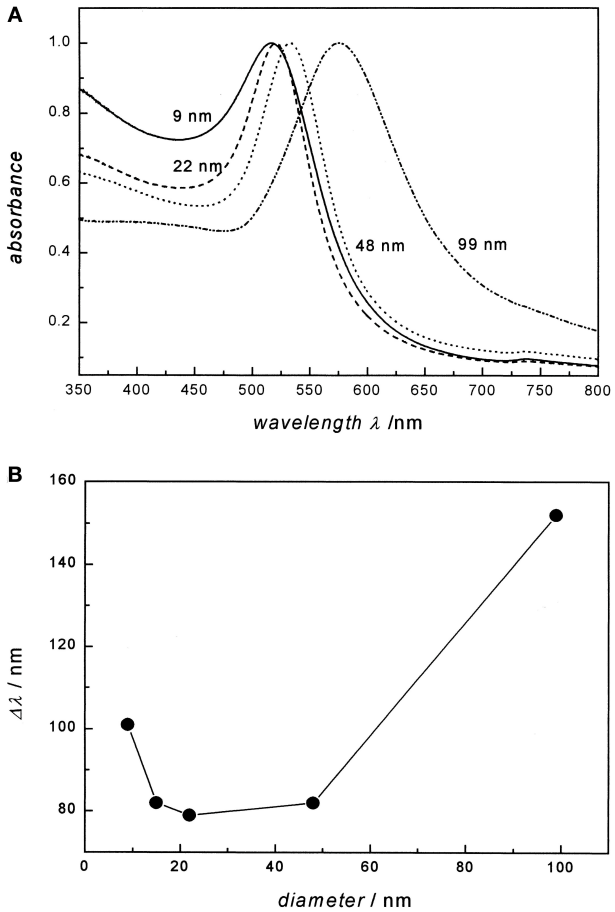

FIGURE 1 | Particle diameter of Au on the absorption spectra and the plasmon bandwidth. **(A)** UV/ Visual absorption spectra of 9, 22, 48, and 99 nm gold nanoparticles in water. All spectra are normalized at their absorption maxima, which are 517, 521, 533, and 575 nm, respectively. **(B)** The plasmon bandwidth $\Delta\lambda$ as a function of particle diameter. Re-printed with permission from American Chemistry Society Publications 1999 (Link and El-Sayed, 1999).

spectrum (Link and El-Sayed, 1999). It is therefore known that the plasmon bandwidth of the gold nanoparticles is affected by the particle diameters of colloidal Au (**Figure 1**).

To modulate the LSPR of the gold, several different shapes and sizes of gold have been studied. Gold (Au) nanorods (GNRs) are able to present longitudinal and transverse surface plasmon absorption peaks (Smitha et al., 2013). The length of Au nanorods presents the longitudinal resonance whereas the transverse resonance is attributed to the diameter of the GNRs. It is well-known that the spectral location of the LSPR can be modulated by changing the aspect ratio of GNRs (Smitha et al., 2013). GNRs with different aspect ratios (length/width) create different-color nanorod solutions due to changes in their reaction with light in the visible light spectrum (**Figure 2**) (Pérez-Juste et al., 2005). Similarly, three-tipped Au nanoparticles fabricated using a wet technique showed a significant red-shift compared to spherical-shaped gold nanoparticles (Hao et al., 2004). The branched colloidal Au particles exhibited a plasma band between 650 and 700 nm, while the maximum absorption spectrum for regular, spherical shaped colloidal Au was between 500 and 530 nm. Because the resonant excitation of plasmons is affected by the surface of nanoparticles, a gold nanostar as defined by a solid core with protruding prolate tips, can exhibit hybridized plasmons because they are made with a solid core that has tips (Hao et al., 2007). Liu et al. manipulated the growth of gold nanostars using a 4-(2-hydroxyethyl)-1-piperazineethanesulfonic acid (HEPES) solution, which acts as a reducing and capping agent for gold nanocrystals (**Figure 3**) (Liu et al., 2014). The fabricated gold nanostars demonstrated a red-shift from 557 to 704 nm. The more HEPES solution was added, the more reducing power was exhibited in the growth of gold branches, appearing at up to 20 nm in length. The elongated Au branches resulted in enhanced longitudinal plasmon resonances.

Another unique shape of Au capable of tuning LSPR that has been developed is Au nanorings. Au nanorings with diameters between 75 and 150 nm were fabricated using colloidal lithography (Larsson et al., 2007). The LSPR of different nanorings between 75 and 150 nm in diameter was between 1,000 and 1,300 nm, indicating that the diameter of the ring-like Au structures contributed to the tunability of the Au nanostructures. Using different fabrication methods, nanospheres, nanocubes, nanobranches, nanorods, and nanobipyramids were prepared and characterized for LSPR (**Figure 4**) (Chen et al., 2008). As expected, Au nanospheres and nanocubes exhibited one surface plasmon peak, whereas nanobranches, nanorods, and nanobipyramids exhibit two major surface plasmon peaks. There is a consistent LSPR shift toward light in the red spectrum from nanospheres (**Figure 5A** wave a), nanocubes (**Figure 5A** wave b), and nanorods with different aspect ratios (**Figure 5A** wave c–e). The larger aspect ratio of the nanorods exhibits a longer red-spectrum shift in the nanorods (**Figure 5A** wave c–e, the aspect ratios were 2.4 $\pm$ 0.3, 3.4 $\pm$ 0.5, and 4.6 $\pm$ 0.8, respectively). Exhibiting a similar pattern, nanobipyramids with different aspect ratios also show a red spectrum shift (**Figure 5B** wave a–d). The highest red spectrum shift was found in fabricated nanobranches due to their considerable longitudinal electron oscillation (**Figure 5B** wave e).

GOLD NANOPARTICLE SYNTHESIS

Gold nanoparticles are synthesized via either physical or chemical approaches wherein either a bottom-up or top-down approach is taken (Cunningham and and Bürgi, 2013; Aminabad et al., 2018). Bottom-up methods typically involve the nucleation of gold on top of smaller structures using either chemical, electrochemical, or thermal reduction techniques (Singh et al., 2011; Cunningham and and Bürgi, 2013; Shah et al., 2014).

The most commonly used of the bottom-up techniques is the Turkevich and Brust method, wherein metal salts are reduced in order to produce spherical, monodisperse GNPs around 10–20 nm in diameter (Cunningham and and Bürgi, 2013; Shah et al., 2014). Sodium citrate salts are commonly used to serve as both a reducing agent and stabilizer that acts to prevent GNP aggregation during synthesis (Zare et al., 2010). In lieu of citrate,

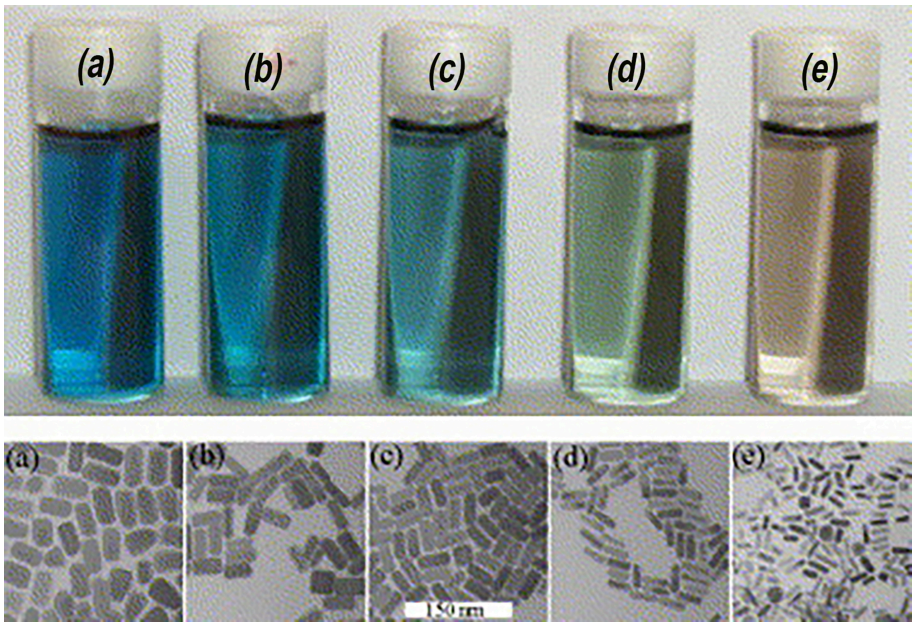

FIGURE 2 | Color of gold nanorods with different aspect ratios. The small difference in the aspect ratio shows distinctive transmitted colors in the samples. Re-printed with permission from Elsevier 2005 (Pérez-Juste et al., 2005).

ascorbic acid, amino acids, and UV light have all been used as reducing agents (Mieszawska et al., 2013). Schiffrin-Brust is an early, two-phase procedure employing tetrabutylammonium bromide (TOAB) to transfer gold from organic to inorganic solutions, enabling the synthesis of GNPs in organic solutions with high stability (Li et al., 2011; Herizchi et al., 2016). Using this method, GNPs ranging from 2 to 6 nm in diameter can be synthesized.

The most commonly employed Top-down techniques usually create nanoscale materials through the processing of larger macroscale structures via techniques such as lithography (Cunningham and and Bürgi, 2013). Other commonly employed physical synthesis methods include sonochemical, microwave, and photochemical based methods (Herizchi et al., 2016). A recently developed technique utilizes N-cholyl-L-valine (NaValC) as a self-reducing and stabilizing agent intended to be coupled with natural sunlight irradiation for the synthesis of GNPs (Annadhasan et al., 2015). By modifying the ratio of Au^{3+} to NaValC ions, the amount of sunlight irradiation, pH, and the reaction time, the size and shape of synthesized GNPs can be changed.

Recently, a new fabrication method was developed in which aqueous $[AuCl_4]$ can be irradiated with 532 nm nanosecond laser pulses to produce monodisperse 5 nm GNPs without the utilization of capping agents or additives, eliminating the possibility of contamination by residual chemicals (Rodrigues et al., 2018). Five hundred and thirty two nanometer nanosecond laser irradiation results in a more uniform monodispersion of 5 nm diameter GNPs compared to older methods using 800 nm femtosecond laser irradiation, which generally results in the growth of nanoparticles as large as 40 nm.

GOLD NANOPARTICLES FOR EFFICIENT CANCER THERAPY

Gold nanoparticles (GNPs) have been investigated in the context of various cancer therapies and are sought after as a potential alternative or adjunct to many non-selective chemotherapeutic agents as a means by which to improve therapeutic outcomes while reducing undesirable side effects (Jain et al., 2012). The efficacy of plasmonic gold nanoparticles for the thermo-ablation of various cell types has been demonstrated in multiple studies. The efficacy of gold nanoparticles for the thermal-mediated induction of cellular death was demonstrated by Pitsillides et al. (2003), wherein anti-CD8-labeled GNPs were used for the selective targeting and destruction of T-cells (Pitsillides et al., 2003).

Biocompatibility of Gold Nanoparticles

GNPs are considered non-cytotoxic overall with the expectation that despite their small size (2–4 nm), they are likely to be rapidly excreted via the kidneys (Longmire et al., 2008; Alric et al., 2013). In terms of localized non-specific cytotoxicity, study results are mixed, with some studies demonstrating no cellular toxicity and others demonstrating the production of cellular reactive oxygen species, apoptosis, necrosis, and acute mitochondrial toxicity (Shukla et al., 2005; Pan et al., 2009; Balasubramanian et al., 2010). Sufficient accumulation of GNPs inside the body can cause nontoxicity, as demonstrated by the fact that when GNPs accumulate within the liver, tissue apoptosis, acute inflammation, and an increase in Kupffer cells can occur (Longmire et al., 2008; Chen et al., 2009; Cho et al., 2009; Khlebtsov and Dykman, 2011). However, this effect is largely size-dependent, as smaller GNPs

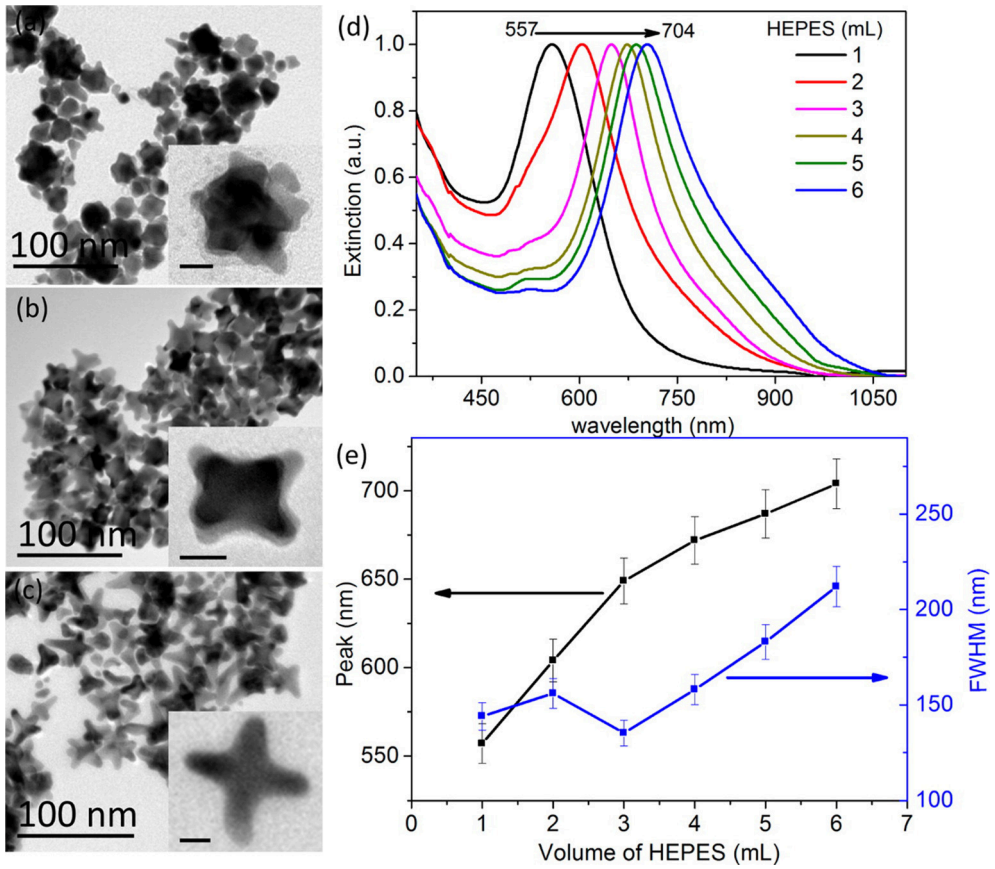

FIGURE 3 | Fabrication of gold nanostars with different shapes. TEM images of gold nanostars prepared at 30°C are shown in the left panel. The authors were able to create different shapes by adding **(a)** 1, **(b)** 3, and **(c)** 6 mL of HEPES solution (0.1 M). The scale bar indicates 10 nm. **(d)** Normalized extinction spectra of gold nanostars with different volumes of HEPES. **(e)** The main extinction peak and FWHM (full width at half-maximum) as a function of HEPES volume. Re-printed with permission from American Chemistry Society Publications 2014 (Liu et al., 2014).

(<8 nm) are capable of passing through the renal filtration system whereas larger GNPs (>10 nm) are more likely to remain in the blood stream, and thus accumulate in the liver and kidney (Bartneck et al., 2012; Zhang et al., 2012; Blanco et al., 2015). It is therefore known that the toxicity of GNPs greatly depends on their specific size and configuration.

The effect of GNPs on the immune system likely depends on their configuration, with one study showing that GNPs can induce pro-inflammatory responses contingent on their size (Yen et al., 2009) and other studies showing anti-inflammatory responses (Tsai et al., 2012; Sumbayev et al., 2013). In these studies, a consistent theme is the role of GNP size on the nature and scale of the inflammatory response with one study illustrating that nanoparticles of 5 nm in size were capable of significantly inhibiting production of IL-1B in THP-1 derived macrophages with 35 nm sized nanoparticles demonstrating no effect (Sumbayev et al., 2013). A similar study showed that 4 nm diameter GNPs inhibited inflammatory responses in RAW269 derived murine macrophages via the inhibition of TLR9 responses, likely by binding and interfering with high-mobility group box-1 (Tsai et al., 2012). In contrast, the enhanced inflammatory response exhibited in another study can be explained by the fact that the sizes were larger on average, with sizes ranging from 14 to 100 nm, with larger sizes demonstrating the greatest upregulations in IL-1, IL-6, and TNF-alpha (Yen et al., 2009).

Surface Modification of Gold Nanoparticles for Specific Tumor Targeting

Because of the leaky nature of immature vasculature found at the sites of tumors, GNPs can passively accumulate at tumor sites, where they are likely taken into cells via non-specific receptor-mediated endocytosis (RME) (Maeda, 2001; Chithrani et al., 2006). However, while GNPs may be capable of passive delivery to tumor sites to some extent, there are still limitations owing to the heterogeneity of vasculature in different types of cancers. Passive delivery is also further inhibited by particles and uptake on behalf of the reticuloendothelial system (RES) (Fang et al., 2011). Therefore, more specific methods for the targeted delivery of GNPs to sites of tumor growth are necessitated.

GNPs also exhibit unique physiochemical properties such as the ability to bind thiol and amine groups along with surface plasmon resonance (SPR), which allows their specific modification for more targeted cancer therapies (Shukla et al., 2005). This property enables the implementation of surface

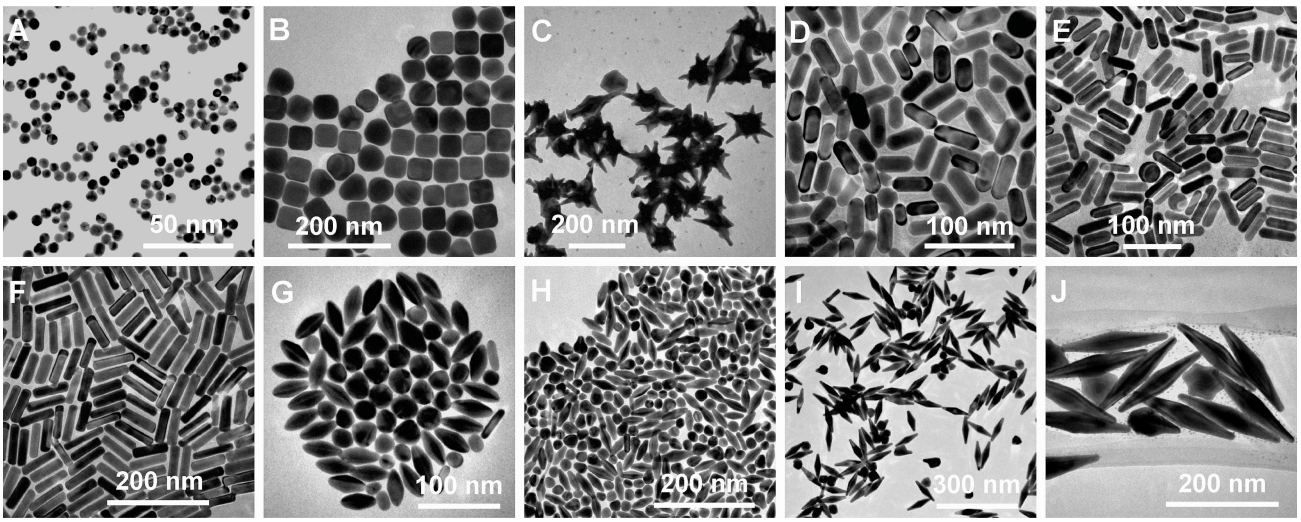

FIGURE 4 | Diversity of gold nanostructures. **(A)** Nanospheres. **(B)** Nanocubes. **(C)** Nanobranches. **(D)** Nanorods (aspect ratio = 2.4 ± 0.3). **(E)** Nanorods (aspect ratio = 3.4 ± 0.5). **(F)** Nanorods (aspect ratio = 4.6 ± 0.8). **(G)** Nanobipyramids (aspect ratio = 1.5 ± 0.3). **(H)** Nanobipyramids (aspect ratio = 2.7 ± 0.2). **(I)** Nanobipyramids (aspect ratio = 3.9 ± 0.2). **(J)** Nanobipyramids (aspect ratio = 4.7 ± 0.2). Re-printed with permission from American Chemistry Society Publications 2008 (Chen et al., 2008).

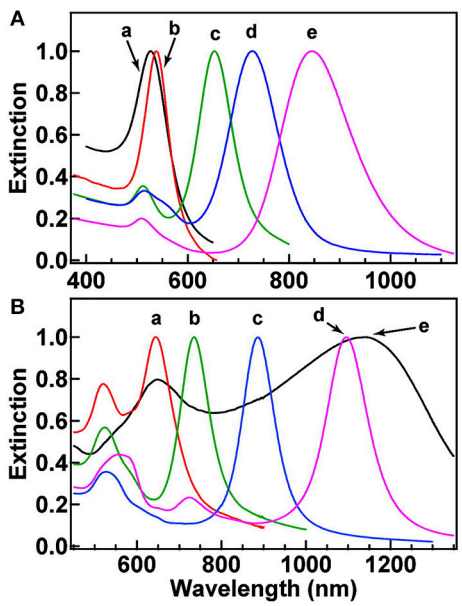

FIGURE 5 | Normalized extinction spectra of the gold nanostructures. **(A)** Spectra a–e correspond to nanospheres (aspect ratio = 2.4 ± 0.3), nanocubes (aspect ratio = 3.4 ± 0.5), and nanorods with aspect ratios of 4.6 ± 0.8. **(B)** Spectra a–d correspond to nanobipyramids with different aspect ratios (as shown 1.5 ± 0.3, 2.7 ± 0.2, 3.9 ± 0.2, and 4.7 ± 0.2, respectively) and nanobranches (spectra e). Re-printed with permission from American Chemistry Society Publications 2008 (Chen et al., 2008).

modifications that can enhance passive cellular uptake. One such method is known as PEGylation, which can be achieved by using thiol-terminated methoxypoly (ethylene glycol) to replace the stabilizing surfactant bilayers that normally surround GNPs (Liao and Hafner, 2005). By modifying the surface of GNPs with polyethylene glycol, cellular uptake may be enhanced due to the affinity of PEG for cellular membranes (Choi et al., 2003; Paciotti et al., 2006).

In one study demonstrating this principle, pH-sensitive, multifunctional gold nanocomposites were created by conjugating the anti-cancer drug doxorubicin hydrochloride to GNPs using Adamantane-PEG(8)-RGDS molecules, thus creating AuNP@CD-AD-DOX/RGD GNPs. The RGD peptide sequence was included to target the alphavbeta3 integrin, which is known to be overexpressed on the surface of cancer cells, therein facilitating receptor-mediated endocytosis of the GNPs into the cancer cells. Following cellular uptake and internalization into endo/lysosomes, the hydrazine linkage between adamantane and doxorubicin is cleaved owing to acid-mediated degradation. Experiments demonstrated the uptake of AuNP@CD-AD-DOX/RGD gold nanoparticles and subsequent release of DOX once internalized into cellular endo/lysosomes, resulting in the induction of apoptosis within cancer cells (Chen et al., 2015).

For example, more specific targeting of tumors can be achieved by conjugating tumor-specific recognition molecules such as transferrin, folic acid, epidermal growth factor (EGF), or any number of monoclonal antibodies to the surface of GNPs (El-Sayed et al., 2005; Chithrani et al., 2006; Eghtedari et al., 2009). This strategy has been employed with promising effects in multiple studies. In one study, citrate-coated GNPs were conjugated with trastuzumab (anti-EGF receptor monoclonal antibodies) to target EGF receptors in human SK-BR-3 breast cancer cells, resulting in downstream expression of EGF receptors and a 2-fold increase in trastuzumab cytotoxicity, even at low GNP concentrations (Jiang et al., 2008). In another study, GNPs

were conjugated to gemcitabine and cetuximab for the treatment of pancreatic cancer (Patra et al., 2010). Furthermore, phase II trials using this combination have been in clinical trials for this purpose (Kullmann et al., 2009). By using this targeted approach, it was shown that it is possible to utilize much higher concentrations of GNPs while simultaneously avoiding substantial accumulation of nanoparticles within the liver and kidneys (Patra et al., 2008).

In a recent study by Kim et al. NIR plasmonic gold nanoparticles possessing both photothermal and photoacoustic properties allowing for both enhanced contrast imaging and therapeutic applications were developed (Kim et al., 2017). To accomplish this, bioconjugates were created in which human methyl binding domain protein 1 (MBD1) binds to methylated cytosine-guanine dinucleotides (mCGs) within sequences of short double-strand DNA (sh-dsDNA), with hexahistidine peptides serving as nucleation sites for GNP synthesis. The synthesis of these hybrid GNP constructs called DMAs (sh-dsDNA-MBD1-AuNPs), allowed for the modification of photothermal and photoacoustic properties by changing the length of the sh-dsDNA backbone. Three sh-dsDNA backbone lengths were investigated (DMA_5mCG, DMA_9mCG, and DMA_21mCG). Interestingly, the DMA_21mCG conjugate exhibited similar photothermal properties and, surprisingly, higher photoacoustic properties compared to regular plasmonic gold nanorods. By further conjugating peptide sequences with a specific affinity to EGF receptor, it is possible to target cancer cells overexpressing the EGF receptor.

Considering that an important component of tumor progression is the ability of many cancers to evade and suppress the host's immune system (Kim et al., 2006; Finn, 2008), finding methods to improve the ability of the immune system to target cancers is of growing interest. Various factors such as nanoparticle shape, charge, particle size, and coating can influence their blood clearance and organ accumulation, with smaller particles and coated particles exhibiting an ability to more widely distribute within the body (Sonavane et al., 2008; Almeida et al., 2011, 2014; Hirn et al., 2011; Khlebtsov and Dykman, 2011). GNPs are further known to accumulate in organs such as the liver and spleen, where they are likely to interact with the patient's immune system (Zhang et al., 2009). Considering that GNPs are known to accumulate within immune cells, the utilization of GNPs as a drug delivery methodology for immunotherapy has seen an increase in interest.

Because of their strong SPR, GNPs are consistently considered for use in photodynamic therapy (PDT), where light-induced heating can be exploited to either induce heating to release a chemical payload or to generate reactive oxygen species to induce either cellular necrosis or apoptosis at specific tumor sites (Harris et al., 2006; Pissuwan et al., 2006, 2009; Norman et al., 2008). In one study, a 4-component antibody-phtalocyanine-polyethyline glycol-gold nanoparticle conjugate was developed for use in a PDT approach to target breast cancer. Zinc-phtalocyanine, a known photosensitizer, was conjugated to GNPs along with Anti-HER2 monoclonal antibodies, which are known to target cancer cells overexpressing the HER2 epidermal growth factor cell surface receptor (Stuchinskaya et al., 2011). Experiments demonstrated the ability of the nanoparticle conjugates to selectively target and induce the apoptosis of breast cancer cells.

COMMONLY USED GOLD NANOPARTICLE CONFIGURATIONS

While tissues have limitations related to PDT mediated by ether laser light or light within the visible spectrum due to limited depth of penetration (Ochsner, 1997; Wilson and Patterson, 2008; Benov, 2015), near-infrared light in the range of 800–1,200 nm has much greater body transparency. Fortunately, by modifying the shape of GNPs, such as by using GNRs or hollow gold nanoshells, their resonance peak can be shifted toward the NIR spectrum (Loo et al., 2004). In this regard, various gold nanoparticle configurations have been employed to modify their photothermal and subsequently therapeutic efficiencies (Vats et al., 2017).

Gold Nanospheres

Gold nanospheres (GNS) are perhaps one of the earliest GNP shape configurations to be studied, with some of the first demonstrations of the use of GNS for PTT being performed by El-Sayed et al. (Huang et al., 2008). GNS were popularized by their ease of fabrication, small size, fast synthesis, and ease of ligand conjugation, making them attractive for PTT applications (Day et al., 2010). Various modified forms of gold nanospheres have been shown to exhibit therapeutic properties when conjugated to antibodies targeting tumors overexpressing specific proteins (Day et al., 2010), and have been modified with other metals to improve their photoacoustic and photothermal properties (Zhang et al., 2015). Thermo-labile liposome-based GNS (LiposAu NPs) have also been developed for the purpose of cancer photo thermal therapy. The bioabsorbable core of these liposome-based gold nanospheres provides a beneficial structure that allows for more efficient body clearance of the gold via hepato-biliary and renal routes (Rengan et al., 2014, 2015).

Gold Nanostars

Gold nanostars have recently gained notoriety because of their enhanced NIR light-absorbing capability in addition to their reduced toxicity (Chen et al., 2015). Further, their thin, branch-like structure gives them tip-enhanced plasmonic properties (Ahmad et al., 2016). Many studies have demonstrated the successful utilization of multifunctional gold nanostars for photothermal applications using NIR wavelength light in the targeting of various types of cancer cells in various modified forms (Chen et al., 2013; Gao et al., 2015; Li et al., 2016). In one study, octahedral solid core Au nanohexapods were fabricated by reducing HAuCl4 with DMF in an aqueous solution containing Au octahedral seeds (Wang et al., 2013). Relative to gold nanorods (GNRs) and nanocages, PEGylated nanohexapods demonstrated the greatest tumor uptake and photothermal conversion efficiency.

Gold Nanoshells

Gold nanoshells are another widely utilized GNP configuration. The gold nanoshell structure consists of dielectric silica gels that are encased within a thin, hollow, outer gold shell (O'Neal et al., 2004). By modifying shell thickness and core diameter, it is possible to configure gold nanoshells to absorb light in the NIR spectrum, making them suitable for photothermal and photoacoustic applications (Hirsch et al., 2003). Various surface modifications have been applied to gold nanoshells to functionalize them for anti-tumor therapy. To encourage natural accumulation of nanoparticles at tumor sites, West et al. synthesized PEGylated gold nanoshells by conjugating nanoshells with PEG-SH (O'Neal et al., 2004). For example, anti-EGFR antibodies have been conjugated to a nanoshell platform for breast cancer therapy (Loo et al., 2005). In another study, branched nanostructure gold nanoshells with PLGA/DOXO-cores underwent a tri-modal modification consisting of functionalization with human serum albumin/indocyanine green/folic acid applied to enhance both their targeting and enhanced photothermal properties on account of the NIR-responsive indocyanine green dye (Topete et al., 2014).

Gold nanoshell configurations provide unique flexibility due to their method of fabrication, allowing them to mimic the specific aspect ratios of other nanomaterial configurations such as nanorods to enhance properties such as cellular uptake and increasing drug loading capabilities due to higher superficial surface areas. As a recent study demonstrates, rod-like, gold nanoshell mesoporous silica nanoparticles (MSNR@Au hybrid) were fabricated and further functionalized via modification with ultrasmall gadolinium (Gd) chelated supramolecular photosensitizers TPPS4 [MSNR@Au-TPPS4(Gd)] to enable quadmodal imaging with near-infrared fluorescence (NIRF), multispectral optoacoustic tomography (MSOT), computed tomography (CT), and magnetic resonance (MR) in addition to its inherent NIR driven photothermal capability (Yang et al., 2019).

Gold Nanorods

Gold nanorods (GNRs) were first synthesized by Wang et al. (Chang et al., 1997), with the first documented use of nanorods for use in NIR spectrum photothermic therapy being reported in 2006 by El-Sayed et al. (Jain et al., 2006). The unique shape of GNRs confers strong photothermal properties due to the presence of both longitudinal and transverse plasmon (Hwang et al., 2014). These strong photothermal properties have been used for anti-tumorigenic applications, many times utilizing various surface modifications such as conjugating surface antibodies for specific targeting, utilizing dendrimer stabilization, or even developing a chitosan oligosaccharide surface modification (Charan et al., 2012; Wang et al., 2016). In one study performed by Cui et al. GNRs were loaded onto induced pluripotent stem cells (AuNR-iPS) for the purpose of targeting human gastric cancer cells. It was demonstrated that AuNR-iPS were able to localize to human gastric cancer tumors and induce thermal-mediated apoptosis and reduction in tumor volume following NIR irradiation (Liu et al., 2016).

GNRs appear to be among the most utilized GNP configurations, with consistent development of GNR based photothermal technologies demonstrated in recent history. In one such recent study, inorganic phototherapeutic nanocomplexes were created by conjugating GNRs with defective TiO2 nanoparticle clusters (AuNR-TiO2 NP clusters) to reduce the need for organic photosensitizers, which are sensitive to photobleaching and unnecessary energy transfer (Lee et al., 2018). These nanoparticle clusters were capable of absorbing both visible and NIR light from the 500 to 1,000 nm spectrum, demonstrating the ability to induce cell death in HeLa cells via the photothermal production of ROS. Notable derivatives of GNR configurations are also coming to the forefront of photothermal cancer therapeutics. In another recent study, the lumens of halloysite nanotubes (HNTs) were loaded with GNRs and doxorubicin (DOX) following which, the GNR filled HNTs were conjugated with folic acid using bovine serum albumin for more specific tumor targeting (Au-HNTs-DOX@BSA-FA) (Zhang et al., 2019). By combining the chemotherapeutic approach of DOX with the photothermal capability of GNRs, it was possible to reduce collateral damage to healthy tissues by DOX while still achieving the same therapeutic outcomes.

Other Gold Nanoparticle Configurations

The development of new GNP configurations continues to evolve as new synthesis methodologies are continually developed. As an example of a recently developed technology, Zhang et al. exploited extracellular vesicles to generate popcorn-like gold nanostructures (Zhang et al., 2019). These extracellular vesicles enabled the encapsulation of DOX while serving as a nucleation site for gold nanoparticle shells, allowing for simultaneous photothermal transduction and chemotherapeutic potential. Overall, this technology provided a novel modality for the green synthesis of GNPs while improving cellular internalization allowing for tumor inhibitory rates of up to 98.6%.

Gold nanoflowers (GNFs) are a unique GNP configuration that was recently developed by Li et al. (2015). This technology takes advantage of the superior photothermal conversion efficiency of gold nanostars over GNRs and gold nanoshells while also providing a hollow core structure to enhance therapeutic efficiency by enabling chemotherapeutic drug loading. Some recent modifications of the GNF technology include the encapsulation of ultrasmall iron oxide nanoparticles for multimodal image therapy (Lu et al., 2018) and self-assembly using vapreotide acetate (Vap) for enhanced photothermal conversion efficiency as well as enhanced biocompatibility (Yin et al., 2018).

FUTURE DIRECTIONS: GREEN SYNTHESIS OF GOLD NANOPARTICLES INCORPORATED WITH NATURAL SUBSTANCES

Isolation and fabrication of gold nanoparticles from natural substances may provide some benefits over traditional synthesis methodologies. It is speculated that the green synthesis of

TABLE 1 | Green chemistry for gold nanoparticle synthesis.

	Source	Size (nm)	Morphology	References
Bacteria	*Bacillus megatherium* D01	1.9 ± 0.8	Spherical	Iravani, 2014
	Bacillus subtilis 168	5–25	Octahedral	
	Escherichia coli DH5α	25 ± 8	Spherical, triangular, and quasi-hexagonal	
	Escherichia coli MC4100	10–25	Spherical, triangular, hexagonal, and rod shape	
	Geobacillus sp.	5–50	Quasi-hexagonal	
	Lactobacillus strains	20–50	Crystalline, hexagonal, triangular, and cluster	
	Plectonema boryanum UTEX 485	10 up to 6 μm	Cubic and octahedral platelet	
	Pseudomonas fluorescens	50–70	Spherical	
	Rhodopseudomonas capsulata	10–20	Nanoplate and spherical	
Fungi	*Fusarium oxysporum*	8–40	Spherical	Mukherjee et al., 2002
	Verticillium sp.	5–200 (average 20 ± 8 nm)	Spherical	Mukherjee et al., 2001
Plant	Apiin extracted from henna leaves	7.5–65	Quasi-spherical	Iravani, 2011
	Camellia sinensis (green tea)	40	Spherical, triangular, irregular	
	Coridandrum sativum (coriander)	6.75–57.91	Spherical, triangular, truncated triangular, decahedral	
	Cymbopogon flexuosus (lemongrass)	200–500	Spherical, triangular	
	Eucalyptus camaldulensis (river red gum)	1.25–17.5	Crystalline, spherical	
	Medicago sativa (alfalfa)	2–40	Irregular, tetrahedral, hexagonal platelet, decahedral, icosahedral	
	Mentha piperita (peppermint)	150	Spherical	
	Murraya koenigii	20	Spherical, triangular	
	Ocimum sanctum (tulsi; leaf extract)	30	Crystalline, hexagonal, triangular	
	Pear fruit extract	200–500	Triangular, hexagonal	
	Pelargonium graveolens (geranium)	20–40	Decahedral, icosahedral	
	Psidium guajava (guava)	25–30	Mostly spherical	
	Scutellaria barbata D. Don (Barbated skullcup)	5–30	Spherical,triangular	
	Sesbania drummondii (leguminous shrub)	6–20	Spherical	
	Syzgium aromaticum (clove)	5–100	Crystalline, irregular, spherical, elliptical	
	Tamarindus indica (tamarind)	20–40	Triangular	
	Terminalia catappa (almond)	10–35	Spherical	
	Trichoderma koningii	30–40	Triangular	

gold nanoparticles using natural substances may enhance their medical properties such as their anti-microbial and anti-cancer activity, and contribute to reducing and stabilizing agents for the synthesis of nanoparticles (Kumar and Yadav, 2008). Synthesis of GNPs in this fashion is considered more cost-effective and may result in the production of GNPs that have fewer to no side effects due to the reduction of residual chemicals necessary for gold nanoparticle synthesis. The most prominent sources for the green synthesis of GNPs include Bacterium, Fungi, and Plants (**Table 1**).

Extracts from the leaves of *Catharanthus roseus* (CR) and *Carica papaya* (CP), which contain active components associated with the treatment and prevention of cancer, were conjugated to gold nanoparticles. It is likely that the stabilizing molecules were alkaloids, flavones, and proteins that are present on the leaf extracts. The biogenic gold nanoparticles have demonstrated a consistent ability to negatively influence the viability of HepG2 liver cancer cells and MCF7 breast cancer cells due to the synergism of delivery with gold nanoparticles and the anti-cancer activity of the plant extracts. The anti-bacterial activity of the gold nanoparticles was also investigated against gram positive bacteria. However, it was noted that gold nanoparticles are considered to have greater activity against gram negative bacteria, meaning that the results may have underestimated their anti-bacterial properties (Muthukumar et al., 2016).

In another study, gold nanoparticles were fabricated and conjugated with baicalin, which is an active flavonoid that can be found in *Scutellaria baicalensis* and has anti-cancer properties. The gold particles synthesized by baicalin demonstrated cytotoxicity against the MCF7 cell line. Western blot analysis showed greater expression of Aparf-1 and cleaved capase-3 bands in the cell groups treated with

baicalin-complexed gold nanoparticles compared to controls, indicating that the baicalin-conjugated gold nanoparticles negatively influenced breast cancer growth by inducing apoptosis (Lee et al., 2016). In another study, croin, which is the main carotenoid found in Saffron stigma (*Crocus sativus*), which exhibits antioxidative activity, mediated the reduction reaction of Au 3^+ ions performing fast formation gold nanoparticles of controlled sizes. Gold nanoparticles conjugated with croin effectively suppressed the proliferation of breast cancer cells in a time- and dose-dependent manner. The study also demonstrated that there was no cytotoxic effect against normal cells (MCF-10A) (Hoshyar et al., 2016).

Gold nanoparticles conjugated with plant extracts derived from the leaves and stems of *Hibiscus sabdariffa* were reported to have selective cytotoxic activity against U87 glioblastoma (GNB) cells. The cellular viability of normal 293 cells and U87 GMB cells treated with gold nanoparticles was analyzed using an MTT assay. The MTT assay results demonstrated that there was a dose-dependent cytotoxicity against U87 GMB cells; however, there was no significant toxicity detected among normal cell lines. Further, it was demonstrated that a concentration of 2.0 ng/mL of biogenic gold nanoparticles induced cell death of more than 80% of cancer cells under both normal and hyperglycemic conditions. In addition, cells treated with a concentration of 2.5 ng/mL of gold nanoparticles demonstrated degradation of GAPDH (glyceraldehyde-3-phosphate dehydrogenase), which is known to be over-expressed in cancer (Mishra et al., 2016).

Overall, the utilization of natural derivatives as an adjunct to cancer therapy using gold nanoparticles appears to be a promising approach for the selective targeting of tumors while subsequently reducing any side effects that may be incurred via the utilization of synthetic drug compounds.

LIMITATIONS OF GOLD NANOPARTICLES FOR PTT

To be considered an ideal candidate for PTT, a specific set of requirements should be met. For example, the ideal PTT candidate should be: (i) of a suitable nanoparticulate size and of uniform shape; (ii) have good dispersibility in aqueous solutions; (iii) respond to light in the NIR range of 650–950 nm to prevent damage to surrounding healthy tissues, provide sufficient photothermal efficiency, and to enable sufficient depth of penetration; (iv) be sufficiently photostable to ensure adequate diffusion time to reach tumors before losing their photosensitivity, (v) exhibit low or no cytotoxicity in living systems (Zhou et al., 2013).

While GNPs fulfill most of these requirements, its long-term cytotoxicity is largely unknown. As discussed earlier, while GNPs are considered to be largely biocompatible, the long-term consequences of nanoparticle accumulation are not fully understood. However, there are some initial studies hinting at potential factors that can influence GNP cytotoxicity. Based on these studies, it is believed that size and surface charge are likely to be the most influential factors. For example, it was demonstrated that 46% of the initial dose of 5 nm positively charged gold-dendrimer complex particles were excreted after 5 days. In contrast, another study found that for 5 nm particles that were negatively or neutrally charged or for nanoparticles measuring above 11 nm, only about 10% of the initial dose was excreted (Balogh et al., 2007). The areas with the largest accumulation tend to be the liver and spleen, with one study finding foreign bodies in 7 out of 8 spleens and 8 out of 8 livers from animals that received intravenous injection of PEG-coated GNRs (Goodrich et al., 2010). It was speculated that these foreign bodies arose from the aggregation of GNRs in these tissues. Furthermore, evidence of chronic inflammation characterized as minimal to mild was observed in the areas around these foreign bodies, although the long-term consequences of this inflammation were not clear from the study.

Unfortunately, studies on GNPs have only taken place in animal models up to a 6-month time-frame, leaving unanswered questions as to how GNPs influence health over longer time courses. Therefore, while initial studies are promising regarding issues of potential cytotoxicity, there are still questions as to whether GNPs eventually clear from the body and if there are potentially long-term consequences resulting from GNP accumulation (Goodrich et al., 2010).

In addition to the fact that the issue of biocompatibility surrounding GNPs is not completely resolved, there are other currently existing technologies that could potentially make the utilization of GNPs obsolete. As an example, the utilization of specific biodegradable polymer systems for PTT has grown in prominence. A recent study highlights the use of a novel polymer based photothermal nanoagent capable of responding to light in the NIR-II spectrum (1,000–1,700 nm) (Sun et al., 2018), which is capable of much greater depth of tissue penetration than light in the NIR-I spectrum. However, it should be noted that GNPs could conceivably be modified via conjugation with NIR-II responsive polymers, although the potential advantages of doing so over using pure NIR-II polymer nanoparticles has not yet been explored.

CONCLUSION

Because of its bacteriostatic, anti-oxidative, and anti-corrosive properties, gold has been utilized for medical applications dating back centuries. In addition, its photothermal and photoacoustic properties, along with its ability to be manufactured at the nano-scale and functionalized with various drugs and targeting molecules, have caused gold nanoparticles to be recognized as an ideal multifunctional material for cancer therapeutics. Because of its successful documented use in *in vitro*, pre-clinical, and clinical studies, it has been demonstrated that GNP technology is a promising tool and it is worth investigating future directions that would allow for a further evolution of the use of GNPs for cancer therapeutics.

AUTHOR CONTRIBUTIONS

JV performed literature search as well as the majority of the authoring and editing. J-HY performed the literature search and writing for Future Directions. N-ER, D-JL, and HP proposed topic of paper and provided overall direction of manuscript. D-JL proposed figures and helped author introduction sections.

FUNDING

This study was supported by the Convergence of Conventional Medicine and Traditional Korean Medicine R&D program funded by the Ministry of Health & Welfare through the Korea Health Industry Development Institute (KHIDI) (HI16C0322) 2018.

REFERENCES

Ahmad, R., Fu, J., He, N., and Li, S. (2016). Advanced gold nanomaterials for photothermal therapy of cancer. *J. Nanosci. Nanotechnol.* 16, 67–80. doi: 10.1166/jnn.2016.10770

Almeida, J. P., Chen, A. L., Foster, A., and Drezek, R. (2011). *In vivo* biodistribution of nanoparticles. *Nanomedicine* 6, 815–835. doi: 10.2217/nnm.11.79

Almeida, J. P., Figueroa, E. R., and Drezek, R. A. (2014). Gold nanoparticle mediated cancer immunotherapy. *Nanomedicine.* 10, 503–514. doi: 10.1016/j.nano.2013.09.011

Alric, C., Miladi, I., Kryza, D., Taleb, J., Lux, F., Bazzi, R., et al. (2013). The biodistribution of gold nanoparticles designed for renal clearance. *Nanoscale.* 5, 5930–5939. doi: 10.1039/c3nr00012e

Aminabad, N. S., Farshbaf, M., and Akbarzadeh, A. (2018). Recent advances of gold nanoparticles in biomedical applications: state of the art. *Cell Biochem Biophys.* doi: 10.1007/s12013-018-0863-4. [Epub ahead of print].

Annadhasan, M., Kasthuri, J., and Rajendiran, N. (2015). Green synthesis of gold nanoparticles under sunlight irradiation and their colorimetric detection of Ni 2+ and Co 2+ ions. *RSC Adv.* 5, 11458–11468. doi: 10.1039/C4RA14034F

Ateh, D. D., Navsaria, H. A., and Vadgama, P. (2006). Polypyrrole-based conducting polymers and interactions with biological tissues. *J. R. Soc. Interface* 3, 741–752. doi: 10.1098/rsif.2006.0141

Balasubramanian, S. K., Jittiwat, J., Manikandan, J., Ong, C. N., Yu, L. E., and Ong, W. Y. (2010). Biodistribution of gold nanoparticles and gene expression changes in the liver and spleen after intravenous administration in rats. *Biomaterials* 31, 2034–2042. doi: 10.1016/j.biomaterials.2009.11.079

Balint, R., Cassidy, N. J., and Cartmell, S. H. (2014). Conductive polymers: towards a smart biomaterial for tissue engineering. *Acta Biomater.* 10, 2341–2353. doi: 10.1016/j.actbio.2014.02.015

Balogh, L., Nigavekar, S. S., Nair, B. M., Lesniak, W., Zhang, C., Sung, L. Y., et al. (2007). Significant effect of size on the *in vivo* biodistribution of gold composite nanodevices in mouse tumor models. *Nanomedicine.* 3, 281–296. doi: 10.1016/j.nano.2007.09.001

Bardhan, R., Lal, S., Joshi, A., and Halas, N. J. (2011). Theranostic nanoshells: from probe design to imaging and treatment of cancer. *Acc. Chem. Res.* 44, 936–946. doi: 10.1021/ar200023x

Bartneck, M., Ritz, T., Keul, H. A., Wambach, M., Bornemann, J., Gbureck, U., et al. (2012). Peptide-functionalized gold nanorods increase liver injury in hepatitis. *ACS Nano.* 6, 8767–8777. doi: 10.1021/nn302502u

Benov, L. (2015). Photodynamic therapy: current status and future directions. *Med. Princ. Pract.* 24(Suppl. 1), 14–28. doi: 10.1159/000362416

Blanco, E., Shen, H., and Ferrari, M. (2015). Principles of nanoparticle design for overcoming biological barriers to drug delivery. *Nat. Biotechnol.* 33, 941–951. doi: 10.1038/nbt.3330

Burke, A., Ding, X., Singh, R., Kraft, R. A., Levi-Polyachenko, N., Rylander, M. N., et al. (2009). Long-term survival following a single treatment of kidney tumors with multiwalled carbon nanotubes and near-infrared radiation. *Proc. Natl. Acad. Sci. USA.* 106, 12897–12902. doi: 10.1073/pnas.0905195106

Cassim, S. M., Giustini, A. J., Baker, I., and Hoopes, P. J. (2011). Development of novel magnetic nanoparticles for hyperthermia cancer therapy. *Proc. SPIE Int. Soc. Opt. Eng.* 7901:790115. doi: 10.1117/12.876514

Chang, S.-S., Lee, C.-L., and Wang, C. R. C. (1997). Gold nanorods: electrochemical synthesis and optical properties. *J. Phys. Chem. B* 101, 6661–6664. doi: 10.1021/jp971656q

Charan, S., Sanjiv, K., Singh, N., Chien, F. C., Chen, Y. F., Nergui, N. N., et al. (2012). Development of chitosan oligosaccharide-modified gold nanorods for *in vivo* targeted delivery and noninvasive imaging by NIR irradiation. *Bioconjug. Chem.* 23, 2173–2182. doi: 10.1021/bc3001276

Chatterjee, D. K., Diagaradjane, P., and Krishnan, S. (2011). Nanoparticle-mediated hyperthermia in cancer therapy. *Ther. Deliv.* 2, 1001–1014. doi: 10.4155/tde.11.72

Chen, H., Kou, X., Yang, Z., Ni, W., and Wang, J. (2008). Shape- and size-dependent refractive index sensitivity of gold nanoparticles. *Langmuir.* 24, 5233–5237. doi: 10.1021/la800305j

Chen, H., Zhang, X., Dai, S., Ma, Y., Cui, S., Achilefu, S., et al. (2013). Multifunctional gold nanostar conjugates for tumor imaging and combined photothermal and chemo-therapy. *Theranostics.* 3, 633–649. doi: 10.7150/thno.6630

Chen, M., Fang, X., Tang, S., and Zheng, N. (2012). Polypyrrole nanoparticles for high-performance *in vivo* near-infrared photothermal cancer therapy. *Chem. Commun.* 48, 8934–8936. doi: 10.1039/c2cc34463g

Chen, W.-H., Lei, Q., Luo, G.-F., Jia, H.-Z., Hong, S., Liu, Y.-X., et al. (2015). Rational design of multifunctional gold nanoparticles via host–guest interaction for cancer-targeted therapy. *ACS Appl. Mater. Interfaces.* 7, 17171–17180. doi: 10.1021/acsami.5b04031

Chen, Y. S., Hung, Y. C., Liau, I., and Huang, G. S. (2009). Assessment of the *in vivo* toxicity of gold nanoparticles. *Nanoscale Res. Lett.* 4, 858–864. doi: 10.1007/s11671-009-9334-6

Cheng, L., Wang, C., Feng, L., Yang, K., and Liu, Z. (2014). Functional nanomaterials for phototherapies of cancer. *Chem. Rev.* 114, 10869–10939. doi: 10.1021/cr400532z

Cheng, L., Yang, K., Chen, Q., and Liu, Z. (2012). Organic stealth nanoparticles for highly effective *in vivo* near-infrared photothermal therapy of cancer. *ACS Nano* 6, 5605–5613. doi: 10.1021/nn301539m

Chithrani, B. D., Ghazani, A. A., and Chan, W. C. (2006). Determining the size and shape dependence of gold nanoparticle uptake into mammalian cells. *Nano Lett.* 6, 662–668. doi: 10.1021/nl052396o

Cho, W. S., Cho, M., Jeong, J., Choi, M., Cho, H. Y., Han, B. S., et al. (2009). Acute toxicity and pharmacokinetics of 13 nm-sized PEG-coated gold nanoparticles. *Toxicol. Appl. Pharmacol.* 236, 16–24. doi: 10.1016/j.taap.2008.12.023

Choi, S. W., Kim, W. S., and Kim, J. H. (2003). Surface modification of functional nanoparticles for controlled drug delivery. *J. Dispers. Sci. Technol.* 24, 475–487. doi: 10.1081/DIS-120021803

Cunningham, A., and Bürgi, T. (2013). "Bottom-up organisation of metallic nanoparticles," in *Amorphous Nanophotonics,* eds C. Rockstuhl and T. Scharf (Genève: Springer), 1–37.

Day, E. S., Bickford, L. R., Slater, J. H., Riggall, N. S., Drezek, R. A., and West, J. L. (2010). Antibody-conjugated gold-gold sulfide nanoparticles as multifunctional agents for imaging and therapy of breast cancer. *Int. J. Nanomed.* 5, 445–454. doi: 10.2147/IJN.S10881

Dennis, C., Jackson, A., Borchers, J., Ivkov, R., Foreman, A., Hoopes, P., et al. (2008). The influence of magnetic and physiological behaviour on the effectiveness of iron oxide nanoparticles for hyperthermia. *J. Phys. D Appl. Phys.* 41:134020. doi: 10.1088/0022-3727/41/13/134020

Dong, Z., Gong, H., Gao, M., Zhu, W., Sun, X., Feng, L., et al. (2016). Polydopamine nanoparticles as a versatile molecular loading platform to enable imaging-guided cancer combination therapy. *Theranostics.* 6, 1031–1042. doi: 10.7150/thno.14431

Eghtedari, M., Liopo, A. V., Copland, J. A., Oraevsky, A. A., and Motamedi, M. (2009). Engineering of hetero-functional gold nanorods for the *in*

vivo molecular targeting of breast cancer cells. *Nano Lett.* 9, 287–291. doi: 10.1021/nl802915q

El-Sayed, I. H., Huang, X., and El-Sayed, M. A. (2005). Surface plasmon resonance scattering and absorption of anti-EGFR antibody conjugated gold nanoparticles in cancer diagnostics: applications in oral cancer. *Nano Lett.* 5, 829–834. doi: 10.1021/nl050074e

El-Sayed, M. A. (2001). Some interesting properties of metals confined in time and nanometer space of different shapes. *Acc. Chem. Res.* 34, 257–264. doi: 10.1021/ar960016n

Everts, M., Saini, V., Leddon, J. L., Kok, R. J., Stoff-Khalili, M., Preuss, M. A., et al. (2006). Covalently linked Au nanoparticles to a viral vector: potential for combined photothermal and gene cancer therapy. *Nano Lett.* 6, 587–591. doi: 10.1021/nl0500555

Fahlgren, A., Bratengeier, C., Gelmi, A., Semeins, C. M., Klein-Nulend, J., Jager, E. W., et al. (2015). Biocompatibility of polypyrrole with human primary osteoblasts and the effect of dopants. *PLoS ONE.* 10:e0134023. doi: 10.1371/journal.pone.0134023

Fang, J., Nakamura, H., and Maeda, H. (2011). The EPR effect: unique features of tumor blood vessels for drug delivery, factors involved, and limitations and augmentation of the effect. *Adv. Drug Deliv. Rev.* 63, 136–151. doi: 10.1016/j.addr.2010.04.009

Fantechi, E., Innocenti, C., Zanardelli, M., Fittipaldi, M., Falvo, E., Carbo, M., et al. (2014). A smart platform for hyperthermia application in cancer treatment: cobalt-doped ferrite nanoparticles mineralized in human ferritin cages. *ACS Nano.* 8, 4705–4719. doi: 10.1021/nn500454n

Finn, O. J. (2008). Cancer immunology. *N. Engl. J. Med.* 358, 2704–2715. doi: 10.1056/NEJMra072739

Gao, Y., Li, Y., Chen, J., Zhu, S., Liu, X., Zhou, L., et al. (2015). Multifunctional gold nanostar-based nanocomposite: synthesis and application for noninvasive MR-SERS imaging-guided photothermal ablation. *Biomaterials.* 60, 31–41. doi: 10.1016/j.biomaterials.2015.05.004

George, P. M., Lyckman, A. W., LaVan, D. A., Hegde, A., Leung, Y., Avasare, R., et al. (2005). Fabrication and biocompatibility of polypyrrole implants suitable for neural prosthetics. *Biomaterials.* 26, 3511–3519. doi: 10.1016/j.biomaterials.2004.09.037

Goodrich, G. P., Bao, L., Gill-Sharp, K., Sang, K. L., Wang, J., and Payne, J. D. (2010). Photothermal therapy in a murine colon cancer model using near-infrared absorbing gold nanorods. *J. Biomed. Opt.* 15:018001. doi: 10.1117/1.3290817

Gordon, A. C., Lewandowski, R. J., Salem, R., Day, D. E., Omary, R. A., and Larson, A. C. (2014). Localized hyperthermia with iron oxide-doped yttrium microparticles: steps toward image-guided thermoradiotherapy in liver cancer. *J. Vasc. Interv. Radiol.* 25, 397–404. doi: 10.1016/j.jvir.2013.10.022

Hao, E., Bailey, R. C., Schatz, G. C., Hupp, J. T., and Li, S. (2004). Synthesis and optical properties of "branched" gold nanocrystals. *Nano Lett.* 4, 327–330. doi: 10.1021/nl0351542

Hao, F., Nehl, C. L., Hafner, J. H., and Nordlander, P. (2007). Plasmon resonances of a gold nanostar. *Nano Lett.* 7, 729–732. doi: 10.1021/nl062969c

Harris, N., Ford, M. J., and Cortie, M. B. (2006). Optimization of plasmonic heating by gold nanospheres and nanoshells. *J. Phys. Chem. B* 110, 10701–10707. doi: 10.1021/jp0606208

Heeger, A. J. (2001). Semiconducting and metallic polymers: the fourth generation of polymeric materials (Nobel Lecture). *J. Phys. Chem. B* 105, 8475–8491. doi: 10.1021/jp011611w

Herizchi, R., Abbasi, E., Milani, M., and Akbarzadeh, A. (2016). Current methods for synthesis of gold nanoparticles. *Artif. Cells Nanomed. Biotechnol.* 44, 596–602. doi: 10.3109/21691401.2014.971807

Heron, M. P. (2018). *Deaths: Leading Causes for 2016*. Centers for Disease Control and Prevention (CDC). U.S. Department of Health and Human Services, Centers for Disease Control and Prevention, National Center for Health Statistics National Vital Statistics System.

Hirn, S., Semmler-Behnke, M., Schleh, C., Wenk, A., Lipka, J., Schaffler, M., et al. (2011). Particle size-dependent and surface charge-dependent biodistribution of gold nanoparticles after intravenous administration. *Eur. J. Pharm. Biopharm.* 77, 407–416. doi: 10.1016/j.ejpb.2010.12.029

Hirsch, L. R., Stafford, R. J., Bankson, J. A., Sershen, S. R., Rivera, B., Price, R. E., et al. (2003). Nanoshell-mediated near-infrared thermal therapy of tumors under magnetic resonance guidance. *Proc. Natl. Acad. Sci. USA.* 100, 13549–13554. doi: 10.1073/pnas.2232479100

Hoshyar, R., Khayati, G. R., Poorgholami, M., and Kaykhaii, M. (2016). A novel green one-step synthesis of gold nanoparticles using crocin and their anti-cancer activities. *J. Photochem. Photobiol. B Biol.* 159, 237–242. doi: 10.1016/j.jphotobiol.2016.03.056

Huang, N., Wang, H., Zhao, J., Lui, H., Korbelik, M., and Zeng, H. (2010). Single-wall carbon nanotubes assisted photothermal cancer therapy: animal study with a murine model of squamous cell carcinoma. *Lasers Surg. Med.* 42, 638–648. doi: 10.1002/lsm.20968

Huang, X., El-Sayed, I. H., Qian, W., and El-Sayed, M. A. (2006). Cancer cell imaging and photothermal therapy in the near-infrared region by using gold nanorods. *J. Am. Chem. Soc.* 128, 2115–2120. doi: 10.1021/ja057254a

Huang, X., Jain, P. K., El-Sayed, I. H., and El-Sayed, M. A. (2008). Plasmonic photothermal therapy (PPTT) using gold nanoparticles. *Lasers Med. Sci.* 23, 217–228. doi: 10.1007/s10103-007-0470-x

Hwang, S., Nam, J., Jung, S., Song, J., Doh, H., and Kim, S. (2014). Gold nanoparticle-mediated photothermal therapy: current status and future perspective. *Nanomedicine.* 9, 2003–2022. doi: 10.2217/nnm.14.147

Iravani, S. (2011). Green synthesis of metal nanoparticles using plants. *Green Chem.* 13, 2638–2650. doi: 10.1039/c1gc15386b

Iravani, S. (2014). Bacteria in nanoparticle synthesis: current status and future prospects. *Int. Sch. Res. Notices* 2014:359316. doi: 10.1155/2014/359316

Jain, P. K., Lee, K. S., El-Sayed, I. H., and El-Sayed, M. A. (2006). Calculated absorption and scattering properties of gold nanoparticles of different size, shape, and composition: applications in biological imaging and biomedicine. *J. Phys. Chem. B* 110, 7238–7248. doi: 10.1021/jp057170o

Jain, S., Hirst, D. G., and O'Sullivan, J. M. (2012). Gold nanoparticles as novel agents for cancer therapy. *Br. J. Radiol.* 85, 101–113. doi: 10.1259/bjr/59448833

Jiang, W., Kim, B. Y., Rutka, J. T., and Chan, W. C. (2008). Nanoparticle-mediated cellular response is size-dependent. *Nat. Nanotechnol.* 3, 145–150. doi: 10.1038/nnano.2008.30

Kampinga, H. H. (2006). Cell biological effects of hyperthermia alone or combined with radiation or drugs: a short introduction to newcomers in the field. *Int. J. Hyperthermia.* 22, 191–196. doi: 10.1080/02656730500532028

Kaur, P., Aliru, M. L., Chadha, A. S., Asea, A., and Krishnan, S. (2016). Hyperthermia using nanoparticles–promises and pitfalls. *Int. J. Hyperthermia* 32, 76–88. doi: 10.3109/02656736.2015.1120889

Kaur, P., Hurwitz, M. D., Krishnan, S., and Asea, A. (2011). Combined hyperthermia and radiotherapy for the treatment of cancer. *Cancers.* 3, 3799–3823. doi: 10.3390/cancers3043799

Kelly, K. L., Coronado, E., Zhao, L. L., and Schatz, G. C. (2003). The optical properties of metal nanoparticles: the influence of size, shape, and dielectric environment. *J. Phys. Chem. B* 107, 668–677. doi: 10.1021/jp026731y

Kennedy, L. C., Bickford, L. R., Lewinski, N. A., Coughlin, A. J., Hu, Y., Day, E. S., et al. (2011). A new era for cancer treatment: gold-nanoparticle-mediated thermal therapies. *Small.* 7, 169–183. doi: 10.1002/smll.201000134

Khaletskaya, K., Reboul, J., Meilikhov, M., Nakahama, M., Diring, S., Tsujimoto, M., et al. (2013). Integration of porous coordination polymers and gold nanorods into core-shell mesoscopic composites toward light-induced molecular release. *J. Am. Chem. Soc.* 135, 10998–11005. doi: 10.1021/ja403108x

Khlebtsov, N., and Dykman, L. (2011). Biodistribution and toxicity of engineered gold nanoparticles: a review of *in vitro* and *in vivo* studies. *Chem. Soc. Rev.* 40, 1647–1671. doi: 10.1039/C0CS00018C

Kievit, F. M., and Zhang, M. (2011). Surface engineering of iron oxide nanoparticles for targeted cancer therapy. *Acc. Chem. Res.* 44, 853–862. doi: 10.1021/ar2000277

Kim, R., Emi, M., and Tanabe, K. (2006). Cancer immunosuppression and autoimmune disease: beyond immunosuppressive networks for tumour immunity. *Immunology.* 119, 254–264. doi: 10.1111/j.1365-2567.2006.02430.x

Kim, S. E., Lee, B. R., Lee, H., Jo, S. D., Kim, H., Won, Y. Y., and Lee, J. (2017). Near-infrared plasmonic assemblies of gold nanoparticles with multimodal function for targeted cancer theragnosis. *Sci. Rep.* 7:17327. doi: 10.1038/s41598-017-17714-2

Kruse, A. M., Meenach, S. A., Anderson, K. W., and Hilt, J. Z. (2014). Synthesis and characterization of CREKA-conjugated iron oxide nanoparticles for hyperthermia applications. *Acta Biomater.* 10, 2622–2629. doi: 10.1016/j.actbio.2014.01.025

Kullmann, F., Hollerbach, S., Dollinger, M. M., Harder, J., Fuchs, M., Messmann, H., et al. (2009). Cetuximab plus gemcitabine/oxaliplatin (GEMOXCET) in first-line metastatic pancreatic cancer: a multicentre phase II study. *Br. J. Cancer.* 100, 1032–1036. doi: 10.1038/sj.bjc.6604983

Kumar, V., and Yadav, S. K. (2008). Plant-mediated synthesis of silver and gold nanoparticles and their applications. *J. Chem. Technol. Biotechnol.* 84, 151–157. doi: 10.1002/jctb.2023

Larsson, E. M., Alegret, J., Käll, M., and Sutherland, D. S. (2007). Sensing characteristics of NIR localized surface plasmon resonances in gold nanorings for application as ultrasensitive biosensors. *Nano Lett.* 7, 1256–1263. doi: 10.1021/nl0701612

Le Renard, P. E., Jordan, O., Faes, A., Petri-Fink, A., Hofmann, H., Rufenacht, D., et al. (2010). The *in vivo* performance of magnetic particle-loaded injectable, *in situ* gelling, carriers for the delivery of local hyperthermia. *Biomaterials.* 31, 691–705. doi: 10.1016/j.biomaterials.2009.09.091

Lee, D., Ko, W. K., Hwang, D. S., Heo, D. N., Lee, S. J., Heo, M., et al. (2016). Use of baicalin-conjugated gold nanoparticles for apoptotic induction of breast cancer cells. *Nanoscale Res. Lett.* 11:381. doi: 10.1186/s11671-016-1586-3

Lee, J., Lee, Y. H., Jeong, C. B., Choi, J. S., Chang, K. S., and Yoon, M. (2018). Gold nanorods-conjugated TiO2 nanoclusters for the synergistic combination of phototherapeutic treatments of cancer cells. *J. Nanobiotechnol.* 16:104. doi: 10.1186/s12951-018-0432-4

Lee, J. H., Jang, J. T., Choi, J. S., Moon, S. H., Noh, S. H., Kim, J. W., et al. (2011). Exchange-coupled magnetic nanoparticles for efficient heat induction. *Nat. Nanotechnol.* 6, 418–422. doi: 10.1038/nnano.2011.95

Li, D., Huang, J., and Kaner, R. B. (2009). Polyaniline nanofibers: a unique polymer nanostructure for versatile applications. *Acc. Chem. Res.* 42, 135–145. doi: 10.1021/ar800080n

Li, M., Li, L., Zhan, C., and Kohane, D. S. (2016). Core-shell nanostars for multimodal therapy and imaging. *Theranostics.* 6, 2306–2313. doi: 10.7150/thno.15843

Li, S., Zhang, L., Wang, T., Li, L., Wang, C., and Su, Z. (2015). The facile synthesis of hollow Au nanoflowers for synergistic chemo-photothermal cancer therapy. *Chem. Commun.* 51, 14338–14341. doi: 10.1039/C5CC05676D

Li, Y., Zaluzhna, O., Xu, B., Gao, Y., Modest, J. M., and Tong, Y. J. (2011). Mechanistic insights into the Brust-Schiffrin two-phase synthesis of organo-chalcogenate-protected metal nanoparticles. *J. Am. Chem. Soc.* 133, 2092–2095. doi: 10.1021/ja1105078

Liao, H., and Hafner, J. H. (2005). Gold nanorod bioconjugates. *Chem. Mater.* 17, 4636–4641. doi: 10.1021/cm050935k

Link, S., and El-Sayed, M. A. (1999). Size and temperature dependence of the plasmon absorption of colloidal gold nanoparticles. *J. Phys. Chem. B* 103, 4212–4217. doi: 10.1021/jp984796o

Liu, X.-L., Wang, J.-H., Liang, S., Yang, D.-J., Nan, F., Ding, S.-J., et al. (2014). Tuning plasmon resonance of gold nanostars for enhancements of nonlinear optical response and raman scattering. *J. Phys. Chem. C* 118, 9659–9664. doi: 10.1021/jp500638u

Liu, Y., Ai, K., Liu, J., Deng, M., He, Y., and Lu, L. (2013). Dopamine-melanin colloidal nanospheres: an efficient near-infrared photothermal therapeutic agent for *in vivo* cancer therapy. *Adv. Mater. Weinheim.* 25, 1353–1359. doi: 10.1002/adma.201204683

Liu, Y., Yang, M., Zhang, J., Zhi, X., Li, C., Zhang, C., et al. (2016). Human induced pluripotent stem cells for tumor targeted delivery of gold nanorods and enhanced photothermal therapy. *ACS Nano.* 10, 2375–2385. doi: 10.1021/acsnano.5b07172

Longmire, M., Choyke, P. L., and Kobayashi, H. (2008). Clearance properties of nano-sized particles and molecules as imaging agents: considerations and caveats. *Nanomedicine.* 3, 703–717. doi: 10.2217/17435889.3.5.703

Loo, C., Lin, A., Hirsch, L., Lee, M. H., Barton, J., Halas, N., et al. (2004). Nanoshell-enabled photonics-based imaging and therapy of cancer. *Technol. Cancer Res. Treat.* 3, 33–40. doi: 10.1177/153303460400300104

Loo, C., Lowery, A., Halas, N., West, J., and Drezek, R. (2005). Immunotargeted nanoshells for integrated cancer imaging and therapy. *Nano Lett.* 5, 709–711. doi: 10.1021/nl050127s

Lu, S., Li, X., Zhang, J., Peng, C., Shen, M., and Shi, X. (2018). Dendrimer-stabilized gold nanoflowers embedded with ultrasmall iron oxide nanoparticles for multimode imaging-guided combination therapy of tumors. *Adv Sci.* 5:1801612. doi: 10.1002/advs.201801612

Luk, K. H., Hulse, R. M., and Phillips, T. L. (1980). Hyperthermia in cancer therapy. *West. J. Med.* 132, 179–185.

Maeda, H. (2001). The enhanced permeability and retention (EPR) effect in tumor vasculature: the key role of tumor-selective macromolecular drug targeting. *Adv. Enzyme Regul.* 41, 189–207. doi: 10.1016/S0065-2571(00)00013-3

Maier-Hauff, K., Ulrich, F., Nestler, D., Niehoff, H., Wust, P., Thiesen, B., et al. (2011). Efficacy and safety of intratumoral thermotherapy using magnetic iron-oxide nanoparticles combined with external beam radiotherapy on patients with recurrent glioblastoma multiforme. *J. Neurooncol.* 103, 317–324. doi: 10.1007/s11060-010-0389-0

Manivasagan, P., Quang Bui, N., Bharathiraja, S., Santha Moorthy, M., Oh, Y.-O., Song, K., et al. (2017). Multifunctional biocompatible chitosan-polypyrrole nanocomposites as novel agents for photoacoustic imaging-guided photothermal ablation of cancer. *Sci. Rep.* 7:43593. doi: 10.1038/srep43593

Mantso, T., Vasileiadis, S., Anestopoulos, I., Voulgaridou, G. P., Lampri, E., Botaitis, S., et al. (2018). Hyperthermia induces therapeutic effectiveness and potentiates adjuvant therapy with non-targeted and targeted drugs in an *in vitro* model of human malignant melanoma. *Sci. Rep.* 8:10724. doi: 10.1038/s41598-018-29018-0

Melancon, M. P., Zhou, M., and Li, C. (2011). Cancer theranostics with near-infrared light-activatable multimodal nanoparticles. *Acc. Chem. Res.* 44, 947–956. doi: 10.1021/ar200022e

Mieszawska, A. J., Mulder, W. J., Fayad, Z. A., and Cormode, D. P. (2013). Multifunctional gold nanoparticles for diagnosis and therapy of disease. *Mol. Pharm.* 10, 831–847. doi: 10.1021/mp3005885

Mishra, P., Ray, S., Sinha, S., Das, B., Khan, M. I., Behera, S. K., et al. (2016). Facile bio-synthesis of gold nanoparticles by using extract of *Hibiscus sabdariffa* and evaluation of its cytotoxicity against U87 glioblastoma cells under hyperglycemic condition. *Biochem. Eng. J.* 105, 264–272. doi: 10.1016/j.bej.2015.09.021

Moyer, H. R., and Delman, K. A. (2008). The role of hyperthermia in optimizing tumor response to regional therapy. *Int. J. Hyperthermia* 24, 251–261. doi: 10.1080/02656730701772480

Mukherjee, P., Ahmad, A., Mandal, D., Senapati, S., Sainkar, S. R., Khan, M. I., et al. (2001). Bioreduction of AuCl4– ions by the fungus, *Verticillium* sp. and surface trapping of the gold nanoparticles formed. *Angew. Chem. Int. Ed.* 40, 3585–3588. doi: 10.1002/1521-3773(20011001)40:19<3585::AID-ANIE3585>3.0.CO;2-K

Mukherjee, P., Senapati, S., Mandal, D., Ahmad, A., Khan, M. I., Kumar, R., et al. (2002). Extracellular synthesis of gold nanoparticles by the fungus *Fusarium oxysporum*. *ChemBioChem.* 3, 461–463. doi: 10.1002/1439-7633(20020503)3:5<461::AID-CBIC461>3.0.CO;2-X

Muthukumar, T., Sudhakumari, Sambandam, B., Aravinthan, A., Sastry, T. P., and Kim, J.-H. (2016). Green synthesis of gold nanoparticles and their enhanced synergistic antitumor activity using HepG2 and MCF7 cells and its antibacterial effects. *Proc. Biochem.* 51, 384–391. doi: 10.1016/j.procbio.2015.12.017

Nolsoe, C. P., Torp-Pedersen, S., Burcharth, F., Horn, T., Pedersen, S., Christensen, N. E., Olldag, E. S., et al. (1993). Interstitial hyperthermia of colorectal liver metastases with a US-guided Nd-YAG laser with a diffuser tip: a pilot clinical study. *Radiology.* 187, 333–337. doi: 10.1148/radiology.187.2.8475269

Norman, R. S., Stone, J. W., Gole, A., Murphy, C. J., and Sabo-Attwood, T. L. (2008). Targeted photothermal lysis of the pathogenic bacteria, *Pseudomonas aeruginosa*, with gold nanorods. *Nano Lett.* 8, 302–306. doi: 10.1021/nl0727056

Ochsner, M. (1997). Photophysical and photobiological processes in the photodynamic therapy of tumours. *J. Photochem. Photobiol. B Biol.* 39, 1–18. doi: 10.1016/S1011-1344(96)07428-3

O'Neal, D. P., Hirsch, L. R., Halas, N. J., Payne, J. D., and West, J. L. (2004). Photo-thermal tumor ablation in mice using near infrared-absorbing nanoparticles. *Cancer Lett.* 209, 171–176. doi: 10.1016/j.canlet.2004.02.004

Paciotti, G. F., Kingston, D. G. I., and Tamarkin, L. (2006). Colloidal gold nanoparticles: a novel nanoparticle platform for developing multifunctional tumor-targeted drug delivery vectors. *Drug Dev. Res.* 67, 47–54. doi: 10.1002/ddr.20066

Pan, Y., Leifert, A., Ruau, D., Neuss, S., Bornemann, J., Schmid, G., et al. (2009). Gold nanoparticles of diameter 1.4 nm trigger necrosis by oxidative stress and mitochondrial damage. *Small* 5, 2067–2076. doi: 10.1002/smll.200900466

Patra, C. R., Bhattacharya, R., Mukhopadhyay, D., and Mukherjee, P. (2010). Fabrication of gold nanoparticles for targeted therapy in pancreatic cancer. *Adv. Drug Deliv. Rev.* 62, 346–361. doi: 10.1016/j.addr.2009.11.007

Patra, C. R., Bhattacharya, R., Wang, E., Katarya, A., Lau, J. S., Dutta, S., et al. (2008). Targeted delivery of gemcitabine to pancreatic adenocarcinoma using cetuximab as a targeting agent. *Cancer Res.* 68, 1970–1978. doi: 10.1158/0008-5472.CAN-07-6102

Peeken, J. C., Vaupel, P., and Combs, S. E. (2017). Integrating hyperthermia into modern radiation oncology: what evidence is necessary? *Front. Oncol.* 7:132. doi: 10.3389/fonc.2017.00132

Pérez-Juste, J., Pastoriza-Santos, I., Liz-Marzán, L. M., and Mulvaney, P. (2005). Gold nanorods: synthesis, characterization and applications. *Coord. Chem. Rev.* 249, 1870–1901. doi: 10.1016/j.ccr.2005.01.030

Petryayeva, E., and Krull, U. J. (2011). Localized surface plasmon resonance: nanostructures, bioassays and biosensing—a review. *Anal. Chim. Acta.* 706, 8–24. doi: 10.1016/j.aca.2011.08.020

Pissuwan, D., Valenzuela, S. M., and Cortie, M. B. (2006). Therapeutic possibilities of plasmonically heated gold nanoparticles. *Trends Biotechnol.* 24, 62–67. doi: 10.1016/j.tibtech.2005.12.004

Pissuwan, D., Valenzuela, S. M., Miller, C. M., Killingsworth, M. C., and Cortie, M. B. (2009). Destruction and control of Toxoplasma gondii tachyzoites using gold nanosphere/antibody conjugates. *Small.* 5, 1030–1034. doi: 10.1002/smll.200801018

Pitsillides, C. M., Joe, E. K., Wei, X., Anderson, R. R., and Lin, C. P. (2003). Selective cell targeting with light-absorbing microparticles and nanoparticles. *Biophys. J.* 84, 4023–4032. doi: 10.1016/S0006-3495(03)75128-5

Poland, C. A., Duffin, R., Kinloch, I., Maynard, A., Wallace, W. A., Seaton, A., et al. (2008). Carbon nanotubes introduced into the abdominal cavity of mice show asbestos-like pathogenicity in a pilot study. *Nat. Nanotechnol.* 3, 423–428. doi: 10.1038/nnano.2008.111

Pricker, S. P. (1996). Medical uses of gold compounds: past, present and future. *Gold Bull.* 29, 53–60. doi: 10.1007/BF03215464

Ray, P. C., Khan, S. A., Singh, A. K., Senapati, D., and Fan, Z. (2012). Nanomaterials for targeted detection and photothermal killing of bacteria. *Chem. Soc. Rev.* 41, 3193–3209. doi: 10.1039/c2cs15340h

Rengan, A. K., Bukhari, A. B., Pradhan, A., Malhotra, R., Banerjee, R., Srivastava, R., et al. (2015). *In vivo* analysis of biodegradable liposome gold nanoparticles as efficient agents for photothermal therapy of cancer. *Nano Lett.* 15, 842–848. doi: 10.1021/nl5045378

Rengan, A. K., Jagtap, M., De, A., Banerjee, R., and Srivastava, R. (2014). Multifunctional gold coated thermo-sensitive liposomes for multimodal imaging and photo-thermal therapy of breast cancer cells. *Nanoscale.* 6, 916–923. doi: 10.1039/C3NR04448C

Rodrigues, C. J., Bobb, J. A., John, M. G., Fisenko, S. P., El-Shall, M. S., and Tibbetts, K. M. (2018). Nucleation and growth of gold nanoparticles initiated by nanosecond and femtosecond laser irradiation of aqueous [AuCl4](). *Phys. Chem. Chem. Phys.* 20, 28465–28475. doi: 10.1039/C8CP05774E

Shah, M., Badwaik, V., Kherde, Y., Waghwani, H. K., Modi, T., Aguilar, Z. P., et al. (2014). Gold nanoparticles: various methods of synthesis and antibacterial applications. *Front Biosci.* 19, 1320–1344. doi: 10.2741/4284

Shaw, C. F. (1999). Gold-based therapeutic agents. *Chem. Rev.* 99, 2589–2600. doi: 10.1021/cr980431o

Shukla, R., Bansal, V., Chaudhary, M., Basu, A., Bhonde, R. R., and Sastry, M. (2005). Biocompatibility of gold nanoparticles and their endocytotic fate inside the cellular compartment: a microscopic overview. *Langmuir.* 21, 10644–10654. doi: 10.1021/la0513712

Singh, M., Manikandan, S., and Kumaraguru, A. (2011). Nanoparticles: a new technology with wide applications. *Res. J. Nanosci. Nanotechnol.* 1, 1–11. doi: 10.3923/rjnn.2011.1.11

Smitha, S. L., Gopchandran, K. G., Smijesh, N., and Philip, R. (2013). Size-dependent optical properties of Au nanorods. *Prog. Nat. Sci. Mater. Int.* 23, 36–43. doi: 10.1016/j.pnsc.2013.01.005

Sonavane, G., Tomoda, K., and Makino, K. (2008). Biodistribution of colloidal gold nanoparticles after intravenous administration: effect of particle size. *Colloids Surf. B Biointerfaces.* 66, 274–280. doi: 10.1016/j.colsurfb.2008.07.004

Stuchinskaya, T., Moreno, M., Cook, M. J., Edwards, D. R., and Russell, D. A. (2011). Targeted photodynamic therapy of breast cancer cells using antibody-phthalocyanine-gold nanoparticle conjugates. *Photochem. Photobiol. Sci.* 10, 822–831. doi: 10.1039/c1pp05014a

Sumbayev, V. V., Yasinska, I. M., Garcia, C. P., Gilliland, D., Lall, G. S., Gibbs, B. F., et al. (2013). Gold nanoparticles downregulate interleukin-1beta-induced pro-inflammatory responses. *Small.* 9, 472–477. doi: 10.1002/smll.201201528

Sun, T., Dou, J.-H., Liu, S., Wang, X., Zheng, X., Wang, Y., et al. (2018). Second near-infrared conjugated polymer nanoparticles for photoacoustic imaging and photothermal therapy. *ACS Appl. Mater. Interfaces.* 10, 7919–7926. doi: 10.1021/acsami.8b01458

Svirskis, D., Travas-Sejdic, J., Rodgers, A., and Garg, S. (2010). Electrochemically controlled drug delivery based on intrinsically conducting polymers. *J. Control Release.* 146, 6–15. doi: 10.1016/j.jconrel.2010.03.023

Thomsen, S. (1991). Pathologic analysis of photothermal and photomechanical effects of laser-tissue interactions. *Photochem. Photobiol.* 53, 825–835. doi: 10.1111/j.1751-1097.1991.tb09897.x

Topete, A., Alatorre-Meda, M., Iglesias, P., Villar-Alvarez, E. M., Barbosa, S., Costoya, J. A., et al. (2014). Fluorescent drug-loaded, polymeric-based, branched gold nanoshells for localized multimodal therapy and imaging of tumoral cells. *ACS Nano.* 8, 2725–2738. doi: 10.1021/nn406425h

Tsai, C. Y., Lu, S. L., Hu, C. W., Yeh, C. S., Lee, G. B., and Lei, H. Y. (2012). Size-dependent attenuation of TLR9 signaling by gold nanoparticles in macrophages. *J. Immunol.* 188, 68–76. doi: 10.4049/jimmunol.1100344

van Landeghem, F. K., Maier-Hauff, K., Jordan, A., Hoffmann, K. T., Gneveckow, U., Scholz, R., et al. (2009). Post-mortem studies in glioblastoma patients treated with thermotherapy using magnetic nanoparticles. *Biomaterials.* 30, 52–57. doi: 10.1016/j.biomaterials.2008.09.044

Vats, M., Mishra, S. K., Baghini, M. S., Chauhan, D. S., Srivastava, R., and De, A. (2017). Near infrared fluorescence imaging in nano-therapeutics and photo-thermal evaluation. *Int. J. Mol. Sci.* 18:E924. doi: 10.3390/ijms18050924

Vines, J. B., Lim, D.-J., and Park, H. (2018). Contemporary polymer-based nanoparticle systems for photothermal therapy. *Polymers.* 10:1357. doi: 10.3390/polym10121357

Vogel, A., and Venugopalan, V. (2003). Mechanisms of pulsed laser ablation of biological tissues. *Chem. Rev.* 103, 577–644. doi: 10.1021/cr010379n

Wang, J., Chen, Y., Chen, B., Ding, J., Xia, G., Gao, C., et al. (2010). Pharmacokinetic parameters and tissue distribution of magnetic Fe(3)O(4) nanoparticles in mice. *Int. J. Nanomed.* 5, 861–866. doi: 10.2147/IJN.S13662

Wang, J., and Qiu, J. (2016). A review of organic nanomaterials in photothermal cancer therapy. *Cancer Res. Front* 2, 67–84. doi: 10.17980/2016.67

Wang, M. (2016). Emerging multifunctional NIR photothermal therapy systems based on polypyrrole nanoparticles. *Polymers* 8:373. doi: 10.3390/polym8100373

Wang, X., Wang, H., Wang, Y., Yu, X., Zhang, S., Zhang, Q., et al. (2016). A facile strategy to prepare dendrimer-stabilized gold nanorods with sub-10-nm size for efficient photothermal cancer therapy. *Sci. Rep.* 6:22764. doi: 10.1038/srep22764

Wang, Y., Black, K. C., Luehmann, H., Li, W., Zhang, Y., Cai, X., et al. (2013). Comparison study of gold nanohexapods, nanorods, and nanocages for photothermal cancer treatment. *ACS Nano.* 7, 2068–2077. doi: 10.1021/nn304332s

Wilson, B. C., and Patterson, M. S. (2008). The physics, biophysics and technology of photodynamic therapy. *Phys. Med. Biol.* 53, R61–R109. doi: 10.1088/0031-9155/53/9/R01

Yang, K., Xu, H., Cheng, L., Sun, C., Wang, J., and Liu, Z. (2012). *In vitro* and *in vivo* near-infrared photothermal therapy of cancer using polypyrrole organic nanoparticles. *Adv. Mater.* 24, 5586–5592. doi: 10.1002/adma.201202625

Yang, S., You, Q., Yang, L., Li, P., Lu, Q., Wang, S., et al. (2019). Rod-like MSN@Au nanohybrids modified supermolecular photosensitizer for NIRF/MSOT/CT/MR quadmodal imaging guided photothermal/photodynamic cancer therapy. *ACS Appl. Mater. Interfaces.* 11, 6777–6788. doi: 10.1021/acsami.8b19565

Yang, X., Liu, X., Liu, Z., Pu, F., Ren, J., and Qu, X. (2012). Near-infrared light-triggered, targeted drug delivery to cancer cells by aptamer gated nanovehicles. *Adv. Mater.* 24, 2890–2895. doi: 10.1002/adma.201104797

Yen, H. J., Hsu, S. H., and Tsai, C. L. (2009). Cytotoxicity and immunological response of gold and silver nanoparticles of different sizes. *Small.* 5, 1553–1561. doi: 10.1002/smll.200900126

Yin, T., Li, Y., Bian, K., Zhu, R., Liu, Z., Niu, K., et al. (2018). Self-assembly synthesis of vapreotidegold hybrid nanoflower for photothermal antitumor activity. *Mater. Sci. Eng. C Mater. Biol. Appl.* 93, 716–723. doi: 10.1016/j.msec.2018.08.017

Zare, D., Akbarzadeh, A., and Bararpour, N. (2010). Synthesis and functionalization of gold nanoparticles by using of poly functional amino acids. *Int. J. Nanosci. Nanotechnol.* 6, 223–230. Available online at: http://www.ijnnonline.net/?_action=articleInfo&article=3958

Zhang, D., Qin, X., Wu, T., Qiao, Q., Song, Q., and Zhang, Z. (2019). Extracellular vesicles based self-grown gold nanopopcorn for combinatorial chemo-photothermal therapy. *Biomaterials* 197, 220–228. doi: 10.1016/j.biomaterials.2019.01.024

Zhang, G., Yang, Z., Lu, W., Zhang, R., Huang, Q., Tian, M., et al. (2009). Influence of anchoring ligands and particle size on the colloidal stability and *in vivo* biodistribution of polyethylene glycol-coated gold nanoparticles in tumor-xenografted mice. *Biomaterials.* 30, 1928–1936. doi: 10.1016/j.biomaterials.2008.12.038

Zhang, J., Luo, X., Wu, Y., Wu, F., Li, Y. F., He, R., et al. (2019). Rod in tube: a novel nanoplatform for highly effective chemo-photothermal combination therapy towards breast cancer. *ACS Appl. Mater. Interfaces.* 11, 3690–3703. doi: 10.1021/acsami.8b17533

Zhang, P., Wang, J., Huang, H., Yu, B., Qiu, K., Huang, J., et al. (2015). Unexpected high photothemal conversion efficiency of gold nanospheres upon grafting with two-photon luminescent ruthenium(II) complexes: a way towards cancer therapy? *Biomaterials.* 63, 102–114. doi: 10.1016/j.biomaterials.2015.06.012

Zhang, X. D., Wu, D., Shen, X., Liu, P. X., Fan, F. Y., and Fan, S. J. (2012). *In vivo* renal clearance, biodistribution, toxicity of gold nanoclusters. *Biomaterials.* 33, 4628–4638. doi: 10.1016/j.biomaterials.2012.03.020

Zheng, S. W., Huang, M., Hong, R. Y., Deng, S. M., Cheng, L. F., Gao, B., et al. (2014). RGD-conjugated iron oxide magnetic nanoparticles for magnetic resonance imaging contrast enhancement and hyperthermia. *J. Biomater. Appl.* 28, 1051–1059. doi: 10.1177/0885328213493486

Zhou, J., Lu, Z., Zhu, X., Wang, X., Liao, Y., Ma, Z., et al. (2013). NIR photothermal therapy using polyaniline nanoparticles. *Biomaterials.* 34, 9584–9592. doi: 10.1016/j.biomaterials.2013.08.075

Zhu, C., Ninh, C., and Bettinger, C. J. (2014). Photoreconfigurable polymers for biomedical applications: chemistry and macromolecular engineering. *Biomacromolecules.* 15, 3474–3494. doi: 10.1021/bm500990z

Conflict of Interest Statement: The authors declare that the research was conducted in the absence of any commercial or financial relationships that could be construed as a potential conflict of interest.

frontiers in Chemistry

ORIGINAL RESEARCH
published: 08 February 2019
doi: 10.3389/fchem.2019.00060

Preparation and Antitumoral Activity of Au-Based Inorganic-Organometallic Nanocomposites

Mariona Dalmases[1,2†], *Andrea Pinto*[1,2†], *Petra Lippmann*[3], *Ingo Ott*[3], *Laura Rodríguez*[1,2*] *and Albert Figuerola*[1,2*]

[1] *Departament de Química Inorgànica i Orgànica, Secció de Química Inorgànica, Universitat de Barcelona, Barcelona, Spain,* [2] *Institut de Nanociència i Nanotecnologia (IN2UB), Universitat de Barcelona, Barcelona, Spain,* [3] *Institute of Medicinal and Pharmaceutical Chemistry, Technische Universität Braunschweig, Braunschweig, Germany*

OPEN ACCESS

Edited by:
Carlos Lodeiro, Faculdade de Ciências e Tecnologia da Universidade Nova de Lisboa, Portugal

Reviewed by:
Ajay Singh Karakoti, Ahmedabad University, India
Zehra Durmus, Zehra Durmuş, Turkey

***Correspondence:**
Laura Rodríguez
laura.rodriguez@qi.ub.es
Albert Figuerola
albert.figuerola@qi.ub.es

[†] *These authors have contributed equally to this work*

Specialty section:
This article was submitted to Nanoscience, a section of the journal Frontiers in Chemistry

Received: *02 October 2018*
Accepted: *22 January 2019*
Published: *08 February 2019*

Citation:
Dalmases M, Pinto A, Lippmann P, Ott I, Rodríguez L and Figuerola A (2019) Preparation and Antitumoral Activity of Au-Based Inorganic-Organometallic Nanocomposites. Front. Chem. 7:60. doi: 10.3389/fchem.2019.00060

The synergy between gelator molecules and nanostructured materials is currently a novel matter of study. The possibility to carefully design the skeleton of the molecular entity as well as the nanostructure's morphological and chemical features offers the possibility to prepare a huge variety of nanocomposites with properties potentially different than just the sum of those of the individual building blocks. Here we describe the synthesis and characterization of nanocomposites made by the unconventional combination of phosphine-Au(I)-alkynyl-based organometallic gelating molecules and plasmonic Au nanoparticles. Our results indicate that the interaction between the two moieties leads to a significant degree of aggregation in both hydrophilic and hydrophobic media, either when using DAPTA or PTA-based organometallic molecules, with the formation of a sponge-like hybrid powder upon solvent evaporation. The biological activity of the nanocomposites was assessed, suggesting the existence of a synergetic effect evidenced by the higher cytotoxicity of the hybrid systems with respect to that of any of their isolated counterparts. These results represent a preliminary proof-of-concept for the exploitation of these novel nanocomposites in the biomedical field.

Keywords: nanoparticles, gold, biological activity, organometallic, hybrid

INTRODUCTION

Metal-organic molecules have attracted much interest in the last decade due to their ability to spontaneously form supramolecular assemblies and metal-organic gels through the establishment of weak non-covalent intermolecular bonds of different nature (Zhang and Su, 2013). In particular, highly luminescent Au(I)-alkynyl-based organometallic complexes have revealed as excellent building blocks for this purpose, forming fibers, gels and other sorts of shape-controlled supramolecular structures, depending on their specific chemical formula and on the reaction conditions, with enhanced optical properties (Lima and Rodríguez, 2015). Noteworthy, Au(I)-alkynyl-based complexes can form aurophilic intra and intermolecular bonds between Au(I) ions, which do not only reinforce the stability of the assembly, but they also play a crucial role in defining the luminescent properties of the final product (Rodríguez et al., 2012; Schmidbaur and Schier, 2012)

On the other hand, phosphine-Au(I) compounds have often revealed themselves as cytotoxic species with interesting biological activity against tumor cell growth (Lima and Rodriguez, 2011). Although most of the studied phosphine-Au(I) metallodrugs contain a thiolate group directly attached to the Au(I) ion, phosphine-Au(I)-alkynyl complexes have been also observed to perform as antitumoral agents in a few cases (Chui et al., 2009; Schuh et al., 2009; Vergara et al., 2010; Meyer et al., 2012). Our group has recently reported some promising results on this topic (Meyer et al., 2013; Arcau et al., 2014; Andermark et al., 2016; Gavara et al., 2016).

In the field of nanoparticles or nanochemistry, Au(I)-alkynyl-based organometallic complexes have been successfully employed as molecular precursors for the synthesis of uniform Au nanoparticles, by means of their controlled thermal decomposition at relatively low temperatures (Aguiló et al., 2013; Ballesteros et al., 2014; Muhich et al., 2015). These studies were motivated by the possibility to obtain size and shape homogeneous metallic nanostructures under soft reaction conditions with interesting plasmonic properties. Nevertheless, recent studies are focusing more into the possible synergy established between gelator molecules and different types of nanostructured materials, i.e., inorganic nanoparticles, carbon nanotubes, etc (Das et al., 2012). In this regard, our group has recently reported on the synergy established between phosphine-Au(I)-alkynyl-based complexes and metallic nanoparticles, which allowed for the complete solubilization of hydrophobic colloids into water as well as for their plasmon tuning (Dalmases et al., 2016). Considering the enormous amount of highly designed systems potentially achieved, the preparation of hybrid organometallic nanocomposites should be strongly pursued, since they might open the doors for the use of a new set of engineered materials with multiple and enhanced properties useful in different fields.

Au nanoparticles have experienced a huge growing interest in the last decades due to their fascinating optical properties that are unfolded in the shape of an intense absorption band in the visible or near infrared region (NIR), known as the Localized Surface Plasmon Resonance (LSPR) (Motl et al., 2014). The origin of this phenomenon in metal nanostructures like Au or Ag is well-understood and is grounded on the collective excitation of surface electrons by means of the electric field of incident light, resulting in a coherent surface-confined oscillation with a resonant frequency that strongly depends on the material itself, as well as on the size, shape, dielectric environment, and separation distance of nanoparticles (NPs). The high level of control achieved in their synthesis and morphological features, as well as on their optical properties, have made of Au nanoparticles an interesting material particularly involved in both the photodiagnostics and photothermal therapy of cancers and other main diseases (Boisselier and Astruc, 2009).

Based on all this, the combination of phosphine-Au(I)-alkynyl-based organometallic complexes and plasmonic nanoparticles seems a promising approach for the design of new theranostic agents, able to perform simultaneously diagnostic and therapeutic tasks when required during the medical treatment. Nevertheless, there are no examples reported on the synthesis of such type of nanocomposites besides our previous work (Dalmases et al., 2016), and thus their potential biological activity is yet to unravel.

In this work, we report on the preparation of novel hybrid nanosystems combining Au nanoparticles and phosphine-Au(I)-alkynyl-based supramolecular structures with the aim of assessing their potential as efficient antitumoral agents, with special emphasis on the identification of synergetic effects between the metallic and the molecular moieties with respect to their isolated counterparts. The antitumoral activity depends on the hydro or lipophilicity of the drug and thus we decided to work with two different types of Au nanoparticles which differ basically on the hydrophilicity of their initial stabilizing molecule after synthesis, being either citrate anions or oleylamine molecules for the hydrophilic and the hydrophobic cases, respectively, as shown in **Scheme 1**. Our results show that significantly lower IC_{50} values are found for all the hybrid systems prepared with respect to their individual counterparts (NPs and organometallic structures), representing a good proof-of-concept for the future development and study of these new type of biologically active nanocomposites.

MATERIALS AND METHODS

General Procedures

Commercial reagents 1,3,5-triaza-7-phosphatricyclo[3.3.1.13.7]decane (PTA; 97%, Aldrich), 3,7-diacetyl-1,3,7-triaza-5-phosphabicyclo[3.3.1]nonane (DAPTA; 97%, Aldrich), Gold(III) chloride trihydrate ($HAuCl_4{\cdot}3H_2O$, ≥99.9, Aldrich), trisodium citrate dihydrate ($HOC(COONa)(CH_2COONa)_2{\cdot}2H_2O$, Aldrich), oleylamine (OLAm, 70%, Aldrich), oleic acid (OLAc, ≥99%, Aldrich), 1-octadecene (ODE, 90%, Aldrich), 2-Propanol (iPrOH, for HPLC, VWR Chemicals), and chloroform ($CHCl_3$, 99.2%, VWR Chemicals) have been used as received. Literature methods have been used to prepare [Au(C≡ C–C_5H_4N)(PTA)] (Gavara et al., 2013). and [Au(C≡ C–C_5H_4N)(DAPTA)] (Aguiló et al., 2013) compounds, that from now on will be named PTA Au(I) complex and DAPTA Au(I) complex, respectively, for the sake of simplicity.

Hydrophilic Au NPs

The synthesis of hydrophilic Au NPs was based on that reported by Turkevish and coworkers (Turkevich et al., 1953). Briefly, 8.8 mg $HAuCl_4{\cdot}3H_2O$ (0.02 mmol) were dissolved in 60 mL of deionized water and the solution was heated to the boiling point. Once the temperature was reached, 5.2 mL of an aqueous solution of sodium citrate at 2% was added and let the reaction for 20 min at this temperature. The color of the solution changed from yellow to dark red as a result of the formation of gold nanoparticles.

Hydrophobic Au NPs

The synthesis of hydrophobic Au NPs was adapted from that described by Yu and co-workers as follows: (Yu et al., 2005) A mixture of ODE (30 mL), OLAc (4.5 mL), and OLAm (5.5 mL) was stirred in a 100 mL three-necked flask for 20 min at

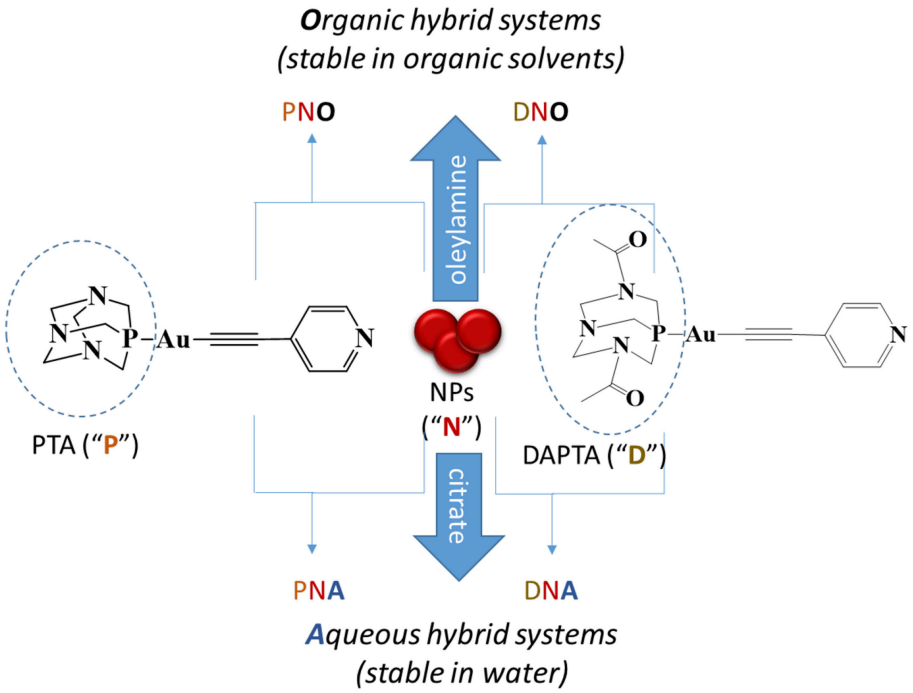

SCHEME 1 | Types of nanocomposites prepared and description of the nomenclature used for each of them. That is, "N" indicates nanoparticles; "P," PTA phosphine derivatives; "D," DAPTA phosphine derivatives; "O," organic medium and "A," aqueous medium.

120°C under vacuum. Meanwhile, in a glovebox $HAuCl_4 \cdot 3H_2O$ (120 mg, 0.30 mmol) was dissolved in ODE (7.5 mL) and OLAm (1.5 mL) in an auxiliary vial. Once the purge was complete and the system under N_2, the solution of gold precursor was injected into the flask and temperature was fixed at 150°C. After 30 min of reaction, the heating was stopped, and the solution was washed with 2 equivalent volumes of iPrOH, and centrifuged at 4,500 rpm for 4 min. The product was redispersed in chloroform.

SYNTHESIS OF HYBRID ORGANOMETALLIC SUPPORTED NPS

Au-DAPTA Nanocomposites in Organic Media (DNO Systems)

The functionalization of hydrophobic Au nanoparticles with DAPTA was performed by a simple reaction at room temperature in chloroform. 4.2 mg of DAPTA (7.94×10^{-3} mmol) were dissolved in 8 mL chloroform and mixed with a solution of hydrophobic Au nanoparticles dispersed in chloroform. The solution was shaken for 24 h. After this time, the solution was centrifuged and the resultant precipitate was redispersed in chloroform.

Au-PTA Nanocomposites in Organic Media (PNO Systems)

The functionalization of hydrophobic Au nanoparticles with PTA was adapted from the protocol described above but using 1.3 mg (2.85×10^{-3} mmol) of PTA instead of DAPTA.

Au-DAPTA and Au-PTA Nanocomposites in Aqueous Media (DNA and PNA Systems, Respectively)

The synthesis of Au-DAPTA (or -PTA) hydrophilic nanocomposites were done following the same procedure described for the nanocomposites in organic media but substituting the chloroform for deionized water.

Three different samples of each nanocomposite were synthesized using different amounts of Au NPs. The volumes of Au NPs solution used in each case are compiled in **Table 1**.

PHYSICAL MEASUREMENTS

Transmission Electron Microscopy (TEM)

Au NPs were prepared for observation by TEM by dilution in chloroform/water followed by sonication. A droplet of the solution was then poured in holey carbon covered copper TEM grids. A JEOL 2000 FX II conventional TEM operating at an accelerating voltage of 80 kV was used.

SEM

Scanning electron microscopy (SEM) was carried out at 20 kV using J-7100F (Jeol) equipped with a thermal field electron source.

DLS

Dynamic Light Scattering (DLS) measurements were carried out in a Zetasizer NanoS Spectrometer. The samples were measured in quartz cuvettes.

TABLE 1 | Volumes of Au NP stock solution used in each synthesis.

Sample	Volume of Au NP stock solution
DNO_1	540 μL hydrophobic Au NPs ($CHCl_3$)
DNO_2	270 μL hydrophobic Au NPs ($CHCl_3$)
DNO_3	54 μL hydrophobic Au NPs ($CHCl_3$)
DNA_1	1600 μL hydrophilic Au NPs (H_2O)
DNA_2	800 μL hydrophilic Au NPs (H_2O)
DNA_3	160 μL hydrophilic Au NPs (H_2O)
PNO_1	540 μL hydrophobic Au NPs ($CHCl_3$)
PNO_2	270 μL hydrophobic Au NPs ($CHCl_3$)
PNO_3	54 μL hydrophobic Au NPs ($CHCl_3$)
PNA_1	1600 μL hydrophilic Au NPs (H_2O)
PNA_2	800 μL hydrophilic Au NPs (H_2O)
PNA_3	160 μL hydrophilic Au NPs (H_2O)

The concentration of Au NPs in aqueous stock solution was 0.015 μM and in organic stock solution 2.33 μM.

Infrared Spectroscopy

IR spectra were recorded with a FTIR 520 Nicolet Spectrophotometer. For the measurements, a pellet of a mixture of the sample and KBr was used.

UV-Vis Absorbance Spectroscopy

A Cary 100 Scan 388 Varian UV/Vis spectrophotometer was used with quartz cuvettes for optical characterization.

ICP-AES

The compositions and concentrations of the nanoparticles solutions were determined by inductively coupled plasma atomic emission spectroscopy (ICP-AES). The measurements were performed with an Optima 3200 RL PerkinElmer spectrometer. For the measurements, 50 mL of the solutions was precipitated in MeOH and redispersed in $CHCl_3$. The solution was evaporated in an oven overnight at 90°C. Aqua regia (2.5 mL) and H_2O_2 (0.7 mL) were added to the precipitate before the vial was sealed and then heated to 90°C for 72 h. The resulting solution was transferred to a 25 mL volumetric flask and diluted with Milli-Q water.

NMR

^{1}H NMR [δ(TMS) = 0.0 ppm], $^{31}P\{^1H\}$ NMR [δ(85% H_3PO_4) = 0.0 ppm] spectra have been obtained on a Varian Mercury 400 and Bruker 400.

Small-Angle X-Ray Scattering (SAXS)

SAXS was performed on the NCD-SWEET beamline at the ALBA Synchrotron at 12.4 keV, and the distance sample/detector was 6.2 m to cover the range of momentum transfer of $0.028 < q < 2.56\ nm^{-1}$. The data were collected on a Pilatus3S 1M detector with a pixel size of 172.0 × 172.0 μm^2. The exposure time was 30 s. The q-axis calibration was obtained by measuring silver behenate (Huang et al., 1993). The program pyFAI was used to integrate the 2D SAXS data into 1D data (Kieffer and Karkoulis, 2013). The data were then subtracted by the background using PRIMUS software (Konarev et al., 2003). The maximum particle dimension Dmax and the pair distance distribution function P(r) were determined with GNOM (Svergun, 1992). The low-resolution structure of the aggregates was reconstructed *ab initio* from the initial portions of the scattering patterns using the program DAMM (Svergun, 1999; Krebs et al., 2004).

Cell Culture and Antiproliferative Effects

MDA-MB-231 breast adenocarcinoma and HT-29 colon carcinoma were maintained in DMEM high glucose (PAA) supplemented with 50 mg/L gentamycin and 10% (V/V) fetal calf serum (FCS) at 37°C under 5% CO_2 atmosphere and passaged every 7 days. Antiproliferative effects were determined as follows: a volume of 100 μL of a 38,000 cells/ml (HT-29) or 40000 cells/ml (MDA-MB-231) suspension were seeded into 96-well plates and incubated for 48 or 72 h at 37°C/5% CO_2. After the incubation period the cells of one individual plate were fixed by addition of 100 μL of a 10% glutaraldehyde solution per well. After 30 min. One hundred and Eighty Microliter PBS were added and the plate was stored at 4°C (t_0 plate) until further procedures (see below). Nanoparticle suspensions were diluted 1:100 with cell culture medium to the final test concentrations. In the remaining plates the medium was replaced by the medium containing the nanoparticles or solvent control (water or $CHCl_3$). Then the plates were incubated for 72 h (HT-29) or 96 h (MDA-MB-231) at 5% CO_2/37°C. The medium was removed and the cells were treated with 100 μl of a 10% glutaraldehyde solution. Afterwards the cells of all plates (including the t_0 plate) were washed with 180 μL PBS and stained with 100 μL of a 0.02% crystal violet solution for 30 min. The crystal violet solution was removed and the plates were washed with water and dried. A volume of 180 μL of ethanol 70% was added to each well and after 2–3 h of gentle shaking the absorbance was measured at 595 nm in a microplate reader (Victor X4, PerkinElmer). The mean absorbance value of the t_0 plate was subtracted from the absorbance values of all other absorbance values in order to correct for the initial cell biomass. The IC_{50}-values were calculated as the concentrations reducing the cellular proliferation in comparison with the solvent control by 50%.

RESULTS AND DISCUSSION

Synthesis and Characterization

Our synthetic strategy started by preparing two samples of Au NPs capped by hydrophilic and hydrophobic stabilizing ligands separately, i.e., citrate anions and oleylamine molecules, respectively (see Materials and Methods section). TEM micrographs of the as-prepared samples allowed to evaluate the morphological and size distribution of the NPs in the two samples. The hydrophilic sample consists of a collection of nanoparticles with a significant distribution of shapes including spherical (the most abundant), triangular, and elongated nanoparticles of low aspect ratio as shown in **Figure 1a**. On the contrary, **Figure 1b** is a TEM representative image of the hydrophobic sample in which only spherical faceted nanoparticles are observed. The size distribution was also much narrower in the hydrophobic sample, even though both samples showed an average diameter of ca. 14 nm and their deposition

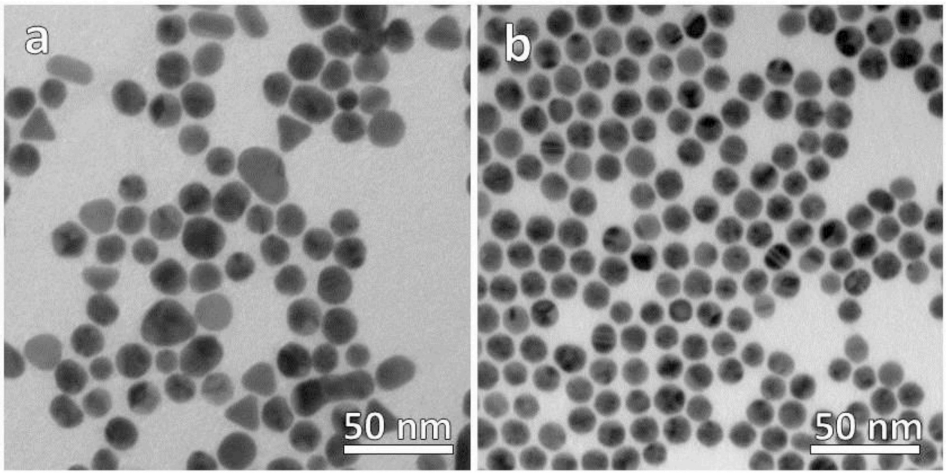

FIGURE 1 | TEM micrographs of **(a)** hydrophilic citrate-capped and **(b)** hydrophobic oleylamine-capped Au NPs.

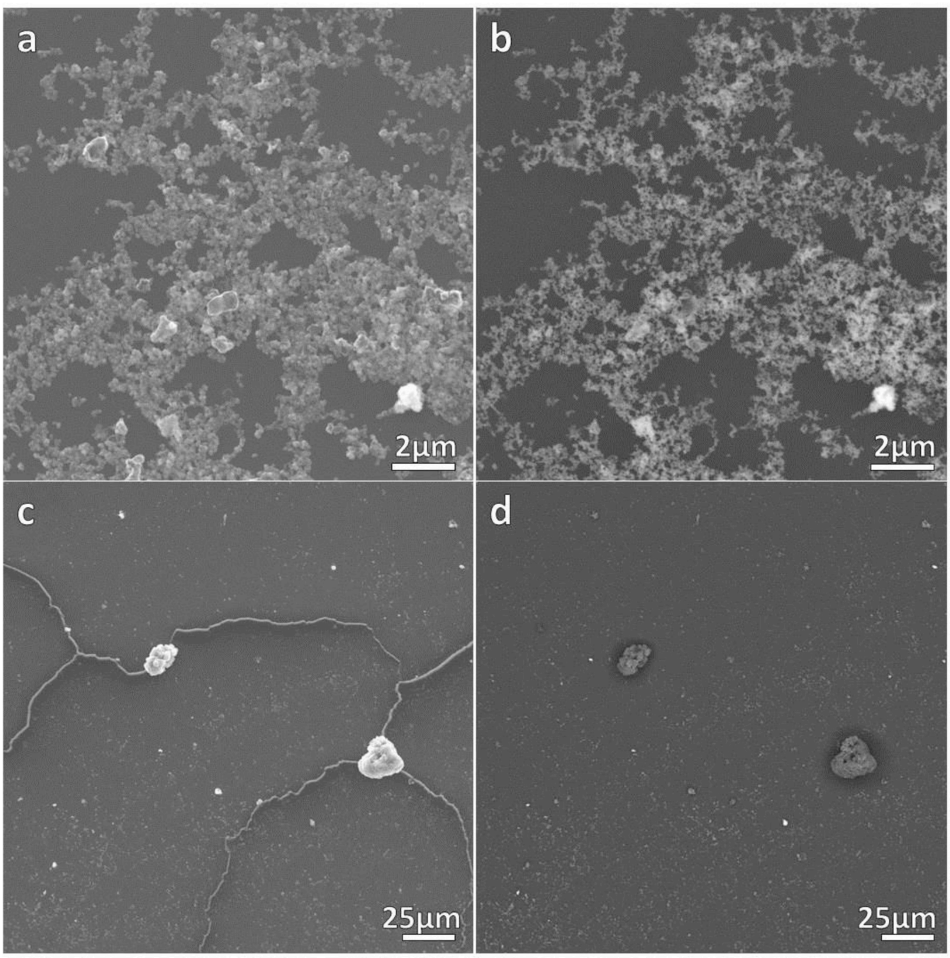

FIGURE 2 | SEM micrographs of DNO_1 sample. **(a,c)** contain topographical micrographs recorded with secondary electrons, while **(b,d)** contain Z-sensitive micrographs recorded with backscattered electrons.

on the TEM grid suggests that the colloids are well-dispersed in solution without evidences of aggregation.

The correct formation of the resulting nanocomposites was evidenced by SEM micrographs as depicted in **Figures 2**, **3** corresponding to DNO_1 and PNA_1 samples, made of DAPTA Au(I) complex in chloroform and PTA Au(I) complex in water respectively, and both with the highest amount of Au NPs in the reaction medium. The images suggest that the samples are mainly constituted by aggregates of Au NPs, with sizes ranging between 100 and 300 nm approximately that are well-interconnected between them forming a kind of sponge-like 3D network. The individual aggregates are likely surrounded by a shell of the organometallic complex. Indeed, a quantitative shrinkage of the aggregates is evident when comparing topographic images in panels (a) and (c) in the figures, recorded with secondary electrons, with the corresponding Z-sensitive images in panels (b) and (d), recorded with backscattered electrons. The significant reduction in volume of the clusters between the two related images is indicative of the presence of an organic shell around the metallic NPs. Besides the presence of the organometallic-NP composites, few long fibers are also observed at low magnifications (**Figures 2c,d**, **3c,d**). The vanishing of these fibers in images recorded using backscattered electrons confirms their organic origin, suggesting that they are formed as a result of the supramolecular interactions between free molecules of the organometallic moiety, as it was observed in previous studies of these organometallic complexes (Aguiló et al., 2013), and that they do not incorporate Au NPs in their structure. Generally speaking, the observed trend with amount of Au NPs was the same, independently of the organometallic molecule and solvent used for the synthesis of the nanocomposites: the larger the amount of Au NPs used for the synthesis, the higher the number of composite aggregates encountered, while few or none nanocomposites were found in samples containing the lowest amount of Au NPs (samples XXX_3 of each group), as shown in **Figures S1**–**S4** in the SI. Some large aggregates of approximately 20 μm can also be appreciated by SEM, although in a much lower frequency compared with the previous smaller ones. DLS measurements performed on these samples mainly confirm the average size of the aggregates, this being of a few hundreds of nanometers as observed by SEM, as well as the presence of a small population of microscale aggregates as indicated

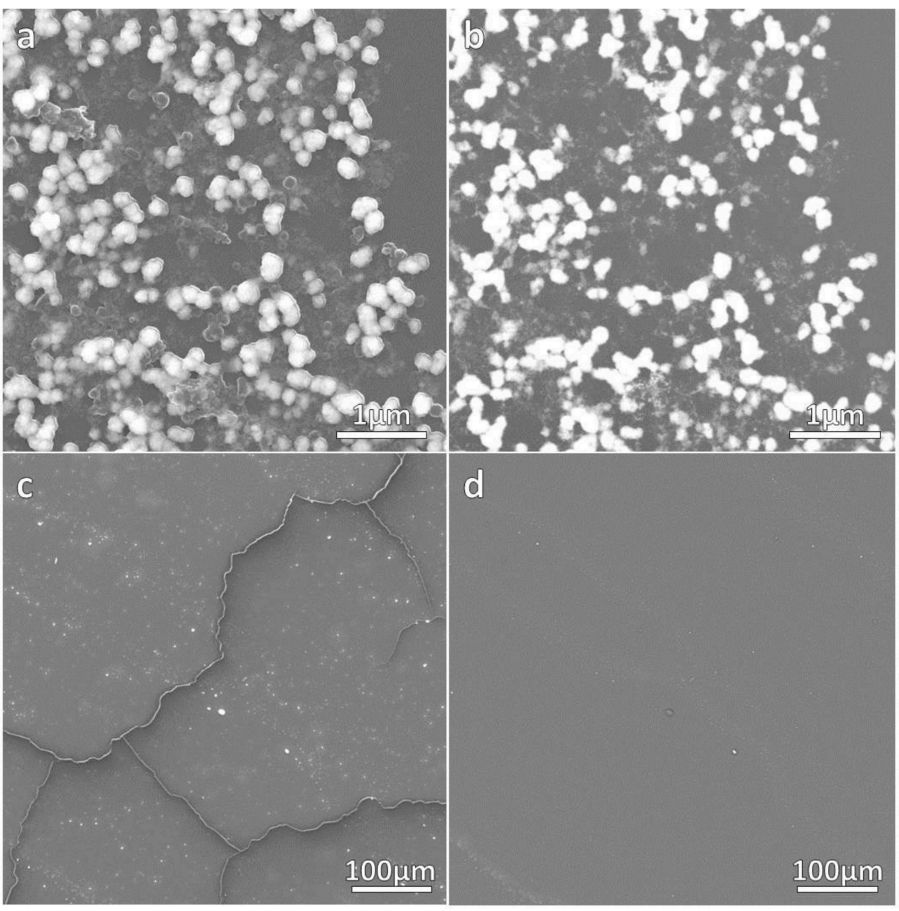

FIGURE 3 | SEM micrographs of PNA_1 sample. **(a,c)** contain topographical micrographs recorded with secondary electrons, while **(b,d)** contain Z-sensitive micrographs recorded with backscattered electrons.

by SEM too (see **Figure S5** in the SI). Noteworthy, DLS data evidence the presence of smaller aggregates with sizes ranging from 20 to 60 nm approximately depending on the sample, which cannot be discerned from the larger ones by previous SEM characterization.

The size and shape of the aggregates were measured by SAXS for those samples prepared with the highest (XXX_1) and medium (XXX_2) amount of Au NP. Samples with less amount of Au NPs were not measured since previous SEM studies revealed the presence of no composites in the solutions. Each of the eight considered samples (DNO_1/2; DNA_1/2; PNO_1/2 and PNA_1/2) was measured as initially prepared and also with two additional diluted concentrations (i.e., with DNO_1_1 being the as-prepared sample, and DNO_1_2 and DNO_1_3 the samples derived from 1/500 and 1/1000 dilution), at different temperatures (from 20 to 40°C in a 5°C gradient, for better analysis of the aggregates' formation) and 1 week after their preparation to favor aggregation. The low-resolution structures were reconstructed *ab initio* from the scattering patterns using the DAMMIN program (see Materials and Methods section). The resulting size and morphologies profile are depicted in **Figures 4** and **Figures S6–S18** for all compounds that display significant aggregation. No significant aggregation was detected for the rest of the cases. Generally speaking, aggregates of sizes between 10 and 30 nm are measured by SAXS depending on the sample, which hardly agrees with the size of the aggregates observed and measured by analysis of SEM micrographs in **Figures 2**, **3**, but on the opposite their sizes roughly coincide with the values observed for the smallest aggregates detected by DLS measurements and shown in **Figure S5**. The values obtained by DLS and SAXS point out the possibility that the relatively large aggregates (100–300 nm) observed by SEM might be formed by smaller subunits (10–60 nm), linked by organometallic domains, that are only appreciable by light and X-ray scattering experiments. From our experimental data it can be concluded that Au NPs are mainly wrapped within a layer of organometallic complex forming small metallic clusters of a few nanoparticles. Additionally, larger 3D aggregates based on non-covalent interactions are formed, which are responsible for the sponge-like structure observed. In general, it can be seen that temperature does not affect substantially the size of the aggregates. Only in the case of DNO2, a significant increase on the size is clearly detected in both diluted samples, DNO2_1 and DNO2_2. This can be ascribed to the higher contribution of hydrophobic interactions at higher temperatures, being DAPTA moieties (more soluble in water) avoiding the contact with organic solvent. Within each set of samples measured at different concentrations, the collected data indicates that no aggregation occurs for the most diluted samples (XXX_X_3), while appreciable degrees of aggregation were measured, in general, for the other two dilutions. This data could indicate the existence of a critical concentration of aggregates below which they lose their stability. Some other trends can be observed looking at this data regarding now the amount of Au NPs used in the reaction. That is, in organic medium, a light increase of size was detected for PNO_2_X samples containing a smaller amount of Au NPs or aggregates compared to analogous PNO_1_X samples. On the contrary, DNO_1_X samples give rise to the formation of larger structures

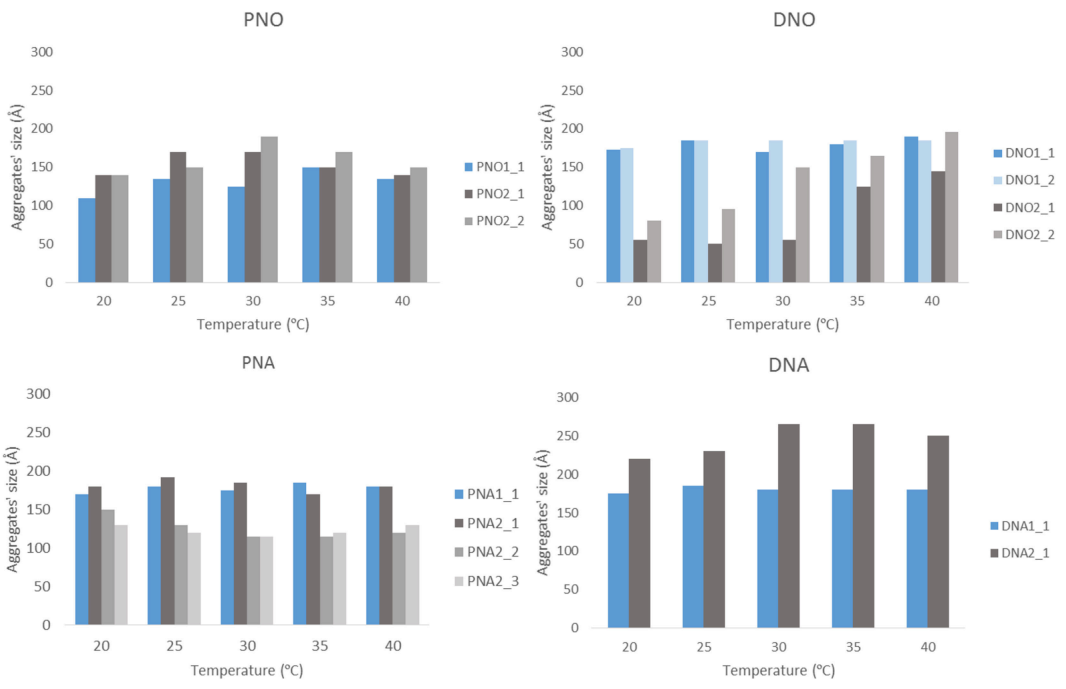

FIGURE 4 | Representation of aggregates' size vs. temperature. The results are plotted separately depending on the phosphine and the medium. Blue bars stand for XXX_1 and gray bars for XXX_2 samples.

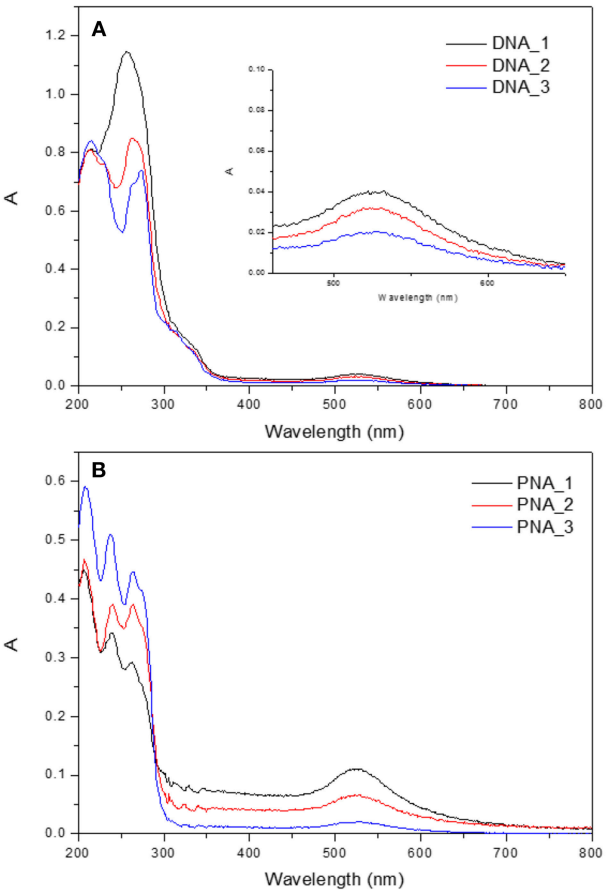

FIGURE 5 | UV-Visible absorption spectra of **(A)** DNA_1-3 and **(B)** PNA_1-3 samples.

compared to the DNO_2_X analogs. These observations could be rationalized based on the lower solubility of DAPTA (in DNO complexes) in organic medium with respect to PTA (in PNO derivatives). Following this reason, it makes sense to understand the contrary effect in water: smaller aggregates for samples PNA_2_X containing a smaller amount of Au NPs or aggregates, and larger aggregates for samples DNA_2_X containing also a smaller amount of Au NPs or aggregates were observed, since the higher solubility in water of DAPTA Au(I) complex makes the formation of aggregates more difficult in this solvent.

The infrared spectra of the nanocomposites display the expected bands both from the organometallic complex and from the stabilizing ligands of the NPs. The resulting broadening of the alkynyl moieties are indicative of Au···π interaction between the NPs' surface and the complex.

The UV/vis absorption spectra of the hybrid system present two different signals, as shown in **Figure 5** for the hydrophilic nanocomposites with DAPTA and PTA. On the one hand, there is the band around 260 nm attributed to the Au(I) complex. On the other hand, the signal at 500–600 nm is assigned to the characteristic LSPR band of Au NPs. To better study the effect of the quantity of gold NPs added to the formation of hybrid system, absorption spectra of three different systems per organometallic molecule were recorded (DNA_1-3 and PNA_1-3). There is a change in the profile of the more energetically part of the absorption spectra, when the amount of nanoparticles used in the synthesis of the hybrid system increases, there is a loss of the vibrational shape in the band as an evidence of interaction between NPs and the corresponding organometallic complex (Ferrer et al., 2008).

TABLE 2 | IC_{50} values of the different hybrid systems and corresponding counterparts.

Compound	HT-29 (μM)	MDA-MB-231 (μM)
DNA1	6.14 ± 0.29	>10
DNA2	>6.4	>7.7
PNA1	>10	>10
PNA2	>10	>10
DNO1	3.41 ± 0.29	1.73 ± 0.44
DNO2	2.76 ± 0.23	>1.4
PNO1	1.82 ± 0.32	1.00 ± 0.17
PNO2	4.16 ± 0.38	2.02 ± 0.40
Org NPs	5.39 ± 0.89	6.01 ± 0.85
Aqueous NPs	>10	>10
AupyPTA[a]	56.09 ± 3.05	52.32 ± 4.76
AypyDAPTA[a]	74.78 ± 9.34	34.07 ± 3.51

[a] *From reference Arcau et al. (2014); mean values and standard errors of 2–3 independent experiments are presented.*

Biological Activity

The biological evaluation was focused on determining the effects against tumor cell growth in HT-29 colon carcinoma and MDA-MB-231 breast cancer (**Table 2**). Inspection of **Table 2** let us retrieve some important conclusions: (i) Hybrid organic systems present higher cytotoxicity than the corresponding aqueous systems; (ii) hybrid systems present higher cytotoxicity than their respective counterparts, both organometallic complexes and NPs, being a nice cooperative effect than makes promising this encapsulation process regarding the study of their biological activity. However, the toxicity of the drug free organic NPs and the role of $CHCl_3$ as solvent for redispersion has to be taken into account in future studies.

Experiments with non-tumor cells were not performed as tumor selectivity in the used assay could not be expected. By theory, nanoparticles would be enriched in tumor tissue by the EPR effect. This effect is not present in static tissue culture models, and thus tissue selectivity of nanoparticles can not be evaluated in this assay (Nakamura et al., 2016).

CONCLUSIONS

The reaction of citrate and oleylamine-capped Au NPs with two different Au(I)-based organometallic complexes gives rise to the successful formation of nanocomposites soluble in

either aqueous or organic media, forming large 3D sponge-like aggregates. SEM, DLS, SAXS, and spectroscopic techniques reveal useful for the verification of interaction between the corresponding building blocks. The lower IC_{50} values measured for nanocomposites compared to those of individual counterparts evidence their better biological activity against MDA-MB-231 and HT-29 tumor cells, opening a promising area of research in this field.

AUTHOR CONTRIBUTIONS

AF, LR, and IO designed the experiments. MD and AP carried out the synthesis and characterization of hybrid systems. PL carried out biological activity experiments. AF, LR, and IO supervised the project. All authors wrote and reviewed the manuscript.

ACKNOWLEDGMENTS

The authors are grateful to the Ministry of Economy, Industry, and Competitiveness of Spain (AEI/FEDER, UE Projects CTQ2016-76120-P and CTQ2015-68370-P). AF is a Serra Húnter fellow. IO acknowledges support from DFG (Deutsche Forschungsgemeinschaft). SAXS experiments were performed at the NCD- SWEET beamline of the ALBA Synchrotron Light Facility in collaboration with the ALBA staff.

SUPPLEMENTARY MATERIAL

The Supplementary Material for this article can be found online at: https://www.frontiersin.org/articles/10.3389/fchem.2019.00060/full#supplementary-material

REFERENCES

Aguiló, E., Gavara, R., Lima, J. C., Llorca, J., and Rodríguez, L. (2013). From Au(i) organometallic hydrogels to well-defined Au(0) Nanoparticles. *J. Mater. Chem. C* 1, 5538–5547. doi: 10.1039/c3tc31168f

Andermark, V., Göke, K., Kokoschka, M., Abu El Maaty, M. A., Lum, C. T., Zou, T., et al. (2016). Alkynyl Gold(I) phosphane complexes: evaluation of structure-activity-relationships for the phosphane ligands, effects on key signaling proteins and preliminary *in vivo* studies with a nanoformulated complex. *J. Inorg. Biochem.* 160, 140–148. doi: 10.1016/j.jinorgbio.2015.12.020

Arcau, J., Andermark, V., Aguiló, E., Gandioso, A., Moro, A., Cetina, M., et al. (2014). Luminescent alkynyl-gold(I) coumarin derivatives and their biological activity. *Dalt. Trans.* 43, 4426–4436. doi: 10.1039/c3dt52594e

Ballesteros, L. M., Martín, S., Cortés, J., Marqués-González, S., Pérez-Murano, F., Nichols, R. J., et al. (2014). From an organometallic monolayer to an organic monolayer covered by metal nanoislands: a simple thermal protocol for the fabrication of the top contact electrode in molecular electronic devices. *Adv. Mater. Interfaces* 1:1400128. doi: 10.1002/admi.201400128

Boisselier, E., and Astruc, D. (2009). Gold nanoparticles in nanomedicine: preparations, imaging, diagnostics, therapies and toxicity. *Chem. Soc. Rev.* 38, 1759–1782. doi: 10.1039/b806051g

Chui, C. H., Wong, R. S. M., Gambari, R., Cheng, G. Y. M., Yuen, M. C. W., Chan, K. W., et al. (2009). Antitumor activity of diethynylfluorene derivatives of Gold(I). *Bioorganic Med. Chem.* 17, 7872–7877. doi: 10.1016/j.bmc.2009.10.034

Dalmases, M., Aguiló, E., Llorca, J., Rodríguez, L., and Figuerola, A. (2016). Exploiting metallophilicity for the assembly of inorganic nanocrystals and conjugated organic molecules. *ChemPhysChem* 17, 2190–2196. doi: 10.1002/cphc.201600239

Das, D., Kar, T., and Das, P. K. (2012). Gel-Nanocomposites: materials with promising applications. *Soft Matter* 8, 2348–2365. doi: 10.1039/C1SM06639K

Ferrer, M., Gutiérrez, A., Rodríguez, L., Rossell, O., Lima, J. C., Font-Bardia, M., et al. (2008). Study of the effect of the phosphane bridging chain nature on the structural and photophysical properties of a series of Gold(I) ethynylpyridine complexes. *Eur. J. Inorg. Chem.* 3, 2899–2909. doi: 10.1002/ejic.200800167

Gavara, R., Aguiló, E., Schur, J., Llorca, J., Ott, I., and Rodríguez, L. (2016). Study of the effect of the chromophore and nuclearity on the aggregation and potential biological activity of Gold(I) alkynyl complexes. *Inorganica Chim. Acta* 446, 189–197. doi: 10.1016/j.ica.2016.03.012

Gavara, R., Llorca, J., Lima, J. C., and Rodríguez, L. (2013). A luminescent hydrogel based on a new Au(I) complex. *Chem. Commun.* 49, 72–74. doi: 10.1039/C2CC37262B

Huang, T. C., Toraya, H., Blanton, T. N., and Wu, Y. (1993). X-Ray powder diffraction analysis of silver behenate, a possible low-angle diffraction standard. *J. Appl. Crystallogr.* 26, 180–184. doi: 10.1107/S0021889892009762

Kieffer, J., and Karkoulis, D. (2013). PyFAI, a versatile library for azimuthal regrouping. *J. Phys. Conf. Ser.* 425, 8–13. doi: 10.1088/1742-6596/425/20/202012

Konarev, P. V., Volkov, V. V., Sokolova, A. V., Koch, M. H. J., and Svergun, D. I. (2003). PRIMUS: a windows PC-Based system for small-angle scattering data analysis. *J. Appl. Crystallogr.* 36, 1277–1282. doi: 10.1107/S0021889803012779

Krebs, A., Durchschlag, H., and Zipper, P. (2004). Small angle x-ray scattering studies and modeling of eudistylia vancouverii chlorocruorin and macrobdella decora hemoglobin. *Biophys. J.* 87, 1173–1185. doi: 10.1529/biophysj.103.037929

Lima, J. C., and Rodriguez, L. (2011). Phosphine-Gold(I) compounds as anticancer agents: general description and mechanisms of action. *Anticancer. Agents Med. Chem.* 11, 921–928. doi: 10.2174/187152011797927670

Lima, J. C., and Rodríguez, L. (2015). Supramolecular gold metallogelators: the key role of metallophilic interactions. *Inorganics* 3, 1–18. doi: 10.3390/inorganics3010001

Meyer, A., Bagowski, C. P., Kokoschka, M., Stefanopoulou, M., Alborzinia, H., Can, S., et al. (2012). On the biological properties of alkynyl phosphine Gold(I) complexes. *Angew. Chem. Int. Ed.* 51, 8895–8899. doi: 10.1002/anie.201202939

Meyer, A., Gutiérrez, A., Ott, I., and Rodríguez, L. (2013). Phosphine-Bridged dinuclear Gold(I) alkynyl complexes: thioredoxin reductase inhibition and cytotoxicity. *Inorganica Chim. Acta* 398, 72–76. doi: 10.1016/j.ica.2012.12.013

Motl, N. E., Smith, A. F., Desantis, C. J., and Skrabalak, S. E. (2014). Engineering plasmonic metal colloids through composition and structural design. *Chem. Soc. Rev.* 43, 3823–3834. doi: 10.1039/C3CS60347D

Muhich, C. L., Qiu, J., Holder, A. M., Wu, Y. C., Weimer, A. W., Wei, W. D., et al. (2015). Solvent control of surface plasmon-mediated chemical deposition of au nanoparticles from alkylgold phosphine complexes. *ACS Appl. Mater. Interfaces* 7, 13384–13394. doi: 10.1021/acsami.5b01918

Nakamura, Y., Mochida, A., and Choyke,P. L., Kobayashi, H. (2016). Nanodrug delivery: is the enhanced permeability and retention effect sufficient for curing cancer? *Bioconjug. Chem.* 27, 2225–2238. doi: 10.1021/acs.bioconjchem.6b00437

Rodríguez, L., Ferrer, M., Crehuet, R., Anglada, J., and Lima, J. C. (2012). Correlation between photophysical parameters and gold-gold distances in Gold(I) (4-Pyridyl) ethynyl complexes. *Inorg. Chem.* 51, 7636–7641. doi: 10.1021/ic300609f

Schmidbaur, H., and Schier, A. (2012). Aurophilic interactions as a subject of current research: an up-date. *Chem. Soc. Rev.* 41, 370–412. doi: 10.1039/C1CS15182G

Schuh, E., Valiahdi, S. M., Jakupec, M. A., Keppler, B. K., Chiba, P., and Mohr, F. (2009). Synthesis and biological studies of some Gold(I) complexes containing functionalised alkynes. *Dalt. Trans.* 10841–10845. doi: 10.1039/b911234k

Svergun, D. I. (1992). Determination of the regularization parameter in indirect-transform methods using perceptual criteria. *J. Appl. Crystallogr.* 25, 495–503. doi: 10.1107/S0021889892001663

Svergun, D. I. (1999). Restoring low resolution structure of biological macromolecules from solution scattering using simulated annealing. *Biophys. J.* 76, 2879–2886. doi: 10.1016/S0006-3495(99)77443-6

Turkevich, J., Stevenson, P. C., and Hillier, J. (1953). The formation of colloidal gold. *J. Phys. Chem.* 57, 670–673. doi: 10.1021/j150508a015

Vergara, E., Cerrada, E., Casini, A., Zava, O., Laguna, M., and Dyson, P. J. (2010). Antiproliferative activity of Gold(I) alkyne complexes containing water-soluble phosphane ligands. *Organometallics* 29, 2596–2603. doi: 10.1021/om100300a

Yu, H., Chen, M., Rice, P. M., Wang, S. X., White, R. L., and Sun, S. (2005). Dumbbell-like bifunctional Au-Fe3O4nanoparticles. *Nano Lett.* 5, 379–382. doi: 10.1021/nl047955q

Zhang, J., and Su, C. Y. (2013). Metal-Organic gels: from discrete metallogelators to coordination polymers. *Coord. Chem. Rev.* 257, 1373–1408. doi: 10.1016/j.ccr.2013.01.005

Conflict of Interest Statement: The authors declare that the research was conducted in the absence of any commercial or financial relationships that could be construed as a potential conflict of interest.

frontiers in Chemistry

ORIGINAL RESEARCH
published: 12 April 2018
doi: 10.3389/fchem.2018.00110

Fast and Simple Microwave Synthesis of TiO_2/Au Nanoparticles for Gas-Phase Photocatalytic Hydrogen Generation

Anna May-Masnou[1], Lluís Soler[2]*, Miquel Torras[1], Pol Salles[1], Jordi Llorca[2] and Anna Roig[1]*

[1] *Institut de Ciència de Materials de Barcelona, CSIC, Bellaterra, Spain,* [2] *Departament d'Enginyeria Química and Barcelona Research, Center for Multiscale Science and Engineering, Institut de Tècniques Energètiques, Universitat Politècnica de Catalunya, EEBE, Barcelona, Spain*

The fabrication of small anatase titanium dioxide (TiO_2) nanoparticles (NPs) attached to larger anisotropic gold (Au) morphologies by a very fast and simple two-step microwave-assisted synthesis is presented. The TiO_2/Au NPs are synthesized using polyvinylpyrrolidone (PVP) as reducing, capping and stabilizing agent through a polyol approach. To optimize the contact between the titania and the gold and facilitate electron transfer, the PVP is removed by calcination at mild temperatures. The nanocatalysts activity is then evaluated in the photocatalytic production of hydrogen from water/ethanol mixtures in gas-phase at ambient temperature. A maximum value of 5.3 $mmol \cdot g_{cat}^{-1} \cdot h^{-1}$ (7.4 $mmol \cdot g_{TiO2}^{-1} \cdot h^{-1}$) of hydrogen is recorded for the system with larger gold particles at an optimum calcination temperature of 450°C. Herein we demonstrate that TiO_2-based photocatalysts with high Au loading and large Au particle size (≈50 nm) NPs have photocatalytic activity.

Keywords: nanotitania, gold nanoparticles, microwave synthesis, gas phase photocatalysis, hydrogen production

OPEN ACCESS

Edited by:
Carlos Lodeiro, Faculdade de Ciências e Tecnologia da Universidade Nova de Lisboa, Portugal

Reviewed by:
Jose M. Palomo, Instituto de Catálisis y Petroleoquímica (CSIC), Spain
Sabine Szunerits, Lille University of Science and Technology, France

****Correspondence:***
Anna May-Masnou
amay@icmab.es
Lluís Soler
lluis.soler.turu@upc.edu

Specialty section:
This article was submitted to Inorganic Chemistry, a section of the journal Frontiers in Chemistry

Received: *13 February 2018*
Accepted: *26 March 2018*
Published: *12 April 2018*

Citation:
May-Masnou A, Soler L, Torras M, Salles P, Llorca J and Roig A (2018) Fast and Simple Microwave Synthesis of TiO_2/Au Nanoparticles for Gas-Phase Photocatalytic Hydrogen Generation. Front. Chem. 6:110. doi: 10.3389/fchem.2018.00110

INTRODUCTION

The prospect of achieving clean and renewable hydrogen at ambient temperatures through the photocatalytic water splitting reaction has gained much attention since the pioneer work of Honda and Fujishima in 1972 using TiO_2 as photocatalyst in a photoelectrochemical cell (Fujishima and Honda, 1972). TiO_2 is an excellent candidate for photocatalysis presenting an effective generation of electron-hole pairs, chemical stability to corrosion and photocorrosion and providing suitable interfaces for charge transfer. However, its large band gap (anatase 3.2 eV; rutile 3.0 eV) restricts its use in the UV fraction of the spectrum, and the fast recombination rate of the charge carriers (electron-hole) after excitation compromises the efficiency of H_2 generation (Ge et al., 2017).

Higher photocatalytic activities have been achieved using more complex nanocatalysts, for instance, by doping TiO_2 with cations or anions or by combining the TiO_2 with metal or semiconductor nanoparticles (NPs). Usually noble metal NPs, such as Au (Bamwenda et al., 1995; Primo et al., 2011; Jovic et al., 2013a,b; Taboada et al., 2014a,b), Pd (Khojasteh et al., 2016), Pt (Jovic et al., 2013b; Al-Azri et al., 2015), Au-Cu (Bonmatí et al., 2015), Au-Pd (Su et al., 2014), or metal oxide NPs, like RuO_2 or CuO (Bandara et al., 2005; Xu and Sun, 2009; Yu et al., 2011) have been used. These doping agents act as a cocatalyst, enhancing the electron-hole charge separation,

avoiding or delaying the recombination rate and increasing the overall photocatalytic activity. However, this technology is still not fully commercially available, mainly due to the low efficiency of the materials, to their low stability during the water splitting reaction, and to its overall high cost.

The influence of metal loading has been studied thoroughly considering small metal percentages, usually up to 10 wt%. In this range, the hydrogen yield increases with increasing metal content, reaches a maximum, and then starts a steady decrease. The optimum loading is usually found between 0.5 and 8 wt% (Murdoch et al., 2011; Jovic et al., 2013a). A common reasoning is that the surface of the semiconductor becomes partially blocked by the metal, decreasing the surface concentration of electrons and holes available for reaction, and hindering light absorption (Bamwenda et al., 1995; Maeda, 2011). Another explanation of the photocatalytic activity decrease at large metal fractions is that the deposited metal particles can themselves act as recombination centers for the photogenerated electrons and holes (Bamwenda et al., 1995). The influence of particle size has also been widely studied. Most authors sustain that the catalytic activity of Au NPs disappears for particles larger than 20 nm, since the activity is correlated with the number of Au atoms on the external surface (Haruta, 1997; Primo et al., 2011). Accordingly, Murdoch et al., 2011 showed that Au NPs in the size range 3–30 nm (especially up to 12 nm) on TiO_2 were the most active in hydrogen production. However, the optimum metal particle size will also depend on the size of TiO_2 NPs and on the type of contact with the semiconductor support. Thus, full implications of the loading, size, and shape of the metal cocatalyst need to be further explored.

The overall activity of the photocatalyst and hydrogen production can also be enhanced by the addition of easily oxidizable sacrificial agents, acting as electron donors (Nadeem et al., 2010). According to previous works (Taboada et al., 2014a,b; Bonmatí et al., 2015), some of us demonstrated that the rate of H_2 production increased due to the irreversible oxidation of the organic molecule with the holes and the concomitant suppression of electron-hole recombination. Although ethanol is not the sacrificial agent with the highest rate of hydrogen production (Bowker, 2012; Taboada et al., 2014a; Chen et al., 2015), it is by far one of the most promising and used, since it is ready available, easy to transport, safe to handle, and it can be produced by renewable biomass. Ethanol is a good option when performing gas-phase reactions, since it can be easily mixed with water and form gaseous mixtures. Moreover, in gas-phase reaction, contrarily to a liquid-phase reaction, as the H_2 and O_2 formed on the surface of the catalyst are rapidly released, there is shorter time for the formation of undesired byproducts. However, acetaldehyde is produced as a result of ethanol dehydrogenation, as stated in Equation (1) (Taboada et al., 2014b).

$$CH_3CH_2OH \rightarrow CH_3CHO + H_2 \quad (1)$$

Producing functional materials with better properties than the existing ones, while using cheaper, faster and cleaner synthesis, is in high demand. The most widespread methods to obtain nanoparticles, such as co-precipitation, thermal decomposition and microemulsion are limited by either the amount of available reagents or the required long unpractical processing times. Microwave energy is becoming an increasingly attractive alternative tool in all areas of synthetic chemistry because it can boost some competitive advantages over other fabrication methods. It is fast, produces high yields, is scalable and is easy to operate, being efficient in terms of energy consumption and environmentally friendly (Michael et al., 1991; Stuerga et al., 1993; Bilecka and Niederberger, 2010). In particular, the versatility of the method for the synthesis of nanoparticles has been reported (Stuerga et al., 1993; Baghbanzadeh et al., 2011).Monodisperse nanoparticles are achieved due to more homogeneous inner core heating with no solvent convective currents due to temperature gradients (Baghbanzadeh et al., 2011), which decreases the possibility of asynchronic nucleation and heterogeneous nanocrystal growth. Indeed, microwave-assisted synthesis has appeared as an attractive way to prepare scalable, uniform and controllable colloids with complex kinetic/thermodynamic control over crystallization processes (Hachtel et al., 2016).

Herein, we report on a facile synthesis of TiO_2/Au nanostructures through a microwave-assisted route (Gonzalez-Moragas et al., 2015; Yu et al., 2015; Hachtel et al., 2016). The obtained nanomaterials consist of two different sizes of Au NPs (*ca.* 50 and *ca.* 10 nm) in contact with smaller crystalline TiO_2-anatase NPs of *ca.* 10 nm in both cases. We then investigate and compare the photocatalytic performance of the TiO_2/Au nanomaterials with Au loading as high as 20 wt%. The photocatalytic activity is studied on H_2 production from a mixture of ethanol and water in gas phase. We analyzed the effect of the calcination temperature on the photocatalytic efficiency of the two TiO_2/Au nanostructures. The use of the same size of TiO_2 NPs and varying the size of Au NPs allows us to elucidate the role of the size of Au NPs/contact points. There are very few previous studies analyzing the photocatalytic activity of TiO_2 NPs with very high Au loading and large Au particle size, which by using smaller TiO_2 NPs could increase the number of Schottky junctions and, therefore, improve the overall photocatalytic performance of the process.

MATERIALS AND METHODS

Materials

Titanium butoxide (TBOT) (97%), polyvinylpyrrolidone (PVP, average molecular weight: 10000 g/mol) and hydrogen tetrachloroaurate trihydrate ($HAuCl_4 \cdot 3H_2O \geq 99.9\%$) were purchased from Sigma-Aldrich. Anhydrous benzyl alcohol (99%) and pure ethanol (> 99.9%) was purchased from Scharlau, and ethylene glycol (EG ≥ 99%), HCl (37%) and acetone were purchased at Panreac. All materials were used as-received without further purification. Milli-Q water (MQ-H_2O) was used in all experiments.

Synthesis of PVP Coated TiO_2 NPs

TiO_2 NPs with a PVP surface coating are synthesized adapting our microwave (MW) synthesis protocol for superparamagnetic iron oxide NPs (SPIONs) (Pascu et al., 2012; Yu et al., 2015;

Hachtel et al., 2016) in a CEM Discover reactor (Explorer 12-Hybrid) at a frequency of 2.45 GHz and 300 W of power. Moreover, the synthesis process is scaled-up a factor of 4 in order to have enough quantity of material. Briefly, 2.72 g PVP (0.272 mmol) are dissolved in 16 mL of anhydrous benzyl alcohol (BA) by continuous sonication. Then, 240 μL TBOT (0.684 mmol) are mixed with the above prepared solution to give a homogeneous solution of a yellowish color. The tubes are then placed in the MW reactor and heated first to 50°C for 5 min to ensure a complete solubilization of the precursor, and then at 190°C for 10 min. The final solution is dark-yellow and no precipitate is observed, indicating that the NPs are dispersed in the solution. TiO_2 NP are collected by adding 35 mL acetone in 4 mL of the solution (4 tubes) to precipitate the NPS and remove the excess PVP, centrifuging at 6,000 rpm for 30 min twice, and redispersing the precipitate of each tube in 16 mL ethylene glycol (EG) to be further used.

Synthesis of TiO_2/Au NPs

Two different synthetic routes were investigated (A and B, see **Figure 1**). The only variation between the two syntheses is the quantity of PVP added: 100 mg of PVP in synthesis A and 600 mg in synthesis B. PVP is added to the as-obtained TiO_2 dispersions in EG (16 mL) and sonicated to obtain a homogenous mixture, followed by the addition of 64 μL of 250 mM $HAuCl_4 \cdot 3H_2O$ (0.016 mmol). The molar ratio of free PVP to $HAuCl_4$ is 0.625:1 in synthesis A and 3.75:1 in synthesis B; and of TiO_2 to $HAuCl_4$ is 6.41:1 in both syntheses. The solution is heated at 120°C for 10 min in the microwave reactor. The final solution is tyrian-purple and no precipitate is observed. As-obtained TiO_2/Au are washed twice with acetone (35 mL acetone in 8 mL of solution, 2 tubes) to remove free PVP, and collected by centrifugation at 6,000 rpm for 30 min twice. The samples are redispersed in 2 mL of MQ-H_2O and kept for further characterization. In total, we will have 4 mL of sample A and 4 mL of sample B. Part of the sample is dried overnight at 100°C, and other parts are annealed in air at 400, 450, 550, or 600°C for 2 h at a heating rate of 2°/min to remove the organic PVP and increase the contact between Au and TiO_2.

Purification of TiO_2/Au NPs

To remove the excess TiO_2 not bonded to the Au NPs, the as-synthesized particles dispersed in 2 mL MQ-H_2O are divided into two Eppendorf tubes with 1 mL each and centrifuged at 6,000 rpm during 25 min (synthesis A) and 4 min (synthesis B). The supernatant is discarded, another 1 mL MQ-H_2O is added, and the centrifugation repeated. This procedure is repeated two more times for synthesis A during 15 min each. The supernatant is further discarded and the total resulting solid is redispersed in 2 mL MQ-H_2O.

Materials Characterization

Ultraviolet-visible-near infrared (UV-Vis-NIR) spectra were collected on a Varian Cary-5000 UV-Vis-NIR spectrophotometer between 350 and 800 nm. The morphologies and crystalline phase of the Au and TiO_2 NPs were analyzed in a JEOL JEM-1210 transmission electron microscopy (TEM) operating at 120 KV. One drop of the NPs dispersion was placed in a carbon film copper grid. High resolution TEM (HRTEM), high angular annular dark field scanning transmission electron microscopy (HAADF-STEM) images, and STEM-Energy dispersive X-ray spectroscopy (STEM-EDX) profiles were acquired using a FEI Tecnai G2 F20 microscope operated at 200 kV equipped with an EDAX super ultra-thin window (SUTW) X-ray detector, on the as-synthesized and calcined at 450°C samples. Elemental analysis of C, H, N and S was performed through combustion of the samples at 1,200°C in oxygen atmosphere, followed by quantification through gas chromatography with a CHNS Thermo scientific Flash 2000 elemental analyzer. From these results, the PVP was calculated. Chemical analysis of Au and Ti was done with inductively coupled plasma optical emission spectroscopy (ICP-OES) with an ICP-OES Perkin-Elmer, model Optima 4300DV. The samples were previously digested with a mixture of concentrated HNO_3, HCl, and HF in a Milestone Ultraware microwave. In all the cases, the mass analyzed was weighed with a microbalance MX5 Mettler Toledo. Samples were carried out in triplicate. The percentage of Au and TiO_2 was calculated from these results. Infrared (IR) analysis was carried out in a FTIR Perkin-Elmer Spectrum One spectrometer, in ATR mode, between 450 and 4000 cm^{-1} energy range. Simultaneous thermogravimetric analysis (TGA)-differential scanning calorimetry/differential thermal analysis (heat flow DSC/DTA) was conducted in a NETZSCH-STA 449 F1 Jupiter equipment, from room temperature to 700°C in air. Scanning electron microscopy (SEM) images of the samples supported in filter paper were obtained at low vacuum mode (50 Pa) with a SEM QUANTA FEI 200, with a voltage of 15 kV.

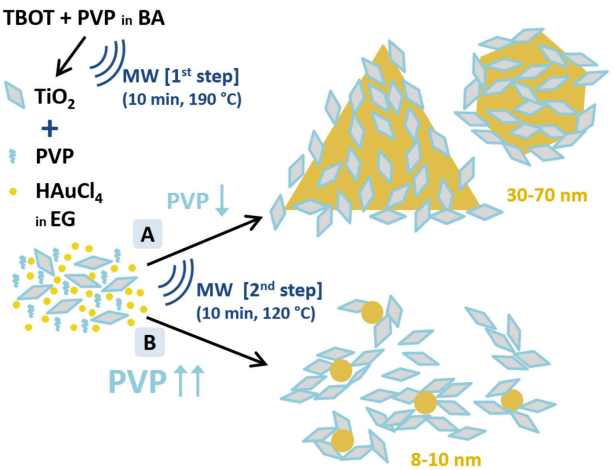

FIGURE 1 | Schematic representation of the two-step microwave-assisted synthesis of Au/TiO_2 nanostructures. A and B depict the two performed synthetic routes to obtain Au and TiO_2 nanoparticles with different Au particle size distributions. (A) TiO_2:PVP:$HAuCl_4$ = 1:0.097:0.155; (B) TiO_2:PVP:$HAuCl_4$ = 1:0.583:0.155 (molar ratios). Notation: TBOT, titanium butoxide; PVP, polyvinylpyrrolidone; BA, benzylalcohol; $HAuCl_4$, hydrogen tetrachloroaurate; EG, ethylene glicol; MW, microwave-assisted synthesis.

Preparation of the Photocatalysts

Four milli grams of each synthesis (A and B), as-synthesized and calcined (at 400, 450, 550, and 600°C), were weighed in an Eppendorf. Then, 200 μL of ethanol were added and the samples were sonicated for 20 min. Filter paper from the laboratory (from Albet, pore size 35-40 μm, 80 $g{\cdot}m^{-2}$, thickness 0.18 mm), used as support, was cut in round-shapes and weighed. Then, the filter paper was impregnated with the NPs solution, by pouring each time 20 μL and evaporating the ethanol in an oven at 50°C. Only the center of the paper was impregnated, corresponding to the inner diameter of the photocatalytic reactor used for the tests. Once dry and at room temperature, the photocatalytic paper was weighted to know the real amount of material added.

Photocatalytic Activity

Photoreactions were carried out in gas phase at room temperature and atmospheric pressure in continuous mode in a tubular glass reactor previously described (Aguiló et al., 2017; Molins et al., 2017). In a typical experiment, the impregnated filter paper is placed between the two parts of the photocatalytic reactor, upside-down (the impregnated photocatalyst facing downwards) on top of the O-ring on the center the reactor, over the UV LED (**Figure 2**). The junction is tightly sealed with parafilm and a screw sealing ring. A saturated Ar gas stream with a water:ethanol vapor mixture (90:10 ratio on a molar basis) was introduced into the photoreactor by bubbling dry Ar gas at a flow rate of 20 mL/min through a saturator (Dreschel bottle) containing a liquid mixture of 87.5g of H_2O and 9.92g of ethanol. The photoreactor effluent was monitored on-line every 4 min by gas chromatography (GC) (Agilent 3000 A MicroGC) using three columns: MS 5 Å, Plot U and Stabilwax. The LED UV-light source (from SACOPA, S.A.U.) consisted of four LEDs at 365 ± 5 nm and a synthetic quartz glass cylindrical lens that transmits the light to the photocatalyst. The UV-light source is located at the bottom part of the reactor, irradiating the filter paper from below, at a distance of 1 cm. Light irradiation is measured directly with a UV-A radiation monitor from Solar Light Co. and is 81.7 ± 0.5 $mW{\cdot}cm^{-2}$. In this set of experiments, we wanted to evaluate the photocatalytic activity of different catalysts under the same experimental conditions, so we did not want to be limited by the amount of irradiation. We worked with excess UVA light (365 nm) to not be limited by this factor. The irradiation area is quite small and is placed very near the light (< 1 cm). This involves a low apparent quantum efficiency (AQE) achieved, since it represents the efficiency of the irradiated light to form hydrogen. The AQE value calculated in the maximum rate of hydrogen production (sample A at 450°C), is equal to AQE = 0.45% (see Supplementary Material for details of AQE calculation). At the beginning of each experiment, the UV light is off, and the reaction system is purged by entering 20 mL/min of saturated Ar gas with the water-ethanol vapor mixture, to remove the maximum possible oxygen (O_2) in the line, up to reaching an O_2 stable value. During this time, the GC chromatograms indicate a reduction of the oxygen content, which decreases down to very low values (< 0.001%). Due to the intrinsic limitations of the system, it is not possible to completely remove the oxygen inside the reaction system. After 30 min, the UV light is turned on and we monitor all photoreaction products during ca. 20–40 min by GC. Control experiments were carried out with only the filter paper support and no photoactivity was measured. Two measurements were made for each as-synthesized sample (A and B) with excellent reproducibility. Experiments with bare TiO_2 NP and Au NP were also performed.

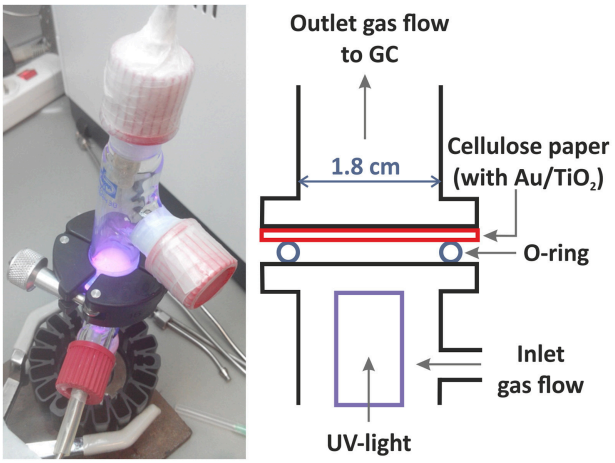

FIGURE 2 | Image and scheme of the photoreactor. The UV-light LED irradiates the sample from below.

RESULTS AND DISCUSSION

The TiO_2/Au nanoparticles were synthesized, in <1 h, through a 2-step microwave-assisted synthesis (**Figure 1**). In the first step, the TiO_2 NPs are formed by sol-gel synthesis in a microwave oven using titanium butoxide (TBOT) as precursor, benzyl alcohol (BA) as solvent, and polyvinylpyrrolidone (PVP) as stabilizer. The PVP capped-TiO_2 NPs with an average size of 9 ± 2 nm are crystalline presenting solely the anatase phase. In the second step, two different syntheses, labeled A and B, are performed to obtain two different sizes of Au NPs (see A and B in **Figure 1**) in order to evaluate their different photocatalytic behavior. In the presence of the pre-formed anatase nanoparticles, the second step is a polyol-synthesis for the formation of Au NPs using $HAuCl_4{\cdot}3H_2O$ as precursor, ethylene glycol (EG) as solvent and PVP as reducing and capping agent. The TiO_2 NPs, dispersed in the reaction media, serve as nucleation sites for the Au NPs. In this second step, the amount of PVP is used to tune the size of the Au NPs as represented in **Figure 1**, confirming the significant role of PVP in the formation of anisotropic nanostructures (Yu et al., 2015). While small PVP/Au precursor molar ratio (0.625:1) lead to large Au NPs with anisotropic shapes including triangles, an increase of PVP/Au precursor molar ratio (3.75:1) yields smaller and rounded Au NPs, as was also observed in the SPIONs/Au system (Yu et al., 2015). The synthesis presented here reinforces the potential of microwave irradiation to fabricate multimaterial NPs in a short time and in a easily scalable process (Gonzalez-Moragas et al., 2015; Yu et al., 2015; Hachtel et al., 2016). Finally,

we also prepared Au NPs using the same protocol of "Synthesis A" but without the PVP capped-TiO_2 NPs, obtaining spherical Au NPs of 9 nm mean size, as previously shown by Yu et al. (2015).

TEM micrographs confirmed the successful formation of the nanoparticles and the differences in particle size and shape of both syntheses. Synthesis A (**Figure 3a**) with Au NPs (average size > 50 nm) of different shapes, including nanotriangles (22%), nanocubes (40%), nanospheres (31%), nanohexagons (5%), and nanopentagons (2%), which are randomly decorated with small TiO_2 NPs (9 ± 2 nm in size). On the other hand, synthesis B (**Figure 4a**) involves the formation of much smaller Au

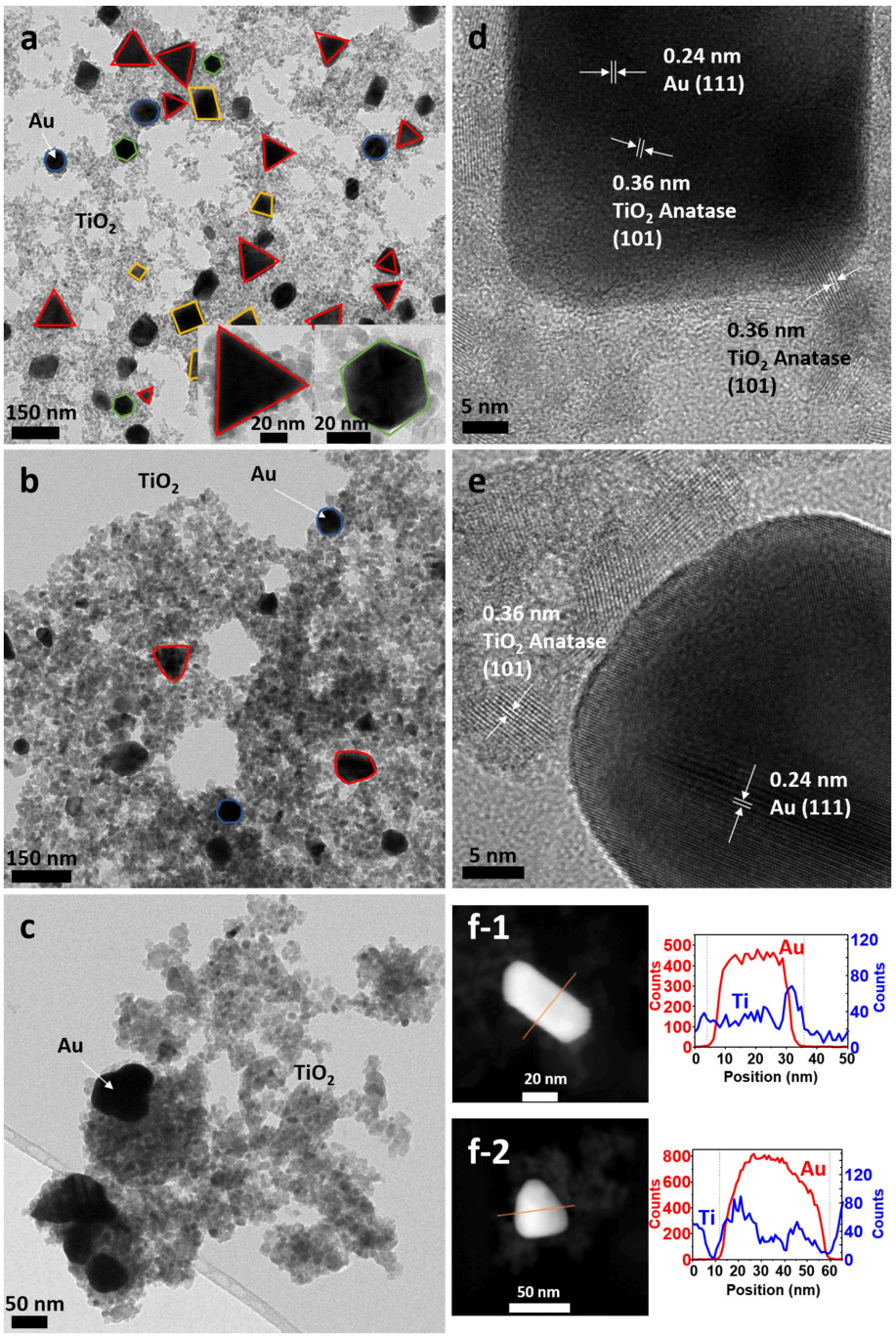

FIGURE 3 | TEM images of sample A **(a)** as-synthesized (NC: not calcined), **(b)** calcined at 450°C and **(c)** calcined at 600°C. HRTEM images of sample A **(d)** as-synthesized, **(e)** calcined at 450°C, **(f)** STEM of sample A of **(f-1)** as-synthesized and **(f-2)** calcined at 450°C, with element profiles.

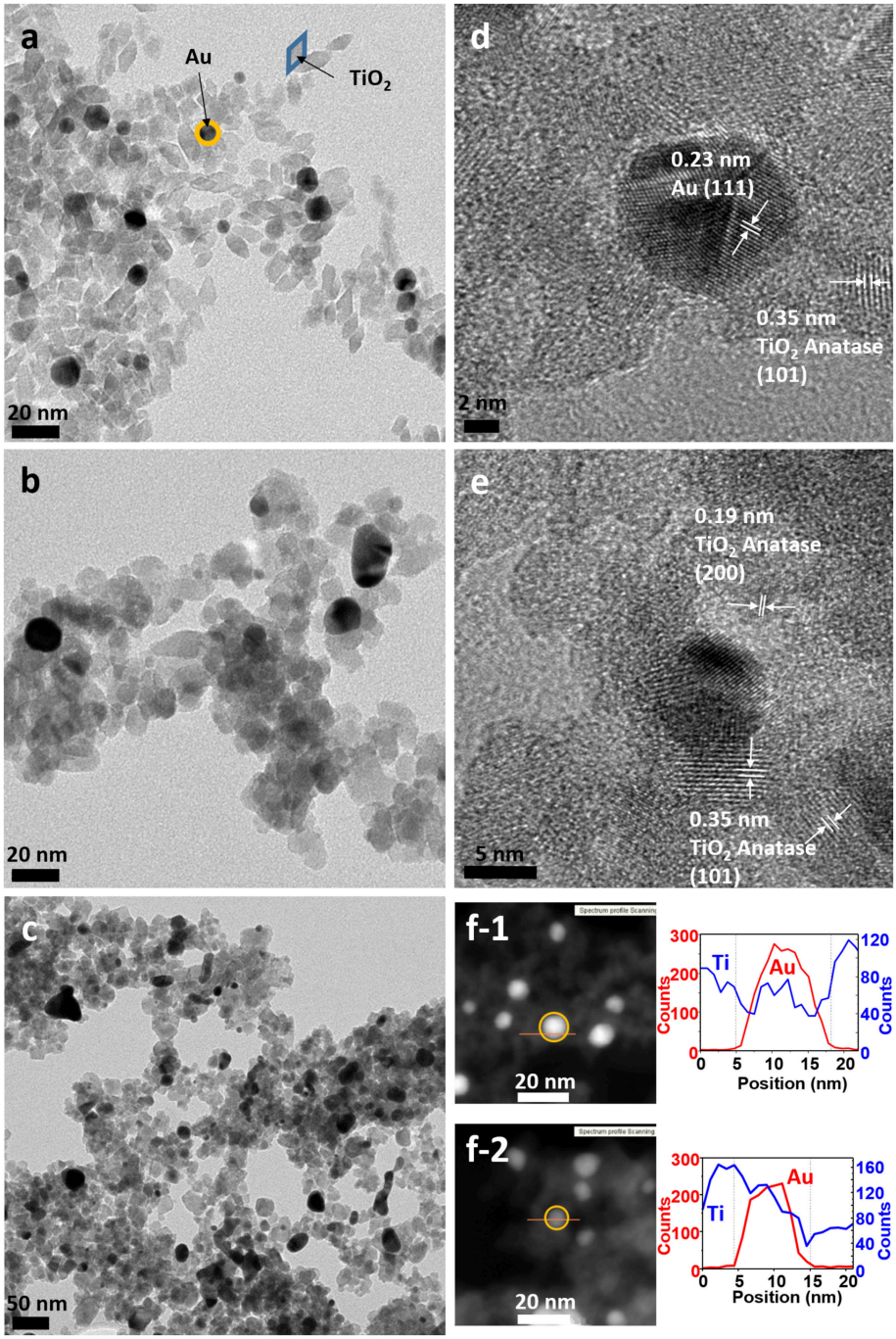

FIGURE 4 | TEM images of sample B **(a)** as-synthesized (NC: not calcined), **(b)** calcined at 450°C and **(c)** calcined at 600°C. HRTEM images of sample B **(d)** as-synthesized, **(e)** calcined at 450°C, **(f)** STEM of sample B of **(f-1)** as-synthesized and **(f-2)** calcined at 450°C, with element profiles.

nanospheres (8 ± 2 nm), very similar in size as that of the TiO_2 NPs (9 ± 2 nm), although different in morphology (TiO_2 NPs have a rhombus shape). Moreover, due to the similar sizes, the Au NPs cannot be decorated with TiO_2 NPs, but they are always surrounded by them: in all the analyzed images, no isolated Au NPs are found.

Electron diffraction patterns of the as-synthesized samples (Supplementary Figures 1a,d in the Supplementary Material) indicate that titanium dioxide is anatase, which is the most photocatalytic active phase. This phase is already formed during the microwave synthesis process, without a further annealing step needed. The electron diffraction patterns also confirm the

presence of metallic gold in the samples. Samples were calcined at different temperatures to remove the organic PVP that keeps the two materials apart, in order to increase the contact between the two inorganic phases and enhance the electron transfer between them (Azhari and Diab, 1998). Calcination has larger effect on the Au than on the TiO_2 NPs. Au NPs of sample A calcined at 450°C show more rounded corners, especially for the triangles and the cubes (**Figure 3b**). These changes are more severe at 600°C (**Figure 3c**) when the gold NPs start to melt and fuse with each other, forming elongated-rounded shapes and resulting in a particle size increase. The average particle size of sample A increases around 7 nm (up to 59 ± 21 nm), whereas that of sample B increases much more (28 ± 9 nm) (**Figures 4b,c**). Regarding TiO_2 NP, they maintain their size up to 450°C whereas after being calcined at 600°C, they increase up to 13 ± 4 nm and 17 ± 5 nm for synthesis A and B, respectively. However, upon calcination at the different temperatures, TiO_2 remains as anatase (Supplementary Figures 1a–c, d–f). The increase of particle size with calcination temperature and the particle size distributions are illustrated in Supplementary Table 1, Supplementary Figures 2, 3. Annealing at 450°C removes almost totally the PVP, largely increasing the intimate contact between Au and TiO_2 NPs, as observed by TGA analysis and IR analysis, included in Supplementary Figures 4, 5.

By HRTEM we can image the interplanar spacing of TiO_2 and gold. A lattice spacing of 0.35 ± 0.01 nm, measured in both samples, matches the (101) lattice plane for TiO_2 anatase. In sample B calcined at 450°C, an additional spacing of 0.19 ± 0.01 nm is detected, that is assigned to the (200) anatase plane. The 0.23 ± 0.01 nm lattice spacing of Au NPs belongs to the (111) plane for metallic Au (**Figures 3d,e**, **4d,e**). Moreover, HRTEM also highlights the homogeneous covering and contact between Au and TiO_2. In sample A, we can see that the large Au NPs are covered by the TiO_2 NPs, since some anatase planes can be identified on top of the Au NPs (**Figure 3d**) and after the PVP is removed we can see an intimate contact between both materials (**Figure 3e**). The coverage of Au NPs by TiO_2 is also confirmed by HAADF STEM (**Figure 3f**), an element profile shows that Ti is identified on the top of the Au particles. In sample B with smaller Au NPs, these are always surrounded by similar-size TiO_2 NPs (**Figure 4f**). We could not find Au NPs that were not in contact by at least one TiO_2 NP. The element profile obtained by HAADF STEM also indicates the presence of Ti where there is the Au NP in this sample.

TEM micrographs also show an excess of TiO_2 NPs that are not in contact with Au NPs, which will have little or no effect on the photocatalytic activity. To remove the excess of TiO_2, both samples were further purified by centrifugation as explained in the experimental section. TEM micrographs of the purified samples (Supplementary Figures 6a–e) show that the excess of TiO_2 was partly removed for sample A. Unfortunately, this purification method was unsuccessful for sample B, due to the similarity of particle size between TiO_2 and Au NPs. Photocatalytic activity for the purified A and B samples (labeled as A* and B*) will also be reported below.

The amount of Au and TiO_2 on the samples has been quantified by ICP-OES. The amount of PVP has been indirectly calculated by elemental analysis of CHNS (carbon, hydrogen, nitrogen and sulfur), considering PVP as $(C_6H_9NO)_n$,. The ICP-OES results compared well with those obtained from the thermogravimetric analysis (TGA) (Supplementary Figure 4). Despite using the same initial amount of gold precursor, sample A (with 20 ± 2 wt%) has nearly double gold content than sample B (with 11 ± 2 wt%), whereas the amount of TiO_2 is similar in both samples (49 ± 7 wt% and 51 ± 7 wt%). From the elemental analysis, it was interfered that the amount of PVP was 31 ± 5 wt% in sample A, and 38 ± 5 wt% in sample B. Infrared (IR) analysis confirmed the presence of PVP in the TiO_2 NPs and in A and B samples, and proved the removal of the PVP on the calcined samples (Supplementary Figure 5).

The purification of the samples from an excess of TiO_2 leads also to a decrease of the PVP content, from 31 to 5 wt% in sample A*, and from 38 to 10 wt% in sample B*, and obviously to a remarkable increase of the Au content, especially in sample A*, from 20 to 67 wt%, whereas in sample B* from 11 to 20 wt%. Supplementary Figure 7, depicts the distribution of the Au/TiO_2/PVP for all samples.

To evaluate the photocatalytic activity of these systems, the TiO_2/Au NPs solutions were deposited on top of ordinary laboratory filter paper. The amount of deposited photocatalyst was set to 4 mg, in order to achieve an optimal photocatalyst loading value of ca. 1.2 mg/cm^2 previously reported by Castedo et al. (2016). The insets in **Figure 5** show the materials corresponding to the as-synthesized samples A and B. The rest of the used samples are shown in Supplementary Figure 8. SEM images were obtained of the as-prepared photocatalytic papers. **Figure 5** shows that the distribution of the nanostructures is very homogenous in both sample A (**Figures 5a,b**) and B (**Figures 5c,d**). This is better confirmed by Au NPs (shown as bright spots) evenly dispersed in all the area. In sample A at 200,000 x (**Figure 5b**) the different shapes of the particles can be differentiated (nanotriangles, squares, spheres…).

UV-Vis absorption spectra collected between 350 and 800 nm were recorded on these materials (**Figure 6**). Both samples show the gold plasmon absorption peak, with absorption of sample A at longer wavelengths (610 nm) than sample B (545 nm), due to the larger particle size and anisotropic shapes (Scarabelli et al., 2014; Yu et al., 2015). The UV-Vis spectra of the purified samples (A*, B*) maintained the gold absorption peaks at the same wavelength and the same TiO_2 absorption at the UV region, indicating the presence of both elements (Supplementary Figures 9a,b). The UV-Vis spectra of the successive supernatants of the different purification steps (Supplementary Figure 9c) and the evolution of sample A (Supplementary Figure 9d) confirm the removal of TiO_2 and the retention of most Au NPs. Some images of the supernatants and of the final purified samples are also provided (Supplementary Figure 9e). Calcination has an effect on the absorption peak of sample A, which decreases to values of 565 nm due to the modification of the particle shape and lose of anisotropy (rounded edges; Pelaz et al., 2012). However, the absorption peak of sample B is not modified. The TiO_2 sample clearly shows an increase of absorption at the UV region, while in the other samples this increase is not so evident, probably due to the lower concentration of TiO_2 on sample A and B.

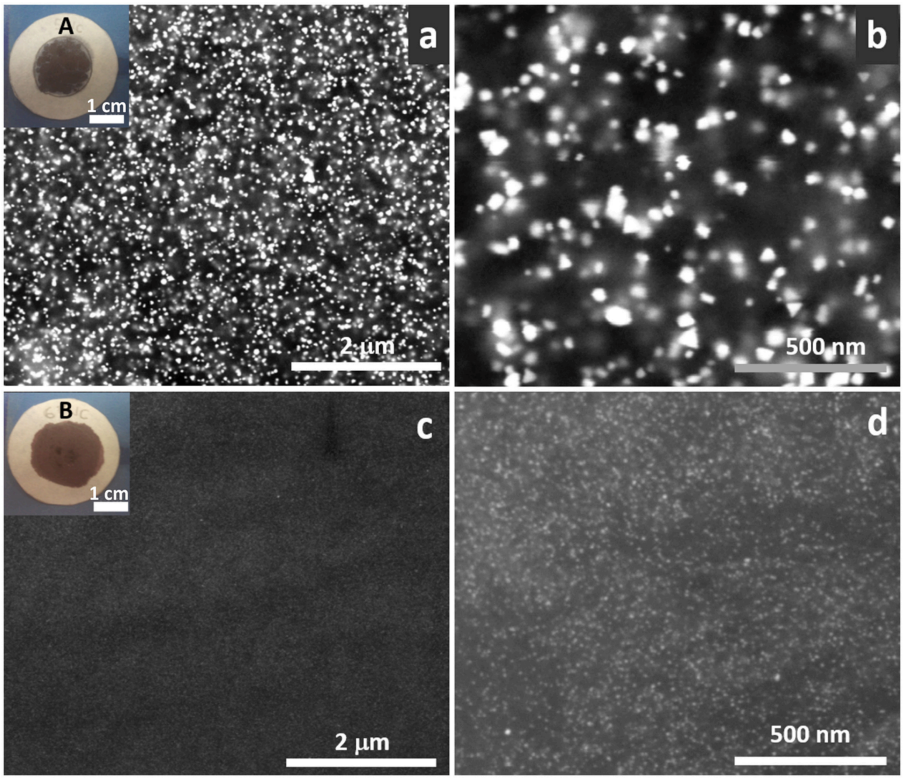

FIGURE 5 | Backscattered SEM images of sample A **(a,b)** and B **(c,d)** on top of the filter paper at 50,000 x **(a,c)** and 200,000 x **(b,d)**. Bright dots correspond to Au NPs. Insets correspond to photographs of the materials deposited on filter paper **(a)** sample A, **(c)** sample B.

All the synthesized photocatalysts were studied in the photoproduction of H_2 under dynamic conditions at atmospheric pressure and room temperature, introducing a saturated Ar gas stream with a water:ethanol vapor mixture at a flow rate of 20 mL/min through a tubular photoreactor. In addition, blank experiments with bare TiO_2 NPs and Au NPs were also carried out for comparison. The gaseous reactants (saturated Ar with water-ethanol mixture 9:1 molar, GHSV$\sim$26,000 h^{-1}) enter the reactor from the lower part, passes through a cellulose paper loaded with the TiO_2/Au catalyst and exits the reactor from the top (see **Figure 2**). The outlet of the photoreactor was continuously monitored by GC. H_2 was produced using the two investigated catalysts (A and B) in both the as-synthesized and the calcined forms. H_2 was also produced using bare TiO_2 NPs. The production of H_2 remained stable with time (from $\sim$7 to 40 min) after an initial transient period and stabilization of the reaction. Acetaldehyde is the only byproduct detected in all the experiments using TiO_2 based photocatalysts. The use of Au NPs in the absence of TiO_2 NPs did not yield H_2 production under our experimental conditions.

Figure 7 shows the UV light driven hydrogen production of sample A (**Figure 7a**) and sample B (**Figure 7b**) calcined at different temperatures and normalized per mass of catalyst. The mass of PVP is non-relevant in the total mass of the catalyst because it is removed with the calcination, except for the non-calcined sample that contains PVP. The percentage of Au and TiO_2 in the calcined samples is higher than in the non-calcined sample, because they are all prepared from the same initial weight fraction of PVP:Au:TiO_2 (see Supplementary Figure 7). The UV light is turned on at $t = 0$ min, and the first result from the GC under UV light is obtained at $t = 4$ min, as shown in **Figure 7**. The time profiles demonstrate that the stable and constant amounts of hydrogen are produced over the photocatalyst under UV light irradiation during all the experiments. A blank experiment using bare anatase TiO_2 in the absence of Au NPs presents a low activity, producing 0.26 mmol $H_2 \cdot g_{cat}^{-1} \cdot h^{-1}$. However, when the surface of Au NPs is decorated with non-calcined TiO_2 NPs, the hydrogen evolution efficiency enhances significantly, 4.5 times for sample A (1.2 mmol $H_2 \cdot g_{cat}^{-1} \cdot h^{-1}$) and 3.3 times for sample B (0.9 mmol $H_2 \cdot g_{cat}^{-1} \cdot h^{-1}$). Murdoch et al. (2011) affirmed that the role of Au NPs is crucial in the water splitting reaction using TiO_2 semiconductor materials, as some steps to achieve the photoproduction of hydrogen by Equation (1) did not take place in its absence. As expected, the calcination treatments further enhance the hydrogen production. As shown in **Figure 7**, the optimal calcination temperature to reach the best photocatalytic performance for H_2 evolution is 450°C. Calcination results in a more intimate contact between TiO_2 NPs and Au NPs. However, calcination temperatures above >550°C detrimentally diminish

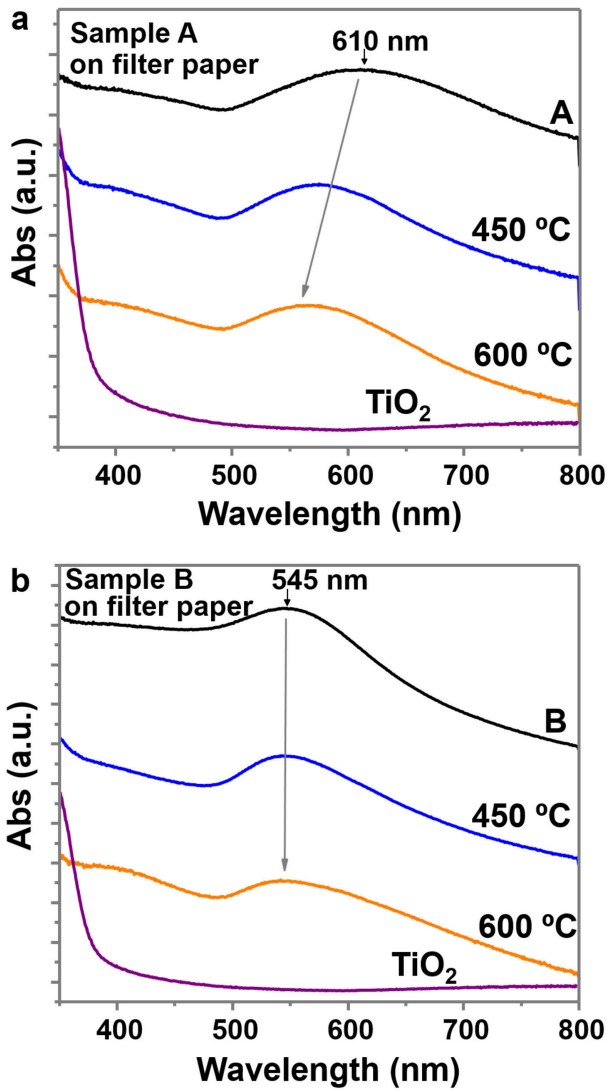

FIGURE 6 | UV-Vis spectra between 350 and 800 nm wavelength of **(a)** sample A and **(b)** sample B, on filter paper and at different calcined temperatures. Both plots include the UV-Vis spectra of TiO_2 NPs on filter paper (before adding the gold precursor).

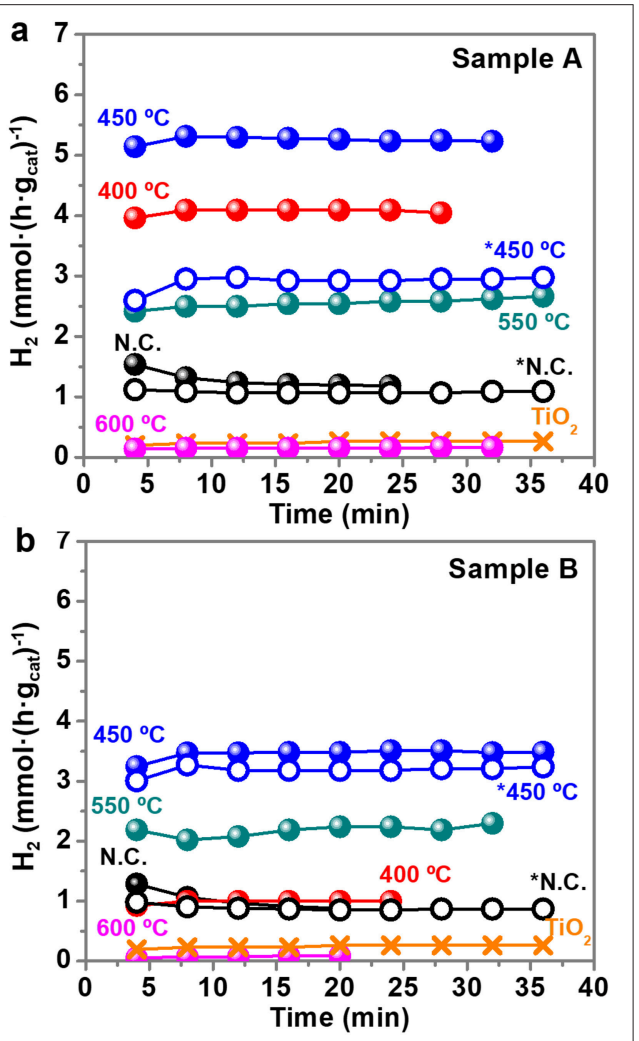

FIGURE 7 | Hydrogen production (mmol·(h·g_{cat})$^{-1}$) with time for sample A **(a)** and sample B **(b)**. Notation: N.C: not calcined; * purified samples. Time = 0 min (UV light on), Time = 4 min (first GC measure with UV light on). The UV light remained on during all the collected data points.

the number of active sites on the surface of the photocatalyst, probably by decreasing the surface area, since the particle size increase and particles aggregate and fuse together. This can also reduce the light penetration, preventing the activation of TiO_2. At 600°C, remarkably low values of hydrogen production, similar to bare TiO_2, are obtained.

Figure 8a depicts the photocatalytic production of H_2 (mmol·g_{cat}^{-1}·h^{-1}) after 20 min of reaction for both samples A and B as-synthesized, i.e., not calcined, and at the different calcination temperatures (from 400 to 600°C). As observed in **Figure 8a**, the photocatalytic activity of the as-synthesized sample is around 1 mmol·g^{-1}·h^{-1}, being higher for sample A than for sample B (1.2 > 0.9). For the samples treated at 400°C, the activity increases up to 4 times for sample A (up to 4 mmol·g^{-1}·h^{-1}), whereas it remains nearly the same for sample B. However, the highest activity is reported when the samples are calcined at 450°C: up to ∼5.3 mmol·g^{-1}·h^{-1} for sample A and 3.5 mmol·g^{-1}·h^{-1} for sample B. From 550°C the activity decreases and at 600°C it is even less than for the as-obtained samples. To achieve a better comparison of the photocatalytic performance of both samples A and B with the previously reported data in the literature, **Figure 8b** presents H_2 production normalized per mass of TiO_2. The overall trend is the same, with higher values of H_2 production rates, reaching a maximum of 7.5 mmol·g^{-1}·h^{-1} in sample A at 450°C. Regarding the purified samples A* and B*, their photocatalytic production of H_2 of normalized per mass of catalyst and per mass of TiO_2 is shown in **Figure 8c**. Interestingly, the production of hydrogen for calcined purified A* presents larger values (> 10 mmol·g_{TiO2}^{-1}·h^{-1}) than that of calcined sample A, because the excess of TiO_2 has been removed

and, consequently, the Au:TiO_2 ratio increases. These results clearly indicate the need of intimate contact within TiO_2 and Au in order to allow electron transfer and the role of Au to act as an electron reservoir.

Considering all the obtained results, sample A has more amount of gold per gram of catalyst than sample B. However, the Au NPs of sample A are bigger with a total specific surface area twenty-fold smaller than for sample B (0.4 m^2_{Au}/g for sample A compared to 8.4 m^2_{Au}/g for sample B). Nevertheless, we can observe from the TEM images (**Figure 3** and Supplementary Figure 6) that the Au NPs of sample A are completely breaded by TiO_2 NP. We thus argue that in sample A there is much bigger interface area between gold and titania, yielding an enhanced photocatalytic activity. The strong contact between Au and TiO_2 NP is indispensable, as clearly observed by Haruta (2002), who found very different activities between Au hemispherical NPs with their flat planes strongly attached to the TiO_2 support, compared to spherical particles simply loaded on the TiO_2. However, the exposed surface area of gold is not directly associated with the activity of TiO_2/Au toward hydrogen production (Bamwenda et al., 1995). Bamwenda et al. (1995) reported that the essential reaction steps occurred on the semiconductor surface, and that the microinterfaces between Au and TiO_2 could also play a role as active sites. Hence, one decisive factor is the contact area between the noble metal and the semiconductor, which is where the Schottky junctions are formed, and enhance the separation of photo-excited electrons and holes. In addition, as the metal acts as a "fast lane" to transfer the electrons injected from the TiO_2 to the active sites, where they are consumed in the hydrogen generation reaction ($2H^+_{(ads)} + 2e^- \rightarrow H_2$), it is necessary that they can move without encountering any barriers. The stronger and more expanded contact area between TiO_2 and Au NPs explains why the H_2 production is larger for TiO_2 NPs supported on large Au NPs (sample A) than for TiO_2 NPs in close contact to Au NPs of similar sizes (sample B).

Our results are consistent with the reaction scheme involved in the photo-production of hydrogen from ethanol over Au/TiO_2 and previously proposed by Murdoch et al. (2011). Equation (1) is a multistep reaction. Briefly, an ethanol molecule is dissociatively adsorbed on the photocatalyst surface to form an ethoxide and a hydrogen ion (as a surface hydroxyl), as follows

$$CH_3CH_2OH + Ti^{4+}_{(surface)} - O^{2-}_{(surface)} \rightarrow CH_3CH_2O - Ti^{4+}_{(surface)} + OH_{(adsorved)} \quad (2)$$

Then, electron-hole pairs are photogenerated on the photocatalyst surface [Equation (3)], ethoxides inject two electrons into the valence band and acetaldehyde is produced [Equations (4, 5)], and two hydrogen ions are reduced to a hydrogen molecule by two electrons from the conduction band [Equation (6)].

$$TiO_2 + UV \rightarrow e^- + h^+ \quad (3)$$

$$CH_3CH_2O - Ti^{4+}_{(surface)} + h^+ + O_{(surface)} \rightarrow CH_3CH^{\bullet}OTi^{4+}_{(surface)} + OH_{(adsorbed)} \quad (4)$$

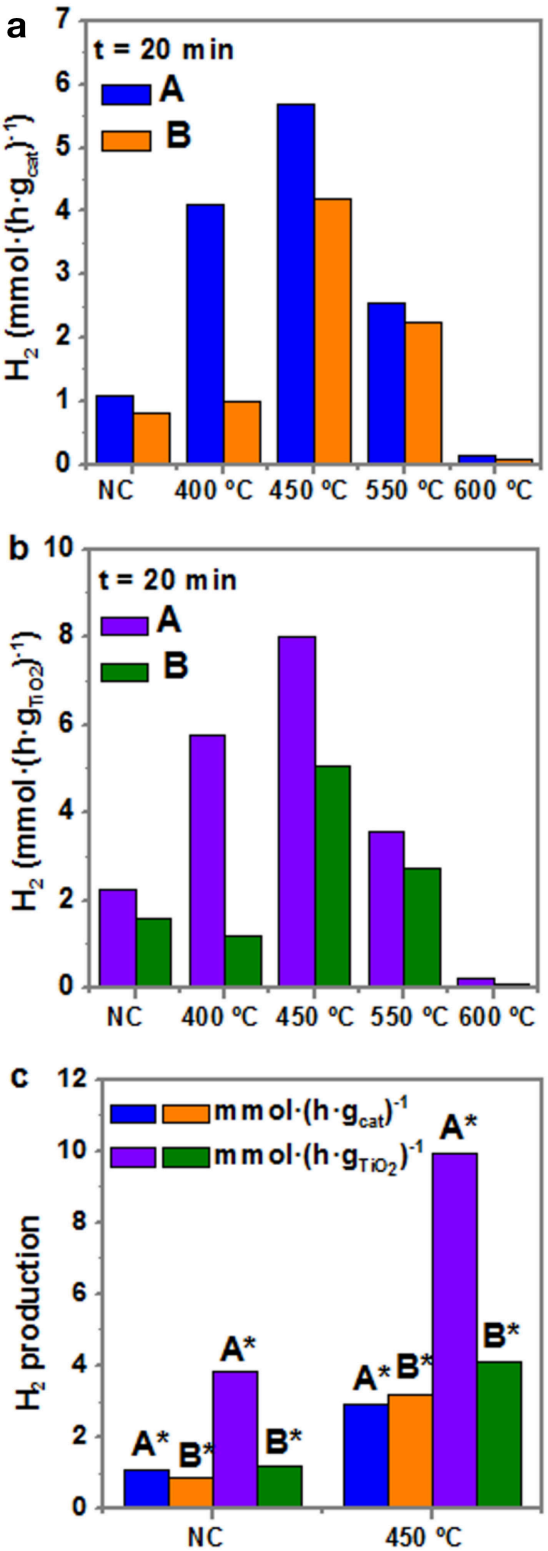

FIGURE 8 | Hydrogen production rate after 20 min of photocatalytic reaction under UV irradiation of samples A and B at different thermal treatments **(a)** per mass of catalyst, and **(b)** per mass of TiO_2. **(c)** Hydrogen production of purified samples after 20 min of reaction, per mass of catalyst and mass of TiO_2 NC and at 450°C. Notation: N.C, not calcined; * purified samples.

$$CH_3CH^{\bullet}OTi^{4+}_{(surface)} + h^+ \rightarrow CH_3CHO_{(g)} + Ti^{4+}_{(surface)} \quad (5)$$

$$2OH_{(adsorbed)} + 2e^- \rightarrow 2O^{2-}_{(surface)} + H_2 \quad (6)$$

The presence of water is important to avoid the blockage of the active sites of the photocatalyst by adsorption of acetaldehyde molecules.

This study also demonstrates that H_2 can be obtained from water-ethanol mixtures in gas-phase with a photocatalyst composed of large Au NPs, and small TiO_2 NPs, containing high amounts of gold (> 10–20 wt%). Hence, the photogeneration of H_2 is not only restricted to small Au particle size and low gold percentages (< 2 wt%), as the majority of studies have reported so far (**Table 1**). The studies reported in **Table 1** are, in general, with a small Au loading (1–2 wt%) and with small Au NPs particle size (1–10 nm). Although the studies that use methanol as hole scavenger achieve higher values of H_2 production, the reported hydrogen activity is of the same order of magnitude as this present study (7-17 $mmol{\cdot}g^{-1}{\cdot}h^{-1}$ compared to 5.3 $mmol{\cdot}g^{-1}{\cdot}h^{-1}$ obtained for the TiO_2/Au sample A calcined at 450°C).

CONCLUSIONS

We have successfully developed a synthetic route to obtain two different sizes of Au/TiO_2 NPs by a fast and simple two-step microwave-assisted synthesis (<1 h of overall synthesis time). Hereby, we have clearly exposed that microwave chemistry is a very efficient method to achieve complex nanostructures. While the larger Au NPs (*ca.* 50 nm) are breaded with the small titanium oxide NPs containing abundant interfacial contacts between gold and titania, the smaller Au NPs (*ca.* 10 nm) form dimers and trimers with the TiO_2 NP of similar size and contain lesser contact points between the metal and the metal oxide.

The photocatalytic activity of the two Au/TiO_2 nanostructures was evaluated in the photoproduction of hydrogen from gaseous water/ethanol mixtures at ambient temperature and pressure. We have shown that H_2 production is accomplished with the two photocatalysts, both containing large co-catalyst fraction (∼ 10–20 wt%). We thus conclude that in these cases the metal is not acting as recombination center for the photogenerated electrons and holes, as earlier postulated.

Our study also exposed that calcining at 450°C significantly facilitated charge transfer between the two materials, without compromising the catalyst surface and active sites and without affecting particle sizes. Importantly, the nanostructure with larger contact area between the metal and the semiconductor provided the best performance in terms of H_2 production. Hence, the number of Schottky junctions is a decisive key parameter on the photocatalytic performance by enhancing the separation of photo-excited electrons and holes. Comparing our two systems, we determine that the later aspect has a more significant impact on the H_2 production than the size or the load fraction of the metal co-catalyst.

Further work will be devoted to investigate the influence of the gold plasmon resonance absorption on the photocatalytic activity using solar light.

TABLE 1 | Reported gas-phase photocatalytic performance in recent catalytic systems formed by Au/TiO_2 NPs.

Material	Au loading (wt%)	Particle size (Au/TiO_2) (nm)	Hole scavenger	Ratio water:hole scavenger	Wavelength and power irrad. lamp	Max. rate of H_2 ($mmol\ g^{-1}\ h^{-1}$)	References
Au/TiO_2 Anatase (A)[a]	20	30–70 (52 av.)/9	Ethanol	90:10 (molar)	365 nm 81.7 mW/cm^2	5.3 QE[d] = 0.45%	This study
Au/TiO_2 Anatase (B)[a]	11	8/9	Ethanol	90:10 (molar)	365 nm 81.7 mW/cm^2	3.5	This study
Au/TiO_2 Anatase (A*)[a]	67	30–70 (52 av.)/9	Ethanol	90:10 (molar)	365 nm 81.7 mW/cm^2	2.9	This study
Au/TiO_2 Anatase (B*)[a]	20	8/9	Ethanol	90:10 (molar)	365 nm 81.7 mW/cm^2	3.2	This study
Au/TiO_2 P90[b]	1.8	4/P90 size[c] (15–20)	Ethanol	90:10 (molar)	365 nm 1.5 mW/cm^2	≈ 5 QE = 9.2%	Castedo et al., 2016
Au/TiO_2	1	3.8/30–40	Ethanol	0:100	365 nm 2.6 mW/cm^2	≈ 2.75[e] ($mmol{\cdot}g^{-1}{\cdot}h^{-1}W^{-1}$)	Bonmatí et al., 2015
Au/TiO_2 Anatase:rutil ≈ 93:7	1-1.5	3.9/20–40	Ethanol	0:100	365 nm 4 × 12 W	≈ 0.6[e,f] QE = 20.8%	Taboada et al., 2014b
Au/TiO_2 P25[b]	1	4–10/P25 size[c] (20–25)	Methanol	94:6 (% v/v)	330-450 nm 250 W	≈ 17[e]	Dozzi et al., 2010
Au/TiO_2 Anatase:rutil ≈ 93:7	1	1–6/5–10	Methanol	94:6 (% v/v)	330-450 nm 250 W	10.2 QE = 6.3%	Chiarello et al., 2009
Au/TiO_2 P25[b]	1	2–3/20	Methanol	94:6 (% v/v)	330-450 nm 250 W	7	Chiarello et al., 2009

[a] All the samples were calcined at 450°C. [b] P25 and P90 are commercial TiO_2 made of a mixture of anatase and rutile phases, with a ratio anatase:rutile of 80:20 and 98:2, respectively (Siah et al., 2016). [c] P25 NP size is around 20-25 nm and P90 NP size is somewhat smaller, around 15-20 nm (Viswanathan and Raj, 2009; Siah et al., 2016). [d] UV irradiation technical details and Apparent Quantum Efficiency can be found at Materials and Methods and Supplementary Material. [e] Values taken from a plot. [f] Original values were in other units, and have been recalculated to $mmol{\cdot}g^{-1}{\cdot}h^{-1}$.

AUTHOR CONTRIBUTIONS

AM-M and LS: Designed the experiments; AM-M, MT, and PS: Carried out the nanocomposites synthesis and characterization studies; AM-M and LS: Carried out the photocatalytic evaluations; JL and AR: Supervised the project. All authors wrote and reviewed the manuscript.

ACKNOWLEDGMENTS

This research received funding from the Spanish Ministry of Economy and Competitiveness (MINECO) in co-funding with European Social Funds through the MAT2015-64442-R and ENE2015-63969-R projects and financial support through the Severo Ochoa Programme for Centers of Excellence in R&D (SEV-2015-0496). MINECO also funded the FPU PhD Fellow of MT (FPU16/05452) and the Juan de la Cierva Postdoctoral Fellow of AM-M (FJCI-2014-21407). Generalitat of Catalunya is acknowledged for the projects 2017SGR752 and 2017SGR128. JL is Serra Hunter Fellow and is grateful to ICREA Academia program. The authors would also like to thank Judith Oró and Belén Ballesteros for the TEM and HRTEM images and Ana Esther Carrillo for the SEM images.

SUPPLEMENTARY MATERIAL

The Supplementary Material for this article can be found online at: https://www.frontiersin.org/articles/10.3389/fchem.2018.00110/full#supplementary-material

REFERENCES

Aguiló, E., Soler, L., Casanovas, A., Moro, A. J., Lima, J. C., Rodríguez, L., et al. (2017). Gold(I)-complex-titania hybrid photocatalyst for hydrogen production. *Chem. Cat. Chem.* 9, 3289–3292. doi: 10.1002/cctc.201700518

Al-Azri, Z. H.N., Chen, W.-T., Chan, A., Jovic, V., Ina, T., Idriss, H., et al. (2015). The roles of metal co-catalysts and reaction media in photocatalytic hydrogen production: performance evaluation of M/TiO_2 photocatalysts (M=Pd, Pt, Au) in different alcohol–water mixtures. *J. Catal.* 329, 355–367. doi: 10.1016/j.jcat.2015.06.005

Azhari, S. J., and Diab, M. A. (1998). Thermal degradation and stability of poly(4-vinylpyridine) homopolymer and copolymers of 4-vinylpyridine with methyl acrylate. *Polym. Degrad. Stab.* 60, 253–256. doi: 10.1016/S0141-3910(97)00073-6

Baghbanzadeh, M., Carbone, L., Cozzoli, P. D., and Kappe, C. O. (2011). Microwave-assisted synthesis of colloidal inorganic nanocrystals. *Angew. Chem. Int. Ed Engl.* 50, 11312–11359. doi: 10.1002/anie.201101274

Bamwenda, G. R., Tsubota, S., Nakamura, T., and Haruta, M. (1995). Photoassisted hydrogen production from a water-ethanol solution: a comparison of activities of Au-TiO_2 and Pt-TiO_2. *J. Photochem. Photobiol. A Chem.* 89, 177–189. doi: 10.1016/1010-6030(95)04039-I

Bandara, J., Udawatta, C. P., and Rajapakse, C. S. (2005). Highly stable CuO incorporated $TiO_{(2)}$ catalyst for photo-catalytic hydrogen production from $H_{(2)}O$. *Photochem. Photobiol. Sci.* 4, 857–861. doi: 10.1039/b507816d

Bilecka, I., and Niederberger, M. (2010). Microwave chemistry for inorganic nanomaterials synthesis. *Nanoscale* 2:1358. doi: 10.1039/b9nr00377k

Bonmatí, E., Casanovas, A., Angurell, I., and Llorca, J. (2015). Hydrogen photoproduction from ethanol–water mixtures over au–cu alloy nanoparticles supported on TiO_2. *Top. Catal.* 58, 77–84. doi: 10.1007/s11244-014-0347-8

Bowker, M. (2012). Photocatalytic hydrogen production and oxygenate photoreforming. *Catal. Lett.* 142, 923–929. doi: 10.1007/s10562-012-0875-4

Castedo, A., Mendoza, E., Angurell, I., and Llorca, J. (2016). Silicone microreactors for the photocatalytic generation of hydrogen. *Catal. Today* 273, 106–111. doi: 10.1016/j.cattod.2016.02.053

Chen, W.-T., Chan, A., Al-Azri, Z. H. N., Dosado, A. G., Nadeem, M. A., Sun-Waterhouse, D., et al. (2015). Effect of TiO_2 polymorph and alcohol sacrificial agent on the activity of Au/TiO_2 photocatalysts for H_2 production in alcohol–water mixtures. *J. Catal.* 329, 499–513. doi: 10.1016/j.jcat.2015.06.014

Chiarello, G. L., Forni, L., and Selli, E. (2009). Photocatalytic hydrogen production by liquid- and gas-phase reforming of CH3OH over flame-made TiO_2 and Au/TiO_2. *Catal. Today* 144, 69–74. doi: 10.1016/j.cattod.2009.01.023

Dozzi, M. V., Chiarello, G. L., and Selli, E. (2010). Effects of surfacemodification on the photocatalytic activity of TiO_2. *J. Adv. Oxid. Technol.* 13, 305–312. doi: 10.1515/jaots-2010-0308

Fujishima, A., and Honda, K. (1972). Electrochemical photolysis of water at a semiconductor electrode. *Nature* 238, 37–38. doi: 10.1038/238037a0

Ge, M., Li, Q., Cao, C., Huang, J., Li, S., Zhang, S., et al. (2017). One-dimensional TiO_2 nanotube photocatalysts for solar water splitting. *Adv. Sci.* 4:1600152. doi: 10.1002/advs.201600152

Gonzalez-Moragas, L., Yu, S.-M., Murillo-Cremaes, N., Laromaine, A., and Roig, A. (2015). Scale-up synthesis of iron oxide nanoparticles by microwave-assisted thermal decomposition. *Chem. Eng. J.* 281, 87–95. doi: 10.1016/j.cej.2015.06.066

Hachtel, J. A., Yu, S., Lupini, A. R., Pantelides, S. T., Gich, M., Laromaine, A., et al. (2016). Gold nanotriangles decorated with superparamagnetic iron oxide nanoparticles: a compositional and microstructural study. *Faraday Discuss.* 191, 215–227. doi: 10.1039/C6FD00028B

Haruta, M. (1997). Size- and support-dependency in the catalysis of gold. *Catal. Today* 36, 153–166. doi: 10.1016/S0920-5861(96)00208-8

Haruta, M. (2002). Catalysis of gold nanoparticles deposited on metal oxides. *Cattech* 6, 102–115. doi: 10.1023/A:1020181423055

Jovic, V., Al-Azri, Z. H. N., Chen, W.-T., Sun-Waterhouse, D., Idriss, H., and Waterhouse, G. I. N. (2013a). Photocatalytic H2 production from ethanol–water mixtures over pt/TiO_2 and au/TiO_2 photocatalysts: a comparative study. *Top. Catal.* 56, 1139–1151. doi: 10.1007/s11244-013-0080-8

Jovic, V., Chen, W.-T., Sun-Waterhouse, D., Blackford, M. G., Idriss, H., and Waterhouse, G. I. N. (2013b). Effect of gold loading and TiO_2 support composition on the activity of Au/TiO_2 photocatalysts for H_2 production from ethanol–water mixtures. *J. Catal.* 305, 307–317. doi: 10.1016/j.jcat.2013.05.031

Khojasteh, H., Salavati-Niasari, M., Abbasi, A., Azizi, F., and Enhessari, M. (2016). Synthesis, characterization and photocatalytic activity of PdO/TiO_2 and Pd/TiO_2 nanocomposites. *J. Mater. Sci. Mater. Electron.* 27, 1261–1269. doi: 10.1007/s10854-015-3884-4

Maeda, K. (2011). Photocatalytic water splitting using semiconductor particles: history and recent developments. *J. Photochem. Photobiol. C Photochem. Rev.* 12, 237–268. doi: 10.1016/j.jphotochemrev.2011.07.001

Michael, D., Mingos, P., and Baghurst, D. R. (1991). Applications of microwave dielectric heating effects to synthetic problems in chemistry. *Chem. Soc. Rev.* 20, 1–47. doi: 10.1039/cs9912000001

Molins, E., Benito, M., Mata, I., Martínez, L., Soler, L., and Llorca, J. (2017). Au/TiO_2 lyogels for hydrogen production. *MRS Adv.* 2, 3499–3504. doi: 10.1557/adv.2017.346

Murdoch, M., Waterhouse, G. I., Nadeem, M. A., Metson, J. B., Keane, M. A., Howe, R. F., et al. (2011). The effect of gold loading and particle size on photocatalytic hydrogen production from ethanol over Au/$TiO_{(2)}$ nanoparticles. *Nat. Chem.* 3, 489–492. doi: 10.1038/nchem.1048

Nadeem, M. A., Murdoch, M., Waterhouse, G. I. N., Metson, J. B., Keane, M. A., Llorca, J., et al. (2010). Photoreaction of ethanol on Au/TiO_2 anatase: comparing the micro to nanoparticle size activities of the support for hydrogen production. *J. Photochem. Photobiol. A Chem.* 216, 250–255. doi: 10.1016/j.jphotochem.2010.07.007

Pascu, O., Carenza, E., Gich, M., Estradé, S., Peiró, F., Herranz, G., et al. (2012). Surface reactivity of iron oxide nanoparticles by microwave-assisted synthesis; comparison with the thermal decomposition route. *J. Phys. Chem. C* 116, 15108–15116. doi: 10.1021/jp303204d

Pelaz, B., Grazu, V., Ibarra, A., Magen, C., del Pino, P., and de la Fuente, J. M. (2012). Tailoring the synthesis and heating ability of gold nanoprisms for bioapplications. *Langmuir* 28, 8965–8970. doi: 10.1021/la204712u

Primo, A., Corma, A., and Garcia, H. (2011). Titania supported gold nanoparticles as photocatalyst. *Phys. Chem. Chem. Phys.* 13, 886–910. doi: 10.1039/C0CP00917B

Scarabelli, L., Coronado-Puchau, M., Giner-Casares, J. J., Langer, J., and Liz-Marzan, L. M. (2014). *ACS Nano* 8, 5833–5842. doi: 10.1021/nn500727w

Siah, W. R., Lintang, H. O., Shamsuddin, M., and Yuliati, L. (2016). High photocatalytic activity of mixed anatase-rutile phases on commercial TiO_2 nanoparticles. *IOP Conf. Ser. Mater. Sci. Eng.* 107:012005. doi: 10.1088/1757-899X/107/1/012005

Stuerga, D., Gonon, K., and Lallemant, M. (1993). Microwave heating as a new way to induce selectivity between competitive reactions. Application to isomeric ratio control in sulfonation of naphthalene. *Tetrahedron* 49, 6229–6234.

Su, R., Tiruvalam, R., Logsdail, A. J., He, Q., Downing, C., Jensen, M. T., et al. (2014). Designer titania-supported aupd nanoparticles for efficient photocatalytic hydrogen production. *ACS Nano* 8, 3490–3497. doi: 10.1021/nn500963m

Taboada, E., Angurell, I., and Llorca, J. (2014a). Dynamic photocatalytic hydrogen production from ethanol–water mixtures in an optical fiber honeycomb reactor loaded with Au/TiO_2. *J. Catal.* 309, 460–467. doi: 10.1016/j.jcat.2013.10.025

Taboada, E., Angurell, I., and Llorca, J. (2014b). Hydrogen photoproduction from bio-derived alcohols in an optical fiber honeycomb reactor loaded with Au/TiO_2. *J. Photochem. Photobiol. A Chem.* 281, 35–39. doi: 10.1016/j.jphotochem.2014.03.004

Viswanathan, B., and Raj, K. J. A. (2009). Effect of surface area, pore volume and particle size of P25 titania on the phase transformation of anatase to rutile. *Indian J. Chem.Sect. A Inorg. Phys. Theor. Anal. Chem.* 48, 1378–1382.

Xu, S., and Sun, D. D. (2009). Significant improvement of photocatalytic hydrogen generation rate over TiO_2 with deposited CuO. *Int. J. Hydrogen Energy* 34, 6096–6104. doi: 10.1016/j.ijhydene.2009.05.119

Yu, J., Hai, Y., and Jaroniec, M. (2011). Photocatalytic hydrogen production over CuO-modified titania. *J. Colloid Interface Sci.* 357, 223–228. doi: 10.1016/j.jcis.2011.01.101

Yu, S., Hachtel, J. A., Chisholm, M. F., Pantelides, S. T., Laromaine, A., and Roig, A. (2015). Magnetic gold nanotriangles by microwave-assisted polyol synthesis. *Nanoscale* 7, 14039–14046. doi: 10.1039/C5NR03113C

Conflict of Interest Statement: The authors declare that the research was conducted in the absence of any commercial or financial relationships that could be construed as a potential conflict of interest.

frontiers in Chemistry

ORIGINAL RESEARCH
published: 05 February 2019
doi: 10.3389/fchem.2018.00677

Exploring the Control in Antibacterial Activity of Silver Triangular Nanoplates by Surface Coating Modulation

Jamila Djafari [1,2,3], Carlos Fernández-Lodeiro [1,2], Adrián Fernández-Lodeiro [1,2,3], Vanessa Silva [3,4,5,6], Patrícia Poeta [3,6], Gilberto Igrejas [3,4,5], Carlos Lodeiro [1,2,3], José Luis Capelo [1,2,3] and Javier Fernández-Lodeiro [1,2,3]**

[1] BIOSCOPE Group, LAQV@REQUIMTE, Chemistry Department, Faculty of Science and Technology, NOVA University Lisbon, Caparica, Portugal, [2] PROTEOMASS Scientific Society, Rua dos Inventores, Madam Parque, Caparica, Portugal, [3] Associated Laboratory for Green Chemistry (LAQV-REQUIMTE), University NOVA of Lisbon, Caparica, Portugal, [4] Department of Genetics and Biotechnology, University of Trás-os-Montes and Alto Douro, Vila Real, Portugal, [5] Functional Genomics and Proteomics Unit, University of Trás-os-Montes and Alto Douro, Vila Real, Portugal, [6] Veterinary Science Department, University of Trás-os-Montes and Alto Douro, Vila Real, Portugal

OPEN ACCESS

Edited by:
Angang Dong,
Fudan University, China

Reviewed by:
Soong Ju Oh,
Korea University, Japan
Jianping Yang,
Donghua University, China

***Correspondence:**
José Luis Capelo
jlcm@fct.unl.pt
Javier Fernández-Lodeiro
j.lodeiro@fct.unl.pt

Specialty section:
This article was submitted to Nanoscience, a section of the journal Frontiers in Chemistry

Received: *13 November 2018*
Accepted: *31 December 2018*
Published: *05 February 2019*

Citation:
Djafari J, Fernández-Lodeiro C, Fernández-Lodeiro A, Silva V, Poeta P, Igrejas G, Lodeiro C, Capelo JL and Fernández-Lodeiro J (2019) Exploring the Control in Antibacterial Activity of Silver Triangular Nanoplates by Surface Coating Modulation. Front. Chem. 6:677. doi: 10.3389/fchem.2018.00677

In the present work, the synthesis and characterization of silver triangular nanoplates (AgNTs) and their silica coating composites are reported. Engineering control on the surface coating has demonstrated the possibility to modulate the antibacterial effect. Several AgNT-coated nanomaterials, such as PVP (Polyvinylpyrrolidone) and MHA (16-mercaptohexadecanoic acid) as a stable organic coating system as well as uniform silica coating (≈5 nm) of AgNTs, have been prepared and fully characterized. The antibacterial properties of the systems reported, organic (MHA) and inorganic (amine and carboxylic terminated SiO_2) coating nanocomposites, have been tested on Gram-positive and Gram-negative bacteria strains. We observed that the AgNTs' organic coating improved antimicrobial properties when compared to other spherical silver colloids found in the literature. We have also found that thick inorganic silica coating decreases the antimicrobial effect, but does not cancel it. In addition, the effect of surface charge in AgNTs@Si seems to play a crucial role toward *S. aureus* ATCC 25923 bacteria, obtaining MIC/MBC values compared to the AgNTs with an organic coating.

Keywords: silver triangular nanoplates, silica coating, succinic anhydride, APTMS, antibacterial properties

INTRODUCTION

Silver nanoparticles (AgNPs) have attracted much attention as a result of their particular optoelectronic (Kelly et al., 2003; Wei, 2011), catalytic (Jiang et al., 2005; Köhler et al., 2008), or antibacterial properties (Morones et al., 2005; Rai et al., 2009).

Engineering modifications of AgNPs' size and shape represent a fascinating synthetic challenge that allow modification of the final nanomaterial's properties. These structural modifications at the nanoscale level strongly affect the macroscopic properties of the silver colloidal solutions. For instance, the intense colors of silver colloids are the result of different electron oscillation modes that arise when an electromagnetic field, in the visible range, is coupled to the collective oscillations of conduction electrons (Kelly et al., 2003). The optical properties can be significantly modified

by adjusting the size and/or the shape of the NPs, allowing a spectral tuning that ranges from the visible to the near-IR region. This is particularly true for anisotropic structures such as nanoprisms or nanoplates, among others (Pastoriza-Santos and Liz-Marzán, 2008; Millstone et al., 2009).

Similarly to optoelectronic properties, the chemical behavior of silver colloids such as catalytic (Kundu et al., 2017) or antibacterial properties (Sadeghi et al., 2012) are also much affected by these structural changes. In this regard, many researchers have stated that AgNPs' chemical performance seems to be related with the different reactivity of the atoms located at the intersections, or in the corners of these nanostructures (Le Beulze et al., 2014; Kundu et al., 2017).

Furthermore, the antibacterial effect is one of the most explored applications owing to its excellent effect against a broad spectrum of bacteriological organisms. During the previous decades, the scientific community has debated over the different mechanisms in which AgNPs exert their toxicity toward bacteria and other microorganisms. It has been proved in numerous studies the crucial role of silver ions (Ag^+) release in the mechanism of antibacterial action of AgNPs (Xiu et al., 2012). In this vein, it has been suggested that the morphology of the AgNPs also affects the antimicrobial activity, as an essential indirect factor that mainly influences the release of Ag^+ (Feng et al., 2000; Xiu et al., 2012).

In this respect, several studies have shown that silver nanoprisms (AgNTs) have more bactericidal action than nanorods or nanospheres, demonstrating that the nanomaterial's shape strongly influences the bactericidal effect of silver nanoparticles (Xue et al., 2007; Van Dong et al., 2012; Pal et al., 2015). Indeed, the presence of high atomic density facets in nanoprim structures such as {111} (like triangular or decahedral shape), induces the increase of nanoparticle antibacterial activity and seems to be important in the direct interaction within the bacteria surface (Morones et al., 2005; Sadeghi et al., 2012). Furthermore, AgNTs exhibit high surface energy, mainly located at their tips and edges, where silver atoms can be readily oxidized, resulting in either truncation of prism tips or their complete dissolution (Pastoriza-Santos and Liz-Marzán, 2008; Millstone et al., 2009). This significant drawback can significantly limit their physicochemical properties' advantages and therefore could reduce the antibacterial application of these nanostructures. Different coating methods have been developed in order to avoid this disadvantage, minimizing the effect, and enabling the manipulation of this material as a building block in future applications.

Many studies around spherical AgNPs have proved that whether there is organic (Xiu et al., 2012; Yang et al., 2012; Abbaszadegan et al., 2015) or inorganic (usually mesoporous silica) coating (Liong et al., 2009; Le et al., 2010; Nuti et al., 2018) has an essential influence on AgNPs' antibacterial effect. In this regard, it has been confirmed that the Ag^+ release could be controlled, and as an important consequence, the environmental impacts could be strongly mitigated.

In contrast, the case of AgNTs has been much less investigated. A. Yu et al. provided a significant advance about AgNT stabilization using different alkanethiols (Jiang et al., 2007). These authors report that the Ag-S interactions considerably delay the dissolution of AgNT structures. These important chemical observations were later exploited by Xue et al. (2007), in an elegant work in which the authors demonstrated the perfect AgNT silica coating.

Additionally, it has been demonstrated that amorphous silica coating over AgNPs presents porosity, allowing the diffusion of ions that can oxidize the silver core (Mulvaney et al., 1997). The porosity of the amorphous silica has already been proved in studies by different groups (Lecloux et al., 1986; van Blaaderen and Vrij, 1993). Nevertheless, unfortunately, according to the best of our knowledge, the antibacterial properties of AgNTs subjected to alkanethiol or silica coating have not yet been explored.

The goal of the present work is, therefore, to investigate the influences of surface coating of well-defined AgNTs (organic and inorganic) on their optical properties as well as the effects of antibacterial activity against *E. coli* and *S. aureus*. The effect of the surface charge and terminal functional groups (NH_2 or COOH) on AgNTs@SiO_2 was also investigated.

MATERIALS AND METHODS

Materials

Silver nitrate 99% ($AgNO_3$), sodium borohydride 99% ($NaBH_4$), Sodium citrate tribasic dihydrate 99%, hydrogen peroxide 30% (H_2O_2), polyvinylpyrrolidone (PVP-29K), 16-mercaptohexadecanoic acid 90% (MHA), dimethylamine (DMA) 40% in water, tetraethylorthosilicate (TEOS), (3-Aminopropyl)trimethoxysilane 97% (APTMS), Succinic anhydride 99% (SA), and anhydrous Tetrahydrofuran (a-THF) were obtained from Sigma-Aldrich, and used without previous purification. Anhydrous Ethanol (a-EtOH) was purchased from Carlo Elba. Water was used at Milli-Q grade by Millipore (MQ).

Methods

Synthesis of AgNTs in Water (AgNTs@PVP) and MHA Stabilization (AgNTs@MHA)

The synthesis was carried out in a total volume of 50 mL of MQ water at 30°C, under ambient atmosphere and laboratory light. Over an aqueous solution of $AgNO_3$ (final concentration of 0.2 mM), under vigorous stirring, trisodium citrate (150 mM, 1 mL), PVP 29K (135 mg/mL, 3 mL), and hydrogen peroxide (30 wt%, 240 μL) aqueous solutions were added. Afterward, a freshly prepared aqueous solution of $NaBH_4$ (final concentration of 1.6 mM) was rapidly added. The solution then immediately turned clear yellow. After 10 min, the colloid solution changed to intense yellow, showing the formation of spherical silver nanoparticles, and then the color solution turned to orange, red, purple, and finally blue. The silver nanoplates were centrifuged at 10,000 rpm during 30 min and re-dispersed in ethanol.

The coating of AgNTs@PVP with 16-MHA was carried out by quickly adding an ethanolic solution of MHA (final concentration of 60 μM) on the AgNTs@PVP in EtOH under vigorous stirring and darkness. After 15 min, the colloid was centrifugated at 11,000 rpm and re-suspended in ethanol.

Silica Coating of AgNTs@MHA to Produce AgNTs@Si-OH

An ethanolic solution of TEOS (final concentrations explored between 0.9 and 0.4 mM) was added to the colloid AgNTs@MHA in EtOH. Then, an aqueous DMA solution was rapidly injected into the mixture (final concentrations explored between 0.6 and 0.4 M). The solution was left stirring for 180 or 90 min. at ambient temperature in the dark. The AgNTs@Si-OH were centrifuged several times and washed in ethanol and ultra-pure water. Then, the purified colloid was resuspended in ethanol.

Amine Derivatization of AgNTs@Si-OH to Produce AgNTs@Si-NH_2

The AgNTs@Si-OH colloid was coated with amine silane to convert the AgNTs' surface with amine function. Briefly, under stirring, APTMS in ethanol solution (final concentration of 33.7 μM) was added to an ethanolic solution of AgNTs@Si-OH. Then, 1.32% (of total volume reaction) of Milli-Q water was added as a catalyzer agent (Bruce and Sen, 2005). The reaction was left under stirring overnight. The resulting solution was purified by repeated centrifugation using ethanol and Milli-Q water.

Carboxylic Acid Derivatization of AgNTs@Si-NH_2 to Produce AgNTs@Si-COOH

The AgNTs@Si-NH_2 were washed several times in a-THF, and finally suspended in anhydrous THF. A solution of succinic anhydride in a-THF was added drop-wise to the colloid solution AgNTs@Si-NH_2 until it reached a concentration of 0.52 mM. The reaction was then stirred for 24 h under dark conditions. The resulting AgNTs@Si-COOH were purified several times using THF and then Milli-Q.

Characterization Technics

UV/Vis spectroscopy analysis

The UV/Vis spectroscopy studies were performed using a JASCO 630 spectrophotometer provided by the PROTEOMASS-BIOSCOPE facility. The spectra were run between 200 and 1,000 nm using a quartz cell (1 cm pathway) under temperature control.

Z-Potential analysis

A MALVERN model ZS instrument provided by the PROTEOMASS-BIOSCOPE facility was used to obtain the Z potential values. A "dip" cell was used to measure the Z potential.

Transmission electron microscopy (TEM) analysis

Microscopy analyses were performed at the CACTI, University of Vigo (Spain). A JEOL JEM1010 TEM operating at 100 kV was used. All TEM samples were prepared by placing a drop of the sample (5 μL) on a TEM copper grid and then air-dried.

Inductively coupled plasma (ICP) analysis

Ag contents in each studied sample were determined in the REQUIMTE-Chemistry Department, FCT-UNL analytical laboratory using an ICP instrument from Horiba Jobin-Yvon (France, model Ultima), equipped with an RF of 40.68 MHz, a 1.00 m Czerny-Turner monochromator (sequential), and an AS500 autosampler.

TABLE 1 | Different strains used in the present study.

Strain	Relevant phenotype	Reference
E. coli K12 ATCC 29425	Gram-negative	ATCC
S. aureus ATCC 25923	Gram-positive	ATCC

Fourier-transform infrared spectroscopy (FTIR) analysis

A Bruker TENSOR spectrophotometer was used to obtain the FT-IR spectra. FT-IR experiments were performed in a KBr disk, provided by the Chemistry Department, LAQV-REQUIMTE, FCT Facilities. To obtain the KBR discs for analysis, each sample was centrifuged and washed in absolute EtOH several times until finally resuspending each sample in 100μL of anhydrous EtOH. These concentrated solutions were mixed with KBr, and the solids were dried under a vacuum pump for 4 h before the preparation of the disks.

Bacterial Strains, Culture Media, and Growth Conditions

The bacterial strains considered in this study were *Escherichia coli* ATCC 29425 and *Staphylococcus aureus* ATCC 25923 (**Table 1**). Bacterial strains were grown in BHI agar (Oxoid, UK) for 24 h at 37°C.

Preparation of Stock Solutions

Each solution containing AgNTs was diluted to final concentrations of 1, 5, 10, 25, 50, 75, 100, 150, 200, 300, and 500 μg/mL, and tested on both bacteria.

Antibacterial Susceptibility Test

The minimum inhibitory concentration (MIC), described as the lowest concentration of nanoparticles that inhibits bacterial growth, was determined by broth-dilution method using a 96-well polystyrene microtiter plate. Luria-Bertani (LB) (Sigma–Aldrich) broth was prepared, and 135 μL was added to each well. Ten microliters of each solution containing different NPs with concentrations ranging from 1 to 500 μg/mL were added to each well, and 10 μL of overnight cultures of the selected bacteria were inoculated into the wells and incubated at 37°C. After 24 h, the absorbance was measured with a microplate spectrophotometer. Positive (inoculated medium) and negative controls (medium supplemented with NPs) were included for all tests. All tests were performed in triplicate.

To determine the minimum bactericidal concentration (MBC), which is characterized by no bacterial growth, 100 μL of the cultures resulting from MIC testing were inoculated onto LB medium plates and incubated at 37°C for 20 h. Control cultures without NPs were included in all experiments.

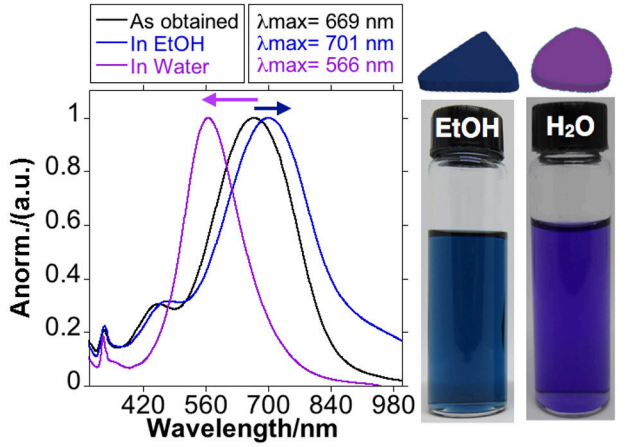

FIGURE 1 | Spectroscopic profile and color of AgNTs@PVP resuspended in EtOH (blue) or Water (purple).

RESULTS AND DISCUSSION

Synthesis of Silver Triangular Nanoplates and Alkane-Thiol Functionalization

In the present work, all the experiments have been conceived to determine the antibacterial effects of AgNTs as a function of the surface coating. In the literature, a variety of works that report the synthesis of different triangular nanoplates or nanoprisms with an organic coating to explore their antibacterial properties can be found, but to the best of our knowledge only two works report the controlled silica deposition on AgNTs, and none of them explores the antibacterial properties of the resulting product (Xue et al., 2007; Brandon et al., 2014).

In the first synthetic step, we synthesized AgNTs@PVP using a *non-seed mediated methodology* based on thermal synthesis developed by Métraux and Mirkin (2005) and lately revisited by Yin and coworkers (Zhang et al., 2011; Yu et al., 2014). This photochemical reaction was performed in water with several modifications (see experimental section). We used PVP (29K) as a stabilizer and sodium borohydride as a reducing agent, in the presence of shape directors: citrate ion and hydrogen peroxide.

As can be seen in **Figure 1** the blue-colored solution obtained and showed an intense absorption band centered at *ca.* 669 nm with a weak shoulder at *ca.* 420 nm that can be assigned to the in-plane dipole and in-plane quadrupole plasmon resonances of AgNTs, respectively. The absence of bands around *ca.* 400 nm (typical of spheres) is indicative of the high yield of AgNTs obtained in this reaction (Millstone et al., 2009; Yu et al., 2014).

This colloid solution showed high sensitivity to the purification processes, using water as a dispersant. When the NPs were re-suspended in ultra-pure water, there was a fast blue shift of in-plane dipole plasmon band to *ca.* 566 nm and a disappearance of the in-plane quadrupole plasmon band, with a change of the color solution to purple (**Figure 1**). This behavior results from the enormous sensitivity of the AgNTs@PVP to suffer tip truncation, or partial dissolution during their manipulation, which strongly affects the final properties (Jiang et al., 2007).

Purification of the AgNTs@PVP using absolute EtOH as a dispersant did not produce this effect. As shown in **Figure 1**, the SPR band red-shifted from *ca.* 669 nm to *ca.* 701 nm as a consequence of the solvent change, which increases the dielectric constant of the medium (Link and El-Sayed, 1999; Szunerits and Boukherroub, 2012).

Another critical factor to be controlled was the centrifugation conditions during the purifications process. We observed that increases in the rotation speed, or in the time cycle, produced the formation of remarkable aggregates, especially when the AgNTs were resuspended in absolute EtOH. The selection of these purification conditions allowed us to obtain well-dispersed AgNTs in the EtOH solution. The final solution obtained was stable for several days without noticeable spectral changes.

Transmission electron microscopy (TEM) analysis of the colloid obtained in EtOH showed the AgNPs@PVP with triangular platelet geometry with an average size of 28.8 ± 5.4 nm and a disc width of 5.9 ± 0.9 nm (**Figures 2B,D–F**).

The marked sensitivity of AgNTs@PVP to manipulation in aqueous solution limits its potential application in antibacterial preparations.

Therefore, in order to increase the stability in aqueous solution, the organic functionalization of the AgNTs' surface was done by rapid addition of an ethanolic solution of 16-mercaptohexadecanoic acid (MHA) over the AgNTs@PVP solution under vigorous magnetic stirring, following previous published methods. The dipole plasmon resonant band red-shifted in 34 nm upon the organic functionalization with MHA (Xue et al., 2007) (**Figures 2A,C**).

As presented by the TEM images in **Figures 2G–I**, the anisotropic geometry does not show important structural modifications. The thiol-stabilized colloid presents high stability in both EtOH and water solution. The Z-potential analysis of AgNTs@MHA in aqueous solution showed a stable potential of −35.8 mV, confirming the presence of carboxylate groups on the surface of the AgNTs (**Figure 5B**).

The FT-IR spectroscopy was employed to inspect the composition of this colloid solution. The CH_2 stretching vibrations peaks detected in AgNTs@MHA correspond to the frequencies observed in the free MHA at 2,919 and 2,851 cm^{-1} (Morales-Cruz et al., 2005). Contrary to the spectrum of the pure compound, for AgNTs@MHA no signals were detected at 2,555 cm^{-1}, which was assigned to the ν(S-H) stretching vibration. This fact is indicative, on the one hand, that MHA molecules have adsorbed to the AgNTs' surface through the sulfur group, and on the other hand, of the absence of unreacted MHA molecules on the AgNTs@MHA colloid suspension (Johnson et al., 1998; Morales-Cruz et al., 2005; Gupta et al., 2012). The band observed at 1,559 cm^{-1} in AgNTs@MHA could be assigned to $\nu(COO^-)$ symmetric stretch (Morales-Cruz et al., 2005) as a consequence of a partial ionization of the carboxylic group of MHA molecules exposed at the silver surface. Finally, the signal observed at 1,652 cm^{-1} could be related to the ν(C=O) stretching vibration of carboxylic acid in MHA, or also to the ν(C=O) stretching

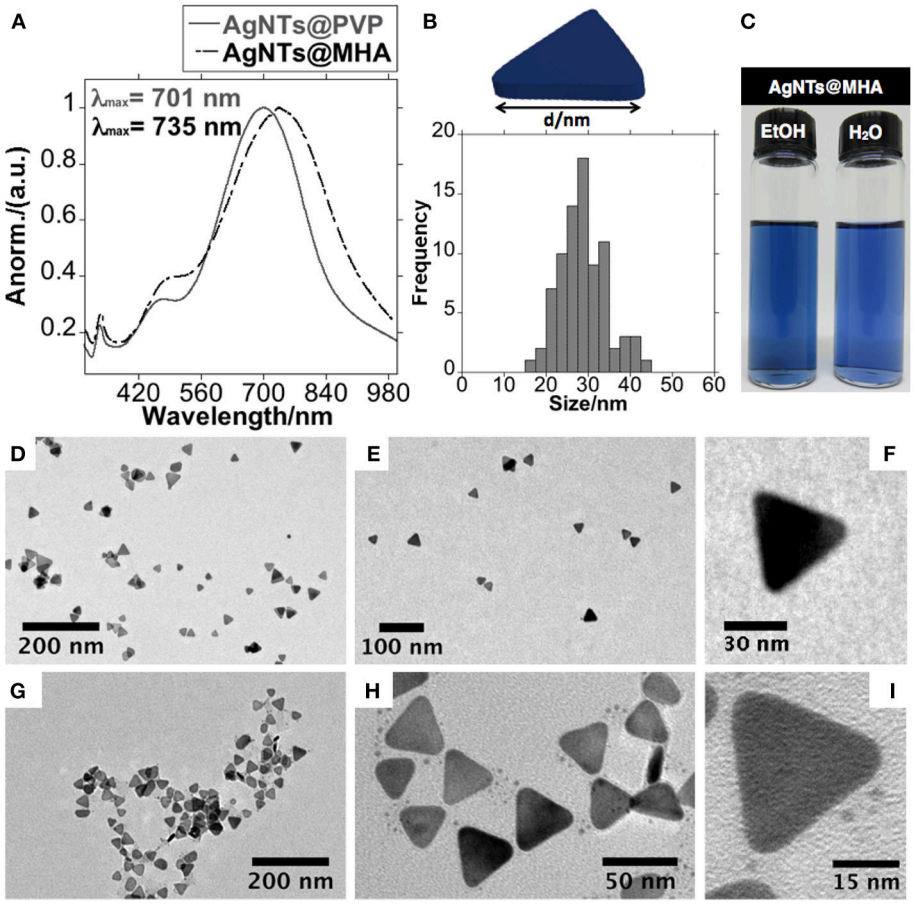

FIGURE 2 | Spectroscopic profile of AgNTs@PVP and AgNTs@MHA in EtOH solution **(A)**, size histogram of lateral distance of AgNTs@MHA **(B)**, color solution of AgNTs@MHA resuspended in EtOH and water **(C)**. TEM images obtained of AgNTs@PVP **(D–F)** and AgNTs@MHA **(G–I)**.

vibration amide group of remnant PVP adsorbed on the surface of AgNTs@MHA (**Figure 3**).

These organic coating AgNTs (AgNTs@MHA) were selected for the antibacterial studies.

Silica Coating of AgNTs@MHA

As reported previously by Mirkin et al. thiol-stabilized AgNTs can be used satisfactorily in the next control of the coating with silica, without affecting the anisotropic structure of the AgNTs (Xue et al., 2007). In that work, the authors started with silver nanoprisms synthesized through a photochemical process, using a single beam excitation system in the presence of citrate and bis (p-sulfonatophenyl) phenylphosphine (BSPP). Then, the AgNTs were functionalized with MHA, and later with a thin and highly uniform silica coating shell using TEOS as a precursor of silica, and DMA as a catalyst.

In our case, we used AgNTs@PVP as starting materials to obtain AgNTs@MHA, and then to produce AgNTs@Si. The silica coating offers an exciting possibility to study how the antibacterial properties of AgNTs@MHA are affected when they are subjected to a dense inorganic coating.

Our intention concerning the silica deposition was to explore the synthetic conditions that allow obtaining a thin but uniform coating, without substantially affecting the anisotropy of the nanoparticles. In this way, keeping constant the DMA concentration (0.5 M) and the reaction time (180 min), we have explored the coating process obtained using different TEOS concentrations between 0.9 and 0.5 mM. As can be seen in **Figure S1**, in our case, the decrease in the concentration of TEOS during the coating does not permit obtaining a fine homogeneous silica coating. Additionally, all the analyzed samples showed in **Figure S1** presented an essential loss of the triangular geometry of the platelets. Interestingly, for the higher concentrations of TEOS explored, we detected the presence of holes within the silica nanostructure (**Figure S1a**).

Considering the nanostructures obtained, the dissolution process suffered by AgNTs during the silica deposition seems to be affected to a large extent by the contact time of the nanostructures with the DMA and/or the concentration of the same.

Based on the previous observations related to the TEOS concentration, using 0.5 mM, we have decreased the reaction

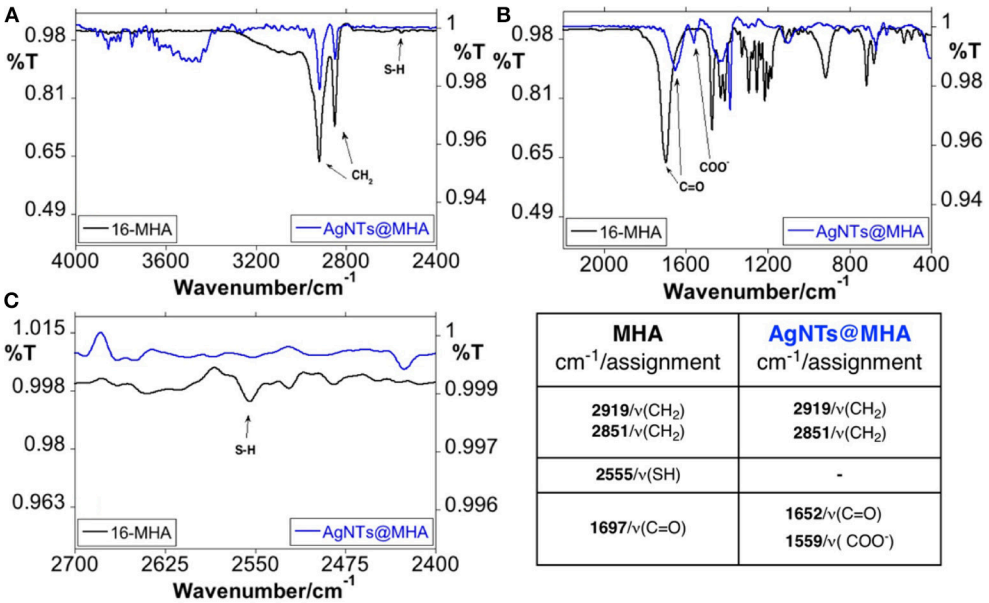

MHA cm^{-1}/assignment	AgNTs@MHA cm^{-1}/assignment
2919/ν(CH_2) **2851**/ν(CH_2)	**2919**/ν(CH_2) **2851**/ν(CH_2)
2555/ν(SH)	-
1697/ν(C=O)	**1652**/ν(C=O) **1559**/ν(COO^-)

FIGURE 3 | FT-IR spectroscopic profile of 16-MHA and AgNTs@MHA in KBr disk. Overview between 4,000 and 2,400 cm^{-1} **(A)** and 2,000–400 cm^{-1} **(B)**. Enlargement spectra in the S-H region between 2,700 and 2,400 cm^{-1} **(C)** and peak table.

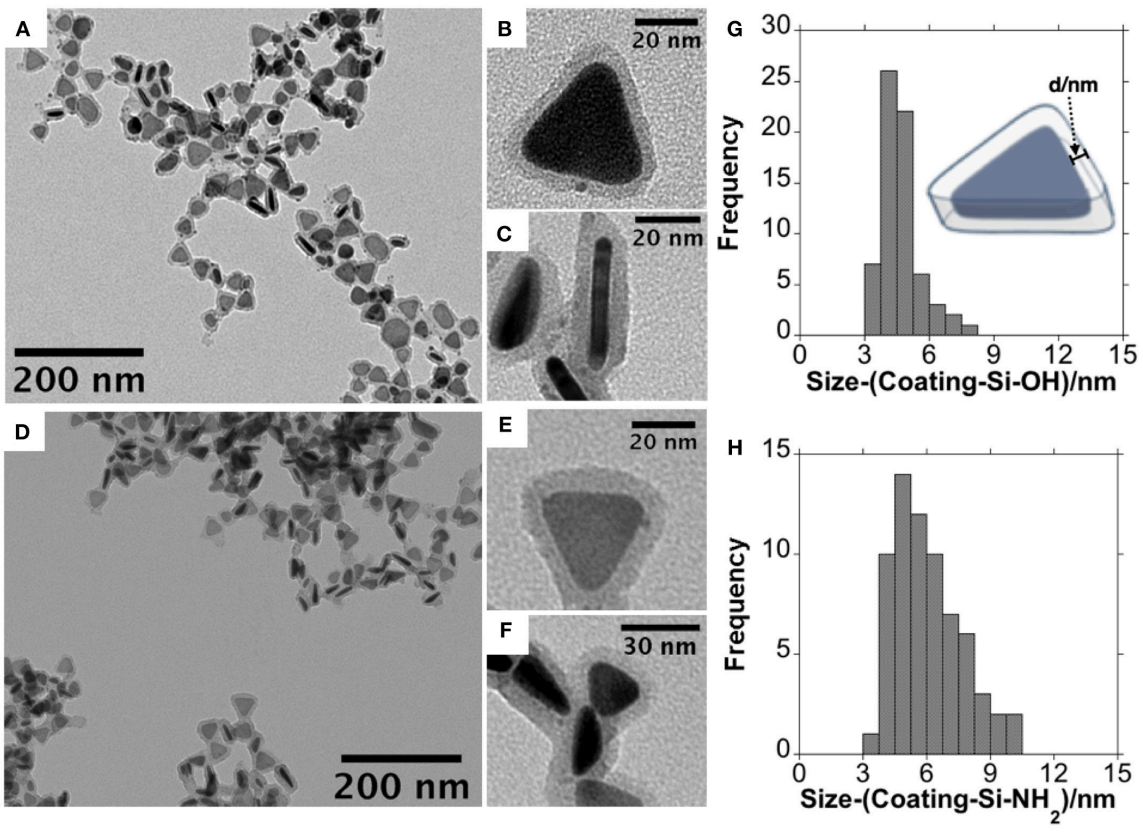

FIGURE 4 | Low magnification TEM images at different magnifications obtained for AgNTs@Si-OH **(A–C)** and AgNTs@Si-NH_2 **(D–F)** and size histogram of silica coating for AgNTs@Si-OH **(G)** and AgNTs@Si-NH_2 **(H)**.

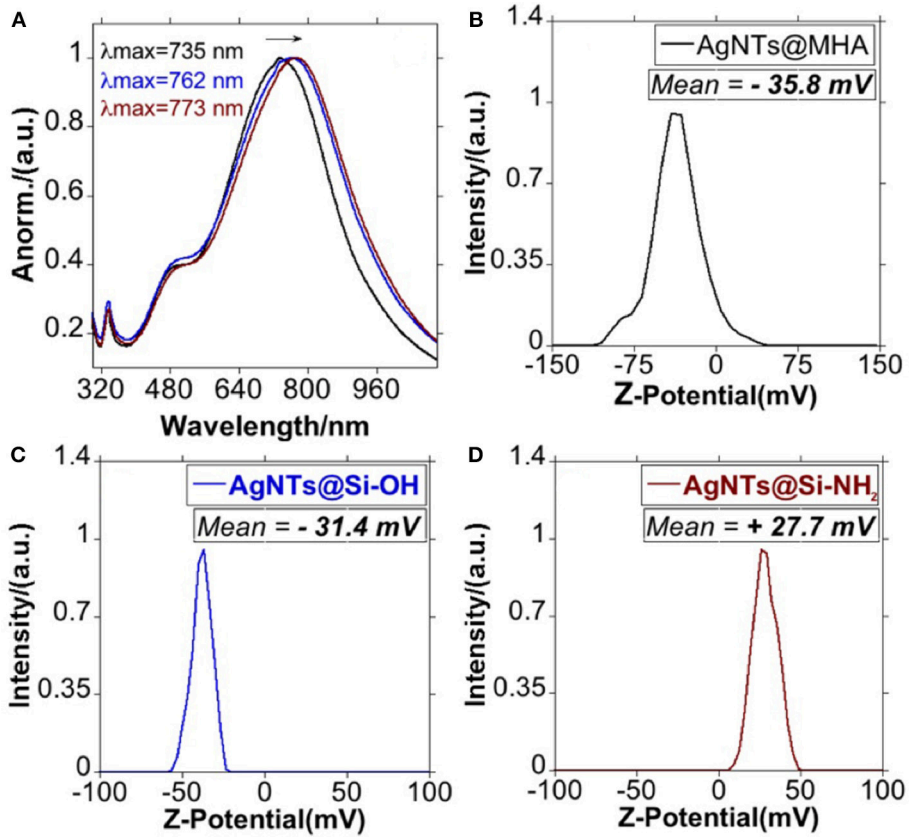

FIGURE 5 | Spectroscopic profile of AgNTs@MHA, AgNTs@Si-OH and AgNTs@Si-NH_2 in EtOH **(A)**, and graphic representation of the Z-potential for AgNTs@MHA **(B)**, AgNTs@Si-OH **(C),** and AgNTs@Si-NH_2 **(D)**.

time to 90 min. In **Figure S2**, it can be seen after just 90 min. of reaction, the silica coating showed a homogenous character overall of silver cores. Remarkably, we conclude that in our process, the re-shaping of AgNTs is preserved to a greater extent for the reaction obtained with 90 min, indicating that more significant contact with DMA produces higher re-shaping of the AgNTs, probably by diffusing of DMA through the already-formed silica shell.

Finally, for a concentration of TEOS of 0.5 mM, and 90 min of reaction, we have explored the decrease in the concentration of DMA to 0.4 M. The reduction of the concentration of DMA not only allowed us to preserve to a greater extent the anisotropy of the AgNTs, but also allowed us to obtain a relatively homogeneous silica coating. Consequently, the refined synthetic conditions were [TEOS] = 0.5 mM, [DMA] = 0.4 M and 90 min., allowing us to obtain a silica coating thickness of around 5 nm (**Figures 4A–C,G**).

The dipole plasmon resonant band of AgNTs@MHA red-shifted in 27 nm, upon silica coating (**Figure 5A**), following previous similar reports (Xue et al., 2007).

Using FT-IR spectroscopy, the characteristic signals for the silica were observed at 467, 800, 960, and 1,094 cm^{-1} (**Figure 6**). These signals can be assigned to the bending vibration of Si-O-Si, stretching, and bending vibrations of Si-OH, and asymmetric stretching vibration of O-Si-O, respectively (Rahman et al., 2009; Azarshin et al., 2017; Sakthisabarimoorthi et al., 2017), confirming the polymerization of the silane on the silver cores.

In a subsequent step, we have derivatized the terminal -OH group of the AgNTs@Si-OH into –NH_2 through a silane coupling reaction with APTMS, based on established protocols (Bruce and Sen, 2005). As shown by the TEM images in **Figures 4D–F** through APTMS coupling on AgNTs@Si-OH, we obtained a slight increase in the shell silica size (≈1.3 nm) (see **Figure 4H**). This functional group conversion can be readily confirmed using Z-potential analysis of the colloids in water. Therefore, the AgNTs@Si-OH have a surface charge equal to −31.4 mV, which is reversed to positive values +27.7 mV for AgNTs@Si-NH_2 (**Figures 5C,D**). This Zeta potential value reversion is the consequence of the different energies of ionization in water presented by the -OH and -NH_2 groups (Jacobasch, 1989; Jesionowski, 2003).

These positively-charged **AgNTs@Si-NH_2** were selected as the second sample for bacteriological analysis.

Finally, to explore if the effect of surface charge can affect the antimicrobial properties of silica-coated AgNTs, we converted the terminal organic amine group (-NH_2) into carboxylic acid (-COOH), reacting AgNTs@NH_2 with succinic anhydride in anhydrous THF. As can be seen in **Figure 7A**, the LSRP was

not significantly affected. On the other hand, upon conversion of an amine into the carboxylic group, the Z-potential of the colloid in ultrapure water moved from +27.7 mV to −26.0 mV, which was in accordance with previous reports about AgNPs@Si functionalization (Bahadur et al., 2011) (**Figure 7B**).

The negatively-charged **AgNTs@Si-COOH** were selected as the third sample for bacteriological analysis.

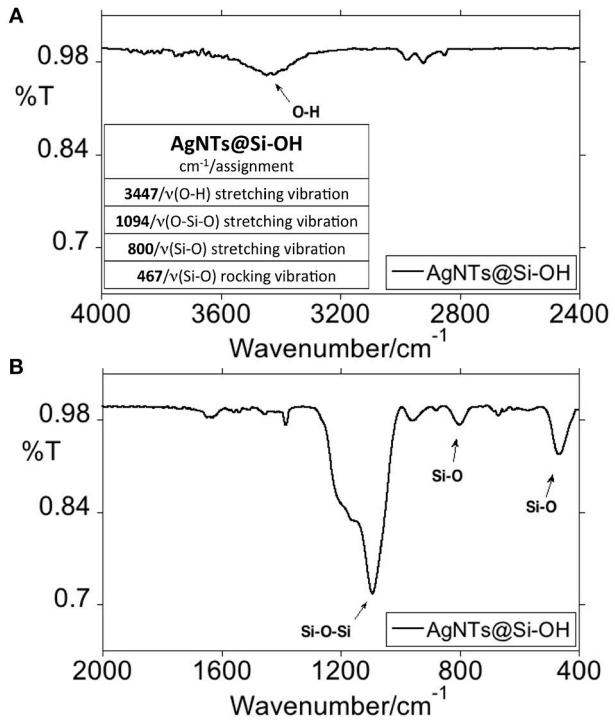

FIGURE 6 | FT-IR spectroscopic profile of AgNTs@Si-OH in KBr disk. Overview between 4,000 and 2,400 cm^{-1} and peak table **(A)** and 2,000 and 400 cm^{-1} **(B)**.

Exploring Bactericidal Properties

The antibacterial susceptibility tests were performed by the broth dilution method. Previous studies have proved that silver nanoparticles alone and silver composites have high antibacterial effectiveness against bacteria, fungi and viruses (Akhavan and Ghaderi, 2009; Liga et al., 2011; Ifuku et al., 2015) (see **Figure S1** and **Figure S3**). The minimum inhibitory concentration (MIC) and the minimal bactericidal concentration (MBC) values are shown in **Table 2**.

Based on the MIC/MBC values obtained for the three selected samples, we have confirmed that the AgNTs that were only subjected to organic coating (AgNTs@MHA) showed the best antimicrobial properties, with MIC/MBC values of 10/10 and 5/10 (μg/mL) for *E. coli* and *S. aureus*, respectively. Compared with other studies using different spherical silver NPs, AgNTs@MHA show suitable antimicrobial properties.

For instance, the AgNPs@citrate ranged in size between 5 and 100 nm, showing MICs that varied from 20 to 160 μg/mL for the two tested strains of *E. coli* (Agnihotri et al., 2014). Besides, AgNPs@PVP in a range of sizes between 9 and 16 nm showed higher MBC values than those obtained in our case for AgNTs@MHA for the same bacterial strain *S. aureus* (ATCC 25923) (Bryaskova et al., 2011).

Note that in our previous study using 15 nm spherical AgNPs stabilized with tetracycline, higher MIC values against the same bacterial strains studied in the present work were visible (between 16 and 32 μg/mL; Djafari et al., 2016). These important results show how the rational selection of the shape in silver NPs could overcome the synergistic effect produced by spherical shape and tetracycline.

The present results, therefore, are in agreement with previous works which elucidate a greater antibacterial effect of nanoparticles with {111} basal plane (Morones et al., 2005). More specifically, Sadeghi and co-workers studied the antimicrobial effect of PVP-stabilized nanospheres, nanobars, and nanoplates against *E. coli* and *S. aureus* (Sadeghi et al., 2012). These

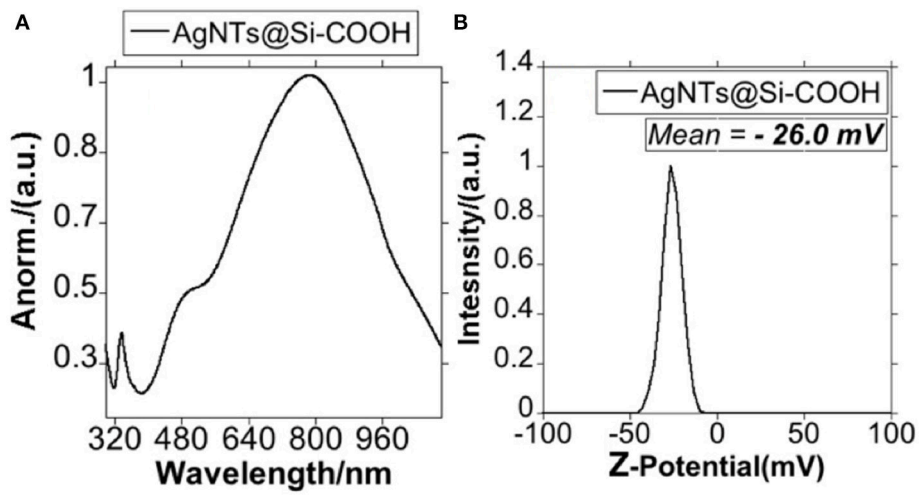

FIGURE 7 | Spectroscopic profile of AgNTs@Si-COOH **(A)** and graphic representation of the Z-potential for AgNTs@Si-COOH **(B)**.

TABLE 2 | The minimum inhibitory concentration (MIC) and minimum bactericidal concentration (MBC) of AgNTs@MHA, AgNTs@Si-NH_2, and AgNTs@Si-COOH toward *E. coli* K12 ATCC 29425 and *S. aureus* ATCC 25923.

Sample	Strain	MIC (μg/ml)	MBC (μg/ml)
AgNTs@MHA	*E. coli* K12 ATCC 29425	10	10
	S. aureus ATCC 25923	5	10
AgNTs@Si-NH_2	*E. coli* K12 ATCC 29425	25	50
	S. aureus ATCC 25923	5	10
AgNTs@Si-COOH	*E. coli* K12 ATCC 29425	25	50
	S. aureus ATCC 25923	10	25

authors proved a marked increase in the antimicrobial effect for nanoplates when compared to nanobars and nanospheres, as a consequence of higher surface area observed for nanoplates.

Studies on the impact of the AgNTs' surface coating on antibacterial activity remain limited to organic coating, and have highlighted antibacterial properties (Tang et al., 2013; Marta et al., 2014; Lu et al., 2015; D'Agostino et al., 2017; Tanvir et al., 2017). For instance, pluronic-coated nanoprisms have been successfully used as a bactericidal agent against two methicillin-resistant *S. aureus* strains. These authors observed strong bacteriostatic and bactericidal activity related to the high sensitivity of the tips and edges of AgNTs to undergo oxidation (Marta et al., 2014).

However, the inorganic coating of AgNTs has never been explored for antibacterial applications. Silica is presented as an ideal candidate since it favors stability to oxidation (Brandon et al., 2014), decreases non-specific interactions between the metallic surface and biomolecules (Bagwe et al., 2006), increases solubility in aqueous media or facile production and post-functionalization processes (Bahadur et al., 2011), among others advantages.

Related the samples subjected to silica coating, a decrease in the antibacterial effect concerning AgNTs@MHA can be noted by the MIC/MBC values summarized in **Table 2**. We believe that the subsequent coating of AgNTs@MHA with silica should delay the dissolution processes of AgNTs, decreasing the Ag^+ ratio released.

Despite this, the MIC/MBC values obtained between 5 and 50 μL/mL showed notably antimicrobial effects. More important, the bactericidal effect against *S. aureus* ATCC 25923 was not altered after silica coating for the case of AgNTs@Si-NH_2, indicating that the release of silver ions is probably not a determinant factor in the antibacterial activity of positively charged AgNTs against this specific strain. Note that the antibacterial effect obtained for AgNTs@Si-COOH in the two bacterial strains studied was decreased when compared to AgNTs@MHA. Therefore, the surface charge of AgNTs should be considered in the mode of action against *S. aureus*. In this regard, it has been previously suggested that positively-charged AgNPs grant a higher antimicrobial effect when compared to similar negatively-charged NPs (Abbaszadegan et al., 2015).

Finally, and supporting our results, it has been pointed out by different authors that after the silica coating the silver nanoparticles, AgNPs retain their antibacterial properties (Xu et al., 2009; Le et al., 2010).

CONCLUSIONS

We have successfully synthesized silver nanotriangles, AgNTs@PVP, in aqueous solution. Afterward, functionalization with 16-mercaptohexadecanoic acid (AgNTs@MHA) and the subsequent silica deposition were deeply investigated. We have determined the ideal synthetic conditions to obtain amorphous silica coating with ≈5 nm. Terminal amine functionality was introduced through a chemical reaction with APTMS, increasing the shell thickness to ≈1.3 nm. Amino group terminated nanoparticles (AgNTs@SiNH_2) then reacted with succinic anhydride in THF to obtain AgNTs@Si-COOH. The bacterial properties of AgNTs with a molecular coating (AgNTs@MHA) and silica coating (AgNTs@Si-NH_2 and AgNTs@Si-COOH) were investigated against Gram-positive and Gram-negative bacteria.

Comparing the three explored samples, the higher antibacterial effect was observed for the silica-free sample as expected, showing the best MIC values against *S. aureus* (ATCC 25923)—equal to 5 μg/mL. We have observed that the silica coating decreases the antibacterial effect for all the strains studied, except for the case of the positively-charged AgNTs@Si-NH_2 against *S. aureus* (ATCC 25923). These results indicate that the release of silver ion is not the unique critical point in the mode of action of AgNTs; nonetheless, the surface charge must also be taken into consideration. Even so, the MIC/MBC values for the silica-coated samples showed a similar range to the values reported in the literature for another type of uncoated-silica AgNPs.

As an important final remark, it should be mentioned that the high aqueous colloidal stability and the presence of terminal organic groups (COOH or NH_2) in the explored nanomaterials, both open the door to the design of more sophisticated nano-antibiotics through rational organic functionalization with bactericide-active molecular agents. Currently the application of these materials as building blocks to produce hybrid nano-antibiotics is under development in our laboratory.

AUTHOR CONTRIBUTIONS

JF-L, JLC and CL designed and supervised the project. JD, CF-L, AF-L, and JF-L performed the synthetic experiments. JF-L, CL, JLC, GI, JD, AF-L, and CF-L analyzed the results. JF-L and CL wrote the first draft. CL, JF-L, JLC, and GI provided the resources related to the project. JF-L, JD, CF-L, and AF-L produced all graphical materials. All authors reviewed and corrected the final manuscript. CL, JLC, and GI financed the project. PP and GI designed the bactericidal experiments. VS performed the bactericidal experiments.

FUNDING

All authors thank the financial support by the Associate Laboratory Research Unit for Green Chemistry—Clean Processes and Technologies—LAQV which is financed by national funds from FCT/MEC (UID/QUI/50006/2013) and co-financed by the

ERDF under the PT2020 Partnership Agreement (POCI-01-0145-FEDER-007265), as well as to the PROTEOMASS Scientific Society General Funds (Portugal) for funding support. All authors thank the grant PDTC/QEQ-MED/2118/2014 financed by FCT-MEC (Portugal).

ACKNOWLEDGMENTS

JF-L thanks FCT/MEC (Portugal) and FCT-UNL for the DL57/2016 Assistant Researcher Contract. JD thanks the Project PTDC/QEQ-MED/2118/2014 for her Ph.D. researcher contract. AF-L thanks the FCT-MEC Portugal for his doctoral grant associated to the Green Chemistry Ph.D. Program with reference SFRH/BD/52528/2014, and the PROTEOMASS Scientific Society Ph.D. grant during April 2018–April 2019. CF-L thanks the ERASMUS agreement between the University of Santiago de Compostela and the University NOVA of Lisbon for a grant.

SUPPLEMENTARY MATERIAL

The Supplementary Material for this article can be found online at: https://www.frontiersin.org/articles/10.3389/fchem.2018.00677/full#supplementary-material

REFERENCES

Abbaszadegan, A., Ghahramani, Y., Gholami, A., Hemmateenejad, B., Dorostkar, S., Nabavizadeh, M., et al. (2015). The effect of charge at the surface of silver nanoparticles on antimicrobial activity against gram-positive and gram-negative bacteria: a preliminary study. *J. Nanomater.* 2015:720654. doi: 10.1155/2015/720654

Agnihotri, S., Mukherji, S., and Mukherji, S. (2014). Size-controlled silver nanoparticles synthesized over the range 5-100 nm using the same protocol and their antibacterial efficacy. *RSC Adv.* 4, 3974–3983. doi: 10.1039/c3ra44507k

Akhavan, O., and Ghaderi, E. (2009). Bactericidal effects of Ag nanoparticles immobilized on surface of SiO_2 thin film with high concentration. *Curr. Appl. Phys.* 9, 1381–1385. doi: 10.1016/j.cap.2009.03.003

Azarshin, S., Moghadasi, J., and Aboosadi, Z. (2017). Surface functionalization of silica nanoparticles to improve the performance of water flooding in oil wet reservoirs. *Energy Explor. Exploit.* 35, 685–697. doi: 10.1177/0144598717716281

Bagwe, R. P., Hilliard, L. R., and Tan, W. (2006). Surface modification of silica nanoparticles to reduce aggregation and nonspecific binding. *Langmuir* 22, 4357–4362. doi: 10.1021/la052797j

Bahadur, N. M., Furusawa, T., Sato, M., Kurayama, F., Siddiquey, I. A., and Suzuki, N. (2011). Fast and facile synthesis of silica coated silver nanoparticles by microwave irradiation. *J. Colloid Interface Sci.* 355, 312–320. doi: 10.1016/j.jcis.2010.12.016

Brandon, M. P., Ledwith, D. M., and Kelly, J. M. (2014). Preparation of saline-stable, silica-coated triangular silver nanoplates of use for optical sensing. *J. Colloid Interface Sci.* 415, 77–84. doi: 10.1016/j.jcis.2013.10.017

Bruce, I. J., and Sen, T. (2005). Surface modification of magnetic nanoparticles with alkoxysilanes and their application in magnetic bioseparations. *Langmuir* 21, 7029–7035. doi: 10.1021/la050553t

Bryaskova, R., Pencheva, D., Nikolov, S., and Kantardjiev, T. (2011). Synthesis and comparative study on the antimicrobial activity of hybrid materials based on silver nanoparticles (AgNps) stabilized by polyvinylpyrrolidone (PVP). *J. Chem. Biol.* 4, 185–191. doi: 10.1007/s12154-011-0063-9

D'Agostino, A., Taglietti, A., Desando, R., Bini, M., Patrini, M., Dacarro, G., et al. (2017). Bulk surfaces coated with triangular silver nanoplates: antibacterial action based on silver release and photo-thermal effect. *Nanomaterials* 7:7. doi: 10.3390/nano7010007

Djafari, J., Marinho, C., Santos, T., Igrejas, G., Torres, C., Capelo, J. L., et al. (2016). New synthesis of gold- and silver-based nano-tetracycline composites. *ChemistryOpen* 5, 206–212. doi: 10.1002/open.201600016

Feng, Q. L., J., Wu, G. Q., Chen, F. Z., and Cui, T. M., Kim, J. O. K. (2000). A mechanistic study of the antibacterial effect of silver ions on *Ecoli* and *S. Aureus*. *J. Biomed. Mater. Res.* 662:23. doi: 10.1002/1097-4636(20001215)52:4<662::AID-JBM10>3.0.CO;2-3

Gupta, R. K., Srinivasan, M. P., and Dharmarajan, R. (2012). Synthesis of 16-Mercaptohexadecanoic acid capped gold nanoparticles and their immobilization on a substrate. *Mater. Lett.* 67, 315–319. doi: 10.1016/j.matlet.2011.09.047

Ifuku, S., Tsukiyama, Y., Yukawa, T., Egusa, M., Kaminaka, H., Izawa, H., et al. (2015). Facile preparation of silver nanoparticles immobilized on chitin nanofiber surfaces to endow antifungal activities. *Carbohydr. Polym.* 117, 813–817. doi: 10.1016/j.carbpol.2014.10.042

Jacobasch, H. J. (1989). Characterization of solid surfaces by electrokinetic measurements. *Prog. Org. Coatings* 17, 115–133. doi: 10.1016/0033-0655(89)80018-4

Jesionowski, T. (2003). Influence of aminosilane surface modification and dyes adsorption on zeta potential of spherical silica particles formed in emulsion system. *Colloids Surfaces A Physicochem. Eng. Asp.* 222, 87–94. doi: 10.1016/S0927-7757(03)00237-1

Jiang, X., Zeng, Q., and Yu, A. (2007). Thiol-frozen shape evolution of triangular silver nanoplates. *Langmuir* 23, 2218–2223. doi: 10.1021/la062797z

Jiang, Z. J., Liu, C. Y., and Sun, L. W. (2005). Catalytic properties of silver nanoparticles supported on silica spheres. *J. Phys. Chem. B* 109, 1730–1735. doi: 10.1021/jp046032g

Johnson, S. R., Evans, S. D., and Brydson, R. (1998). Influence of a terminal functionality on the physical properties of surfactant-stabilized gold nanoparticles. *Langmuir* 14, 6639–6647. doi: 10.1021/la9711342

Kelly, K. L., Coronado, E., Zhao, L. L., and Schatz, G. C. (2003). The optical properties of metal nanoparticles: the influence of size, shape, and dielectric environment. *J. Phys. Chem. B* 107, 668–677. doi: 10.1021/jp026731y

Köhler, J. M., Abahmane, L., Wagner, J., Albert, J., and Mayer, G. (2008). Preparation of metal nanoparticles with varied composition for catalytical applications in microreactors. *Chem. Eng. Sci.* 63, 5048–5055. doi: 10.1016/j.ces.2007.11.038

Kundu, S., Dai, W., Chen, Y., Ma, L., Yue, Y., Sinyukov, A. M., et al. (2017). Shape-selective catalysis and surface enhanced Raman scattering studies using Ag nanocubes, nanospheres and aggregated anisotropic nanostructures. *J. Colloid Interface Sci.* 498, 248–262. doi: 10.1016/j.jcis.2017.03.058

Le Beulze, A., Duguet, E., Mornet, S., Majimel, J., Tréguer-Delapierre, M., Ravaine, S., et al. (2014). New insights into the side-face structure, growth aspects, and reactivity of Ag_n Nanoprisms. *Langmuir* 30, 1424–1434. doi: 10.1021/la4039705

Le, Y., Hou, P., Wang, J., and Chen, J.-F. (2010). Controlled release active antimicrobial corrosion coatings with Ag/SiO_2 core–shell nanoparticles. *Mater. Chem. Phys.* 120, 351–355. doi: 10.1016/j.matchemphys.2009.11.020

Lecloux, A. J., Bronckart, J., Noville, F., Dodet, C., Marchot, P., and Pirard, J. P. (1986). Study of the texture of monodisperse silica sphere samples in the nanometer size range. *Colloids Surfaces* 19, 359–374. doi: 10.1016/0166-6622(86)80345-6

Liga, M. V., Bryant, E. L., Colvin, V. L., and Li, Q. (2011). Virus inactivation by silver doped titanium dioxide nanoparticles for drinking water treatment. *Water Res.* 45, 535–544. doi: 10.1016/j.watres.2010.09.012

Link, S., and El-Sayed, M. A. (1999). Spectral properties and relaxation dynamics of surface plasmon electronic oscillations. *J. Phys. Chem. B* 103, 8410–8426. doi: 10.1021/jp9917648

Liong, M., France, B., Bradley, K. A., and Zink, J. I. (2009). Antimicrobial activity of silver nanocrystals encapsulated in mesoporous silica nanoparticles. *Adv. Mater.* 21, 1684–1689. doi: 10.1002/adma.200802646

Lu, W., Yao, K., Wang, J., and Yuan, J. (2015). Ionic liquids-water interfacial preparation of triangular Ag nanoplates and their shape-dependent antibacterial activity. *J. Colloid Interface Sci.* 437, 35–41. doi: 10.1016/j.jcis.2014.09.001

Marta, B., Jakab, E., Potara, M., Simon, T., Imre-Lucaci, F., Barbu-Tudoran, L., et al. (2014). Pluronic-coated silver nanoprisms: synthesis, characterization and their antibacterial activity. *Colloids Surfaces A Physicochem. Eng. Asp.* 441, 77–83. doi: 10.1016/j.colsurfa.2013.08.076

Métraux, G. S., and Mirkin, C. A. (2005). Rapid thermal synthesis of silver nanoprisms with chemically tailorable thickness. *Adv. Mater.* 17, 412–415. doi: 10.1002/adma.200401086

Millstone, J. E., Hurst, S. J., Métraux, G. S., Cutler, J. I., and Mirkin, C. A. (2009). Colloidal gold and silver triangular nanoprisms. *Small* 5, 646–664. doi: 10.1002/smll.200801480

Morales-Cruz, A. L., Tremont, R., Martínez, R., Romañach, R., and Cabrera, C. R. (2005). Atomic force measurements of 16-mercaptohexadecanoic acid and its salt with CH_3, OH, and $CONHCH_3$ functionalized self-assembled monolayers. *Appl. Surf. Sci.* 241, 371–383. doi: 10.1016/j.apsusc.2004.07.058

Morones, J. R., Elechiguerra, J. L., Camacho, A., Holt, K., Kouri, J. B., Ramírez, J. T., et al. (2005). The bactericidal effect of silver nanoparticles. *Nanotechnology* 16, 2346–2353. doi: 10.1088/0957-4484/16/10/059

Mulvaney, P., Giersig, M., Ung, T., and Liz-Marzán, L. M. (1997). Direct observation of chemical reactions in silica-coated gold and silver nanoparticles. *Adv. Mater.* 9, 570–575. doi: 10.1002/adma.19970090712

Nuti, S., Fernández-Lodeiro, J., Del Secco, B., Rampazzo, E., Rodríguez-González, B., Capelo, J. L., et al. (2018). Engineered nanostructured materials for ofloxacin delivery. *Front. Chem.* 6, 1–14. doi: 10.3389/fchem.2018.00554

Pal, S., Tak, Y. K., and Song, J. M. (2015). Does the antibacterial activity of silver nanoparticles depend on the shape of the nanoparticle? A study of the gram-negative bacterium *Escherichia coli. J. Biol. Chem.* 290, 1712–1720. doi: 10.1128/AEM.02218-06

Pastoriza-Santos, I., and Liz-Marzán, L. M. (2008). Colloidal silver nanoplates. State of the art and future challenges. *J. Mater. Chem.* 18, 1724–1737. doi: 10.1039/b716538b

Rahman, I. A., Vejayakumaran, P., Sipaut, C. S., Ismail, J., and Chee, C. K. (2009). Size-dependent physicochemical and optical properties of silica nanoparticles. *Mater. Chem. Phys.* 114, 328–332. doi: 10.1016/j.matchemphys.2008.09.068

Rai, M., Yadav, A., and Gade, A. (2009). Silver nanoparticles as a new generation of antimicrobials. *Biotechnol. Adv.* 27, 76–83. doi: 10.1016/j.biotechadv.2008.09.002

Sadeghi, B., Garmaroudi, F. S., Hashemi, M., Nezhad, H. R., Nasrollahi, A., Ardalan, S., et al. (2012). Comparison of the anti-bacterial activity on the nanosilver shapes: nanoparticles, nanorods and nanoplates. *Adv. Powder Technol.* 23, 22–26. doi: 10.1016/j.apt.2010.11.011

Sakthisabarimoorthi, A., Dhas, S. A. M. B., and Jose, M. (2017). Fabrication and nonlinear optical investigations of SiO_2@Ag core-shell nanoparticles. *Mater. Sci. Semicond. Process.* 71, 69–75. doi: 10.1016/j.mssp.2017.07.008

Szunerits, S., and Boukherroub, R. (2012). Sensing using localised surface plasmon resonance sensors. *Chem. Commun.* 48:8999. doi: 10.1039/c2cc33266c

Tang, B., Li, J., Hou, X., Afrin, T., Sun, L., and Wang, X. (2013). Colorful and antibacterial silk fiber from anisotropic silver nanoparticles. *Ind. Eng. Chem. Res.* 52, 4556–4563. doi: 10.1021/ie3033872

Tanvir, F., Yaqub, A., Tanvir, S., and Anderson, W. (2017). Poly-L-arginine coated silver nanoprisms and their anti-bacterial properties. *Nanomaterials* 7:296. doi: 10.3390/nano7100296

van Blaaderen, A., and Vrij, A. (1993). Synthesis and characterization of monodisperse colloidal organo-silica spheres. *J. Colloid Interface Sci.* 156, 1–18. doi: 10.1006/jcis.1993.1073

Van Dong, P., Ha, C., Binh, L., and Kasbohm, J. (2012). Chemical synthesis and antibacterial activity of novel-shaped silver nanoparticles. *Int. Nano Lett.* 2:9. doi: 10.1186/2228-5326-2-9

Wei, H. (2011). "Plasmonic silver nanoparticles for energy and optoelectronic applications," in *Advances in Nanomaterials and Nanostructures*, eds K. Lu, N. Manjooran, M. Radovic, E. Medvedovski, E. A. Olevsky, C. Li, G. Singh, N. Chopra, G. Pickrell. (Hoboken, NJ: John Wiley and Sons, Inc.), 171–184. doi: 10.1002/9781118144602.ch17

Xiu, Z. M, Zhang, Q. B, Puppala, H. L., Colvin, V. L., and Alvarez, P. J. (2012). Negligible particle-specific antibacterial activity of silver nanoparticles. *Nano Lett.* 12, 4271–4275. doi: 10.1021/nl301934w

Xu, K., Wang, J. X., Kang, X. L., and Chen, J. F. (2009). Fabrication of antibacterial monodispersed Ag-SiO_2 core-shell nanoparticles with high concentration. *Mater. Lett.* 63, 31–33. doi: 10.1016/j.matlet.2008.08.039

Xue, C., Chen, X., Hurst, S. J., and Mirkin, C. A. (2007). Self-assembled monolayer mediated silica coating of silver triangular nanoprisms. *Adv. Mater.* 19, 4071–4074. doi: 10.1002/adma.200701506

Yang, X., Gondikas, A. P., Marinakos, S. M., Auffan, M., Liu, J., Hsu-Kim, H., et al. (2012). Mechanism of silver nanoparticle toxicity is dependent on dissolved silver and surface coating in caenorhabditis elegans. *Environ. Sci. Technol.* 46, 1119–1127. doi: 10.1021/es202417t

Yu, H., Zhang, Q., Liu, H., Dahl, M., Joo, J. B., Li, N., et al. (2014). Thermal synthesis of silver nanoplates revisited: a modified photochemical process. *ACS Nano* 8, 10252–10261. doi: 10.1021/nn503459q

Zhang, Q., Li, N., Goebl, J., Lu, Z., and Yin, Y. (2011). A systematic study of the synthesis of silver nanoplates: is citrate a 'magic' reagent? *J. Am. Chem. Soc.* 133, 18931–18939. doi: 10.1021/ja2080345

Conflict of Interest Statement: The authors declare that the research was conducted in the absence of any commercial or financial relationships that could be construed as a potential conflict of interest.

frontiers in Chemistry

ORIGINAL RESEARCH
published: 27 November 2018
doi: 10.3389/fchem.2018.00554

Engineered Nanostructured Materials for Ofloxacin Delivery

Silvia Nuti[1,2], Javier Fernández-Lodeiro[1,3], Benedetta Del Secco[2], Enrico Rampazzo[2], Benito Rodríguez-González[4], José L. Capelo[1,3], Vanessa Silva[5,6,7,8], Gilberto Igrejas[5,6,8], Patrícia Poeta[7,8], Cármen Torres[9], Nelsi Zaccheroni[2], Luca Prodi[2], Elisabete Oliveira[1,3]* and Carlos Lodeiro[1,3]**

[1] BIOSCOPE Group, LAQV@REQUIMTE, Chemistry Department, Faculty of Science and Technology, NOVA University of Lisbon, Almada, Portugal, [2] G. Ciamician Department of Chemistry, University of Bologna, Bologna, Italy, [3] Proteomass Scientific Society, Costa de Caparica, Portugal, [4] Scientific and Technological Research Assistance Centre (CACTI), University of Vigo, Vigo, Spain, [5] Department of Genetics and Biotechnology, University of Trás-os-Montes and Alto Douro, Vila Real, Portugal, [6] Functional Genomics and Proteomics Unit, University of Trás-os-Montes and Alto Douro, Vila Real, Portugal, [7] Veterinary Science Department, University of Trás-os-Montes and Alto Douro, Vila Real, Portugal, [8] LAQV-REQUIMTE, Faculty of Science and Technology, Nova University of Lisbon, Lisbon, Portugal, [9] Área de Bioquímica y Biología Molecular, Universidad de La Rioja, Logroño, Spain

OPEN ACCESS

Edited by:
Xiaomin Li,
Fudan University, China

Reviewed by:
Chun Xu,
The University of Queensland, Australia
Teng Long,
Shanghai JiaoTong University School of Medicine, China

***Correspondence:**
Luca Prodi
luca.prodi@unibo.it
Elisabete Oliveira
ej.oliveira@fct.unl.pt
Carlos Lodeiro
cle@fct.unl.pt

Specialty section:
This article was submitted to Nanoscience, a section of the journal Frontiers in Chemistry

Received: *21 August 2018*
Accepted: *29 October 2018*
Published: *27 November 2018*

Citation:
Nuti S, Fernández-Lodeiro J, Del Secco B, Rampazzo E, Rodríguez-González B, Capelo JL, Silva V, Igrejas G, Poeta P, Torres C, Zaccheroni N, Prodi L, Oliveira E and Lodeiro C (2018) Engineered Nanostructured Materials for Ofloxacin Delivery. Front. Chem. 6:554. doi: 10.3389/fchem.2018.00554

Antibiotic resistance is emerging as a growing worldwide problem and finding solutions to this issue is becoming a new challenge for scientists. As the development of new drugs slowed down, advances in nanotechnology offer great opportunities, with the possibility of designing new systems for carrying, delivery and administration of drugs already in use. Engineered combinations of the synthetic, broad-spectrum antibiotic ofloxacin, rarely studied in this field, with different types of silver, mesoporous silica-based and Pluronic/silica-based nanoparticles have been explored. The nanocarriers as silver core@silica mesoporous (AgMSNPs) and dye-doped silica nanoparticles functionalized with ofloxacin were synthesized and their antibacterial properties studied against *S. aureus* and *E. coli*. The best antibacterial results were obtained for the AgMSNPs nanosystem@ofloxacin for the strain *S. aureus* ATCC 25923, with MIC and MBC values of 5 and 25 μg/mL, proving the efficacy and synergetic effect of the antibiotic and the Ag core of the nanoparticles.

Keywords: mesoporous silica nanoparticles, silver nanoparticles, ofloxacin, bacteria, antibiotics

INTRODUCTION

Antibiotics are one of the most important discoveries in modern medicine, because of their significant contribution in reducing the mortality and morbidity determined by infectious diseases. In the years ranging from 1945 to 1960 a lot of new antibiotics, still in use, were discovered and characterized (Wright, 2007).

Massive and often indiscriminate use of antibiotics has led to a dramatic increase in manifestations of antibiotic resistance (Wright, 2007). Antibiotic resistance is present for example in hospitals, where significant quantities of drugs are used, or in countries where antibiotics were available without a prescription or medical advice (Levy and Marshall, 2004; Andersson and Hughes, 2010). Moreover, the use of sub-lethal doses of an antibiotic can end up in manifestations of multidrug resistance (MDR) (Kohanski et al., 2010). The most common bacterial infections that require hospitalization are caused by *Staphylococcus aureus* (*S. aureus*), followed by *Escherichia coli* (*E. coli*) (Sen Karaman et al., 2016).

Bacteria can develop antibiotic resistance with a variety of mechanisms such as horizontal gene transfer mechanism, which enables bacteria to "share" resistant gene sequences (Davies, 1994).

Bactericidal antibiotics as quinolones are often used as last chance when no other therapy is effective, but they can induce bacteria to produce reactive oxygen species (ROS) (Dwyer et al., 2007), causing DNA damage and mutations accumulation (Kohanski et al., 2010).

Antibiotic resistance poses several problems regarding public health, and it lowers the possibility of treating the infection and increases the possibility of a deadly outcome.

Aware of this problem, there is an increased need for the development of new platforms for overcoming antibiotic resistance (Pelgrift and Friedman, 2013). Antibacterial nanomaterials have been proved to be very efficient against antimicrobial resistance, allowing effective delivery of the antibiotics (Pelgrift and Friedman, 2013). In this framework, many different nanomaterials have been investigated and reported as carrier for antibiotics, in particular, metal-based nanocarriers (silver, zinc, titanium and gold nanoparticles), polymeric and silica nanoparticles. However, the synthesis and preparation of some of these nanocarriers could represent a drawback being more cost-effective than that of antibiotics (Zhang et al., 2010; Li et al., 2011; Tang et al., 2012; Webster and Seil, 2012; Bagga et al., 2017).

In this paper, we present a study on the combination of the most promising nanocarriers (silver and silica-based ones), for ofloxacin loading and release against Gram-positive and Gram-negative bacteria.

Silver nanoparticles (AgNPs) are known for their broader spectrum of antibacterial activity, in comparison to other metal nanoparticles, but they can undergo degradation and slow release of silver ions. It is possible, however, to prevent this inconvenience by incorporating them within silica nanoparticles, leading to more effective nanocarriers with a wider range of antibacterial applications than bare AgNPs (Guzman et al., 2012; Le Ouay and Stellacci, 2015; Tang and Zheng, 2018).

We chose to use the antibiotic ofloxacin (9-fluoro-3-methyl-10-(4-methyl-1 -piperazinyl)- 7-oxo-2, 3-dihydro-7H-pyrido-(1, 2, 3-de)l, 4-benzoxazine-6-carboxylic) in our studies since it is active against Gram-positive, Gram-negative, and anaerobes bacteria (Sato et al., 1982). The activity of ofloxacin against *Enterobacteriaceae, Pseudomonas aeruginosa, Haemophilus influenzae, Neisseria gonorrhoeae, and Clostridium perfringens* is comparable to that of norfloxacin and far exceeds that of pipemidic and nalidixic acids. Some Gram-positive bacteria belonging to *Staphylococcus* spp. and *Streptococcus* spp., which are resistant to nalidixic acid, are instead susceptible to norfloxacin and ofloxacin, which provide a better bactericidal activity (Sato et al., 1982).

Recently Ding et al. reported on the antibacterial activity against two strains of *Pseudomonas aeruginosa* (WT and ΔABM) of AgNPs with three different sizes and all covalently functionalized with ofloxacin (Ding et al., 2018). They found that the inhibitory effect of ofloxacin is highly dependent on the concentration and size of the nanocarrier. The lowest MIC (Minimum Inhibitory Concentration) values ($0.11 \pm 0.01\,\mu M$ for WT and $0.010 \pm 0.001\,\mu M$ for ΔABM) were obtained for the largest nanocarrier conjugated with 6.5×10^5 ofloxacin molecules/nanoparticle against the free ofloxacin [$0.59 \pm 0.16\,\mu M$ for WT and $0.096 \pm 0.096\,\mu M$ for ΔABM; (Ding et al., 2018)].

Despite the tremendous antibacterial properties of AgNPs, silica nanoparticles (SNPs) are also very promising nanomaterials due to their versatility, chemical and thermal stability (He and Shi, 2011; Tang et al., 2012). Silica nanoparticles and in particular mesoporous silica nanoparticles (MSNPs), in fact, are very often applied in the biomedical field, both in diagnosis and therapeutics, while examples of their use as antibacterial agents are much more seldom (Tang et al., 2012). High surface and pore volume of MSNPs allow the loading of several antibiotics, leaving their surface free and adaptable for a better cell internalization, leading to the creation of a new generation of antibacterial agents with improved synergistic effects (Tang et al., 2012). Moreover, surface functionalization allows better control of antibiotic release (Bhattacharyya et al., 2012). Recently, an antibacterial study of mesoporous silica nanoparticles with silver ion doping and chitosan surface coating was carried out against *E. coli,* and *V. cholera* and an efficacy improvement were achieved by the synergistic antibacterial effect of MSNPs combined with kanamycin (Sen Karaman et al., 2016). To the best of our knowledge, we present here for the first-time silver core @ silica mesoporous and dye-doped silica nanocarriers functionalized with ofloxacin, as well as, the study of their antibacterial properties against *S. aureus* and *E. coli*.

MATERIALS AND METHODS

Chemicals

1,6-diaminohexane (98%), Acetic Acid (HOAc ≥ 99.7%), Acetone, Borate Buffered Saline (tablets), Dichloromethane (DCM, reagent grade), Diethyl Ether, Dimethylformamide (DMF, reagent grade), Ethyl Ether (reagent grade), Hydrochloric Acid (≥37%), Hydrogen Peroxide (30%), N-Hydroxysulfosuccinimide sodium salt (NHS-Sulfo), N-N'-disuccinimidyl carbonate (DSC, ≥98%), Ofloxacin, Phosphate Buffered Saline (tablets), Pluronic F-127, Rhodamine B base (≥98%), Silver Nitrate (99%), Sodium Borohydride (99%), Sodium Citrate tribasic dehydrate (99%), Tetraethyl Orthosilicate (TEOS, 99.99%), Tetrahydrofuran (THF), Trimethylchlorosilane (TMSCl, ≥98%), Toluene were purchased from Sigma Aldrich. 3-(triethoxysilyl)propyl isocyanate (≥95%), Sodium Chloride, Piperazine (≥98%), Triethylamine (≥99.5 %) were purchased from Fluka. Absolute Ethanol, Dimethyl Sulfoxide (DMSO), Ethylene Glycol were purchased from Carlo Erba Reagents. Ammonium Nitrate, Hexadecyltrimethylammonium bromide (CTAB, 98%) were purchased from Alfa Aesar. Potassium Bromide and Sodium Hydroxide were purchased from Panreac. All reagents were used without further purification.

Instrumentation and Characterization Techniques

Absorption spectra were acquired using the spectrophotometers JASCO V-630, JASCO V-650, and emission and excitation spectra were acquired using a spectrofluorometer Horiba-Jobin-Yvon Flouromax-4, from the PROTEOMASS-BIOSCOPE Facility at the Chemistry Department of the FCT-UNL, Portugal, and a spectrofluorometer Perkin Elmer LS55 (University of Bologna—Italy). The size, size distribution and the zeta potential of the nanoparticles were evaluated via Dynamic Light Scattering (DLS) using a Malvern Zetasizer Nano ZS equipped with a He-Ne laser source (633 nm, 5 mW), from the PROTEOMASS-BIOSCOPE Facility at the Chemistry Department of the FCT-UNL, Portugal.

Freeze drying of AgMSNPs with ofloxacin was achieved using a Christ Alpha 1-2 LD Plus, from the PROTEOMASS-BIOSCOPE Facility at the Chemistry Department of the FCT-UNL, Portugal. NPs were dried over 24 h.

TEM images were acquired using a JEOL JEM 1010 working at 100 kV at the Centro de Apoyo Científico y Tecnológico a la Investigación (CACTI), University of Vigo, Spain.

Scanning electron micrographs (SEM) were obtained with a high-resolution SEM-FIB microscope Zeiss Auriga CrossBeam System, CENIMAT—FCT-UNL.

The lifetime measurements were performed in a Horiba Jobin-Yvon Tempro, from the PROTEOMASS-BIOSCOPE Facility at the Chemistry Department of the FCT-UNL, Portugal.

Pore size distribution and surface area determination result from the measurement of N_2 adsorption/desorption, at 77 K, in a Micromeritics ASAP 2010 (Accelerated Surface Area and Porosimetry), at the Laboratory of Analysis from FCT - UNL. The specific surface areas (S_{BET}) were calculated from the adsorption data in the low pressures range using the BET model. Pore size was determined following the BJH (Barrett-Joyner-Halenda analysis) method.

The fluorescence quantum yield (Montalti et al., 2006) of dye-doped silica nanoparticles was measured using as standard rhodamine B ($\varphi = 0.70$) (Arbeloa et al., 1989) in ethanol and calculated using equation (1).

$$\Phi_S = \Phi_{std}(I_s/I_{std})(n_s/n_{std})^2 \quad (1)$$

Where Φ_S and Φ_{std} are the radiative quantum yields of the sample and standard respectively, n_s and n_{std} are the refractive indexes (respectively, pure solvents were assumed), I_s and I_{std} the emission areas. The sample and the standard were excited at the same wavelength in an isosbestic point.

Synthesis of Nanoparticles

Synthesis of Silver Nanoparticles (AgNPs)

The AgNPs with spherical shape were synthesized using the method proposed by Frank et al. (2010). In a round bottom flask were added, 2.0 mL of a solution 1.25×10^{-2} M of sodium citrate, 5.0 mL of a solution 3.75×10^{-4} M of silver nitrate, 5.0 mL of a solution 5.0×10^{-2} M of hydrogen peroxide, 40 μL of a solution 1.0×10^{-3} M of potassium bromide in MilliQ water. The mixture was gently stirred for approximately 3 min, until a yellow color was observed. The solution of AgNPs was finally stored at 4°C.

Synthesis of Mesoporous Silica Nanoparticles (MSNPs)

MSNPs were synthesized in aqueous media, using TEOS as silica precursor, according to the following protocol published by E. Oliveira et al. (2018). Briefly, 100 mg of CTAB ($CH_3(CH_2)_{15}N(Br)(CH_3)_3$ were dissolved in 10 mL of H_2O MilliQ, stirred and heated to about 50°C. To this solution were added 30 mL of H_2O MilliQ, 10 mL of ethylene glycol and 157 μL of a 0.95 M aqueous solution of NaOH. This mixture was stirred at 70°C for 30 min, then 750 μL of TEOS were added drop wise and left stirring at 70°C for 3 more hours.

The template was removed by the addition of ammonium nitrate in ethanol at 60°C (Zhang et al., 2011). The final mesoporous nanoparticles were washed several times with water and ethanol and left to dry at room temperature (r.t.).

Synthesis of Silver Core- Mesoporous Silica Shell Nanoparticles (AgMSNPs)

For the synthesis of silver core-mesoporous silica shell nanoparticles, approximately 10 mL of AgNPs solution, obtained with the Frank method (Frank et al., 2010), were added in the first phase of the synthesis of mesoporous silica nanoparticles.

The template removal and the final washing were performed with a solution of NH_4NO_3 in EtOH.

PDMAC (Poly(diallyldimethylammonium chloride) covering

The covering was applied on 10 mg of NPs using 20 μL of a PDMAC solution 10 mg/mL in a total volume of 2 mL of MilliQ water. After 2 h stirring at r.t. the solution was centrifuged and washed 7 times with 2 mL of MilliQ water (10,000 rpm, 15 minutes), then finally resuspended in 2 mL of MilliQ water. The size and zeta potential measurements were conducted on 0.5 mL of the previous solution diluted in 1.5 mL of MilliQ water.

The final mesoporous nanoparticles were obtained as a powder, and characterized by TEM, SEM, DLS, ICP and N_2 isotherms.

Synthesis of Dye-Doped Silica Nanoparticles (SNPS)

Pluronic F127 derivatives, the triethoxysilane derivative of Rhodamine B and dye-doped silica NPs, presenting $-NH_2$ functional groups (NPs-NH_2), were synthesized following procedures previously reported (Rampazzo et al., 2010, 2013). The final nanostructure was then conjugated to ofloxacin as described hereafter.

Synthesis of Pluronic F-127-amino

Synthesis of Pluronic F-127-carbonate Pluronic F127-carbonate was synthesized (**Scheme 1**) adapting reported procedures (Rampazzo et al., 2013). A toluene solution of Pluronic F127 (4.01 g, 100 mL) was distilled under reduced pressure at 50–60°C in a 250 mL round bottom flask. The residue was dried under vacuum and solubilized in 15 mL of dry THF. To this solution first 0.80 g of N,N'- disuccinimidyl carbonate was added in 7.0 mL of acetone and then 0.41 g of 4-(Dimethylamino)pyridine (DMAP, 99%) were slowly added by a dropping funnel at room temperature and under stirring. After

12 h, Pluronic F127-carbonate was precipitated with ethyl ether and recovered after circa 20 h of dialysis vs. MilliQ water, in regenerated cellulose dialysis tubing (Sigma, 12 kDa cut-off) under gentle stirring. The dialyzed solution was centrifugated at 7,000 rpm using 50 mL plastic falcon vials with acetone and finally dried under vacuum and directly used for amine functionalization.

Synthesis of Pluronic F-127-amino Pluronic F127-amino was synthesized (**Scheme 2**) adapting reported procedures (Rampazzo et al., 2013). In a flamed 100 mL round bottom flask dried under vacuum, 1.9 g of 1,6-diaminopropane were solubilized with 10 mL of dry dichloromethane. 10 mL of a dichloromethane solution containing 2.0 g of F127-carbonate was then slowly added under stirring at room temperature. After 3 h the reaction mixture was distilled under reduced pressure and the residue was solubilized with 20 mL of water. The resulting solution was dialyzed vs. MilliQ water, for about 20 h, in regenerated cellulose dialysis tubing (Sigma, 12 kDa cut-off) under gentle stirring. The dialyzed solution was evaporated under reduced pressure and finally dried under vacuum.

Synthesis of the triethoxysilane derivative of Rhodamine B (R)

Synthesis of the tertiary amide from Rhodamine B base The tertiary amide **1** (**Scheme 3**) was obtained from Rhodamine B base following a previously reported procedure by Nguyen and Francis (Nguyen and Francis, 2003).

*Synthesis of the triethoxysilane derivative of Rhodamine B **(R)**.* In a dried flask under N_2 atmosphere, 500 mg of the tertiary amide **1** and 2.02 mL of triethylamine were dissolved in 7.5 mL of anhydrous DMF. 6.77 mL of 3-(triethoxysilyl)propyl isocyanatin in 10 mL of CH_2Cl_2 were added dropwise to this solution, at room temperature under stirring. After 12 h, the reaction mixture was dried under reduced pressure. We solubilized the obtained solid adding the minimal amount of EtOH and then we precipitated it by dropwise addition of a large volume (∼300 mL) of Et_2O. The resulting heterogeneous mixture was cooled under gentle stirring and the product was obtained by filtration under reduced pressure. The retained dark red-purple solid was rinsed with Et_2O and recrystallized with EtOH/Et_2O. The product **R** was obtained by filtration as a dark red-purple solid (**Scheme 3**).

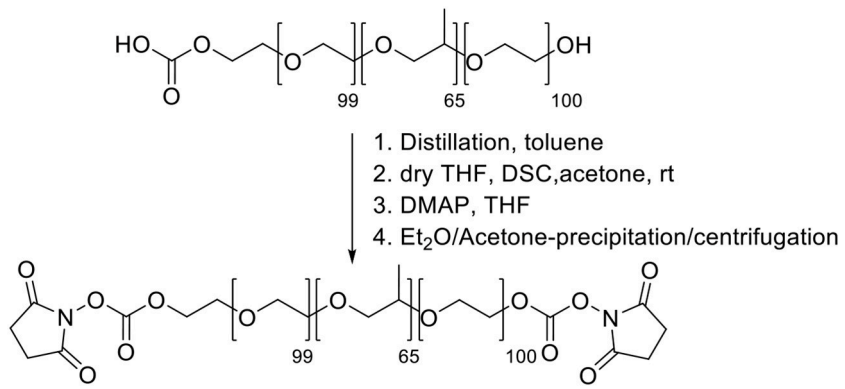

SCHEME 1 | Synthesis of Pluronic F127-carbonate.

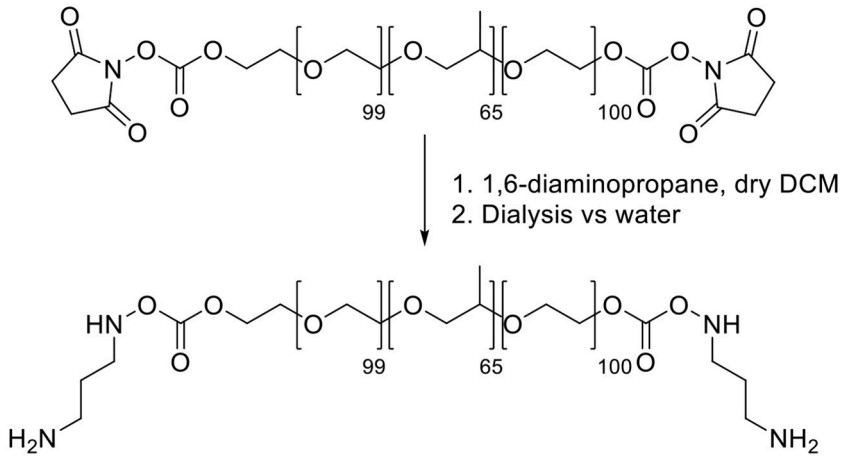

SCHEME 2 | Synthesis of Pluronic F127-amino.

Synthesis of dye-doped silica nanoparticles

Dye-doped silica NPs, presenting $-NH_2$ functional groups at the surface were prepared following the synthesis sketched in **Scheme 4**. 140 mg of Pluronic F127, 60 mg of Pluronic F127-amino and 3.60 mg of the triethoxysilane derivative of Rhodamine B were carefully solubilized with 1 mL of dichloromethane in a 20 mL glass scintillation vial.

The solvent was evaporated from the homogeneous solution by means of a gentle nitrogen flow and subsequently under vacuum at room temperature. One hundred and thirty seven milligram of NaCl were subsequently added, and the mixture was solubilized at 30°C under magnetic stirring with 3.1 mL of CH_3COOH 1M. 360 µL of TEOS were added to the solution and reacted for 3 h then 20 µL of TMSCl were added. The mixture was kept under stirring for 20 h at 30°C. The purification was carried out by dialysis vs. MilliQ water, during approximately 48 h, in regenerated cellulose dialysis tubing (Sigma, 12 kDa cut-off) at RT under gentle stirring (Montalti et al., 2014).

Encapsulation and Functionalization of Ofloxacin Into Nanoparticles

The interaction of AgNPs with ofloxacin was studied by mean of spectrophotometric titrations and in batch mode for 24 h incubations.

Ofloxacin was encapsulated in MSNPs and AgMSNPs stirring for 24 h at room temperature and dark conditions. The encapsulation was conducted in DMSO for MSNPs and both in DMSO and PBS pH 7.4 for AgMSNPs.

The encapsulation percentage (%E) was evaluated after centrifuging NPs (MSNPs and AgMSNPs; 5 min, 10,000 rpm) and acquiring the absorption spectra of the supernatant. Encapsulation percentage (% E) final values were calculated through the following equation (2).

$$E\,(\%) = \frac{C_i - C_e}{C_i} \times 100\% \quad (2)$$

Where, C_i (M) is the initial concentration of ofloxacin, C_e (M) is the concentration of the ofloxacin in the supernatant.

Ofloxacin was covalently linked to the dye-doped SNPs terminal amine groups according to the following protocol: a 0.03 M aqueous solution of ofloxacin was mixed with 304 µL of a 0.2 M aqueous solution of Sulfo-NHS and with 152 µL of a 0.2 M aqueous solution of EDC-HCl, this mixture was stirred for 30 min a room temperature with the aid of a vortex. To this mixture, we added 3.36 mL of a solution of NPs and the solution was stirred for 12 h at room temperature. The coupling procedure was carried out in 10.0 mL of borate buffer (0.05 M, pH 9.0; **Scheme 5**). The resulting solution was dialyzed vs. MilliQ water, for about 20 h (regenerated cellulose dialysis tubing Sigma, 10 kDa cut-off).

Bactericidal Activity Test

Bacterial Strains, Culture Media, and Growth Conditions

Bacterial strains considered in this study were *E. coli* C999 and *S. aureus* C5932 both resistant to ofloxacin, and the control strains *E. coli* ATCC 29425 and *S. aureus* ATCC 25923, both sensitive to ofloxacin (**Table 1**). The strains were supplied by the University of La Rioja and University of Trás-os-Montes and Alto Douro collection. All bacterial strains were grown in BHI agar (Oxoid, UK) for 24 h at 37°C.

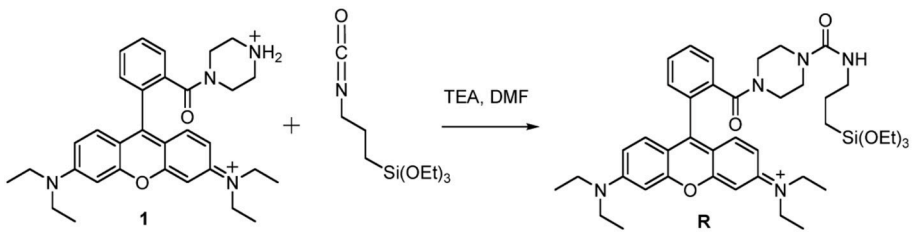

SCHEME 3 | Synthesis of Silanized Rhodamine B.

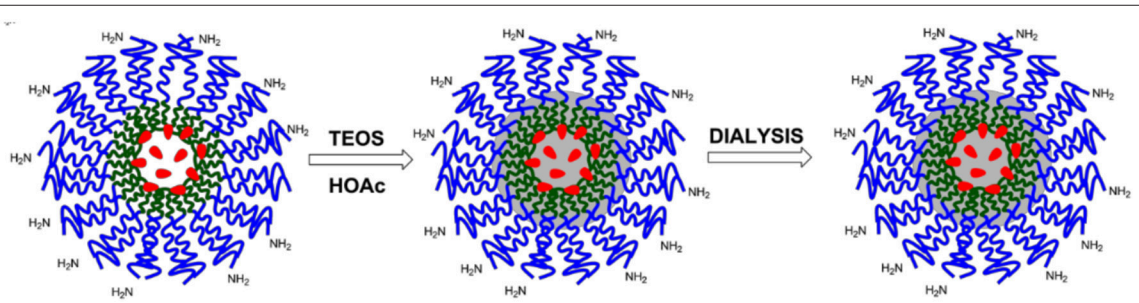

SCHEME 4 | Schematization of the synthesis of SNPs-NH_2.

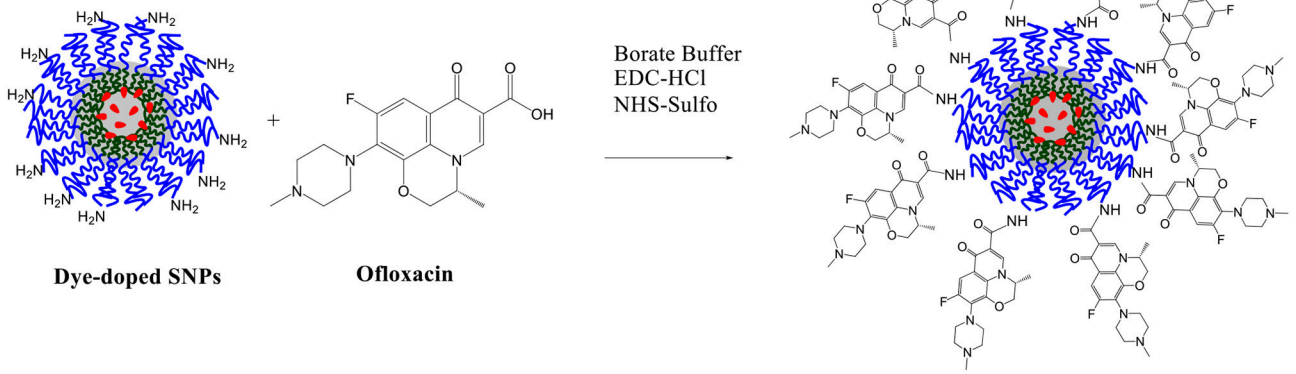

SCHEME 5 | Functionalization of dye-doped SNPs with ofloxacin.

Preparation of Stock Solutions

Each solution containing NPs (MSNPs, AgMSNPs, and Dye-doped SNPs) was diluted to final concentrations of 1, 10, 25, 50, 75, 100, 150, 200, 300, and 500 μg/mL in DMSO, and tested on all bacteria. Ofloxacin was tested in the range 1–500 μg/mL. As a control sample, the DMSO was also tested.

Antibacterial Susceptibility Test

The minimum inhibitory concentration (MIC), described as the lowest concentration of nanoparticles that inhibits the bacterial growth, was determined by broth-dilution method using a 96-well polystyrene microtiter plate. Luria-Bertani (LB) (Sigma–Adrich) broth was prepared and 135 μL were added to each well. Ten microliters of each solution containing different NPs with final concentrations ranging from 1 to 500 μg/mL were added to each well and 10 μL of overnight cultures of the selected bacteria were inoculated into the wells and incubated at 37°C. After 24 h, we measured the absorbance with a microplate spectrophotometer. The test was performed in triplicate. Positive and negative controls were performed using ofloxacin, Ag@MSNPs, MSNPs and DMSO.

To determine the minimum bactericidal concentration (MBC), which is characterized by no bacterial growth, 100 μL of the cultures resulting from MIC testing were inoculated onto LB medium plates and incubated at 37°C for 20 h. Control cultures without NPs were included in all experiments. The number of colony-forming units (CFUs) was determined by plate counting for each concentration and each sample.

RESULTS AND DISCUSSION

Synthesis of Silver Nanoparticles and Interaction With Ofloxacin

Silver nanoparticles (AgNPs) were synthesized following the Frank method (Frank et al., 2010), and characterized by UV-Vis absorption measurements and DLS to determine their size and zeta potential. Diluting 1 mL of AgNPs obtained from the synthesis with 1.5 mL of MilliQ water a yellow solution was obtained with an absorption spectrum showing a plasmonic band at ca. 400 nm (**Figure 1**).

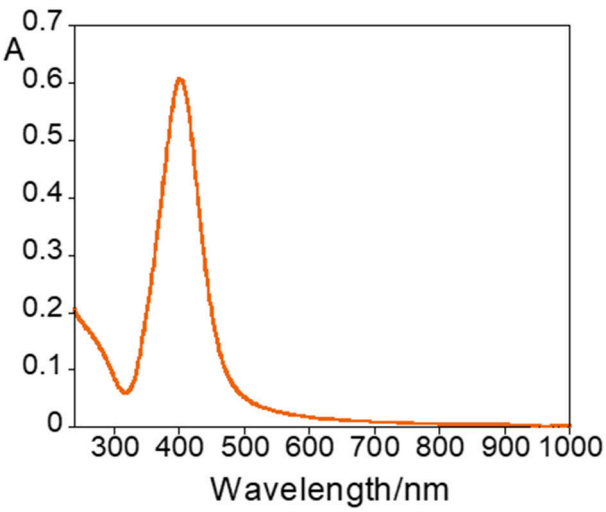

FIGURE 1 | Absorption spectra of AgNPs.

The average values of the hydrodynamic diameter, PDI and zeta potential were of 57 ± 30 nm, 0.3 ± 0.1 and −40 ± 4 mV, respectively, for $n = 13$ (n = number of replicates). In general, the AgNPs are very stable due to their high negative zeta potential.

The interaction with ofloxacin was initially studied by means of spectrophotometric titration. To 2.5 mL of aqueous AgNPs solution, obtained from the Frank method synthesis, a solution of 1 mg/mL of ofloxacin was added in 2 μL aliquots until a total of 78 μL was added, corresponding to a final concentration of 0.03 mg/mL

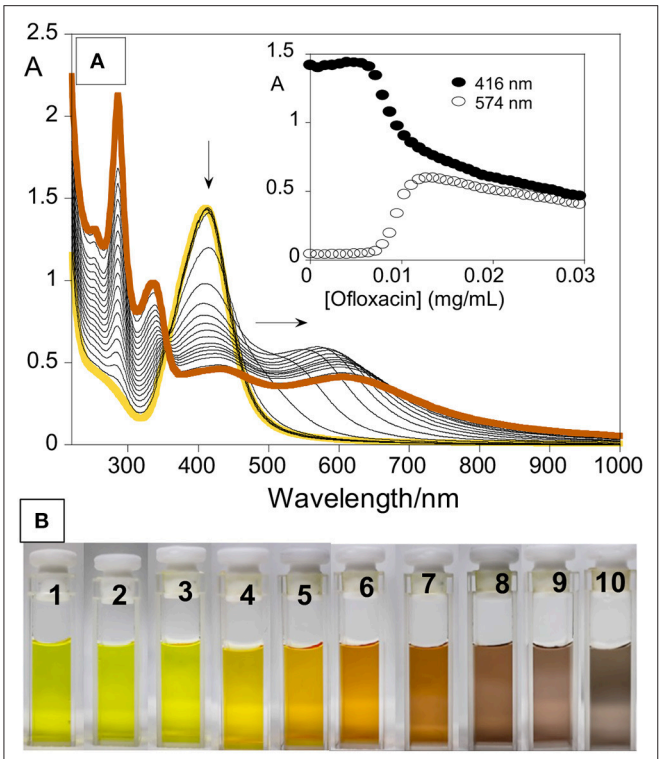

FIGURE 2 | (A) Spectrophotometric titration of AgNPs with increasing amounts of ofloxacin in water. Inset represents the absorption as a function of ofloxacin concentration (mg/mL) at 416 nm and 574 nm. **(B)** Naked-eye colorimetric response of AgNPs with increasing amount of ofloxacin; 1–0, 2–2, 3–14, 4–22, 5–26, 6–30, 7–34, 8–38, 9–42, 10–46 μL from a stock solution of ofloxacin (1 mg/mL).

During the titration, a redshift of the resonance plasmon band from 400 to 574 nm, was observed (**Figure 2A**), but the nanoparticles did not stabilize and precipitate after 2 h. The broadening and shift toward lower energies of the absorption band are very reasonable due to the nanoparticle surface exchange of the labile citrate molecules with ofloxacin, via its carboxylic group. Ofloxacin is a large organic molecule that is not able to efficiently protect the metal surface of the NP and, as well-known and documented when the surface coverage is inefficient metal particles aggregate and precipitate. The evolution of the AgNPs@ofloxacin interaction was denoted by a clearly visible change in the color of the solution (**Figure 2B**): from the characteristic yellow color of a spherical AgNPs solution (**Figure 2B**; 1-3) to orange (**Figure 2B**; 4-6), brown (**Figure 2B**;7-9), and finally gray (**Figure 2B**; 10).

Following abovementioned results, the AgNPs were incubated for 24 h with different amounts of 1 mg/mL ofloxacin solution (30, 15, 45, 78 μL). Immediately after the addition of the antibiotic solution a change in the color was observed (**Figure 3**). After 24 h stirring at r.t. and in dark environment conditions all solutions were colorless and transparent and a dark precipitate was formed, the nanoparticles aggregated and precipitated.

Synthesis and Characterization of MSNPs and AgMSNPs

Silver mesoporous nanoparticles were obtained by encapsulation of AgNPs inside a silica matrix to generate mesoporous nanoparticles. In this synthesis, TEOS was used as a silica source, CTAB as template and cationic surfactant, ethylene glycol as stabilizer and NaOH as a morphological agent. This approach was based on MCM-41 synthesis (Kresge et al., 1992; Oliveira et al., 2018), and different amounts of TEOS (250 μL−1mL) were tested in order to find the most stable system. As a control, mesoporous silica nanoparticles (MSNPs) were also obtained but without the silver nanoparticle core. As expected both systems were of spherical shape: MSNPs and AgMSNPs were obtained as a powder, and were characterized by dynamic light scattering (size and zeta potential), TEM, SEM, ICP, and N_2 isotherms (**Figure 4**).

Concerning the MSNPs, they were characterized from a zeta potential point of view to choose the most stable batch to proceed with encapsulation of ofloxacin. The measure was conducted solubilizing 1 mg of nanoparticles in 1.5 mL of DMSO and using a dip cell for the measurement of the zeta potential. The average value is −30.8 ± 0.3 mV. TEM images reveal high porosity of the MSNPs, as can be seen by the white dots, showing an average diameter of 80 ± 11 nm (**Figure 4C**).

In the synthesis of AgMSNPs different quantities of TEOS were used to find the amount that leads to the most stable particles, for subsequent ofloxacin encapsulation. The AgMSNPs obtained were characterized by DLS measurements for size and zeta potential (see **Table 2**).

The AgMSNPs synthesized with 500 μL of TEOS turned out to be the most stable, presenting the most negative zeta potential (−44 mV). AgMSNPs (500 μL TEOS) were also covered with PDMAC, a polyelectrolyte, to improve their solubility and reduce their aggregation. Size and zeta potential measurements were conducted; the results revealed a decrease in size (from 430 ± 180 nm to 270 ± 40 nm) and PDI (from 0.9 ± 0.1 to 0.24 ± 0.01), and as expected a total inversion of the zeta potential (from −44.1 ± 1.6 to +47.7 ± 0.9 mV), confirming the total surface coverage by the polyelectrolyte and the higher stability in water. As can be seen in TEM images AgMSNPs have a silver core with a silica shell, having a total average radius of 92 ± 12 nm (**Figure 4F**). ICP confirmed the silver core nature and the amount of 2,879 ppm of silver was determined, with a ratio of 2.8 mg of Ag per gram of nanoparticles. The size and the spherical shape were also confirmed by SEM studies (**Figure 4D**).

Moreover, AgMSNPs showed nitrogen adsorption-desorption type IV isotherms of ordered mesoporous with an adsorption step behavior at p/p^0 around 0.30–0.35. Surface area, pore size and pore volume were assessed using Brunauer-Emmett-Teller (BET) and Barrett-Joyner-Halenda (BJH) theories (data in **Table 3**). From these curves pore volumes of 1.2 cm^3/g were calculated by the BJH model for AgMSNPs, on the adsorption branch of the isotherm. Through the application of the BET model, the average pore width and surface area were also estimated and resulted in 52 Å and 759 m^2/g, respectively. Besides, the presence of mesoporosity in the

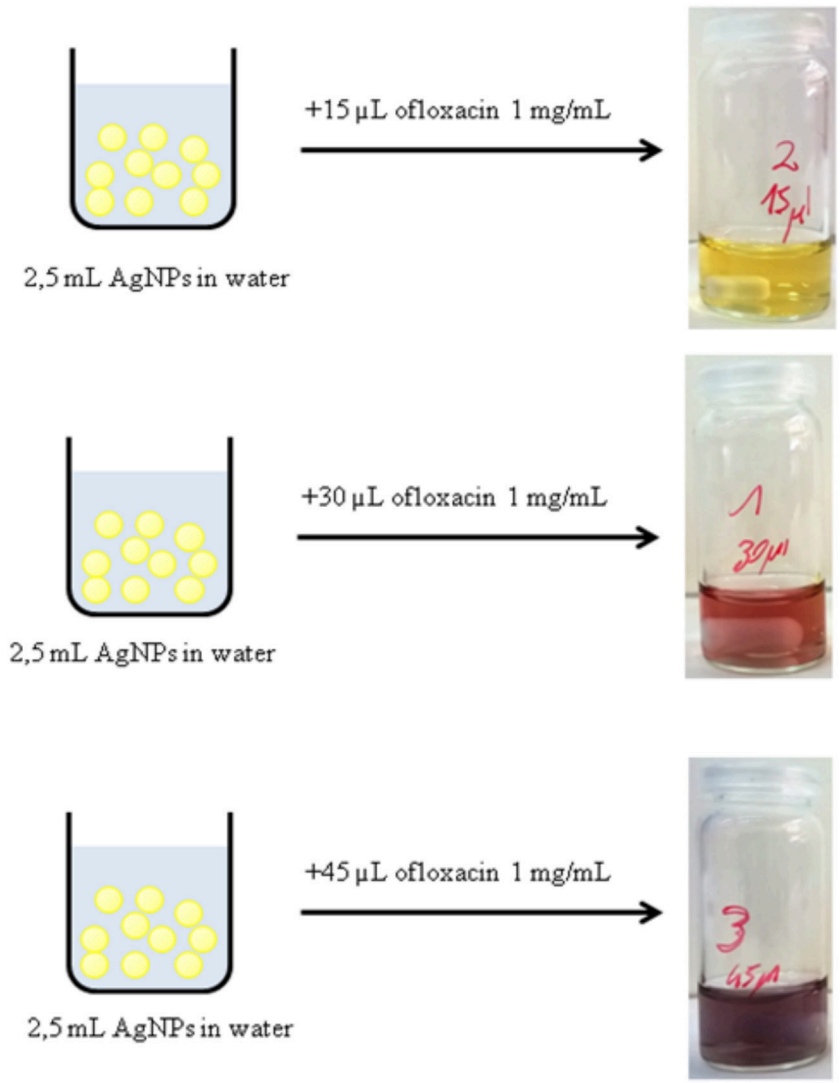

FIGURE 3 | Immediate color change of a solution of AgNPs after the addition of different amounts of a solution 1 mg/mL of ofloxacin.

synthesized systems, the BET surface areas are slightly lower than the traditional MCM-41 mesoporous nanoparticles [1110 ± 2 m^2/g; (Huang et al., 2014)], which is compatible with the presence of the silver nanoparticles forming the core of these nanosystems.

Encapsulation of Ofloxacin Into MSNPs and AgMSNPs

Ofloxacin loading was evaluated after 24 h incubations of 1 mL of a solution of ofloxacin in DMSO and PBS pH 7.4 at various concentrations with approximately 4.5–5 mg of MSNPs or AgMSNPs. After incubation, the nanoparticles were centrifuged, and the supernatant was collected to perform absorption measurements and calculate the encapsulation percentages accordingly with equation (2) (section Encapsulation and functionalization of ofloxacin into nanoparticles; **Table 4**).

As a control, a solution of free ofloxacin 1×10^{-5} M was characterized in DMSO, PBS pH 7.4 and PBS pH 5.0 (**Figure 5**). Absorption, emission and excitation spectra of ofloxacin were collected at r.t and in DMSO it presents an absorption maximum at 300 nm with a shoulder at ca. 350 nm and an emission maximum at 450 nm (**Figure 5A**).

Concerning further applications in biological media, the ofloxacin was characterized by absorption and emission in PBS pH 7.4 and PBS pH 5.0. In PBS pH 5.0 (**Figure 5B**) ofloxacin exhibits an absorption band with the maximum centered at 293 nm and a shoulder at 330 nm, in the emission spectra the maximum is at 500 nm.

In PBS pH 7.4 (**Figure 5B**) ofloxacin exhibits an absorption band slightly different from the one in PBS pH 5.0, with the maximum centered at 286 nm and a shoulder at 300 nm, in the emission spectra the maximum is also shifted to 456 nm.

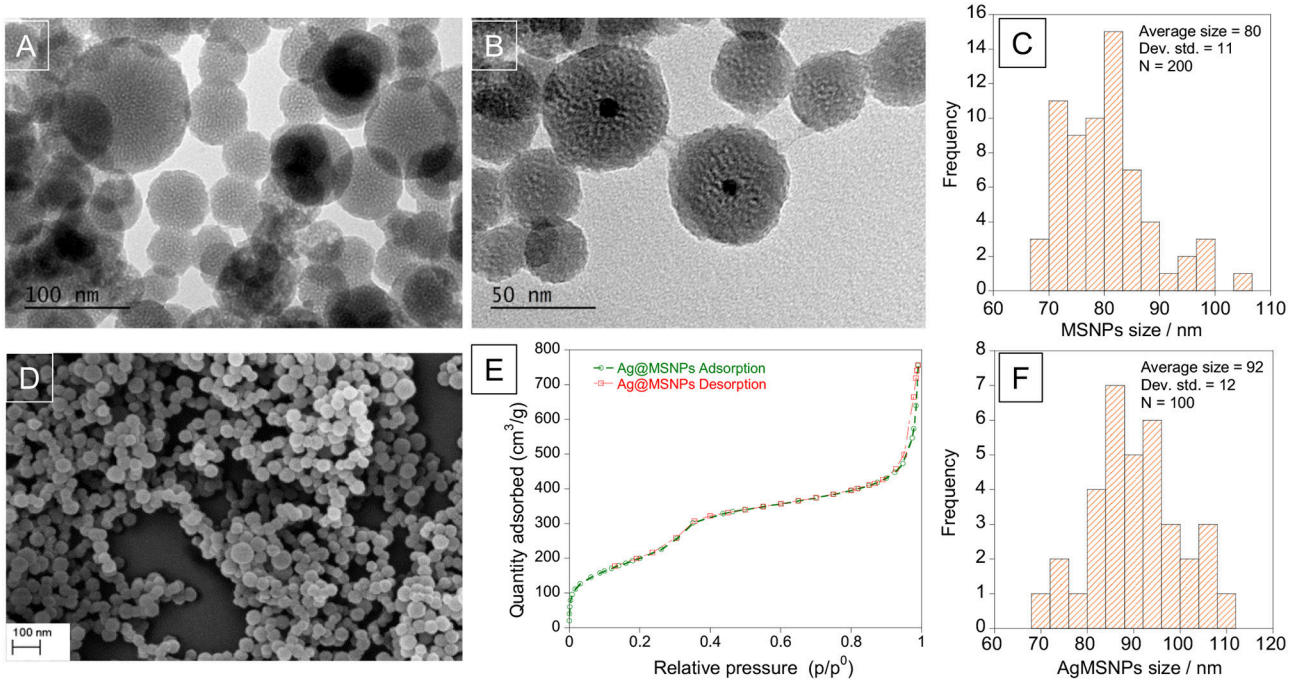

FIGURE 4 | TEM images of mesoporous silica nanoparticles, MSNPs **(A)** and silver doped mesoporous silica nanoparticles, AgMSNPs **(B)**, SEM image **(D)**, and Nitrogen isotherms **(E)** of AgMSNPs. Size distribution histograms of MSNPs **(C)** and AgMSNPs **(F)**.

TABLE 1 | Bacterial strains used in this study.

Strain	Relevant phenotype	Reference
E. coli K12 ATCC 29425	Non-pathogenic, Gram-negative; sensitive to ofloxacin	ATCC
E. coli C999 (CTX-M-15)	Pathogenic, Gram-negative; resistant to ofloxacin	Ruiz et al., 2012
S. aureus ATCC 25923	Gram-positive, sensitive to ofloxacin	ATCC
S. aureus C5932 (MRSA CC398)	Non-pathogenic, Gram-positive, resistant to ofloxacin	Benito et al., 2014

TABLE 2 | Results for the size and ζ potential characterization of AgMSNPs.

TEOS amount	Hydrodynamic diameter (nm)	PDI	Zeta potential (mV)
250 μL	267 ± 47	0.89 ± 0.18	−36.67 ± 1.02
500 μL	433 ± 181	0.9 ± 0.1	−44.12 ± 1.64
750 μL	416 ± 251	1	−41.7 ± 2.08
1 mL	633 ± 265	0.83 ± 0.16	−40.4 ± 1.99

TABLE 3 | BET and BJH porosimetry measurements for Ag@MSNPs (500 μL TEOS) AgMSNPs.

SURFACE AREA	
BET Surface Area	759.4336 m²/g
BJH Adsorption cumulative surface area of pores between 17,548 Å and 1 585,580 Å diameter	878.015 m²/g
BJH Desorption cumulative surface area of pores between 17,000 Å and 3 000,000 Å diameter	882.0866 m²/g
PORE VOLUME	
BJH Adsorption cumulative volume of pores between 17,548 Å and 1 585,580 Å diameter	1.226786 cm^3/g
BJH Desorption cumulative volume of pores between 17,000 Å and 3 000,000 Å diameter	1.231038 cm^3/g
PORE SIZE	
Adsorption average pore diameter (BET)	52.1688 Å
BJH Adsorption average pore diameter	55.889 Å
BJH Desorption average pore diameter	55.824 Å

It is possible to notice a variation both in the absorption and emission bands, suggesting an influence of the solvent and of the pH on the photochemical behavior of ofloxacin.

Concerning the MSNPs, the encapsulation values are quite uniform, in the range of 10^{-4} M, with % E values around 30%. Regarding the AgMSNPs in a general way, the trend for the encapsulation performed in DMSO is not regular, conversely, when the encapsulations were performed in PBS the trend shows a regular progress with a bigger amount of ofloxacin encapsulated for lower initial concentrations. This can be attributed to the fact that the drug is poorly soluble in aqueous environment, showing then the tendency to migrate to the pores of the silica mesoporous nanoparticles.

MSNPs with ofloxacin were also characterized with DLS measurement for the size (hydrodynamic diameter: 243 ±

208 nm, PDI = 1) and zeta potential (−27.7 ± 1.6 mV). These results indicate that with the addition of ofloxacin, the nanoparticles were slightly destabilized, if compared to the crude MSNPs.

TABLE 4 | Encapsulation % of ofloxacin in MSNPs and AgMSNPs in DMSO (1), (2), and PBS pH 7.4 (3).

[Ofloxacin](M)	Encapsulation % in MSNPs (1)	Encapsulation % in AgMSNPs (2)	Encapsulation % in AgMSNPs (3)
1×10^{-5}	~10	~35	~84
1×10^{-4}	~23	~29	~50
5×10^{-4}	~34	–	–
7×10^{-4}	~30	–	–
1×10^{-3}	~30–89	~29	38
1×10^{-2}	–	~35	~9

Some preliminary tests for the release of ofloxacin were performed at 37°C in PBS at various pH to simulate a physiological media. The release was followed mainly by absorption measurements, recording the absorption of the supernatant over approximately 20 hours. The total observed release % was of 9.5, 4.9, and 5.4% for pH 7.4, 5.0, and 2.0, respectively. Despite the lower release percentage observed in PBS (*in vitro* simulation), it was clear the antibacterial effect of our nanosystem in the strains used, showing an effective synergetic effect between the silver core and the antibiotic.

Synthesis of Dye-Doped SNPs and Ofloxacin Functionalization

The synthesis of the dye-doped SNPs, as well as, the covalent ofloxacin functionalization was performed according to the protocol described in the experimental section.

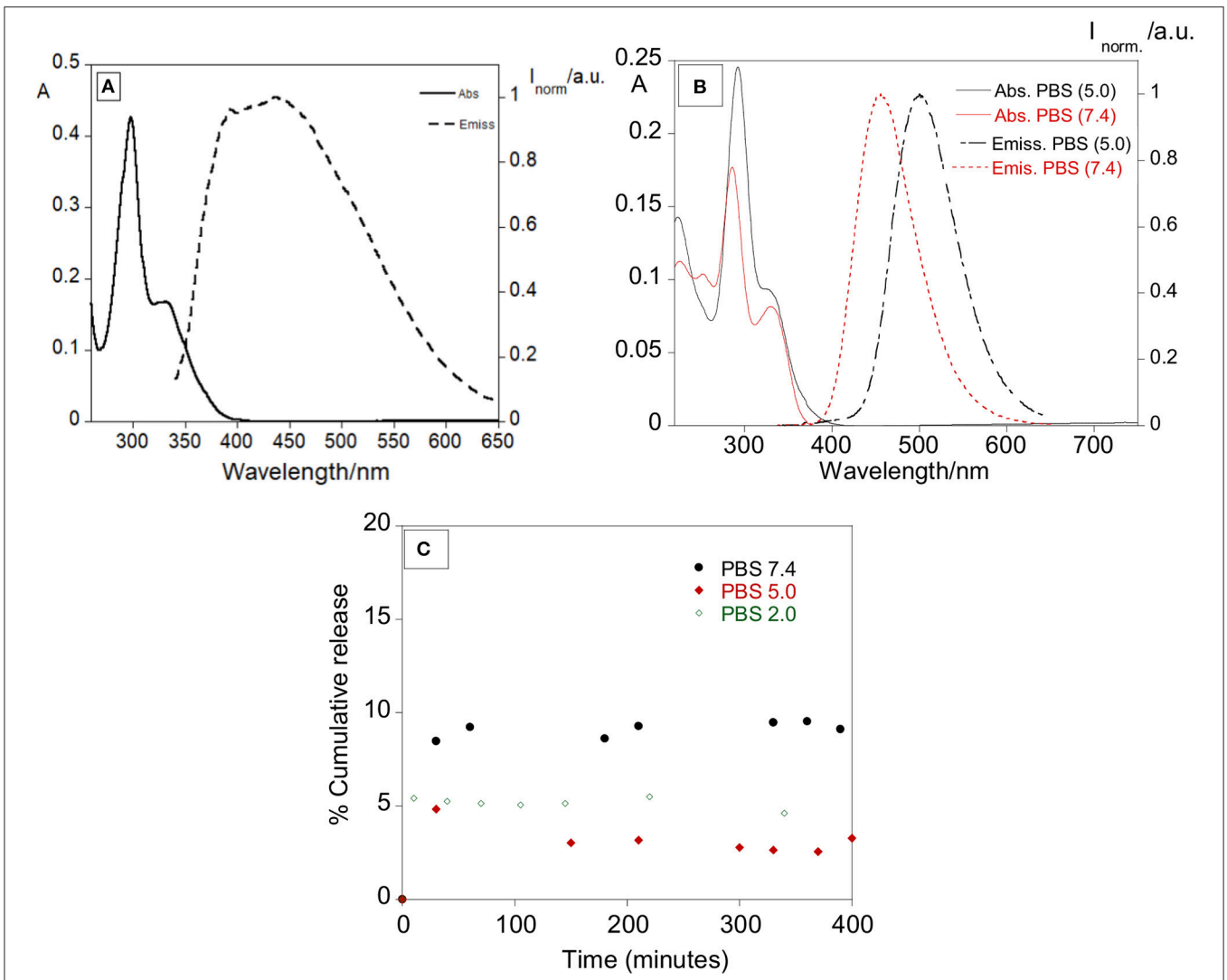

FIGURE 5 | (A) Absorption and emission spectra of ofloxacin in DMSO (λexc= 330 nm). **(B)** Absorption and emission spectra of ofloxacin in PBS at pH 5.0 and pH 7.4. (λexc = 330 nm). [Ofloxacin] = 1×10^{-5} M, r.t. **(C)** Percentage of cumulative release with time of ofloxacin in PBS pH 7.4, PBS pH 5.0, and PBS pH 2.0.

Photophysical Characterization

To quantitatively assess the functionalization of the nanoparticle surface with ofloxacin, absorption spectra were performed for both ofloxacin and functionalized SNPs in PBS 0.01 M pH 7.4 (**Figure 6**). Assuming that ofloxacin, when conjugated to the nanoparticles presents the same absorption than the free drug, we could estimate that the average number of ofloxacin molecules per NP is 13.

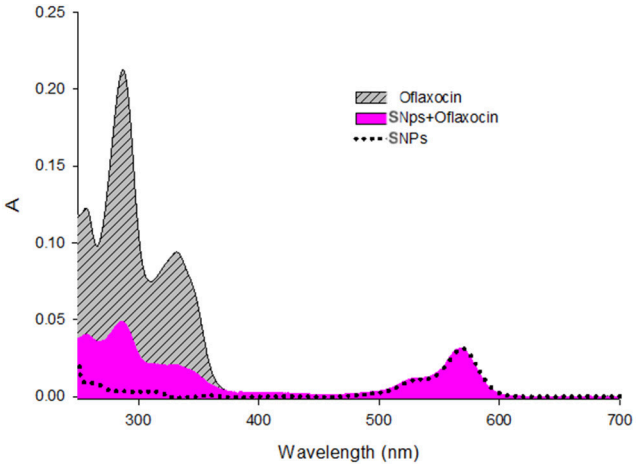

FIGURE 6 | Absorption spectra of Ofloxacin [9.3μM], SNPs (nanoparticles) [0.18μM], and SNPs+Ofloxacin [0.18 μM] in PBS pH 7.4.

DLS measurements confirm the narrow distribution of the dispersion of the NPs with a hydrodynamic diameter around 25 nm.

The final nanoparticles (dye (rhodamine)-doped SNPs@ofloxacin) were characterized by recording absorption and emission spectra, lifetimes, DLS and Z-potential, also the fluorescence quantum yield was calculated. The absorption and emission spectra show bands centered at 569 and 595 nm, respectively, characteristic of the rhodamine dye (**Figure 7**). A fluorescence quantum yield of 0.21 was determined for the rhodamine-doped silica nanoparticles, using as standard the rhodamine. Concerning the lifetime measurements, the exponential decay was fitted for two species with values of 2.2 ns, 4.5 ns, and a chi sq of 1.19. The standard rhodamine compound presents a lifetime of 2.8 ns.

Z-potential values are −4.6 mV for SNPs-NH_2 and −10.6 mV for SNPs-Ofloxacin; DLS measurements show once again the functionalization of the SNPs surface: the hydrodynamic radius

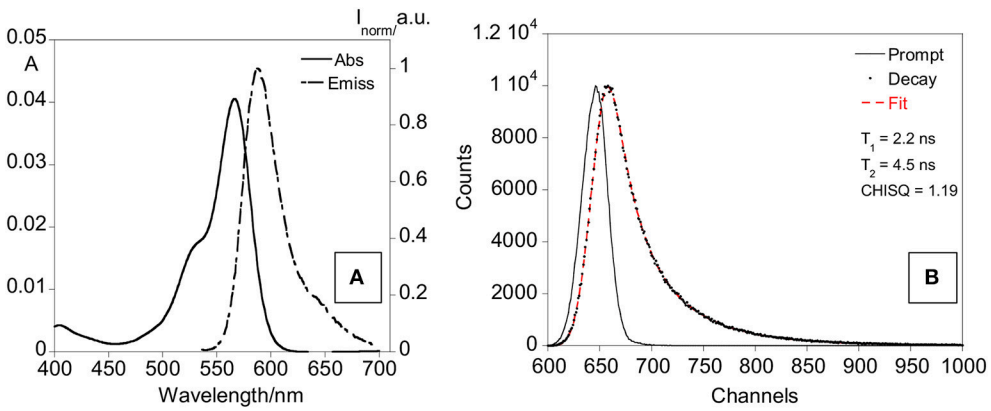

FIGURE 7 | Absorption and emission spectra **(A)** and lifetime decay **(B)** of rhodamine-doped SNPs in water.

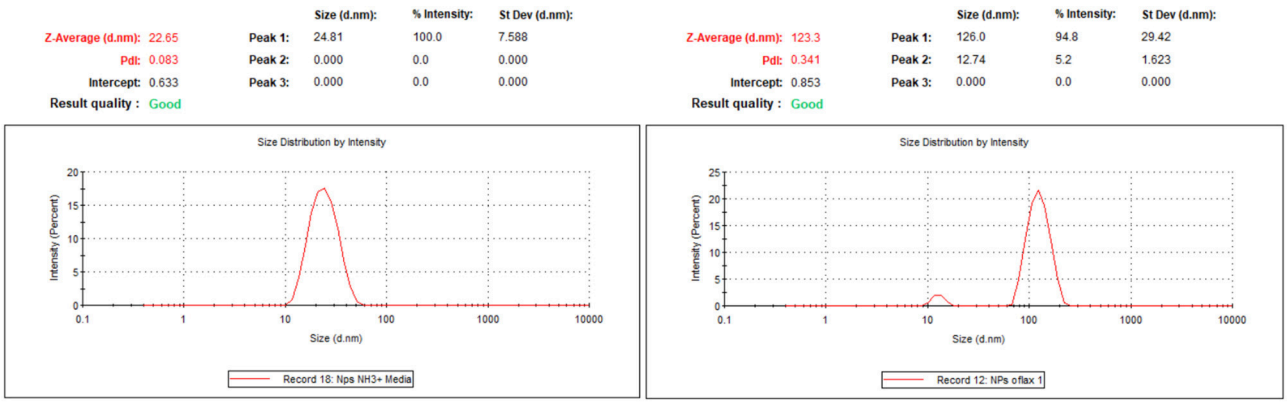

FIGURE 8 | DLS measurements for SNPs-NH_2 and SNPs-Ofloxacin on the right both in PBS at pH 7.4.

for SNPs is around 20 nm while for the functionalized SNPs is around 100 nm (**Figure 8**).

Bactericidal Activity Assays

Samples of MSNPs and AgMSNPs with different concentrations of ofloxacin (Oflx) and dye-doped SNPs decorated with ofloxacin were all tested to assess their bactericidal activity.

Minimum inhibitory concentration (MIC) and minimum bactericidal concentration (MBC), against both susceptible and resistant *E. coli* and *S. aureus* strains, were evaluated according to the procedures described in the experimental section (section Antibacterial Susceptibility Test). The results for all the nanoparticle samples that represent new formulations are listed in **Table 5**.

The tests show that the best performance is obtained with the AgMSNPs@Oflx samples. All the other systems are not effective against the *S. aureus* C5932, the MSNPs@Oflx systems are only able to inhibit their growth but not to kill the bacteria. The AgMSNPs@Oflx samples can inhibit the growth and kill all of the bacterial strains. This interesting result can be explained hypothesizing a synergic effect of the antibiotic and the Ag core of the nanoparticles, as silver has antibacterial properties itself. The strain that was more susceptible was the *S. aureus* ATCC 25923, and the lowest values for MIC and MBC among all the samples tested were again presented by the AgMSNPs@Oflx sample (MIC = 5 and 10 and MBC = 25 μg/mL for [Oflx] = 50 and 8 μM). The results also showed that the inhibitory effects of ofloxacin are highly dependent on its concentration as already mentioned and as attended.

As a control, non-loaded AgMSNPs and MSNPs, DMSO and free ofloxacin were tested in the presence of the same bacterial strains (**Table 1**). As expected, free AgMSNPs show a certain rate of bactericidal activity proving the effectiveness of the silver cores, while MSNPs and DMSO exhibit no antibacterial activity (Liong et al., 2009; Xu et al., 2009; Xiu et al., 2012; Yu et al., 2015; D'Agostino et al., 2017). Moreover, it is interesting to notice the difference in values of MBC between free AgMSNPs (MBC = 50 μg/mL) and AgMSNPs@Oflx (MBC = 25 μg/mL) loaded with the lowest ofloxacin concentration, in the presence of strain *S. aureus* ATCC 25923. These results prove the synergistic antibacterial effect of the silver nanoparticles combined with ofloxacin. On the other hand, this could be also considered together with the high surface/mass ratio typically present in nanomaterials: the smaller the particles, the higher the metallic surface exposed, and subsequently higher microbicidal effect can be expected (El Badawy et al., 2011).

Ofloxacin was also tested alone, in the same concentrations it has in the samples when loaded in the nanoparticles (**Table 5**). As a result, in the case of *E. coli* K12 ATCC 29425 and *S. aureus* ATCC 25923 only their growth was inhibited and no bacteria were killed, again proving the importance of the association between antibiotics and silver nanoparticles.

The dye-doped SNPs functionalized with Ofloxacin did not show a significant antibacterial activity against the tested bacterial strains, suggesting again the crucial role of silver in increasing the therapeutic efficacy and maybe a role of the silica shell in the bacterial uptake of the nanoparticles. In Gram$^-$negative bacteria AgNPs toxicity may arise directly from physical processes caused by nano-objects, like disruption of cell membrane and penetration of NPs into the cytoplasm with subsequent Ag^+-DNA binding or interaction

TABLE 5 | Minimum inhibitory concentration and minimal bactericidal concentration under nanoparticle plus antibiotic system.

Nanoparticle description	Strain	MIC (μg/mL)	MBC (μg/mL)
AgMSNPs ofloxacin ~ 50 μM	*E. coli* K12 ATCC 29425	10	25
	E. coli C999 (CTX-M-15)	50	75
	S. aureus ATCC 25923	5	25
	S. aureus C5932 (MRSA CC398)	100	200
AgMSNPs ofloxacin ~ 8 μM	*E. coli* K12 ATCC 29425	25	25
	E. coli C999 (CTX-M-15)	50	75
	S. aureus ATCC 25923	10	25
	S. aureus C5932 (MRSA CC398)	100	200
MSNPs ofloxacin ~ 750 μM	*E. coli* K12 ATCC 29425	10	25
	E. coli C999 (CTX-M-15)	100	300
	S. aureus ATCC 25923	10	25
	S. aureus C5932 (MRSA CC398)	200	ND
MSNPs ofloxacin ~ 650 μM	*E. coli* K12 ATCC 29425	10	25
	E. coli C999 (CTX-M-15)	200	500
	S. aureus ATCC 25923	50	50
	S. aureus C5932 (MRSA CC398)	300	ND
MSNPs ofloxacin ~ 270 μM	*E. coli* K12 ATCC 29425	25	50
	E. coli C999 (CTX-M-15)	200	500
	S. aureus ATCC 25923	50	75
	S. aureus C5932 (MRSA CC398)	500	ND
Dye-doped SNPs Ofloxacin ~ 20 μM	*E. coli* K12 ATCC 29425	100	ND
	E. coli C999 (CTX-M-15)	ND	ND
	S. aureus ATCC 25923	ND	ND
	S. aureus C5932 (MRSA CC398)	ND	ND
AgMSNPs	*E. coli* K12 ATCC 29425	25	50
	• *E. coli* C999 (CTX-M-15)	50	100
	S. aureus ATCC 25923	10	50
	S. aureus C5932 (MRSA CC398)	100	300
	E. coli K12 ATCC 29425	500	ND
MSNPs	• *E. coli* C999 (CTX-M-15)	ND	ND
	S. aureus ATCC 25923	500	ND
	S. aureus C5932 (MRSA CC398)	ND	ND
DMSO	*E. coli* K12 ATCC 29425	ND	ND
	• *E. coli* C999 (CTX-M-15)	ND	ND
	S. aureus ATCC 25923	ND	ND
	S. aureus C5932 (MRSA CC398)	ND	ND
Free ofloxacin	*E. coli* K12 ATCC 29425	10	10
	E. coli C999 (CTX-M-15)	ND	ND
	S. aureus ATCC 25923	5	5
	S. aureus C5932 (MRSA CC398)	ND	ND

MIC, minimum inhibitory concentration; MBC, minimal bactericidal concentration.

with bacterial ribosome (Xu et al., 2004; Yamanaka et al., 2005).

CONCLUSIONS

Mesoporous based nanocarriers with and without a silver core, MSNPs and, AgMSNPs, as well as, dye (rhodamine)-doped silica nanocarriers were successfully obtained and characterized. The MSNPs and AgMSNPs showed a negative zeta potential of -30.8 ± 0.3 mV and -44.1 ± 1.6 mV, as well as, diameter sizes of 80 ± 11 and 92 ± 12 nm, respectively. Regarding the rhodamine-doped silica nanoparticles a hydrodynamic ratio of 25 nm was obtained and a zeta potential of -4.6 mV.

The antibiotic ofloxacin was encapsulated and functionalized in all synthesized nanocarriers and the study of their antibacterial properties performed against *S. aureus* and *E. coli*.

The best performance was obtained with the AgMSNPs@ofloxacin samples, being able to inhibit the growth and kill all bacterial strains. The strain *S. aureus* ATCC 25923 was the most susceptible to the AgMSNPs@ofloxacin nanocarrier, presenting the lowest values for MIC (5 μg/mL), and MBC (25 μg/mL) for an ofloxacin concentration of 50 μM. The results also prove a synergistic antibacterial effect of the silver nanoparticles combined with ofloxacin.

AUTHOR CONTRIBUTIONS

LP, CL, and EO design and supervised the project. SN, JF-L, VS, EO, ER, and BR-G performed the experiments. EO, SN, LP, NZ, JF-L, CL, and GI analyzed the results and wrote the paper. EO, LP, CL, JC, GI, PP, NZ, and CT provide the resources related to the project. EO, LP, NS, CL, and JC financed the project. All authors reviewed the manuscript and approved the final version.

FUNDING

CL, JC, JF-L, and EO thank the financial support by the Associate Laboratory Research Unit for Green Chemistry–Clean Processes and Technologies–LAQV which is financed by national funds from FCT/MEC (UID/QUI/50006/2013) and co-financed by the ERDF under the PT2020 Partnership Agreement (POCI-01-0145-FEDER−007265), as well as the PROTEOMASS Scientific Society (Portugal) for funding support (General Funding Grant). EO and JF-L thank FCT/MEC (Portugal) for their post-doctoral grants, SFRH/BPD/108660/2015 and SFRH/BPD/93982/2013, respectively. SN thanks the ERASMUS grant included in the agreement between the University of Bologna (Italy) and the Faculty of Science and Technology, University NOVA of Lisbon (Portugal), and to the PROTEOMASS Scientific Society for the travel grant support.

REFERENCES

Andersson, D. I., and Hughes, D. (2010). Antibiotic resistance and its cost: is it possible to reverse resistance? *Nat. Rev. Microbiol.* 8, 260–271. doi: 10.1038/nrmicro2319

Arbeloa, F. L., Ojeda, P. R., and Arbeloa, I. L. (1989). Flourescence self-quenching of the molecular forms of Rhodamine B in aqueous and ethanolic solutions. *J. Lumin.* 44, 105–112. doi: 10.1016/0022-2313(89)90027-6.

Bagga, P., Siddiqui, H. H., Akhtar, J., Mahmood, T., Zahera, M., and Khan, M. S. (2017). Gold nanoparticles conjugated levofloxacin: for improved antibacterial activity over levofloxacin alone. *Curr. Drug Deliv.* 14, 1114–1119. doi: 10.2174/1567201814666170316113432.

Benito, D., Gómez, P., Lozano, C., Estepa, V., Gómez-Sanz, E., Zarazaga, M., et al. (2014). Genetic lineages, antimicrobial resistance, and virulence in *Staphylococcus aureus* of meat samples in spain: analysis of Immune Evasion Cluster (IEC) Genes. *Foodborne Pathog. Dis.* 11, 354–356. doi: 10.1089/fpd.2013.1689.

Bhattacharyya, S., Wang, H., and Ducheyne, P. (2012). Polymer-coated mesoporous silica nanoparticles for the controlled release of macromolecules. *Acta Biomater.* 8, 3429–3435. doi: 10.1016/j.actbio.2012.06.003.

D'Agostino, A., Taglietti, A., Desando, R., Bini, M., Patrini, M., Dacarro, G., et al. (2017). Bulk surfaces coated with triangular silver nanoplates: antibacterial action based on silver release and photo-thermal effect. *Nanomaterials* 7:7. doi: 10.3390/nano7010007.

Davies, J. (1994). Inactivation of antibiotics and the dissemination of resistance genes. *Science* 264, 375–82.

Ding, F., Songkiatisak, P., Cherukuri, P. K., Huang, T., and Xu, X. H. N. (2018). Size-dependent inhibitory effects of antibiotic drug nanocarriers against pseudomonas aeruginosa. *ACS Omega* 3, 1231–1243. doi: 10.1021/acsomega.7b01956

Dwyer, D. J., Kohanski, M. A., Hayete, B., and Collins, J. J. (2007). Gyrase inhibitors induce an oxidative damage cellular death pathway in *Escherichia coli*. *Mol. Syst. Biol.* 3:91. doi: 10.1038/msb4100135

El Badawy, A. M., Silva, R. G., Morris, B., Scheckel, K. G., Suidan, M. T., and Tolaymat, T. M. (2011). Surface charge-dependent toxicity of silver nanoparticles. *Environ. Sci. Technol.* 45, 283–287. doi: 10.1021/es1034188

Frank, A. J., Cathcart, N., Maly, K. E., and Kitaev, V. (2010). Synthesis of silver nanoprisms with variable size and investigation of their optical properties: a first-year undergraduate experiment exploring plasmonic nanoparticles. *J. Chem. Educ.* 87, 1098–1101. doi: 10.1021/ed100166g

Guzman, M., Dille, J., and Godet, S. (2012). Synthesis and antibacterial activity of silver nanoparticles against gram-positive and gram-negative bacteria. *Nanomed. Nanotechnol. Biol. Med.* 8, 37–45. doi: 10.1016/j.nano.2011.05.007

He, Q., and Shi, J. (2011). Mesoporous silica nanoparticle based nano drug delivery systems: synthesis, controlled drug release and delivery, pharmacokinetics and biocompatibility. *J. Mater. Chem.* 21:5845. doi: 10.1039/c0jm03851b

Huang, X., Young, N. P., and Townley, H. E. (2014). Characterization and comparison of mesoporous silica particles for optimized drug delivery. *Nanomater. Nanotechnol.* 4:1. doi: 10.5772/58290

Kohanski, M. A., DePristo, M. A., and Collins, J. J. (2010). Sublethal antibiotic treatment leads to multidrug resistance via radical-induced mutagenesis. *Mol. Cell* 37, 311–320. doi: 10.1016/j.molcel.2010.01.003

Kresge, C. T., Leonowicz, M. E., Roth, W. J., Vartuli, J. C., and Beck, J. S. (1992). Ordered mesoporous molecular sieves synthesized by a liquid-crystal template mechanism. *Nature* 359, 710–712. doi: 10.1038/359710a0

Le Ouay, B., and Stellacci, F. (2015). Antibacterial activity of silver nanoparticles: a surface science insight. *Nano Today* 10, 339–354. doi: 10.1016/j.nantod.2015.04.002

Levy, S. B., and Marshall, B. (2004). Antibacterial resistance worldwide: causes, challenges and responses. *Nat. Med.* 10, S122–S129. doi: 10.1038/nm1145

Li, X., Cao, Y., Qi, W., Saraf, L. V., Xiao, J., Nie, Z., et al. (2011). Optimization of mesoporous carbon structures for lithium–sulfur battery applications. *J. Mater. Chem.* 21:16603. doi: 10.1039/c1jm12979a

Liong, M., France, B., Bradley, K. A., and Zink, J. I. (2009). Antimicrobial activity of silver nanocrystals encapsulated in mesoporous silica nanoparticles. *Adv. Mater.* 21, 1684–1689. doi: 10.1002/adma.200802646

Montalti, M., Prodi, L., Rampazzo, E., and Zaccheroni, N. (2014). Dye-doped silica nanoparticles as luminescent organized systems for nanomedicine. *Chem. Soc. Rev.* 43, 4243–4268. doi: 10.1039/C3CS60433K

Montalti, M. A., Credi, L., and Prodi, M. G. (2006). *Handbook of Photochemistry. 3rd Edn*. (Boca Raton, FL: Taylor & Francis).

Nguyen, T., and Francis, M. B. (2003). Practical synthetic route to functionalized rhodamine dyes. *Org. Lett.* 5, 3245–3248. doi: 10.1021/ol035135z

Oliveira, E., Santos, H. M., Jorge, S., Rodríguez-González, B., Novio, F., Lorenzo, J., et al. (2018). Sustainable synthesis of luminescent CdTe quantum dots coated with modified silica mesoporous nanoparticles: towards new proteins scavengers and smart drug delivery carriers. *Dye. Pigment.* 161, 360–369. doi: 10.1016/j.dyepig.2018.09.047

Pelgrift, R. Y., and Friedman, A. J. (2013). Nanotechnology as a therapeutic tool to combat microbial resistance. *Adv. Drug Deliv. Rev.* 65, 1803–1815. doi: 10.1016/j.addr.2013.07.011

Rampazzo, E., Bonacchi, S., Juris, R., Montalti, M., Genovese, D., Zaccheroni, N., et al. (2010). Energy transfer from silica core–surfactant shell nanoparticles to hosted molecular fluorophores †. *J. Phys. Chem. B* 114, 14605–14613. doi: 10.1021/jp1023444

Rampazzo, E., Voltan, R., Petrizza, L., Zaccheroni, N., Prodi, L., Casciano, F., et al. (2013). Proper design of silica nanoparticles combines high brightness, lack of cytotoxicity, and efficient cell endocytosis. *Nanoscale* 5:7897. doi: 10.1039/c3nr02563b

Ruiz, E., Sáenz, Y., Zarazaga, M., Rocha-Gracia, R., Martínez-Martínez, L., Arlet, G., et al. (2012). qnr, aac(6′)-Ib-cr and qepA genes in Escherichia coli and Klebsiella spp.: genetic environments and plasmid and chromosomal location. *J. Antimicrob. Chemother.* 67, 886–897. doi: 10.1093/jac/dkr548

Sato, K., Matsuura, Y., Inoue, M., Une, T., Osada, Y., Ogawa, H., et al. (1982). *In vitro* and *in vivo* activity of DL-8280, a new oxazine derivative. *Antimicrob. Agents Chemother.* 22, 548–553. doi: 10.1128/AAC.22.4.548

Sen Karaman, D., Sarwar, S., Desai, D., Björk, E. M., Odén, M., Chakrabarti, P., et al. (2016). Shape engineering boosts antibacterial activity of chitosan coated mesoporous silica nanoparticle doped with silver: a mechanistic investigation. *J. Mater. Chem. B* 4, 3292–3304. doi: 10.1039/C5TB02526E

Tang, F., Li, L., and Chen, D. (2012). Mesoporous silica nanoparticles: synthesis, biocompatibility and drug delivery. *Adv. Mater.* 24, 1504–1534. doi: 10.1002/adma.201104763

Tang, S., and Zheng, J. (2018). Antibacterial activity of silver nanoparticles: structural effects. *Adv. Healthc. Mater.* 7:1701503. doi: 10.1002/adhm.201701503

Webster, T. J., and Seil, I. (2012). Antimicrobial applications of nanotechnology: methods and literature. *Int. J. Nanomed.* 7, 2767. doi: 10.2147/IJN.S24805

Wright, G. D. (2007). The antibiotic resistome: the nexus of chemical and genetic diversity. *Nat. Rev. Microbiol.* 5, 175–186. doi: 10.1038/nrmicro1614

Xiu, Z., Zhang, Q., Puppala, H. L., Colvin, V. L., and Alvarez, P. J. J. (2012). Negligible particle-specific antibacterial activity of silver nanoparticles. *Nano Lett.* 12, 4271–4275. doi: 10.1021/nl301934w

Xu, K., Wang, J. X., Kang, X. L., and Chen, J. F. (2009). Fabrication of antibacterial monodispersed Ag–SiO_2 core–shell nanoparticles with high concentration. *Mater. Lett.* 63, 31–33. doi: 10.1016/j.matlet.2008.08.039

Xu, X.-H. N., Brownlow, W. J., Kyriacou, S. V., Wan, Q., and Viola, J. J. (2004). Real-Time Probing of Membrane Transport in Living Microbial Cells Using Single Nanoparticle Optics and Living Cell Imaging †. *Biochemistry* 43, 10400–10413. doi: 10.1021/bi036231a.

Yamanaka, M., Hara, K., and Kudo, J. (2005). Bactericidal actions of a silver ion solution on *Escherichia coli*, studied by energy-filtering transmission electron microscopy and proteomic analysis. *Appl. Environ. Microbiol.* 71, 7589–7593. doi: 10.1128/AEM.71.11.7589-7593.2005

Yu, L., Zhang, Y., Zhang, B., and Liu, J. (2015). Enhanced antibacterial activity of silver nanoparticles/halloysite nanotubes/graphene nanocomposites with sandwich-like structure. *Sci. Rep.* 4:4551. doi: 10.1038/srep04551

Zhang, J., Li, X., Rosenholm, J. M., and Gu, H. (2011). Synthesis and characterization of pore size-tunable magnetic mesoporous silica nanoparticles. *J. Colloid Interface Sci.* 361, 16–24. doi: 10.1016/j.jcis.2011.05.038

Zhang, L., Pornpattananangku, D., Hu, C. M. J., and Huang, C. M. (2010). Development of nanoparticles for antimicrobial drug delivery. *Curr. Med. Chem.* 17, 585–94. doi: 10.2174/092986710790416290

Conflict of Interest Statement: The authors declare that the research was conducted in the absence of any commercial or financial relationships that could be construed as a potential conflict of interest.

frontiers in Chemistry

ORIGINAL RESEARCH
published: 16 October 2018
doi: 10.3389/fchem.2018.00487

Laser-Assisted Production of Carbon-Encapsulated Pt-Co Alloy Nanoparticles for Preferential Oxidation of Carbon Monoxide

Gema Martinez[1,2]*, *Ana Malumbres*[2], *Angela Lopez*[2], *Reyes Mallada*[1,2], *Jose L. Hueso*[1,2] *and Jesus Santamaria*[1,2]*

[1] Networking Research Center on Bioengineering, Biomaterials and Nanomedicine, CIBER-BBN, Zaragoza, Spain,
[2] Department of Chemical Engineering, Nanoscience Institute of Aragon (INA), Universidad de Zaragoza, Zaragoza, Spain

C-encapsulated highly pure Pt_xCo_y alloy nanoparticles have been synthesized by an innovative one-step *in-situ* laser pyrolysis. The obtained X-ray diffraction pattern and transmission electron microscopy images correspond to Pt_xCo_y alloy nanoparticles with average diameters of 2.4 nm and well-established crystalline structure. The synthesized Pt_xCo_y/C catalyst containing 1.5 wt% of Pt_xCo_y nanoparticles can achieve complete CO conversion in the temperature range 125–175°C working at weight hourly space velocities (WHSV) of 30 L $h^{-1}g^{-1}$. This study shows the first example of bimetallic nanoalloys synthesized by laser pyrolysis and paves the way for a wide variety of potential applications and metal combinations.

Keywords: bimetallic alloy, nanoparticles, Pt_xCo_y/C catalyst, laser pyrolysis, preferential CO oxidation

OPEN ACCESS

Edited by:
Carlos Lodeiro, Universidade Nova de Lisboa, Portugal

Reviewed by:
Ajay Singh Karakoti, Ahmedabad University, India
Emilia Morallon, University of Alicante, Spain

***Correspondence:**
Gema Martinez
gemamar@unizar.es
Jesus Santamaria
Jesus.Santamaria@unizar.es

Specialty section:
This article was submitted to Nanoscience, a section of the journal Frontiers in Chemistry

Received: *03 July 2018*
Accepted: *25 September 2018*
Published: *16 October 2018*

Citation:
Martinez G, Malumbres A, Lopez A, Mallada R, Hueso JL and Santamaria J (2018) Laser-Assisted Production of Carbon-Encapsulated Pt-Co Alloy Nanoparticles for Preferential Oxidation of Carbon Monoxide. Front. Chem. 6:487. doi: 10.3389/fchem.2018.00487

INTRODUCTION

Increasing interest is currently being devoted to the use of supported bimetallic alloy and intermetallic nanoparticles as a promising way to modify activity and selectivity, to improve stability and partially substitute expensive noble metals in conventional supported metallic catalysts, such as Pt, Pd, and Rh system (Yu et al., 2012; Furukawa and Komatsu, 2017). In general, the properties of the bimetallic catalysts differ from their monometallic counterparts owing to the synergistic effects of geometry and electronic effects between metals. Therefore, their catalytic performance can be tuned, because an additional degree of freedom, for modifying the geometric and electronic structures is applicable by changing their composition and size (Tao et al., 2012; Wang et al., 2014).

Pt_xCo_y alloy is one of the most widely studied bimetallic systems because of its stability and broad catalytic scope (Service, 2002; Stamenkovic et al., 2007; Huang et al., 2017). One of the reactions in which these multimetallic alloys may offer greater benefits than conventional Pt catalysts is the preferential oxidation (PROX) of carbon monoxide (CO; Liu et al., 2012), a case of substrate-selective oxidation of CO in excess of hydrogen (H_2). The main requirements to be fulfilled by the catalysts used in PROX reaction are: (i) high activity at low temperatures achieving CO conversion to CO_2 higher than 99%, (ii) high selectivity to the CO oxidation reaction, avoiding the oxidation of hydrogen in a wide operation temperature window (e.g., 80–180°C) between the low temperature shift reactor operation around 200°C and (iii) the low temperature feed to the PEMFC. Hence the catalyst should not be deactivated by the presence of CO_2 and H_2O in the reformate

feed stream (Liu et al., 2012). In fact, an improved performance in the catalytic activity for this reaction when using Pt_xCo_y alloy catalysts, instead of Pt/C, is observed as a consequence of the special synergic effect between cobalt and platinum (Yan et al., 2004; Ko et al., 2007; Snytnikov et al., 2007; Wang et al., 2013; Furukawa et al., 2016). The formation of the intermetallic alloy induced an extension of the Pt-Pt atomic distance and electron transfer from Pt to Co. Both effects result in weaker adsorption of CO, compared to the pure metal resulting in higher activity at lower temperature (Komatsu and Tamura, 2008). However, there are still serious limitations in their synthesis, because of the difference in standard reduction potential between the two metals ions and the distinct atom sizes. A challenge is to maintain simultaneously (i) a narrow nanoscale size distribution; (ii) a uniform composition throughout the nanoparticles; (iii) a fully alloyed degree, and (iv) high dispersion on the support, which represents a serious challenge in conventional synthesis approaches.

Routine synthesis approaches typically involve the impregnation of an already synthesized carbon-supported Pt metal catalyst with a second metal precursor salt, followed by alloying at high temperatures ($\geq$900°C) under inert gas or reducing conditions (Tamizhmani and Capuano, 1994; Min et al., 2000; Takenaka et al., 2010). Nevertheless, this thermal treatment gives rise to undesired particle growth by sintering and coalescence of the particles with the concurrent increase of average particle size, resulting in a lower catalysts active area (Antolini, 2003). As an alternative to overcome these problems, other procedures such as reduction of Pt and the second metal at low temperature (Xiong et al., 2002), micro emulsion methods (Xiong and Manthiram, 2005) or polyol methods (Jang et al., 2011) are aimed to synthesize bimetallic nanoparticles under milder conditions. However, these methods offer low alloying degree (Zignani et al., 2008; Jang et al., 2011; Vinayan et al., 2012; Lopez et al., 2016), mainly because the formation of alloyed intermetallic phases generally needs high temperatures(Furukawa and Komatsu, 2017). In addition, these processes require longer synthesis time (including cleaning protocols) and deployment on supports.

Alternatively, multimetallic nanoparticles have been also produced in gas phase by procedures such as flame pyrolysis (Strobel et al., 2005), laser ablation (Senkan et al., 2006) or plasma-assisted dissociation of organometallic vapor (Lin and Sankaran, 2011; Saedy et al., 2017). Unfortunately, these gas-phase approaches have also suffered from excessive particle growth and aggregation, reducing the surface area and number of actives sites (Rodriguez et al., 2011; Wang and Li, 2011). Therefore, in order to preserve the catalytic properties of the nanoparticles, particle agglomeration must be prevented. For this purpose, encapsulating shells appear as a promising and elegant strategy. Among these encapsulating candidates, carbon offers many advantages, such as high stability under various physical and chemical conditions, high electrical conduction for electrochemical applications, and low manufacturing cost. Various techniques for carbon encapsulation of metal nanoparticles have been investigated including laser ablation of organometallic targets (Munoz et al., 2010; Seral-Ascaso et al., 2013), solution plasma processes (Kang et al., 2013), one-step pyrolysis using cyanamide and metal salts as precursor (Han et al., 2015) or one-pot light-assisted evaporation induced self-assembly approach (Ghimbeu et al., 2015). Unfortunately, most of them render broad particle size distribution or at least less controllable and limited availability of control in stoichiometry requirements, making them very restricted methods for the synthesis of alloy nanoparticles.

Therefore, further developments are still needed in order to design a versatile one-pot synthesis that allows high nanoparticle dispersion, tuneable stoichiometry and at the same time preserving small particle size and achieving good alloying and stability. In this work, we propose a simple one-pot synthesis method for alloying nanoparticles containing C shells, based on laser pyrolysis processing. Previous studies in our group have shown that this technique could be used to successfully synthesize a variety of nanoparticles with extremely high purity (Martínez et al., 2012; Malumbres et al., 2015). Although most of the research in this area is limited to metal precursors which are gases or liquid having sufficient vapor pressure at moderate temperature, which restricts its application to certain elements or makes necessary to synthesize specific organometallic precursors or even use highly flammable and toxic precursors as it is the case of silane for the synthesis of Si nanoparticles. Recently, much attention is being focused on the interaction between the laser beam and the aerosols droplets containing solid precursors, that may expand the application of the technique to all the elements as far as their salts are soluble in spray-able solvents (Wang et al., 2017). The most important merits of laser pyrolysis processing include the well-defined interaction volume, spatial uniformity of the reaction zone, short millisecond scale residence times, high heating/cooling rates, the fact that the nanoparticles properties can be tuned by adjusting the process parameters, the continuous nature that avoids the intrinsic variability of batch processing and the high purity of the prepared materials.

In this paper we present a flexible and continuous Pt_xCo_y/C catalysts synthesis, which is much more time and cost saving than current multi-step processes. As far as we are concerned this is the first time that bimetallic nanoparticles have been synthesized by laser pyrolysis. The innovative, versatile, and continuous single step strategy involves interaction between the laser beam and the organometallics precursors in a liquid spray form. The role of the solvent it is not only to transport the solid metal precursors at the reaction zone but also to provide the source to form the carbon framework avoiding agglomerating of the particles. By carefully combining precursor's ratio, bimetallic nanoparticles of controlled composition can be tailored by this approach. The chemical and structural characterization of the synthesized material revealed that the obtained Pt_xCo_y alloy nanoparticles were encapsulated in C matrix and exhibited a uniform size distribution, average diameters below 3 nm, and high crystallinity. Finally, the Pt_xCo_y/C (Pt:Co, 3:1) nanoparticles were deposited on a ETS-10 microporous support (1.5 wt.% Pt_xCo_y/C) and their catalytic activity was tested in PROX reaction feeding a simulated steam reforming stream (1%CO, 21%CO_2, 3%H_2O, 1%O_2, and H_2 balance).

MATERIALS AND METHODS

Chemicals

Platinum (II) acetylacetonate [$Pt(acac)_2$, 97%], cobalt (III) acetylacetonate [$Co(acac)_3$, 99.99%], toluene (99.5%) and absolute ethanol (≥98%) were supplied from Sigma Aldrich and used without further purification.

Pt_xCo_y/C Composite Nanoparticles Synthesis

The synthesis of Pt_xCo_y/C composite nanoparticles with different compositions has been carried out by laser pyrolysis in a continuous flow reactor described elsewhere (Martínez et al., 2012; Malumbres et al., 2013, 2015). The starting solution employed for the synthesis of Pt_xCo_y/C was prepared by dissolving $Pt(acac)_2$ (47 mg, 0.12 mmol) and the corresponding amount of $Co(acac)_3$ [11 mg (0.04 mmol) or 30 mg (0.12 mmol)] in toluene, to get a molar ratio Pt:Co = 3 or Pt:Co = 1. The technique is based on the interaction between the laser beam (Rofin SCx30, $\lambda = 10.6\,\mu m$) at 100 W power and the starting materials in a liquid spray form (aerosol). Sulfur hexafluoride (SF_6) was added as sensitizer gas. The liquid mixture was introduced in the reactor by a syringe pump working at 15 ml/h. The aerosol spray was produced by a nebulizer immediately located before the chamber. Aerosol droplets were transported in a flow of Ar/SF_6, 130 and 30 sccm, respectively, into the reaction chamber through a ¼ inch inner diameter nozzle. A flow of hydrogen (10 sccm) and argon (100 sccm) was used as coaxial gas flow to confine the reaction in a very small volume without any interaction with reactor walls. The aerosol and laser beam are designed to intersect orthogonally, and the beam diameter (d_{laser}) and the aerosol spray diameter (d_{spray}) were controlled in such way that $d_{spray} < d_{laser}$. This configuration ensured that all the spray molecules were confined within the beam area to complete the pyrolysis (see **Scheme 1**). In order to prevent powder deposition onto the vertical and horizontal windows they were continuously flushed with 600 and 200 sccm of Ar and N_2, respectively. The pressure was maintained constant at 200 mbar through a diaphragm valve located between the reaction chamber and the vacuum pump. The gas flows were controlled by mass flow controllers. The reaction proceeded with color change from green light (color of the precursor solution) to black (color of the nanostructures powder obtained). To capture and isolate nanoparticles, the freshly nucleated particles were directly collected onto cellulose filters (F2044). Typical values and ranges of the experimental parameters are listed in **Table 1**. This work has been performed by the ICTS "NANBIOSIS" by the Synthesis of Nanoparticles Unit of the CIBER in Bioengineering, Biomaterials &Nanomedicine (CIBER-BBN) at the Institute of Nanoscience of Aragon (INA)-Universidad de Zaragoza.

Structural Characterization

A battery of techniques was used to characterize the Pt_xCo_y/C composite nanoparticles. Particle morphology and size distribution were determined by a FEI Tecnai thermoionic

TABLE 1 | Experimental parameters for the optimized synthesis of carbon-encapsulated Pt_xCo_y bimetallic nanoparticles.

Synthesis conditions	
Flow rate of windows gases (sccm)	800
Flow rate of coaxial gas Ar/H_2 (sccm)	100/10
Aerosol spray flow Ar/SF_6 (sccm)	130/30
Precursor solution flow (mL/h)	15
Power of laser beam (W)	100
Working pressure (mbar)	200

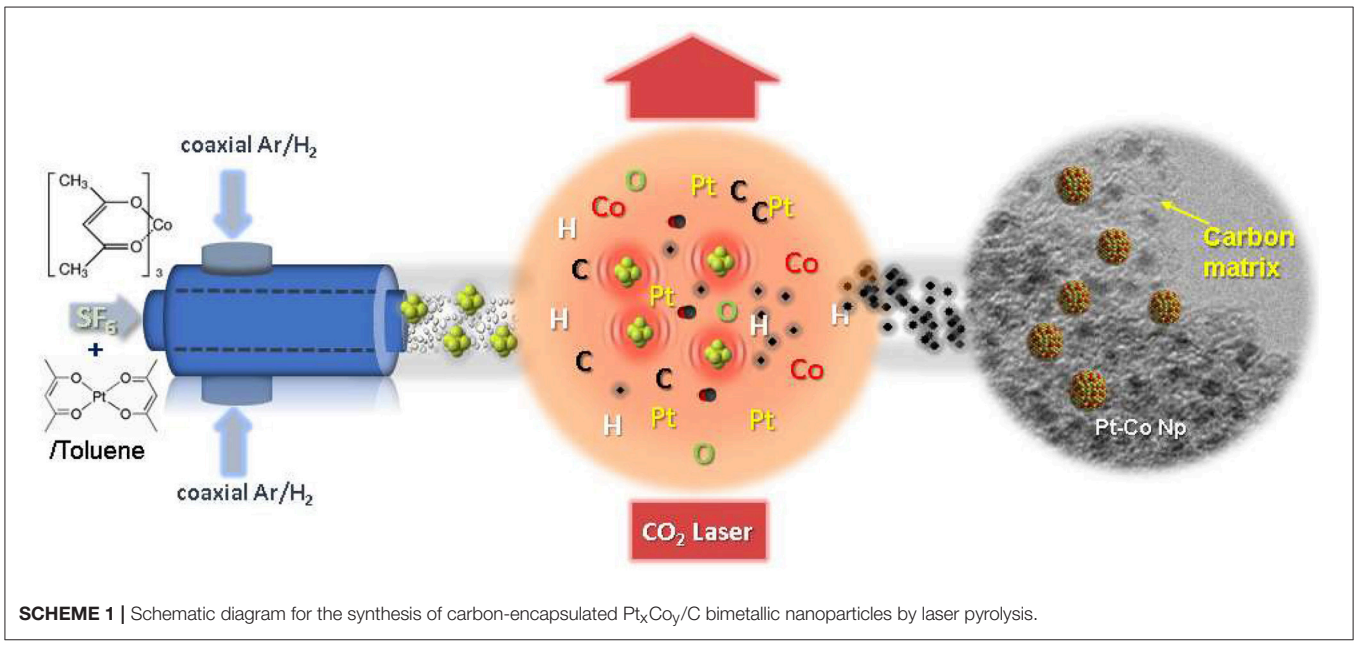

SCHEME 1 | Schematic diagram for the synthesis of carbon-encapsulated Pt_xCo_y/C bimetallic nanoparticles by laser pyrolysis.

transmission electron microscopy (TEM) operated at 200 kV. More than 200 particles were measured to evaluate the mean diameter. The data were fitted with a normal distribution function and the standard deviation was obtained for all the samples. To determine the crystalline structure and the composition of the particles, High Resolution Transmission Electron Microscope (HRTEM), Scanning Transmission Electron Microscope with high angle annular dark field (STEM-HAADF) and Energy Dispersive X-ray Spectroscopy (EDS) analysis were performed by using a FEI TECNAI F30 and FEI Titan^{TM} Cube (80–300 kV) microscopes at an acceleration voltage of 300 kV. To prepare the sample, 10 μL of a ethanol particle suspension were dropcasted on a lacey carbon TEM grid. Powder X-ray diffraction (XRD) analyses were performed in a Rigaku/Max System diffractometer with Cu Kα radiation source ($\lambda = 0.15418$ nm). Surface composition was analyzed by X-ray photoelectron spectroscopy (XPS) with an Axis Ultra DLD (Kratos Tech.) The spectra were excited by a monochromatic Al Kα source (1486.6 eV) run at 12 kV and 10 mA and pass energy of 20 eV was used. The binding energies were referenced to the internal C 1 s (284.6 eV) standard. Analysis of the peaks was performed with CasaXPS software, using a weighted sum of Lorentzian and Gaussian component curves after Shirley background subtraction. To characterize the carbon shell of the nanoparticles, Raman spectra were obtained with a Laser Raman WiTec Alpha 300 spectrometer, with the 532 nm line of an Ar^+ ion laser. The bulk chemical composition of digested samples was analyzed using microwave plasma atomic emission spectroscopy (Agilent 4100 MP-AES).

Catalytic Activity Tests

The as synthesized Pt_xCo_y nanoparticles were incorporated to the microporous titanosilicates ETS-10 support by incipient wetness impregnation method, to get 1.5 wt.% Pt_xCo_y, following our previous protocol (Lopez et al., 2016). The activity measurements were carried out in an experimental set-up described elsewhere (Lopez et al., 2016). The supported catalyst, 100 mg together with 200 mg of quartz, used as diluent, was loaded in a quartz tube of 9 mm internal diameter. The reaction temperature was measured with a thermocouple located in the center of the catalyst bed. The composition of the feed stream was: 1% CO, 1% O_2, 3% H_2O, 21% CO_2, and hydrogen balance. The feed flow was 50 STP mL/min which corresponds to a (weight hourly space velocity) WHSV = 30 L $h^{-1}g^{-1}$. Prior to catalytic activity tests, the solids were heated in air at a heating rate of 5°C/min, up to 500°C and kept at this temperature for 3 h. Then the catalyst was cooled down to room temperature under N_2 atmosphere. Feed and products were analyzed by gas chromatography with a Varian CP-4,900 Micro-GC equipped with two modules containing, molecular sieve and Pora PLOT Q columns, respectively and using helium as carrier gas. Under the analysis conditions the detection limit of CO was 5 ppm.

The CO conversion and the selectivity for the PROX reaction were calculated according to:

$$X_{co} = \frac{F_{CO\ feed} - F_{CO\ outlet}}{F_{CO\ outlet}}$$

$$S_{co_2} = \frac{2(F_{CO\ feed} - F_{CO\ outlet})}{(F_{O_2 feed} - F_{O_2 outlet})}$$

Being F_i the corresponding molar flow of each component. The conversion values were obtained after the reactor temperature was stable for at least 30 min. and the reported values represent the average of 3 samples taken at the reactor exit. CH_4 was not detected in any of the experiments carried out. The C mass balance was measured and was always in the range 98–102%.

RESULTS AND DISCUSSION

Synthesis and Characterization of Pt-Co Nanoalloys

As a first step toward accessing carbon dispersed bimetallic alloy nanoparticles, we separately studied the conversion of individual acetylacetonate metal precursors [$Pt(acac)_2$ and $Co(acac)_3$] into the corresponding monometallic nanoparticles. **Figure S1** indicates that both organometallics precursors were successfully decomposed under similar experimental conditions (**Table 1** in experimental section) to yield highly uniform and well-dispersed monometallic nanoparticles within a carbonaceus matrix. The nanoparticles are characterized by spherical shapes, narrow size distributions and particles diameters from ∼2.5 to 3.5 nm.

Once the experimental conditions, for the pyrolysis of the aerosol, were established, the synthesis of Pt_xCo_y/C composite nanoparticles was accomplished by one-step pyrolysis of a toluene solution containing a mixture of both $Pt(acac)_2$ and $Co(acac)_3$ precursors in the required stoichiometric amount. As illustrated in **Scheme 1**, the fabrication process involves interaction between the laser beam and the starting materials in a toluene spray. When the laser beam intersects the SF_6/Ar nebulized toluene solution reactant stream, a fast-atomic decomposition of the organometallic precursors is produced into the reaction area resulting in the formation of well-dispersed Pt_xCo_y bimetallic nanoparticles within a carbonaceous shell.

Figure 1A shows the TEM image and particle size distribution (inset **Figure 1A**) of the Pt_xCoy/C obtained nanoparticles when the molar ratio of Pt to Co precursors was 3. The TEM image (**Figure 1A**) reveals that numerous individual nanoparticles with mean size of 2.4 ± 0.3 nm (inset) are well dispersed and perfectly C-encapsulated. **Figure 1B** shows a STEM-HAADF image (the contrast depends directly on the atomic number Z^2), where the bright bimetallic nanoparticles are easily spotted against the C matrix. The nanocrystals appear as well-crystallized spherical particles. The semi-quantitatively chemical composition of the nanoparticles was determined by energy-dispersive X-ray (EDX) spectroscopy (**Figure 1C**). The analysis of the elemental distribution within a single nanoparticle (selected area on **Figure 1B**) corroborates the coexistence of both Pt and Co with atomic percentages of 79.5 ± 0.7 and 20.5 ± 0.5%, respectively. The EDS also shows high resolution 2D mapping of elemental Pt and Co (**Figure 1D**), which are homogeneously distributed throughout the entire nanoparticle. The bulk composition of the sample determined by Inductively coupled plasma (ICP) further confirmed an overall atomic ratio Pt:Co of 3.97 ± 0.04. The experimental ratios (Pt:Co = 4) determined by both measurements matched very

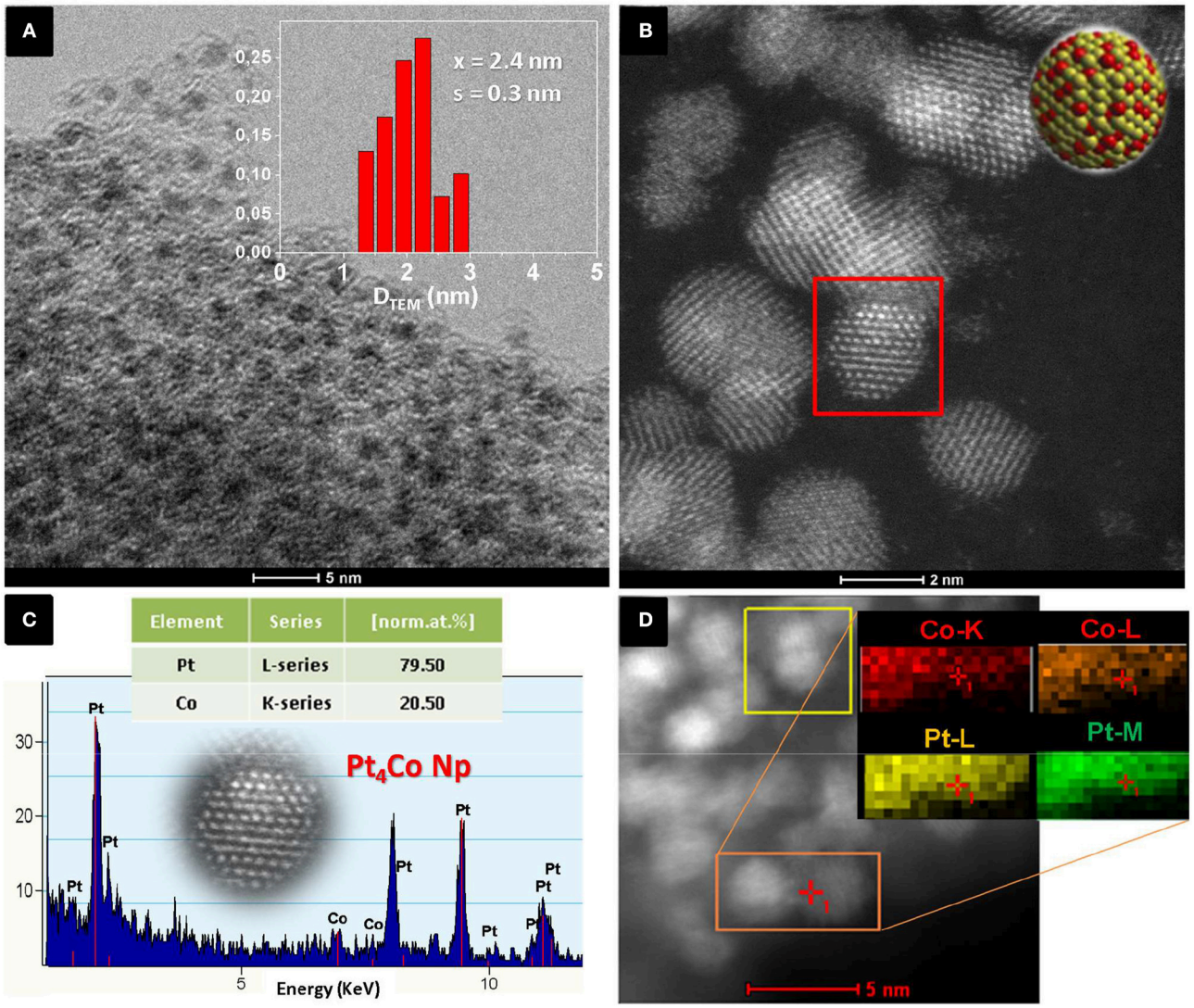

FIGURE 1 | (A) Representative TEM image of Pt_4Co nanoparticles encased in a C matrix, (*inset*) Particle size histogram, **(B)** STEM-HAADF image of the Pt_4Co/C nanoparticles synthesized when the molar ratio of starting Pt:Co precursors is set to 3, **(C)** EDX analysis of an individual particle (selected area in **B**) indicating an experimental atomic ratio of Pt to Co of ~4 (Pt_4Co/C), and **(D)** EDS mapping of elemental Pt (green) and Co (red) with corresponding STEM-HAADF image of the Pt_4Co/C composite nanoparticles.

well and were slightly higher than expected from the initial molar ratio fed to the reactor (Pt:Co = 3). The Pt-enrichment of the as-prepared Pt_4Co/C composite nanoparticles can be tentatively attributed to different physicochemical features, such as different decomposition temperature of the organometallic acetylacetonates (Vonhoene et al., 1958). On the other hand, carbon is segregated and deposits as a mixture of amorphous carbon with randomly distributed graphitic domains, confirmed by Raman spectroscopy (**Figure S2**). The peak centered at 1.595 cm^{-1} (G-band) is assigned to graphite (Ferrari, 2007), while the peak at 1.348 cm^{-1} is the D-band mainly derived from the disordered carbon structures (Arbizzani et al., 2011; Liu et al., 2015).

By indexing X-ray diffraction (XRD) pattern (**Figure 2A**), we examined the crystalline structure of the Pt_4Co/C composite nanoparticles. The XRD diffraction peaks are slightly shifted toward higher 2θ values compared to those of the cubic-face centered crystalline Pt (JCPDS card. No. 87-0646), peaks at 40.68°, 47.52°, 68.84°, and 82.36°, corresponding to the (111), (200), (220), and (311) planes, without any additional peak indicating that the Pt_4Co/C catalyst maintains the face-centered cubic (fcc) structure of platinum. This shift can be due to the lattice contraction that occurs when larger Pt atoms are progressively substituted by smaller Co atoms, thus demonstrating the formation of bimetallic alloy nanoparticles (Xiong and Manthiram, 2004; Salgado et al., 2005; Huang et al., 2006; Jiang et al., 2009; Xia et al., 2015). Moreover, diffraction signals that could be associated to the presence of crystalline cobalt (JCPDS card. No. 01-1277) or its oxides have not been observed for the prepared binary Pt_4Co/C composite

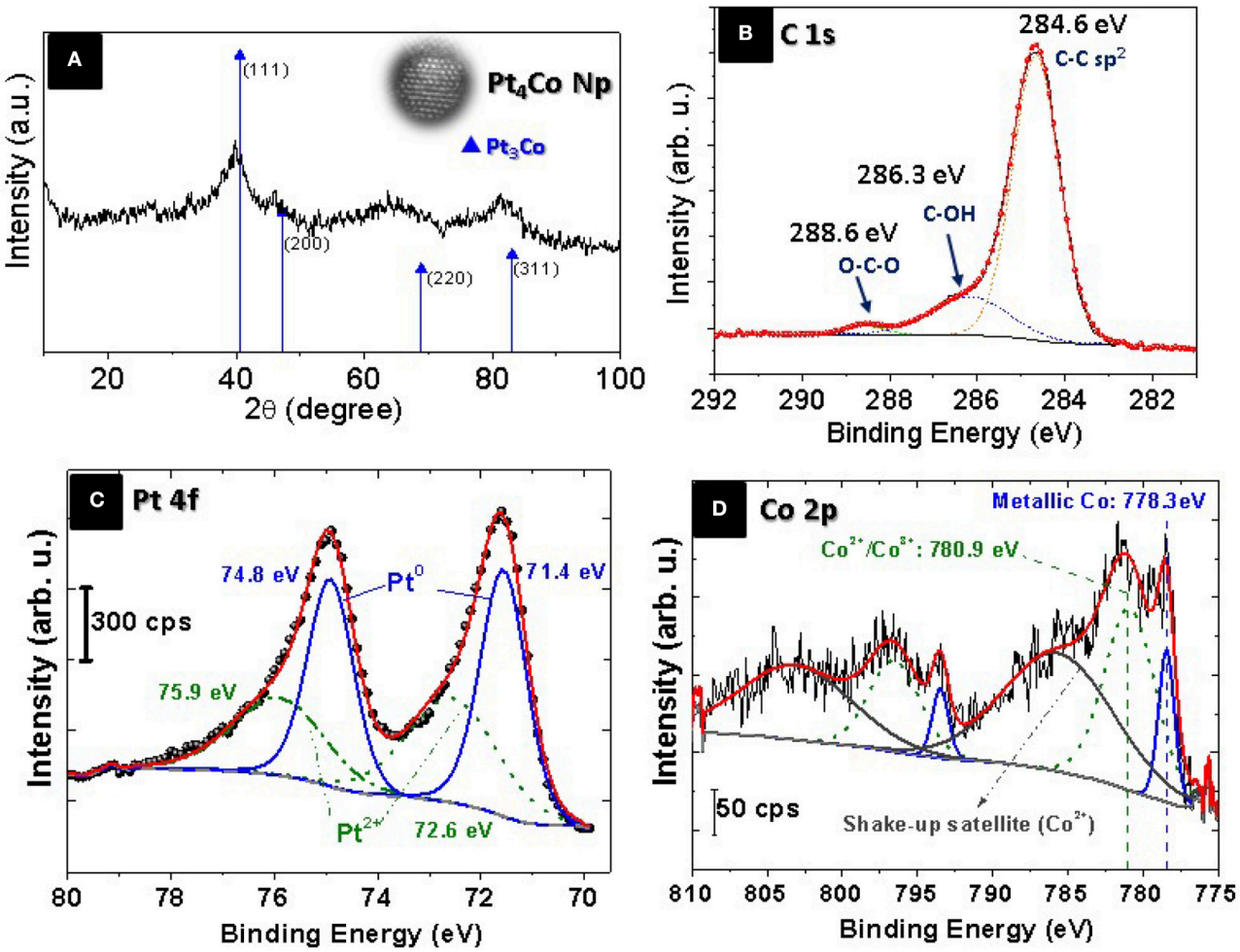

FIGURE 2 | (A) XRD patterns of Pt_4Co/C composite nanoparticles, and XPS spectra of: **(B)** C 1s region, **(C)** Pt 4f region and **(D)** Co 2p region showing the oxidation states of the Pt and Co in the Pt_4Co/C composite nanoparticles.

nanoparticles. The cobalt contents within the Pt_4Co/C sample derived from the Vergad's law (Santiago et al., 2007) was calculated by comparing the lattice parameter obtained from the measured (111) 2θ Bragg peak (a_{exp} = 0.3850 nm) with those of the metallic Pt (a = 0.39231 nm; Swanson and Eleanor, 1953) and metallic cobalt (a = 0.35441 nm; Owen and Jones, 1954), respectively. The Co atomic content in the alloy, as determined by this XRD measurement, was about 19.3%. This is close to the nominal content 20%, detected by ICP and EDX analysis.

The oxidation states of Pt_4Co/C catalyst were studied by X-ray photoemission spectroscopy (XPS). The survey XP-spectrum reveals the presence of carbon, cobalt, platinum and oxygen. The high-resolution C 1s spectrum is depicted in **Figure 2B**. The relative intensity of the peaks indicates primarily graphitic carbon C-C/C=C (284.6 eV) with small percentage of oxidized carbon as C-O and C=O species (286.3 and 288.6 eV), respectively (Arico et al., 1995). The analytical peaks related to Pt 4f orbitals and 2p orbitals for Co are shown in **Figures 2C,D**, respectively. The binding energies (BE) of 74.8 and 71.4 eV in **Figure 2C** correspond with Pt $4f_{5/2}$ and Pt $4f_{7/2}$, respectively, which can be splitted into two pairs of doublets: metallic Pt at 74.8 and 71.4 eV, while the second contribution at 75.9 and 72.6 eV correspond to Pt^{2+} species (Zsoldos and Guczi, 1992; Zheng et al., 2014a,b). The XPS signals in the Co $2p_{3/2}$ region (**Figure 2D**) reveal the presence of Co (0) at 778.5 eV shifted 0.4 eV toward higher BE in Pt-Co alloys compared with the monometallic cobalt phase at 778.1 eV) which is another confirmation of the formation of the Pt_3Co alloy nanoparticle (Bardi et al., 1990). A Co $2p_{3/2}$ peak contribution at 780.9 eV can be assigned to both Co surface phase and Co oxide (Co^{2+}/Co^{3+}; Zsoldos and Guczi, 1992). Although, the Co $2p_{3/2}$ peaks are clearly accompanied by strong shake-up satellites, which are characteristic of CoO (Co^{+2}), at 5 eV higher than its main peak, as well as a spin-orbit coupling of around 15.5 eV (Zsoldos and Guczi, 1992) the presence of Co_3O_4 (Co^{3+}) cannot completely be ruled (Jimenez et al., 1995; Hueso et al., 2008). The low metallic Co content compared to the higher metallic Pt content confirms the oxide-cleansing

action of Co addition (Arico et al., 2001). The electronegativity difference between Co and Pt (1.8 and 2.2, respectively; Shukla et al., 1999) implies an electron-drawing effect from Pt to the neighboring Co atoms, which make the latter more difficult to reduce.

To demonstrate the versatility and robustness of this synthesis method, we performed the one-step laser-driven pyrolysis of a toluene solution containing a mixture of both $Pt(acac)_2$ and $Co(acac)_3$ precursors in molar ratio of 1. The structure of the as-prepared Pt_xCo_y/C composite nanoparticles was characterized by TEM (**Figure S3A**) and STEM-HAADF (**Figure S3C**). The corresponding micrographs show highly crystalline spherical nanoparticles with average size of 2.3 ± 0.4 nm (**Figure S3B**) which are well-dispersed across the C matrix. The coexistence of Pt and Co elements in the particles is also demonstrated by the EDS analysis with the bimetallic composition of 55.5% and 44.5%, respectively (**Figure S3D**). The shift of XRD lines indicates proper alloying (**Figure S4**). Additional characterization by Raman and X-ray photoemission spectroscopy is provide in **Figure S5**. These results contributed to demonstrate that the proposed laser-assisted synthesis method is a general and feasible route for the synthesis of well dispersed, stable and highly pure C-encapsulated Pt_xCo_y bimetallic nanoparticles. The nanoparticles were properly alloyed, while different stoichiometric ratios could be easily tuned by changing the the molar ratio of Pt and Co precursors.

PROX Catalytic Tests

A systematic evaluation of the catalytic capability of the Pt-Co alloy nanoparticles was performed after deployment onto an ETS-10 support. The preferential oxidation of CO in the presence of a hydrogen excess was thoroughly evaluated and compared with analogous bimetallic compositions available in the literature (**Table 2**). The evolution of CO conversion and selectivity as a function of temperature is presented in **Figure 3A**. The decrease in CO conversion at higher temperatures occurs due to oxygen scarcity caused by a surface fully covered with chemisorbed hydrogen and acceleration of undesirable concurrent hydrogen oxidation reaction which results in selectivity decrease. The carbon monoxide starts to convert at 50°C following a typical light-off curve and the total conversion is achieved at 125°C, which maintains constant in a temperature window of 50°C. The PROX unit is located between the outlet of the low temperature water gas shift reactor, working at 200°C, and the inlet of the fuel cell operating in the range of 80–120°C, in the case of low temperature proton exchange membrane fuel cell (PEMFC). **Table 2** shows the operation temperature window reported by other authors, who synthesized bimetallic Pt-Co NPs by different methods. Except in the case of (Komatsu and Tamura, 2008), the highest temperature windows encountered in the literature,

TABLE 2 | Comparison with literature data for bimetallic PtCo, including composition, preparation method, characterization of intermetallic phases and temperature operation window.

References	Catalyst composition metal load % wt.	Preparation method	Active phases reported	WHSW ($l\ g\ h^{-1}$)	Temperature operating window
Yan et al., 2004	3%Pt 1%Co/γ-Al_2O_3	Sequential impregnation method Pt followed by Co. In both cases after impregnation calcination and reduction steps.	Pt_3Co phase identified by XRD	40	120–160°C
Ko et al., 2007	0.5%Pt-Co/YSZ (Co/Pt=5)	Sequential impregnation method Pt followed by Co. In both cases after impregnation calcination and reduction steps.	TEM: Isolated Pt-Co and Co nanoparticles. No XRD or XPS available	60	100–120°C
Snytnikov et al., 2007	2 % (Co–Pt)/C	Sequential impregnation of Pt and Co salts to obtain $[Co(NH_3)_5NO_2][Pt(NO_2)_4]$ $1.5H_2O$ followed by reduction in H_2	$Co_{0.5}Pt_{0.5}$ phase identified by XRD	N.A.	120–150°C
Komatsu and Tamura, 2008	Pt_3Co/SiO_2 (3% Pt and Pt/Co=3)	Co-impregnation method	Pt_3Co phase identified by XRD	8.4	180°C
Wang et al., 2013	Pt-Co/AlPO-5 (1%Pt-2%Co)	Co-impregnation method	EDX analysis of Pt-Co, presence of both metals	24	110–125°C
Furukawa et al., 2016	Pt_3Co/MgO (3 wt%, Pt, Pt/Co = 3)	Co-impregnation method	Pt_3Co phase identified by XRD	162	120–160°C
Lopez et al., 2016	1.4%PtCoOx/ETS-10	$PtCoO_x$ NPs synthesized by sequential chemical wet reduction of Co and Pt salts, followed by incipient wetness impregnation of NPs in support	EDX analysis of Pt-Co, presence of both metals. Absence of Pt_3Co phase discarded by XRD and XPS analysis	30	125–150°C
This work	1.4%Pt_4Co/ETS-10	Pt_4Co NPs synthesized by pyrolysis laser followed by incipient wetness impregnation of NPs in support	Pt_3Co phase identified by XRD and XPS	30	125–175°C

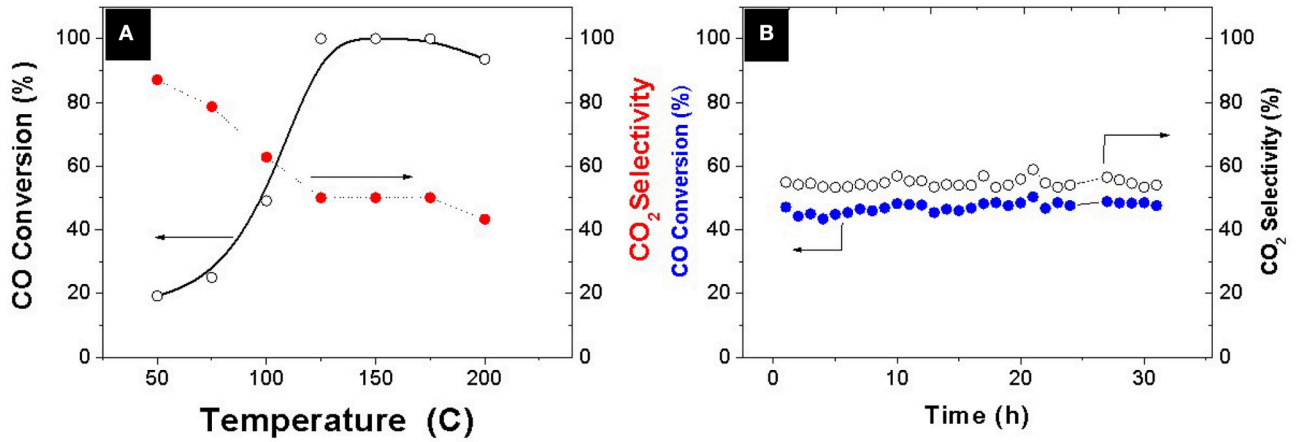

FIGURE 3 | (A) Evolution of CO conversion and CO_2 selectivity as a function of temperature **(B)** Time at T = 100°C. Feed composition: 1% CO, 1% O_2, 3% H_2O, 21% CO_2, and H_2 balance WHSW = 30 L·g^{-1}·h^{-1}.

40°C, correspond to the cases where the intermetallic Pt_3Co phase has been identified by XRD or XRD and XPS. In our previous work (Lopez et al., 2016) we synthesized NPs by successive chemical impregnation at low temperature, where the intermetallic phase was discarded by XRD and XPS analysis. The bimetallic NPs consist of CoO_x on the surface of Pt, and the high activity at low temperature was associated to the presence of cobalt oxides that act as an oxygen reservoir. Oxygen is supplied by the reducible oxides to the CO adsorbed on the surface and the adsorption of oxygen on the surface, which is proposed as rate determining step in the case of non-promoted Pt catalysts, it is not necessary. However, the conversion in this work at a temperature as low as 50°C, is slightly higher, 20% compared to 12% (Lopez et al., 2016) at the same WHSV and similar metal load 1.4wt.%. Thus, the geometric effect associated to the Pt_3Co alloy, widening the Pt-Pt atomic distance and electron transfer from Pt to Co, has lower sensitivity to temperature. The experimental results obtained in the present work remark the importance of the alloy formation in the catalytic results, increasing the activity of the catalyst, and widening the temperature operation window. Finally, the catalyst stability was tested for 30 h (**Figure 3B**) and no deactivation was observed.

Analogous wide temperature windows in PROX have been only reported when bimetallic alloy nanoparticles are present. Wang et al. (2013) prepared a PtCo catalyst (4%wt.) supported on $AlPO_4$ and reported the complete removal of CO, in a simulated reformate stream at temperatures ranging from 80 to 130°C working at 30 L g^{-1} h^{-1} with an optimized catalyst containing a load of Pt as high as 4 and 0.7% Co supported on carbon nanotubes. Recently Furukawa et al. (2016) also reported a wide temperature window 90 to 160°C with a catalyst 3 wt.% Pt, Pt_3Co supported in MgO at 162 L g^{-1} h^{-1} without the presence of CO_2 and H_2O.

CONCLUSIONS

In summary, carbon-encapsulated alloy nanoparticles (Pt_xCo_y/C) have been successfully synthesized with controllable composition by a facile one-pot laser-assisted method. The carbon encapsulation strategy not only allows to prepare stable and well-dispersed bimetallic nanoparticles < 3 nm in size, but also prevents nanoparticles from agglomeration. The as-prepared Pt_4Co/C catalyst has exhibited superior activity for the oxidation of CO in a simulated reformate gas stream. The solid containing 1.5 wt.% of nanoparticles can achieve complete CO conversion in a wide temperature window range of 125 to 175°C working at WHSV = 30 L h^{-1} g^{-1}. The stability of this solid was tested for 30 h, showing no changes in CO conversion or selectivity. This work offers not only an important strategy to prepare stable Pt-Co bimetallic nanoparticles, but also provides an innovative alternative for the synthesis of high-performance catalysts, which may enable a wide variety of potentials applications in many fields, such as catalytic electrodes in the oxygen evolution reaction ORR.

AUTHOR CONTRIBUTIONS

GM, AM, RM, and JS designed the experiments. GM, AM, and AL performed the reaction experiments. JLH contributed in the characterization. GM, AM, and AL designed and performed the experimental setup to determine the catalytic activity. GM, RM, and JS co-wrote the manuscript with the contribution and approval of all the authors.

ACKNOWLEDGMENTS

Financial support from MINECO (Spain) and the CIBER-BBN (initiative funded by the VI National R&D&i Plan 2008–2011, Iniciativa Ingenio 2010, Consolider Program, CIBER Actions and financed by the Instituto de Salud Carlos III with assistance from the European Regional Development Fund) is gratefully acknowledged. The synthesis of materials has been performed by the Platform of Production of Biomaterials and Nanoparticles of the NANOBIOSIS ICTS, more specifically by the Nanoparticle Synthesis Unit of the CIBER in BioEngineering, Biomaterials & Nanomedicine (CIBER-BBN). The microscopy works have been conducted in the Laboratorio de Microscopias

Avanzadas at Instituto de Nanociencia de Aragon—Universidad de Zaragoza. Authors acknowledge the LMA-INA for offering access to their instruments and expertise. Authors thank Sr. Silvia Irusta for many helpful discussions and for performing the XPS measurements.

SUPPLEMENTARY MATERIAL

The Supplementary Material for this article can be found online at: https://www.frontiersin.org/articles/10.3389/fchem.2018.00487/full#supplementary-material

REFERENCES

Antolini, E. (2003). Formation of carbon-supported PtM alloys for low temperature fuel cells: a review. *Mater. Chem. Phys.* 78, 563–573. doi: 10.1016/S0254-0584(02)00389-9

Arbizzani, C., Righi, S., Soavi, F., and Mastragostino, M. (2011). Graphene and carbon nanotube structures supported on mesoporous xerogel carbon as catalysts for oxygen reduction reaction in proton-exchange-membrane fuel cells. *Int. J. Hydrogen Energy* 36, 5038–5046. doi: 10.1016/j.ijhydene.2011.01.083

Arico, A. S., Poltarzewski, Z., Kim, H., Morana, A., Giordano, N., and Antonucci, V. (1995). Investigation of a carbon-supported quaternary pt-ru-sn-w catalyst for direct methanol fuel-cells. *J. Power Sources* 55, 159–166. doi: 10.1016/0378-7753(94)02178-6

Arico, A. S., Shukla, A. K., Kim, H., Park, S., Min, M., and Antonucci, V. (2001). An XPS study on oxidation states of Pt and its alloys with Co and Cr and its relevance to electroreduction of oxygen. *Appl. Surf. Sci.* 172, 33–40. doi: 10.1016/S0169-4332(00)00831-X

Bardi, U., Beard, B. C., and Ross, P. N. (1990). CO chemisorption on the 111 and 100 oriented single-crystal surfaces of the alloy $CoPt_3$. *J. Catal.* 124, 22–29. doi: 10.1016/0021-9517(90)90100-X

Ferrari, A. C. (2007). Raman spectroscopy of graphene and graphite: Disorder, electron-phonon coupling, doping and nonadiabatic effects. *Solid State Commun.* 143, 47–57. doi: 10.1016/j.ssc.2007.03.052

Furukawa, S., Ehara, K., and Komatsu, T. (2016). Unique reaction mechanism of preferential oxidation of CO over intermetallic Pt_3Co catalysts: surface-OH-mediated formation of a bicarbonate intermediate. *Catal. Sci. Technol.* 6, 1642–1650. doi: 10.1039/C5CY01652E

Furukawa, S., and Komatsu, T. (2017). Intermetallic compounds: promising inorganic materials for well-structured and electronically modified reaction environments for efficient catalysis. *ACS Catal.* 7, 735–765. doi: 10.1021/acscatal.6b02603

Ghimbeu, C. M., Sopronyi, M., Sima, F., Delmotte, L., Vaulot, C., Zlotea, C., et al. (2015). One-pot laser-assisted synthesis of porous carbon with embedded magnetic cobalt nanoparticles. *Nanoscale* 7, 10111–10122. doi: 10.1039/C5NR01687H

Han, C., Bo, X. J., Zhang, Y. F., Li, M., Nsabimana, A., and Guo, L. P. (2015). N-doped graphitic layer encased cobalt nanoparticles as efficient oxygen reduction catalysts in alkaline media. *Nanoscale* 7, 5607–5611. doi: 10.1039/C4NR07571D

Huang, H. H., Hu, X. L., Zhang, J. B., Su, N., and Cheng, J. X. (2017). Facile fabrication of platinum-cobalt alloy nanoparticles with enhanced electrocatalytic activity for a methanol oxidation reaction. *Sci. Rep.* 7:45555. doi: 10.1038/srep45555

Huang, Q. H., Yang, H., Tang, Y. W., Lu, T. H., and Akins, D. L. (2006). Carbon-supported Pt-Co alloy nanoparticles for oxygen reduction reaction. *Electrochem. commun.* 8, 1220–1224. doi: 10.1016/j.elecom.2006.05.027

Hueso, J. L., Caballero, A., Ocana, M., and Gonzalez-Elipe, A. R. (2008). Reactivity of lanthanum substituted cobaltites toward carbon particles. *J. Catal.* 257, 334–344. doi: 10.1016/j.jcat.2008.05.012

Jang, J. H., Kim, J., Lee, Y., H., Kim, I., Y., Park, M., H., et al. and Kwon, Y., U. (2011). One-pot synthesis of core shell-like Pt_3Co nanoparticle electrocatalyst with Pt-enriched surface for oxygen reduction reaction in fuel cells. *Energy Environ. Sci.* 4, 4947–4953. doi: 10.1039/c1ee01825f

Jiang, S. J., Ma, Y., W., Jian, G., Q., Tao, H., S., Wang, X., Z., et al. and Chen, Y. (2009). Facile construction of Pt-Co/CNx nanotube electrocatalysts and their application to the oxygen reduction reaction. *Adv. Mater.* 21, 4953–4956. doi: 10.1002/adma.200900677.

Jimenez, V. M., Fernandez, A., Espinos, J. P., and Gonzalezelipe, A. R. (1995). The state of the oxygen at the surface of polycrystalline cobalt oxide. *J. Electron Spectros. Relat. Phenom.* 71, 61–71. doi: 10.1016/0368-2048(94)02238-0

Kang, J., Li, O. L., and Saito, N. (2013). A simple synthesis method for nano-metal catalyst supported on mesoporous carbon: the solution plasma process. *Nanoscale* 5, 6874–6882. doi: 10.1039/c3nr01229h

Ko, E. Y., Park, E. D., Lee, H. C., Lee, D., and Kim, S. (2007). Supported Pt-Co catalysts for selective CO oxidation in a hydrogen-rich stream. *Angew. Chem. Int. Edn.* 46, 734–737. doi: 10.1002/anie.200603144

Komatsu, T., and Tamura, A. (2008). Pt_3Co and PtCu intermetallic compounds: promising catalysts for preferential oxidation of CO in excess hydrogen. *J. Catal.* 258, 306–314. doi: 10.1016/j.jcat.2008.06.030

Lin, P. A., and Sankaran, R. M. (2011). Plasma-assisted dissociation of organometallic vapors for continuous, gas-phase preparation of multimetallic nanoparticles. *Angew. Chem. Int. Edn.* 50, 10953–10956. doi: 10.1002/anie.201101881

Liu, K., Wang, A. Q., and Zhang, T. (2012). Recent advances in preferential oxidation of CO reaction over platinum group metal catalysts. *ACS Catal.* 2, 1165–1178. doi: 10.1021/cs200418w

Liu, X. J., Zhou, Y. C., Zhou, W. J., Li, L. G., Huang, S. B., and Chen, S. W. (2015). Biomass-derived nitrogen self-doped porous carbon as effective metal-free catalysts for oxygen reduction reaction. *Nanoscale* 7, 6136–6142. doi: 10.1039/C5NR00013K

Lopez, A., Navascues, N., Mallada, R., and Irusta, S. (2016). Pt-CoOx nanoparticles supported on ETS-10 for preferential oxidation of CO reaction. *Appl. Catal.* 528, 86–92. doi: 10.1016/j.apcata.2016.09.018

Malumbres, A., Martinez, G., Hueso, J. L., Gracia, J., Mallada, R., and Santamaria, J. (2015). Facile production of stable silicon nanoparticles: laser chemistry coupled to in situ stabilization via room temperature hydrosilylation. *Nanoscale* 7, 8566–8573. doi: 10.1039/C5NR01031D

Malumbres, A., Martinez, G., Mallada, R., Hueso, J. L., Bomati-Miguel, O., and Santamaria, J. (2013). Continuous production of iron-based nanocrystals by laser pyrolysis. Effect of operating variables on size, composition and magnetic response. *Nanotechnology* 24:325603. doi: 10.1088/0957-4484/24/32/325603

Martínez, G., Malumbres, A., Mallada, R., Hueso, J. L., Irusta, S., and Santamaria, J. (2012). Use of a polyol liquid collection medium to obtain ultrasmall magnetic nanoparticles by laser pyrolysis. *Nanotechnology* 23:425605. doi: 10.1088/0957-4484/23/42/425605

Min, M. K., Cho, J. H., Cho, K. W., and Kim, H. (2000). Particle size and alloying effects of Pt-based alloy catalysts for fuel cell applications. *Electrochim. Acta* 45, 4211–4217. doi: 10.1016/S0013-4686(00)00553-3

Munoz, E., Ruiz-Gonzalez, M. L., Seral-Ascaso, A., Sanjuan, M. L., Gonzalez-Calbet, J. M., de la Fuente, et al. (2010). Tailored production of nanostructured metal/carbon foam by laser ablation of selected organometallic precursors. *Carbon* 48, 1807–1814. doi: 10.1016/j.carbon.2010.01.025

Owen, E. A., and Jones, D. M. (1954). Effect of grain size on the crystal structure of cobalt. *Proc. Phys. Soc. B* 67:456.

Rodriguez, P., Tichelaar, F. D., Koper, M. T. M., and Yanson, A. I. (2011). Cathodic corrosion as a facile and effective method to prepare clean metal alloy nanoparticles. *J. Am. Chem. Soc.* 133, 17626–17629. doi: 10.1021/ja208264e

Saedy, S., Palagin, D., Safonova, O., van Bokhoven, J. A., Khodadadi, A. A., and Mortazavi, Y. (2017). Understanding the mechanism of synthesis of Pt3Co intermetallic nanoparticles via preferential chemical vapor deposition. *J. Mater. Chem. A* 5, 24396–24406. doi: 10.1039/C7TA06737B

Salgado, J. R. C., Antolini, E., and Gonzalez, E. R. (2005). Carbon supported Pt-Co alloys electrocatalysts for as methanol-resistant oxygen-reduction direct methanol fuel cells. *Appl. Catal. B Environ.* 57, 283–290. doi: 10.1016/j.apcatb.2004.11.009

Santiago, E. I., Varanda, L. C., and Villullas, H. M. (2007). Carbon-supported Pt-Co catalysts prepared by a modifled polyol process as cathodes for PEM fuel cells. *J. Phys. Chem. C* 111, 3146–3151. doi: 10.1021/jp0670081

Senkan, S., Kahn, M., Duan, S., Ly, A., and Leidhom, C. (2006). High-throughput metal nanoparticle catalysis by pulsed laser ablation. *Catal. Today* 117, 291–296. doi: 10.1016/j.cattod.2006.05.051

Seral-Ascaso, A., Garriga, R., Sanjuan, M. L., Razal, J. M., Lahoz, R., et al. (2013). Laser chemistry' synthesis, physicochemical properties, and chemical processing of nanostructured carbon foams. *Nanoscale Res. Lett.* 8:233. doi: 10.1186/1556-276X-8-233

Service, R. F. (2002). Fuel Cells: Shrinking fuel cells promise power in your pocket. *Science* 296, 1222–1224. doi: 10.1126/science.296.5571.1222

Shukla, A. K., Arico, A. S., El-Khatib, K. M., Kim, H., Antonucci, P. L., and Antonucci, V. (1999). An X-ray photoelectron spectroscopic study on the effect of Ru and Sn additions to platinised carbons. *Appl. Surf. Sci.* 137, 20–29. doi: 10.1016/S0169-4332(98)00483-8

Snytnikov, P. V., Yusenko, K. V., Korenev, S. V., Shubin, Y. V., and Sobyanin, V. A. (2007). Co-Pt bimetallic catalysts for the selective oxidation of carbon monoxide in hydrogen-containing mixtures. *Kinetics Catal.* 48, 276–281. doi: 10.1134/S0023158407020127

Stamenkovic, V. R., Mun, B. S., Arenz, M., Mayrhofer, K. J. J., Lucas, C. A., and Markovic, N. M. (2007). Trends in electrocatalysis on extended and nanoscale Pt-bimetallic alloy surfaces. *Nat. Mater.* 6, 241–247. doi: 10.1038/nmat1840

Strobel, R., Grunwaldt, J. D., Camenzind, A., Pratsinis, S. E., and Baiker, A. (2005). Flame-made alumina supported Pd-Pt nanoparticles: Structural properties and catalytic behavior in methane combustion. *Catal. Lett.* 104, 9–16. doi: 10.1007/s10562-005-7429-y

Swanson, H. E., and Eleanor, T. (1953). Circular of the Bureau of Standards no. 539 volume 1: standard X-ray diffraction powder patterns. *Nat. Bureau Standards Circular* 1:539.

Takenaka, S., Hirata, A., Tanabe, E., Matsune, H., and Kishida, M. (2010). Preparation of supported Pt-Co alloy nanoparticle catalysts for the oxygen reduction reaction by coverage with silica. *J. Catal.* 274, 228–238. doi: 10.1016/j.jcat.2010.07.005

Tamizhmani, G., and Capuano, G. A. (1994). Improved electrocatalytic oxygen reduction performance of platinum ternary alloy-oxide in solid-polymer-electrolyte fuel-cells. *J. Electrochem. Soc.* 141, 968–975. doi: 10.1149/1.2054866

Tao, F., Zhang, S. R., Nguyen, L., and Zhang, X. Q. (2012). Action of bimetallic nanocatalysts under reaction conditions and during catalysis: evolution of chemistry from high vacuum conditions to reaction conditions. *Chem. Soc. Rev.* 41, 7980–7993. doi: 10.1039/c2cs35185d

Vinayan, B. P., Jafri, R. I., Nagar, R., Rajalakshmi, N., Sethupathi, K., and Ramaprabhu, S. (2012). Catalytic activity of platinum-cobalt alloy nanoparticles decorated functionalized multiwalled carbon nanotubes for oxygen reduction reaction in PEMFC. *Int. J. Hydrogen Energy* 37, 412–421. doi: 10.1016/j.ijhydene.2011.09.069

Vonhoene, J., Charles, R. G., and Hickam, W. M. (1958). Thermal decomposition of metal acetylacetonates mass spectrometer studies. *J. Phys. Chem.* 62, 1098–1101. doi: 10.1021/j150567a019

Wang, C. X., Zhang, L. H., and Liu, Y. T. (2013). Aluminumphosphate molecular sieves supported Pt-Co catalysts for the preferential oxidation of CO in H-2-rich gases. *Applied Catalysis B-Environmental* 136: 48–55. doi: 10.1016/j.apcatb.2013.02.001

Wang, D. S., and Li, Y. D. (2011). Bimetallic nanocrystals: liquid-phase synthesis and catalytic applications. *Adv. Mater.* 23, 1044–1060. doi: 10.1002/adma.201003695

Wang, G. H., Hilgert, J., Richter, F. H., Wang, F., Bongard, H. J., and Schuth, F. (2014). Platinum-cobalt bimetallic nanoparticles in hollow carbon nanospheres for hydrogenolysis of 5-hydroxymethylfurfural. *Nat. Mater.* 13, 294–301. doi: 10.1038/nmat3872

Wang, L. P., Leconte, Y., Feng, Z. X., Wei, C., Zhao, Y., and Xu, Z. J. (2017). Novel preparation of N-doped SnO_2 nanoparticles via laser-assisted pyrolysis: demonstration of exceptional lithium storage properties. *Adv. Mater.* 29:1603286. doi: 10.1002/adma.201603286

Xia, B. Y., Wu, H. B., Li, N., Yan, Y., Lou, X. W., and Wang, X. (2015). One-pot synthesis of Pt-Co alloy nanowire assemblies with tunable composition and enhanced electrocatalytic properties. *Angew. Chem. Int. Edn.* 54, 3797–3801. doi: 10.1002/anie.201411544

Xiong, L., Kannan, A. M., and Manthiram, A. (2002). Pt-M (M = Fe, Co, Ni and Cu) electrocatalysts synthesized by an aqueous route for proton exchange membrane fuel cells. *Electrochem. commun.* 4, 898–903. doi: 10.1016/S1388-2481(02)00485-X

Xiong, L., and Manthiram, A. (2005). Nanostructured Pt-M/C (M = Fe and Co) catalysts prepared by a microemulsion method for oxygen reduction in proton exchange membrane fuel cells. *Electrochim. Acta* 50, 2323–2329. doi: 10.1016/j.electacta.2004.10.046

Xiong, L. F., and Manthiram, A. (2004). Influence of atomic ordering on the electrocatalytic activity of Pt-Co alloys in alkaline electrolyte and proton exchange membrane fuel cells. *J. Mater. Chem.* 14, 1454–1460. doi: 10.1039/B400968C

Yan, J., Ma, J. X., Cao, P., and Li, P. (2004). Preferential oxidation of CO in H-2-rich gases over Co-promoted Pt-gamma-Al2O3 catalyst. *Catal. Lett.* 93, 55–60. doi: 10.1023/B:CATL.0000016949.72039.38

Yu, W. T., Porosoff, M. D., and Chen, J. G. G. (2012). Review of Pt-based bimetallic catalysis: from model surfaces to supported catalysts. *Chem. Rev.* 112, 5780–5817. doi: 10.1021/cr300096b

Zheng, J. N., He, L. L., Chen, C., Wang, A. J., Ma, K. F., and Feng, J. J. (2014a). One-pot synthesis of platinum(3)cobalt nanoflowers with enhanced oxygen reduction and methanol oxidation. *J. Power Sources* 268, 744–751. doi: 10.1016/j.jpowsour.2014.06.109

Zheng, J. N., Li, S. S., Ma, X. H., Chen, F. Y., Wang, A. J., and Feng, J. J. (2014b). Popcorn-like PtAu nanoparticles supported on reduced graphene oxide: facile synthesis and catalytic applications. *J. Mater. Chem. A* 2, 8386–8395. doi: 10.1039/C4TA00857J

Zignani, S. C., Antolini, E., and Gonzalez, E., R. (2008). Evaluation of the stability and durability of Pt and Pt-Co/C catalysts for polymer electrolyte membrane fuel cells. *J. Power Sources* 182, 83–90. doi: 10.1016/j.jpowsour.2008.03.061

Zsoldos, Z., and Guczi, L. (1992). Structure and catalytic activity of alumina supported platinum cobalt bimetallic catalysts.3. effect of treatment on the interface layer. *J. Phys. Chem.* 96, 9393–9400. doi: 10.1021/j100202a061

Conflict of Interest Statement: The authors declare that the research was conducted in the absence of any commercial or financial relationships that could be construed as a potential conflict of interest.

frontiers in Chemistry

MINI REVIEW
published: 11 December 2018
doi: 10.3389/fchem.2018.00619

Magnetic Drug Delivery: Where the Field Is Going

Paige M. Price[1], *Waleed E. Mahmoud*[2], *Ahmed A. Al-Ghamdi*[2] and *Lyudmila M. Bronstein*[1,2,3]*

[1] Department of Chemistry, Indiana University, Bloomington, IN, United States, [2] Department of Physics, Faculty of Science, King Abdulaziz University, Jeddah, Saudi Arabia, [3] A.N. Nesmeyanov Institute of Organoelement Compounds, Russian Academy of Sciences, Moscow, Russia

Targeted delivery of anticancer drugs is considered to be one of the pillars of cancer treatment as it could allow for a better treatment efficiency and less adverse effects. A promising drug delivery approach is magnetic drug targeting which can be realized if a drug delivery vehicle possesses a strong magnetic moment. Here, we discuss different types of magnetic nanomaterials which can be used as magnetic drug delivery vehicles, approaches to magnetic targeted delivery as well as promising strategies for the enhancement of the imaging-guided delivery and the therapeutic action.

Keywords: magnetic drug delivery, magnetic targeting, theranostics, iron oxide, magnetic implant

OPEN ACCESS

Edited by:
Carlos Lodeiro, Universidade Nova de Lisboa, Portugal

Reviewed by:
Anna Roig, Instituto de Ciencia de Materiales de Barcelona (ICMAB), Spain
Paolo Saccardo, Autonomous University of Barcelona, Spain

***Correspondence:**
Lyudmila M. Bronstein
lybronst@indiana.edu

Specialty section:
This article was submitted to Nanoscience, a section of the journal Frontiers in Chemistry

Received: *11 September 2018*
Accepted: *30 November 2018*
Published: *11 December 2018*

Citation:
Price PM, Mahmoud WE, Al-Ghamdi AA and Bronstein LM (2018) Magnetic Drug Delivery: Where the Field Is Going. Front. Chem. 6:619. doi: 10.3389/fchem.2018.00619

INTRODUCTION

The majority of anticancer drugs are delivered intravenously and accumulated in tumors containing the abundance of leaking blood vessels. However, this affects healthy tissue and causes numerous side effects. The more efficient approach is realized when drug nanocarriers are functionalized with target molecules [for example, folate (FA) groups], which interact with specific receptors located in certain tumors, allowing for the attachment of the drug delivery vehicles solely to the tumor (Fernandez et al., 2018; Rosiere et al., 2018; Sun, Q. et al., 2018; Sun, W. et al., 2018). This approach allows for a significant decrease of side effects caused by chemotherapy agents (Li et al., 2017; Peng et al., 2017; Sun, W. et al., 2018). Another drug delivery approach which can be used for many types of tumors is magnetic drug targeting which can be achieved if a drug delivery vehicle possesses a strong magnetic moment and can be manipulated by a magnetic field (Lee et al., 2017; Luong et al., 2017; Wei et al., 2017).

Magnetic drug delivery was first introduced in the 80's (Widder et al., 1980; Kost and Langer, 1986) but in the last decade the interest to magnetic targeting soared due to the development of stronger magnets and higher sophistication magnetic probes with multiple functions, i.e., theranostic probes (Nan et al., 2017; Sun, Q. et al., 2018; Tang et al., 2018). Such probes allow for a combination of diagnostics (magnetic resonance imaging (MRI) or magnetic particle imaging), and therapeutics, which could include hyperthermia and drug release as well as targeted drug delivery (for example, with an applied magnetic field).

A substantial number of reviews has been published on magnetic drug delivery (Kost and Langer, 1986; Lubbe et al., 2001; Duran et al., 2008; Herrmann et al., 2009; Williams et al., 2009; Foy and Labhasetwar, 2011; Tietze et al., 2012, 2015; Mody et al., 2014; Lyer et al., 2015; Mitra et al., 2015; Shapiro et al., 2015), the latest of which appeared as recently as 2016–2017 (Ulbrich et al., 2016; Grillone and Ciofani, 2017; Kralj et al., 2017; Mosayebi et al., 2017). However, the explosive development of this field in the last two years reveals the need in reviewing recent findings and better understanding of the major trends and shortcomings.

DEVELOPMENT OF MAGNETIC DRUG DELIVERY PROBES

Currently, there are many different types of magnetic bioprobes which are being explored for magnetic targeting. In this review, we will focus on the most promising bioprobes from the viewpoint of magnetic manipulation and loading/release of specific drugs.

Magnetic Nano/Microparticles

Magnetic microspheres were developed to overcome two major issues that are present with non-magnetic microcarriers: reticuloendothelial system clearance and poor site specificity (Kakar et al., 2013). One of the approaches is to develop porous or hollow/porous microspheres from magnetic spinel ferrites $M_xFe_{3-x}O_4$ (M=Fe, Zn). Their high magnetism means the microspheres can be easily manipulated by a magnet within the vascular system and, more specifically, remain in the target organ capillaries. Chen et al. utilized a hollow nanoparticle (NP) with a mesoporous shell which creates a higher surface area and a large cavity where drug can be encapsulated in both the mesopores and the cavities (Chen et al., 2017). Additionally, $M_xFe_{3-x}O_4$ (M=Fe, Zn) produce more heat under microwave irradiation which allows easier release of the loaded drug. However, doping of iron oxide causes the decrease of the saturation magnetization which diminishes the microsphere potential for magnetic targeting (Chen et al., 2017).

Another approach to synthesizing microspheres is the combination of a polymer with inorganic NPs. Wang et al. utilized poly(ε-caprolactone) (PCL) to encapsulate both Fe_3O_4 NPs and the anti-cancer drug, doxorubicin hydrochloride (DOX) (Wang, G. et al., 2018). The superparamagnetic composite microspheres showed a high drug loading and a quick magnetic response. The drug release was shown to be pH-sensitive with a high initial release and sustained release over many days.

Microparticles of dry powder chemotherapeutic containing iron oxide NPs (called nano-in-microparticles, NIMs) were used for magnetic delivery into lungs with an applied magnetic field (Price et al., 2017). Mice were endotracheally administered fluorescently labeled NIMs as a dry powder in the presence of an external magnet placed over one lung. It was demonstrated that in the magnetically activated lung, DOX loaded NIMs were therapeutically efficient, thus allowing for a targeted delivery.

Specific gene delivery has been realized with biomimetic magnetic microparticles (magnetosomes) synthesized utilizing magnetic nanocluster (MNC) core and Arg–Gly–Asp (RGD) decorated macrophage shell (Zhang et al., 2018). The magnetosome synthesis was accomplished via several steps including MNC preparation, azide-membrane engineering, electrostatic assembly, and click chemistry. This complex approach to magnetosomes is well-justified, allowing for high-performance siRNA delivery through a superior stealth effect, MRI, magnetic accumulation via an external magnetic field, RGD targeting, and favorable cytoplasm trafficking.

Drug-loaded microparticles prepared by layer-by-layer (LbL) deposition of polyelectrolytes with embedded magnetic NPs were attached to *Escherichia coli* bacteria, creating stochastic "microswimmers" which moved at average speeds of up to 22.5 μm/s (Park et al., 2017). These "microswimmers" displayed biased and directional motion under a chemoattractant gradient and a magnetic field, respectively. This work demonstrates that multifunctional bacteria-driven magnetic bioprobes can be used for targeted drug delivery with significantly enhanced drug transfer in comparison to passive microparticles. Another interesting example of "microswimmers" was reported in (Stanton et al., 2017). The non-pathogenic magnetotactic bacteria Magnetosopirrillum gryphiswalense (MSR-1) was combined with antibiotic loaded mesoporous silica microtubes for targeting an infectious biofilm. Combining magnetic guidance property and swimming power of the MSR-1 cells, the biocomposite particles have been delivered to the matured *E. coli* (*E. coli*) biofilm followed by the antibiotic release and the biofilm disruption, revealing a potential for antibiofilm applications.

Xu et al. reported the development of an unprecedented sperm-hybrid micromotor for targeted drug delivery (Xu et al., 2018). This micromotor consists of a motile sperm cell which is both a propulsion source and a drug carrier (**Figure 1**). The other component is a 3D-printed magnetic tubular microstructure (called "tetrapod") made of a polymer and coated with 10 nm Fe and 2 nm Ti (to protect Fe from oxidation). The tetrapod contains four arms which release the sperm cell *in situ* when they are pushed into a tumor. A magnetic field allows for controllable magnetic guidance as well as release, allowing drug delivery to tumor cells without damaging the healthy tissue. This system combines high drug loading capacity, self-propulsion, *in situ* mechanical trigger release of the drug-loaded sperm, sperm penetration ability, and improved drug availability.

In order to develop multifunctional NPs combining a near-infrared (NIR) plasmonic response with magnetic targeting, Tsai et al. deposited a double layer of Au/Ag alloy on the surface of truncated octahedral iron oxide NPs (Tsai et al., 2018). The rattle-shaped nanostructures exhibited a response for photothermal therapy (PTT) and magnetic guidance for hyperthermia and MRI as well as accumulation of the probes using an external magnetic field. The distance between the layers was controlled for maximum NIR absorption. These probes do not require a drug for chemotherapy as a dual action is already realized with PTT and hyperthermia.

Nanoparticle Clustering/Assembly

One of the primary issues with using superparamagnetic iron oxide NPs is that the individual NPs do not display high magnetization which is unfavorable for guiding them through the body (Kralj et al., 2017). A way to overcome this problem is clustering of NPs to increase their overall magnetic response. Zheng et al. synthesized copolymers of hyaluronic acid (HA) and C_{16} micelles using peptide formation followed by encapsulation of docetaxel (DTX, an anti-cancer agent) and NPs to develop multifunctional micelles (Zheng et al., 2018). HA is especially attractive because it binds to the CD-44 receptor which is overexpressed in various types of cancer in addition to its biocompatibility and biodegradability (Lee et al., 2012). Cellular uptake occurred via CD-44 receptor-mediated endocytosis and was enhanced by the presence of a magnetic field. This uptake

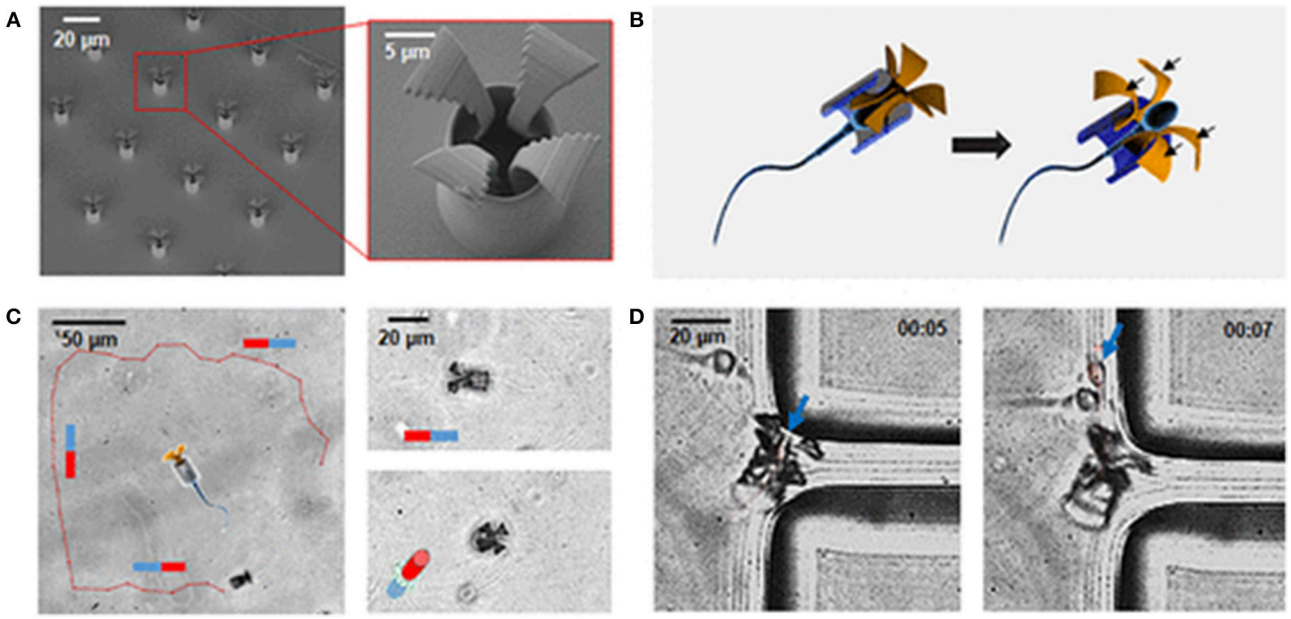

FIGURE 1 | (A) SEM images of an array of printed tetrapod microstructures. **(B)** Schematic illustrating the mechanical release mechanism. **(C)** Track (red line) of a sperm-hybrid motor under magnetic guidance in the horizontal and vertical planes. **(D)** Image sequence of a sperm release process when the arms hit the corner of a polydimethylsiloxane wall. Blue arrows point at the sperm head. Time lapse in min:s (Xu et al., 2018). Reproduced with the permission of the copyright holder [American Chemical Society].

method increases the amount of micelles in the tumor tissues compared to the normal tissues that creates a favorable contrast in MR images. Furthermore, drug release was triggered by NIR irradiation.

Assembly of iron oxide NPs on polydopamine (PDA) NPs allowed for an enhanced magnetic response and stimuli-controlled drug release for *in vivo* cancer theranostics (Ao et al., 2018). The high reactivity of the PDA surface furnishes a possibility for reduction-responsive prodrugs, while poly(ethylene glycol) (PEG) chains allow for *in vivo* cancer therapy. Due to a combination of MRI/photoacoustic dual-modal tumor imaging and controlled magnetic drug targeting, the effective tumor obliteration was accomplished via synergy of NIR photothermal ablation (due to PDA) and anticancer drug magnetic delivery.

Iron oxide NPs with the grafted poly(styrene)-*b*-poly(acrylic acid) (PS-*b*-PAA) block copolymer were self-assembled into multilayer magneto-vesicles (MVs) and utilized for incorporation of drugs in the hollow cavity (Yang et al., 2018). High packing density of iron oxide NPs in MVs allowed for the high magnetization and transverse relaxivity rate ($r2$) in MRI. When injected, DOX-loaded MVs conjugated with RGD peptides were efficiently accumulated in tumor cells due to magnetic targeting.

Innovative magnetic drug delivery vehicles were developed based on magnetite NP clusters (Wang, Y. et al., 2018). Two shells were built on the NP cluster surface: an inner shell of PDA with attached triphenylphosphonium (TPP) and an outer shell of methoxy PEG (mPEG) linked to PDA by disulfide bonds. At the first stage of targeting, the magnetic NP clusters allow for the bioprobe accumulation at the tumor site using an external magnetic field. At the second stage, mitochondrial targeting takes place as the mPEG shell is removed from the NPs by a redox reaction to expose TPP. Upon NIR irradiation at the tumor site, a photothermal effect is produced from the PDA photosensitizer, resulting in a strong decrease in mitochondrial membrane potential. At the same time, DOX is released, leading to the damage of mitochondrial DNA and cell death. Thus, photothermal therapy and chemotherapy are combined with magnetic drug delivery resulting in an enhancement of the DOX performance.

Magnetic Microbubbles

Image-guided and targeted modulation of drug delivery by external physical triggers at the site of pathology has been promising for drug targeting (Vlaskou et al., 2010; Cai et al., 2012). Magnetic microbubbles (MagMB) that are responsive to magnetic and acoustic field changes and visible to ultrasonography were suggested for magnetic drug targeting. Recently, MagMB were prepared by mixing the suspension of protamine-functionalized microbubbles (MB-Prot) with the suspension of the heparinized NPs (Chertok and Langer, 2018). MagMB were gathered in tumor by magnetic targeting and observed by ultrasonography. Using focused ultrasound, MagMB were collapsed when necessary to release a drug. The authors demonstrated drug delivery to tumors could be enhanced by optimizing magnetic and acoustic fields, using ultrasonographic monitoring of MagMB in real-time.

Tang et al. synthesized multifunctional MagMB utilizing poly(lactic-*co*-glycolic acid) (PLGA), FA, perofluorohexane (PFH), Fe_3O_4, and DOX (Tang et al., 2018). These nanocomposites are able to move intravenously due to their initial nanometer-range size. However, when high-intensity focused ultrasound (HIFU) is used, PFH is transformed from the liquid to the gas phase due to an increase in temperature. The PFH gas forms microbubbles which enhance the ultrasound image. Fe_3O_4 allows for the nanocomposite to be efficiently targeted through MRI guidance. Additionally, the FA ligands on the surface of the nanocomposites specifically target the tumor cells via conjugation. The DOX release is triggered by HIFU exposure, and the release is accelerated due to the tumor-acidic microenvironment. Finally, Fe_3O_4 NPs enhance the sensitivity of the tumor via the hyperthermia effect (Moroz et al., 2001). This nanocomposite is an efficient and comprehensive theranostics probe.

Another multifunctional MagMB are based on magnetic liposomes (Liu et al., 2017a). Liposomes range in size from 50 to 1,000 nm and are biocompatible. Both water-soluble and water-insoluble drugs/NPs can be loaded into the core while maintaining high MRI contrast (Liu et al., 2017a). In magnetic liposomes synthesized by Yang et al. γ-Fe_2O_3 were encapsulated by liposomes doped with anethole ditholethione (Liu et al., 2017b). MR imaging was used to follow the accumulation of the magnetic liposomes in the tumor. Additionally, ultrasound was used to produce microbubbles (H_2S) in order to ablate the tumor tissue via an increase in size (Liu et al., 2017b).

Magnetic Microcapsules

Magnetic multilayer microcapsules composed of poly(allylamine hydrochloride) and poly(sodium 4-styrenesulfonate) and prepared by LbL deposition were utilized as magnetic delivery vehicles *in vitro* and *in vivo* (Voronin et al., 2017) *in vivo* experiments performed on mesenteric vessels of white mongrel rats reveal that capsules can be successfully trapped by the magnetic field and even stay there after the magnetic field is turned off. This work validates the effective control of microcapsules in a blood flow, making them promising drug delivery systems with remote navigation by the external magnetic field.

Microcapsules called iMushbots and prepared from mesoporous mushroom (*Agaricus bisporus*) fragments coated with magnetite NPs showed promising properties for targeted delivery (Bhuyan et al., 2017). The magnetite NPs played two roles (i) helping to pH-induced chemotaxis via the heterogeneous catalytic decomposition of the peroxide fuel in the presence of iron oxide and (ii) allowing a remote magnetic control of the iMushbot movement. The iMushbots also demonstrated higher drug retaining ability inside alkaline pH regions (human blood) and easy drug release in acidic medium (cancerous tissue) (**Figure 2**).

Magnetic Fibers

Polyvinyl alcohol fibers filled with magnetite NPs were synthesized via infusion gyration and studied as biocompatible magnetically triggered drug delivery vehicles (Perera et al., 2018). The authors demonstrated that acetaminophen (model drug) uploaded via impregnation can be controllably released by magnetic actuation. Moreover, upon creating a magnetic field 90% cumulative release was observed in 15 min which was much higher than that without magnetic field. These results demonstrate a potential for remote delivery of drugs or other substances.

DRUG UPTAKE/RELEASE

Uptake of drugs in magnetic drug delivery vehicles is carried out similar to non-magnetic carriers via conjugation (Chaudhary et al., 2015; Pourmanouchehri et al., 2018), hydrophobic interactions (Cho et al., 2018), absorption within porous structures (Kakar et al., 2013), etc. The drug release can be triggered by pH changes in the microenvironment (Wang et al., 2017; Wei et al., 2017; Wang, G. et al., 2018), by mechanical forces (Xu et al., 2018), NIR irradiation (Wang, Y. et al., 2018; Zheng et al., 2018), chemical reduction (Ao et al., 2018), HIFU (Moroz et al., 2001), and magnetic hyperthermia (Cho et al., 2018).

CYTOTOXICITY

Cytotoxity of DOX bearing magnetic bioprobes has been discussed in a number of publications both for cancer cells and for healthy tissues (Lee et al., 2017; Ao et al., 2018; Sun, Q. et al., 2018). Cytotoxicity toward healthy cells is limited because most systems are localized and made biocompatible. It is demonstrated that the bioprobes without DOX do not kill cancer cells (Ao et al., 2018), while efficacy of magnetic bioprobes with DOX is comparable to that of free DOX (Ao et al., 2018). Cytotoxicity also increases with increasing amounts of DOX and/or upon NIR irradiation (Sun, Q. et al., 2018).

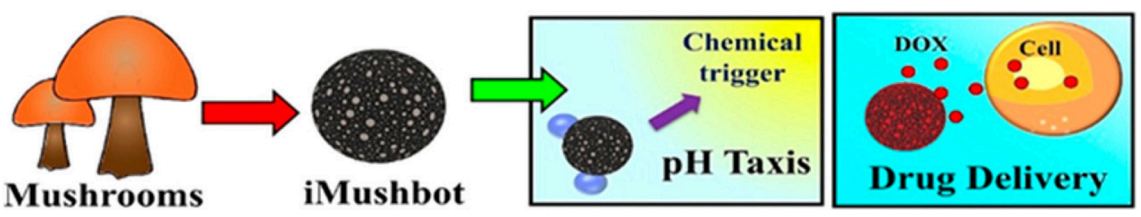

FIGURE 2 | Schematic representation of the iMushbot action (Bhuyan et al., 2017). It is being reproduced with the permission of the copyright holder [American Chemical Society].

APPROACHES TO MAGNETIC DRUG TARGETING

External Magnetic Field

In the majority of cases, the magnetic drug targeting/delivery is realized upon the application of an external magnetic field from electromagnetic coils (Hoshiar et al., 2017) or various types of permanent magnets (Carenza et al., 2014; Price et al., 2017; Shaw et al., 2017; Venugopal et al., 2017; Voronin et al., 2017; Shamsi et al., 2018). It was demonstrated that magnet geometry and tumor-magnet distance can be of crucial importance for the effective magnetic drug delivery (Shamsi et al., 2018; Wang, X. et al., 2018).

Delivery Deep Inside the Body

Utilizing stationary external magnets to attract the magnetic drug carriers, it is difficult to target areas below 5 cm under the skin. A dynamic control of magnets to focus magnetic carriers to deep tissue targets has been proposed (Shapiro, 2009). Using first-principles magneto-statics and ferrofluid transport model, the author demonstrated that a sequence of actuations can push magnetic NPs through a center region, thus generating a focus at a deep target. In the other theoretical work, by rotating the magnet and setting a central axis to the target part, ferromagnetic drugs were accumulated in the target (Chuzawa et al., 2013). However, to the best of our knowledge no experimental studies have confirmed the conclusions of the theoretical work.

Magnetic Implants

Instead of using an external magnetic field which could be problematic in the case of delivery to some organs, magnetic implants seem to be a viable alternative. Ge et al. reported targeted drug delivery to a biocompatible magnetic implant scaffold made of a magnetite/poly(lactic-co-glycolic acid) nanocomposite (Ge et al., 2017). In this case, a drug was attached to magnetic NPs to create a driving force for delivery. Such magnetic implants can be promising for a bone cancer, providing a precise cancer treatment. Magnetic implants can be imbedded in a fatty tissue to treat obesity (Saatchi et al., 2017) and in the inner ear to treat deafness (Le et al., 2017).

SUMMARY AND OUTLOOK

In summary, we can identify several essential rules which need to be followed for the development of successful magnetic drug delivery vehicles. The magnetic bioprobes need to be sufficiently large to possess high magnetization for efficient magnetic targeting. They have to allow for controlled drug uptake and release mechanisms to make them efficient delivery systems. Finally, they have to possess theranostic features (both diagnostic and therapeutic) to enhance the delivery and the drug action. The other key feature of promising magnetic drug delivery vehicles is long-circulating, stealthy systems which will not be cleared by a phagocyte system (Zhang et al., 2017, 2018). This can be realized by a combination of peptides and polymers in the particle outer shells. It is worth noting, however, that the degree of bioprobe sophistication is only warranted by the wealth of properties it delivers, as sometimes simpler systems can be quite satisfactory and less expensive.

It is worth noting that despite FDA approval and commercialization of iron oxide based bioprobes for MRI and hyperthermia, clinical trials of magnetic drug delivery received less attention. To the best of our knowledge, there were several small clinical trials (even in Phase III), but none resulted in FDA approval or commercialization (Wang et al., 2013; Min et al., 2015; Ulbrich et al., 2016).

We believe that the major unsolved problem in magnetic drug delivery is the absence of mechanisms for delivery into the depth of the body. The recent strategy of magnetic or magnetiziable implants seems to be promising but it requires a surgical intervention and in some cases cannot be implemented. Currently, efforts from physicists and engineers are required to move this field forward to real life applications.

AUTHOR CONTRIBUTIONS

PP carried out analysis of the literature and wrote a part on magnetic bioprobe synthesis. WM collected the literature and wrote the rest of the discussion on magnetic bioprobes. AA-G wrote part on approaches to magnetic targeting. LB wrote all other sections and oversaw the project.

REFERENCES

Ao, L., Wu, C., Liu, K., Wang, W., Fang, L., Huang, L., et al. (2018). Polydopamine-derivated hierarchical nanoplatforms for efficient dual-modal imaging-guided combination *in vivo* cancer therapy. *ACS Appl. Mater. Interfaces* 10, 12544–12552. doi: 10.1021/acsami.8b02973

Bhuyan, T., Singh, A. K., Dutta, D., Unal, A., Ghosh, S. S., and Bandyopadhyay, D. (2017). Magnetic field guided chemotaxis of iMushbots for targeted anticancer therapeutics. *ACS Biomater. Sci. Eng.* 3, 1627–1640. doi: 10.1021/acsbiomaterials.7b00086

Cai, X., Yang, F., and Gu, N. (2012). Applications of magnetic microbubbles for theranostics. *Theranostics* 2, 103–112. doi: 10.7150/thno.3464

Carenza, E., Barcelo, V., Morancho, A., Levander, L., Boada, C., Laromaine, A., et al. (2014). *In vitro* angiogenic performance and *in vivo* brain targeting of magnetized endothelial progenitor cells for neurorepair therapies. *Nanomedicine* 10, 225–234. doi: 10.1016/j.nano.2013.06.005

Chaudhary, A., Dwivedi, C., Gupta, A., and Nandi, C. K. (2015). One pot synthesis of doxorubicin loaded gold nanoparticles for sustained drug release. *RSC Advances* 5, 97330–97334. doi: 10.1039/C5RA12892G

Chen, P., Cui, B., Bu, Y., Yang, Z., and Wang, Y. (2017). Synthesis and characterization of mesoporous and hollow-mesoporous MxFe3-xO4 (M=Mg, Mn, Fe, Co, Ni, Cu, Zn) microspheres for microwave-triggered controllable drug delivery. *J. Nanoparticle Res.* 19:398. doi: 10.1007/s11051-017-4096-z

Chertok, B., and Langer, R. (2018). Circulating magnetic microbubbles for localized real-time control of drug delivery by ultrasonography-guided magnetic targeting and ultrasound. *Theranostics* 8, 341–357. doi: 10.7150/thno.20781

Cho, H. Y., Lee, T., Yoon, J., Han, Z., Rabie, H., Lee, K. B., et al. (2018). Magnetic oleosome as a functional lipophilic drug carrier for cancer therapy. *ACS Appl. Mater. Interfaces* 10, 9301–9309. doi: 10.1021/acsami.7b19255

Chuzawa, M., Mishima, F., Akiyama, Y., and Nishijima, S. (2013). Precise control of the drug kinetics by means of non-invasive magnetic drug

delivery system. *Phys. C* 484, 120–124. doi: 10.1016/j.physc.2012.03.070

Duran, J. D. G., Arias, J. L., Gallardo, V., and Delgado, A.V. (2008). Magnetic colloids as drug vehicles. *J. Pharm. Sci.* 97, 2948–2983. doi: 10.1002/jps.21249

Fernandez, M., Javaid, F., and Chudasama, V. (2018). Advances in targeting the folate receptor in the treatment/imaging of cancers. *Chem. Sci.* 9, 790–810. doi: 10.1039/C7SC04004K

Foy, S. P., and Labhasetwar, V. (2011). Oh the irony: Iron as a cancer cause or cure? *Biomaterials* 32, 9155–9158. doi: 10.1016/j.biomaterials.2011.09.047

Ge, J., Zhang, Y., Dong, Z., Jia, J., Zhu, J., Miao, X., et al. (2017). Initiation of targeted nanodrug delivery *in vivo* by a multifunctional magnetic implant. *ACS Appl. Mater. Interfaces* 9, 20771–20778. doi: 10.1021/acsami.7b05009

Grillone, A., and Ciofani, G. (2017). Magnetic nanotransducers in biomedicine. *Chem. Eur. J.* 23, 16109–16114. doi: 10.1002/chem.201703660

Herrmann, I. K., Grass, R. N., and Stark, W. J. (2009). High-strength metal nanomagnets for diagnostics and medicine: carbon shells allow long-term stability and reliable linker chemistry. *Nanomedicine* 4, 787–798. doi: 10.2217/nnm.09.55

Hoshiar, A. K., Le, T. A., Amin, F. U., Kim, M. O., and Yoon, J. (2017). Studies of aggregated nanoparticles steering during magnetic-guided drug delivery in the blood vessels. *J. Magn. Magn. Mater.* 427, 181–187. doi: 10.1016/j.jmmm.2016.11.016

Kakar, S., Batra, D., Singh, R., and Nautiyal, U. (2013). Magnetic microspheres as magical novel drug delivery system: A review. *Journal of Acute Disease* 2, 1–12. doi: 10.1016/S2221-6189(13)60087-6

Kost, J., and Langer, R. (1986). Magnetically modulated drug delivery systems. *Pharm. Int.* 7, 60–63.

Kralj, S., Potrc, T., Kocbek, P., Marchesan, S., and Makovec, D. (2017). Design and fabrication of magnetically responsive nanocarriers for drug delivery. *Curr. Med. Chem.* 24, 454–469. doi: 10.2174/0929867323666160813211736

Le, T. N., Straatman, L., Yanai, A., Rahmanian, R., Garnis, C., Hafeli, U. O., et al. (2017). Magnetic stem cell targeting to the inner ear. *J. Magn. Magn. Mater.* 443, 385–396. doi: 10.1016/j.jmmm.2017.07.033

Lee, D. E., Kim, A. Y., Yoon, H. Y., Choi, K. Y., Kwon, I. C., Jeong, S. Y., et al. (2012). Amphiphilic hyaluronic acid-based nanoparticles for tumor-specific optical/MR dual imaging. *J. Mater. Chem.* 22, 10444–10447. doi: 10.1039/c2jm31406a

Lee, K., David, A. E., Zhang, J., Shin, M. C., and Yang, V. C. (2017). Enhanced accumulation of theranostic nanoparticles in brain tumor by external magnetic field mediated *in situ* clustering of magnetic nanoparticles. *J. Ind. Eng. Chem.* 54, 389–397. doi: 10.1016/j.jiec.2017.06.019

Li, Y., Song, L., Lin, J., Ma, J., Pan, Z., Zhang, Y., et al. (2017). Programmed nanococktail based on pH-responsive function switch for self-synergistic tumor-targeting therapy. *ACS Appl. Mater. Interfaces* 9, 39127–39142. doi: 10.1021/acsami.7b08218

Liu, Y., Li, M., Yang, F., and Gu, N. (2017a). Magnetic drug delivery systems. *Sci. China Mater.* 60, 471–486. doi: 10.1007/s40843-017-9049-0

Liu, Y., Yang, F., Yuan, C., Li, M., Wang, T., Chen, B., et al. (2017b). Magnetic nanoliposomes as *in situ* microbubble bombers for multimodality image-guided cancer theranostics. *ACS Nano* 11, 1509–1519. doi: 10.1021/acsnano.6b06815

Lubbe, A. S., Alexiou, C., and Bergemann, C. (2001). Clinical Applications of magnetic drug targeting. *J. Surg. Res.* 95, 200–206. doi: 10.1006/jsre.2000.6030

Luong, D., Sau, S., Kesharwani, P., and Iyer, A. K. (2017). Polyvalent folate-dendrimer-coated iron oxide theranostic nanoparticles for simultaneous magnetic resonance imaging and precise cancer cell targeting. *Biomacromolecules* 18, 1197–1209. doi: 10.1021/acs.biomac.6b01885

Lyer, S., Tietze, R., Unterweger, H., Zaloga, J., Singh, R., Matuszak, J., et al. (2015). Nanomedical innovation: the SEON-concept for an improved cancer therapy with magnetic nanoparticles. *Nanomedicine* 10, 3287–3304. doi: 10.2217/nnm.15.159

Min, Y., Caster, J. M., Eblan, M. J., and Wang, A. Z. (2015). Clinical translation of nanomedicine. *Chem. Rev.* 115, 11147–11190. doi: 10.1021/acs.chemrev.5b00116

Mitra, A. K., Agrahari, V., Mandal, A., Cholkar, K., Natarajan, C., Shah, S., et al. (2015). Novel delivery approaches for cancer therapeutics. *J. Controlled Release* 219, 248–268. doi: 10.1016/j.jconrel.2015.09.067

Mody, V. V., Cox, A., Shah, S., Singh, A., Bevins, W., and Parihar, H. (2014). Magnetic nanoparticle drug delivery systems for targeting tumor. *Appl. Nanosci.* 4, 385–392. doi: 10.1007/s13204-013-0216-y

Moroz, P., Jones, S. K., Winter, J., and Gray, B. N. (2001). Targeting liver tumors with hyperthermia: Ferromagnetic embolization in a rabbit liver tumor model. *J. Surg. Oncol.* 78, 22–29. doi: 10.1002/jso.1118

Mosayebi, J., Kiyasatfar, M., and Laurent, S. (2017). Synthesis, functionalization, and design of magnetic nanoparticles for theranostic applications. *Adv. Healthcare Mater.* 6:1700306. doi: 10.1002/adhm.201700306

Nan, X., Zhang, X., Liu, Y., Zhou, M., Chen, X., and Zhang, X. (2017). Dual-targeted multifunctional nanoparticles for magnetic resonance imaging guided cancer diagnosis and therapy. *ACS Appl. Mater. Interfaces* 9, 9986–9995. doi: 10.1021/acsami.6b16486

Park, B. W., Zhuang, J., Yasa, O., and Sitti, M. (2017). Multifunctional bacteria-driven microswimmers for targeted active drug delivery. *ACS Nano* 11, 8910–8923. doi: 10.1021/acsnano.7b03207

Peng, Y., Zhao, Z., Liu, T., Li, X., Hu, X., Wei, X., et al. (2017). Smart human-serum-albumin-As2O3 nanodrug with self-amplified folate receptor-targeting ability for chronic myeloid leukemia treatment. *Angew. Chem. Int. Ed.* 56, 10845–10849. doi: 10.1002/anie.201701366

Perera, A. S., Zhang, S., Homer-Vanniasinkam, S., Coppens, M. O., and Edirisinghe, M. (2018). Polymer-magnetic composite fibers for remote-controlled drug release. *ACS Appl. Mater. Interfaces* 10, 15524–15531. doi: 10.1021/acsami.8b04774

Pourmanouchehri, Z., Jafarzadeh, M., Kakaei, S., and Khameneh, E. S. (2018). Magnetic nanocarrier containing 68Ga–DTPA complex for targeted delivery of doxorubicin. *J. Inorgan. Organometal. Polymers Mater.* 28, 1980–1990. doi: 10.1007/s10904-018-0826-7

Price, D. N., Stromberg, L. R., Kunda, N. K., and Muttil, P. (2017). *In vivo* pulmonary delivery and magnetic-targeting of dry powder nano-in-microparticles. *Mol. Pharmaceut.* 14, 4741–4750. doi: 10.1021/acs.molpharmaceut.7b00532

Rosiere, R., Van Woensel, M., Gelbcke, M., Mathieu, V., Hecq, J., Mathivet, T., et al. (2018). New folate-grafted chitosan derivative to improve delivery of paclitaxel-loaded solid lipid nanoparticles for lung tumor therapy by inhalation. *Mol. Pharmaceut.* 15, 899–910. doi: 10.1021/acs.molpharmaceut.7b00846

Saatchi, K., Tod, S. E., Leung, D., Nicholson, K. E., Andreu, I., Buchwalder, C., et al. (2017). Characterization of alendronic- and undecylenic acid coated magnetic nanoparticles for the targeted delivery of rosiglitazone to subcutaneous adipose tissue. *Nanomedicine* 13, 559–568. doi: 10.1016/j.nano.2016.08.012

Shamsi, M., Sedaghatkish, A., Dejam, M., Saghafian, M., Mohammadi, M., and Sanati-Nezhad, A. (2018). Magnetically assisted intraperitoneal drug delivery for cancer chemotherapy. *Drug Deliv.* 25, 846–861. doi: 10.1080/10717544.2018.1455764

Shapiro, B. (2009). Towards dynamic control of magnetic fields to focus magnetic carriers to targets deep inside the body. *J. Magn. Magn. Mater.* 321, 1594–1599. doi: 10.1016/j.jmmm.2009.02.094

Shapiro, B., Kulkarni, S., Nacev, A., Muro, S., Stepanov, P. Y., and Weinberg, I. N. (2015). Open challenges in magnetic drug targeting. *Wiley Interdiscip. Rev.: Nanomed. Nanobiotechnol.* 7, 446–457. doi: 10.1002/wnan.1311

Shaw, S., Sutradhar, A., and Murthy, P. (2017). Permeability and stress-jump effects on magnetic drug targeting in a permeable microvessel using Darcy model. *J. Magn. Magn. Mater.* 429, 227–235. doi: 10.1016/j.jmmm.2017.01.023

Stanton, M.M., Park, B. W., Vilela, D., Bente, K., Faivre, D., Sitti, M., et al. (2017). Magnetotactic bacteria powered biohybrids target, *E. coli* biofilms. *ACS Nano* 11, 9968–9978. doi: 10.1021/acsnano.7b04128

Sun, Q., You, Q., Wang, J., Liu, L., Wang, Y., Song, Y., et al. (2018). Theranostic nanoplatform: triple-modal imaging-guided synergistic cancer therapy based on liposome-conjugated mesoporous silica nanoparticles. *ACS Appl. Mater. Interfaces* 10, 1963–1975. doi: 10.1021/acsami.7b13651

Sun, W., Fan, J., Wang, S., Kang, Y., Du, J., and Peng, X. (2018). Biodegradable drug-loaded hydroxyapatite nanotherapeutic agent for targeted drug release in tumors. *ACS Appl. Mater. Interfaces* 10, 7832–7840. doi: 10.1021/acsami.7b19281

Tang, H., Guo, Y., Peng, L., Fang, H., Wang, Z., Zheng, Y., et al. (2018). *In vivo* targeted, responsive, and synergistic cancer nanotheranostics by magnetic resonance imaging-guided synergistic high-intensity focused ultrasound

ablation and chemotherapy. *ACS Appl. Mater. Interfaces* 10, 15428–15441. doi: 10.1021/acsami.8b01967

Tietze, R., Lyer, S., Duerr, S., and Alexiou, C. (2012). Nanoparticles for cancer therapy using magnetic forces. *Nanomedicine* 7, 447–457. doi: 10.2217/nnm.12.10

Tietze, R., Zaloga, J., Unterweger, H., Lyer, S., Friedrich, R. P., Janko, C., et al. (2015). Magnetic nanoparticle-based drug delivery for cancer therapy. *Biochem. Biophys. Res. Commun.* 468, 463–470. doi: 10.1016/j.bbrc.2015.08.022

Tsai, M. F., Hsu, C., Yeh, C. S., Hsiao, Y. J., Su, C. H., and Wang, L. F. (2018). Tuning the distance of rattle-shaped IONP@shell-in-shell nanoparticles for magnetically-targeted photothermal therapy in the second near-infrared window. *ACS Appl. Mater. Interfaces* 10, 1508–1519. doi: 10.1021/acsami.7b14593

Ulbrich, K., Hola, K., Subr, V., Bakandritsos, A., Tucek, J., and Zboril, R. (2016). Targeted drug delivery with polymers and magnetic nanoparticles: covalent and noncovalent approaches, release control, and clinical studies. *Chem. Rev.* 116, 5338–5431. doi: 10.1021/acs.chemrev.5b00589

Venugopal, I., Habib, N., and Linninger, A. (2017). Intrathecal magnetic drug targeting for localized delivery of therapeutics in the CNS. *Nanomedicine* 12, 865–877. doi: 10.2217/nnm-2016-0418

Vlaskou, D., Mykhaylyk, O., Kroetz, F., Hellwig, N., Renner, R., Schillinger, U., et al. (2010). Magnetic and acoustically active lipospheres for magnetically targeted nucleic acid delivery. *Adv. Funct. Mater.* 20, 3881–3894. doi: 10.1002/adfm.200902388

Voronin, D. V., Sindeeva, O. A., Kurochkin, M. A., Mayorova, O., Fedosov, I. V., Semyachkina-Glushkovskaya, O., et al. (2017). *In vitro* and *in vivo* visualization and trapping of fluorescent magnetic microcapsules in a bloodstream. *ACS Appl. Mater. Interfaces* 9, 6885–6893. doi: 10.1021/acsami.6b15811

Wang, G., Zhao, D., Li, N., Wang, X., and Ma, Y. (2018). Drug-loaded poly (ε-caprolactone)/Fe3O4 composite microspheres for magnetic resonance imaging and controlled drug delivery. *J. Magnet. Magn. Mater.* 456, 316–323. doi: 10.1016/j.jmmm.2018.02.053

Wang, R., Billone, P. S., and Mullett, W. M. (2013). Nanomedicine in action: an overview of cancer nanomedicine on the market and in clinical trials. *J. Nanomater.* 2013:629681. doi: 10.1155/2013/629681

Wang, X., Hu, C., Schurz, L., De, M. C., Chen, X., Pane, S., et al. (2018). Surface-chemistry-mediated control of individual magnetic helical microswimmers in a swarm. *ACS Nano* 12, 6210–6217. doi: 10.1021/acsnano.8b02907

Wang, Y., Wei, G., Zhang, X., Huang, X., Zhao, J., Guo, X., et al. (2018). Multistage targeting strategy using magnetic composite nanoparticles for synergism of photothermal therapy and chemotherapy. *Small* 14:e1702994. doi: 10.1002/smll.201702994

Wang, Y. P., Liao, Y. T., Liu, C. H., Yu, J., Alamri, H. R., Alothman, Z.A., et al. (2017). Trifunctional Fe3O4/CaP/alginate core-shell-corona nanoparticles for magnetically guided, pH-Responsive, and chemically targeted chemotherapy. *ACS Biomater. Sci. Eng.* 3, 2366–2374. doi: 10.1021/acsbiomaterials.7b00230

Wei, J., Shuai, X., Wang, R., He, X., Li, Y., Ding, M., et al. (2017). Clickable and imageable multiblock polymer micelles with magnetically guided and PEG-switched targeting and release property for precise tumor theranosis. *Biomaterials* 145, 138–153. doi: 10.1016/j.biomaterials.2017.08.005

Widder, K. J., Senyei, A. E., and Ranney, D. F. (1980). *In vitro* release of biologically active adriamycin by magnetically responsive albumin microspheres. *Cancer Res.* 40, 3512–3517.

Williams, P. S., Carpino, F., and Zborowski, M. (2009). Magnetic nanoparticle drug carriers and their study by quadrupole magnetic field-flow fractionation. *Mol. Pharmaceut.* 6, 1290–1306. doi: 10.1021/mp900018v

Xu, H., Medina-Sanchez, M., Magdanz, V., Schwarz, L., Hebenstreit, F., and Schmidt, O. G. (2018). Sperm-hybrid micromotor for targeted drug delivery. *ACS Nano* 12, 327–337. doi: 10.1021/acsnano.7b06398

Yang, K., Liu, Y., Liu, Y., Zhang, Q., Kong, C., Yi, C., et al. (2018). Cooperative assembly of magneto-nanovesicles with tunable wall thickness and permeability for MRI-guided drug delivery. *J. Am. Chem. Soc.* 140, 4666–4677. doi: 10.1021/jacs.8b00884

Zhang, F., Zhao, L., Wang, S., Yang, J., Lu, G., Luo, N., et al. (2018). Construction of a biomimetic magnetosome and its application as a siRNA carrier for high-performance anticancer therapy. *Adv. Funct. Mater.* 28:1703326. doi: 10.1002/adfm.201703326

Zhang, K. L., Zhou, J., Zhou, H., Wu, Y., Liu, R., Wang, L. L., et al. (2017). Bioinspired "Active" stealth magneto-nanomicelles for theranostics combining efficient, MRI and enhanced drug delivery. *ACS Appl. Mater. Interfaces* 9, 30502–30509. doi: 10.1021/acsami.7b10086

Zheng, S., Han, J., Jin, Z., Kim, C. S., Park, S., Kim, K. P., et al. (2018). Dual tumor-targeted multifunctional magnetic hyaluronic acid micelles for enhanced MR imaging and combined photothermal-chemotherapy. *Coll. Surf. B Biointerfaces* 164, 424–435. doi: 10.1016/j.colsurfb.2018.02.005

Conflict of Interest Statement: The authors declare that the research was conducted in the absence of any commercial or financial relationships that could be construed as a potential conflict of interest.

frontiers in Chemistry

ORIGINAL RESEARCH
published: 28 March 2019
doi: 10.3389/fchem.2019.00168

Self-Assembled Biocompatible Fluorescent Nanoparticles for Bioimaging

*Valeria Caponetti[1], Jakub W. Trzcinski[2], Andrea Cantelli[1], Regina Tavano[3], Emanuele Papini[3], Fabrizio Mancin[2] and Marco Montalti[1]**

[1] Dipartimento di Chimica "Giacomo Ciamician", Università di Bologna, Bologna, Italy, [2] Dipartimento di Scienze Chimiche, Università di Padova, Padova, Italy, [3] Dipartimento di Scienze Biomediche, Università di Padova, Padova, Italy

Fluorescence is a powerful tool for mapping biological events in real-time with high spatial resolution. Ultra-bright probes are needed in order to achieve high sensitivity: these probes are typically obtained by gathering a huge number of fluorophores in a single nanoparticle (NP). Unfortunately this assembly produces quenching of the fluorescence because of short-range intermolecular interactions. Here we demonstrate that rational structural modification of a well-known molecular fluorophore N-(7-nitrobenz-2-oxa-1,3-diazol-4-yl) (NBD) produces fluorophores that self-assemble in nanoparticles in the biocompatible environment without any dramatic decrease of the fluorescence quantum yield. Most importantly, the resulting NP show, in an aqueous environment, a brightness which is more than six orders of magnitude higher than the molecular component in the organic solvent. Moreover, the NP are prepared by nanoprecipitation and they are stabilized only via non-covalent interaction, they are surprisingly stable and can be observed as individual bright spots freely diffusing in solution at a concentration as low as 1 nM. The suitability of the NP as biocompatible fluorescent probes was demonstrated in the case of HeLa cells by fluorescence confocal microscopy and MTS assays.

Keywords: fluorescence, fluorescent probes, ultra-bright, nanoparticles, nanoprecipitation, tracking, single particle imaging, bioimaging

OPEN ACCESS

Edited by:
José Luis Capelo, Universidade Nova de Lisboa, Portugal

Reviewed by:
Anna Roig, Instituto de Ciencia de Materiales de Barcelona (ICMAB), Spain
César Laia, Universidade Nova de Lisboa, Portugal

****Correspondence:***
Marco Montalti
marco.montalti2@unibo.it

Specialty section:
This article was submitted to Nanoscience, a section of the journal Frontiers in Chemistry

Received: *08 November 2018*
Accepted: *05 March 2019*
Published: *28 March 2019*

Citation:
Caponetti V, Trzcinski JW, Cantelli A, Tavano R, Papini E, Mancin F and Montalti M (2019) Self-Assembled Biocompatible Fluorescent Nanoparticles for Bioimaging. Front. Chem. 7:168. doi: 10.3389/fchem.2019.00168

INTRODUCTION

Fluorescence imaging is a not invasive, highly sensitive, technique that allows to investigate biological organisms with high tridimensional resolution in real time, by making use of suitable fluorescent contrast agents (Rio-Echevarria et al., 2011; Cauzzi et al., 2012; Chen et al., 2015; Grimm et al., 2015; Lee et al., 2015; Mei et al., 2015; Tang et al., 2015; Antaris et al., 2016; Proetto et al., 2016; Xu et al., 2016). Tailored fluorescent nanoparticles (NP) (Jiang et al., 2015; Ma et al., 2015; Pyo et al., 2015; Wolfbeis, 2015; Muller et al., 2018), promise to surpass conventional molecular probes as fluorescent markers especially as far as sensitivity is concerned: in fact, NPs potentially emit a much brighter signal, with respect to molecules, in the same excitation conditions. Nevertheless, achieving such an enhanced brightness (defined as $B = \varepsilon QY$, where ε is the molar absorption coefficient of the NP and QY is fluorescence quantum yield of the NP) is still a challenge (Ow et al., 2005; Wu et al., 2006; Sun et al., 2010; Cho et al., 2011; Volkov et al., 2011; Trofymchuk et al., 2017; Melnychuk and Klymchenko, 2018).

Most of the NP proposed and applied for bio-imaging, in fact, result from the assembly of molecular fluorophores (MF) in an organized nanostructure. These assemblies may be stabilized: (i) via covalent bonds, hence by modifying the MF chemical structure with reactive terminal groups [e.g., alkoxysilanes (Rio-Echevarria et al., 2010; Rampazzo et al., 2011; Selvestrel et al., 2013), acrylates (Chen et al., 2009), or thiolates (Battistini et al., 2008; Bonacchi et al., 2016)] to form polymer/copolymer or by (ii) non-covalent interactions, that involve either the MF or additional groups specifically introduced in the structure to achieve supramolecular polymerization (Genin et al., 2014; Montalti et al., 2014; Reisch and Klymchenko, 2016; Faucon et al., 2017; Boucard et al., 2018). Control of size and size distribution is a critical issue in NP design and it can be achieved by exploiting surfactants or stabilizers as templates, hence molecules that are physically or chemically incorporated in the NP typically giving a compartmentalized structure (e.g., core-shell).

From the point of view of fluorescence brightness, the ability of NP to generate an intense fluorescence signal, even in the low intensity excitation regime, results from the co-presence of a high number of MF in each NP. Here, we report the preparation in a bio-compatible environment of NP with a diameter of about 90 nm containing as much as about 1×10^6 MF/NP obtained by the self-assembling of new molecular fluorophores specifically designed to achieve highly bright NP.

We would like to stress that without a rational design, MF normally aggregate in highly densely packed NP undergoing strong fluorescence quenching, a process which reduces their QY to almost zero. This phenomenon known as aggregation caused quenching (ACQ) (Genovese et al., 2013), typically occurs in self-assembled multi-fluorophoric systems and it is the result of short-range interactions between MF in the NP.

ACQ is particularly severe in the case of actual contact between the MF, as it occurs when aggregates are formed, and it can be prevented, at least in part, by spacing the MF (Mak et al., 1999) by incorporating them in an inactive matrix (e.g., silica) as in typical dye-doped NP. A major drawback of this strategy, that becomes effective for NP with a dye/matrix ratio below ∼1%, is a drastic reduction of the density of emitting molecules in the NP and hence of the ε of the NP with respect to matrix-free NP.

Here we describe the synthesis and the properties of a new family of MF, which are water insoluble and do not suffer from ACQ, and we demonstrate that a rational design of the molecular structure allows us to achieve a molecular unit that self-organizes in highly bright, and fluorescent NPs which are very stable in PBS (phosphate buffered saline) solution.

In designing the new MF, our attention was attracted by the N-(7-Nitrobenz-2-oxa-1,3-diazol-4-yl) (NBD) dye derivatives (Fery-Forgues et al., 1993; Mukherjee et al., 1994). This family of dyes has very interesting properties for imaging applications. In particular the synthetic precursor NBD chloride is quite inexpensive and it is easily conjugated with amine derivatives yielding fluorescent dyes featuring absorption and emission in the visible range, large Stokes shift and good quantum yields.

Unfortunately, emission of NBD derivative in the aggregated form is often very low and it is almost completely quenched in aqueous environment (Fery-Forgues et al., 1993). We reasoned that such a limitation could be overcome by the introduction of a triphenylphosphazene group in the NBD structure. Indeed such chemical modification, even if scarcely studied, has been reported to result, in the case of fluorescent dyes, into a red shift of both the absorption and luminescence maxima, an increase of the Stokes shift and of the luminescence intensity (Bodige et al., 1999; Nifant'ev et al., 2008; Joshi et al., 2014; Xu et al., 2015; Ragab et al., 2016).

Three different NBD-triarylphosphazene derivatives were prepared in high yields with straightforward procedures. The NP were then prepared via nanoprecipitation in the presence of Pluronic F127 as a stabilizer and they were characterized, from the photo-physical point of view, via UV-Vis absorption spectroscopy and steady-state and time resolved fluorescence spectroscopy. Although different surfactants have been proposed as stabilizer for nanoprecipitation we chose Pluronic F127 in virtue of its well-known biocompatibility (Pitto-Barry and Barry, 2014). The formation and stability of the NPs were demonstrated by dynamic light scattering (DLS) and transmission electron microscopy (TEM). Moreover, wide field fluorescence microscopy proved that these NP are stable at a concentration as low as 1 nM.

By comparing the NP to the molecular precursors, an increase of the brightness of about five order of magnitude, with respect to the fluorophore in organic solvent, could be estimated as a result of the self-assembly. A direct comparison with the fluorophore in aqueous medium was not possible because of the lack of solubility but making reference to an NBD water soluble derivative, we could appraise for the NP a brightness of more than six orders of magnitude higher. In order to demonstrate that these NPs were suitable for bio-imaging, they were incubated with living HeLa cells and their ability to label the cells was demonstrated via confocal scanning fluorescence microscopy. Finally, toxicity assays demonstrated the high biocompatibility of the NPs. We believe that these highly bright, functionalizable NPs are very promising platform for the design of new versatile multifunctional nanoprobes.

RESULTS AND DISCUSSION

Photophysical Properties of the Molecules in Solution

Molecular fluorophores **1**-**3** are shown in **Figure 1** and they were synthesized following the general reaction reported in **Figure 1**. Photophysical properties of molecules **1**-**3** where investigated in CH_2Cl_2 solution at the concentration 5×10^{-5} M and they are summarized in **Table 1**. In particular, the effect of the substituent on the phenyl ring was investigated. We would like to stress that fluorophores **1**-**3** are insoluble in water but that they can be dispersed in water in the form of NPs as discussed in the next section.

UV-Vis electronic absorption spectra are shown in **Figure 2** (continuous lines) together with the normalized fluorescence spectra. The absorption spectrum of compound **1** shows a maximum at $\lambda = 482$ nm ($\varepsilon = 34{,}300\ M^{-1}cm^{-1}$) while the fluorescence band presents a peak at 534 nm. Both absorption

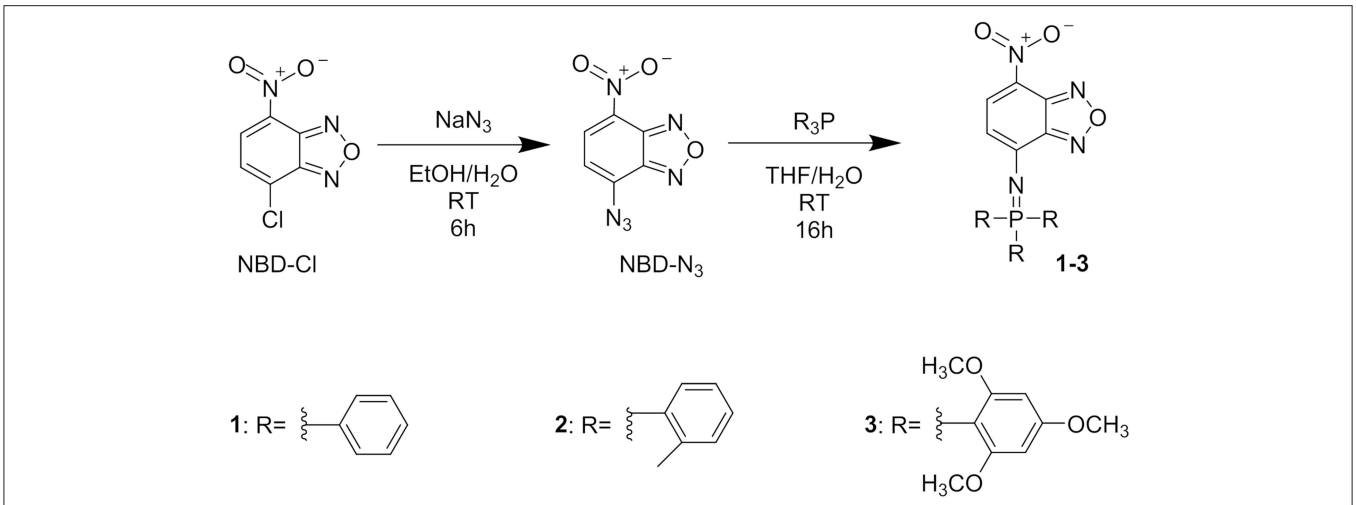

FIGURE 1 | Chemical formula of compounds 1, 2, 3 and scheme of the synthetic reactions for their preparation.

TABLE 1 | Photophysical data of compounds 1, 2, 3, 4 and of 2NP and 3NP.

Compounds	Solvents	$\lambda_{max,ass}$ (nm)	ε_{max} ($M^{-1}cm^{-1}$)	$\lambda_{max,fluo}$ (nm)	QY	<n>[b]	B[b] ($M^{-1}cm^{-1}$)	<d>[b] (nm)
1	CH_2Cl_2	482	34,300	536	0.50	–	1.7×10^4	–
2	CH_2Cl_2	488	32,600	526	0.65	–	2.1×10^4	–
3	CH_2Cl_2	524	26,200	555	0.09	–	2.6×10^3	–
4[c]	H_2O	482	28,000	566	0.03	–	8.4×10^2	–
2NP	H_2O[a]	480	29,300	536	0.31	1.1×10^6	1.0×10^{10}	91 ± 13
3NP	H_2O[a]	520	17,800	556	0.01	1.6×10^5	2.8×10^7	54 ± 9

[a] *PBS.*
[b] *Calculated from TEM.*
[c] *From Fery-Forgues et al. (1993).*

and fluorescence maxima are very close to those reported for the same molecule in acetonitrile (Ragab et al., 2016), and they are very similar to those reported for the parent compound, diethylamino-NBD (**4**) (Fery-Forgues et al., 1993). The photophysical properties of NBD derivatives in different solvents have been investigated by Lopez and coworkers who reported for **4** in dichloromethane an absorption and fluorescence band with maxima at 482 and 534 nm, respectively (Fery-Forgues et al., 1993). These bands are attributed to an electronic transition with charge transfer (CT) character, the amino group acting as the electron donor and the nitro group as the acceptor. Because of its nature, the CT bands are affected both by the polarity of the environment (e.g., the solvent) and of substituents. Considering the similarity between NBD-amine and **1,** we can conclude that the triphenylphosphazene group and the diethylamino group have a very similar electronic effect on the nitro-aromatic system. Moreover, the fluorescence QY = 0.50 and the excited state lifetime $\tau = 5.7$ ns of 1 in CH_2Cl_2 are very similar to those of NBD.

The introduction of the methyl group on the phenyl substituent to give **2** produces a shift of the absorption maximum to 488 nm and of the fluorescence to 524 nm. It is interesting observing that going from **1** to **2,** only a very small decrease of the energy of the lowest singlet excited state is observed, from 2.44 eV for **1** to 2.45 eV for **2**, but a relevant decrease of the Stokes shift from 0.26 to 0.18 eV occurs. This indicates that the effect of the methylation is to increase the hindrance of the bulky triphenylphosphazene substituents on the phosphorous atom and hence it reduces the degree of conformational reorganization of the excited states which produces the Stokes shift. The electronic effect of the weak electron donor methyl group, on the other hand, is marginal and since the electronic transition has a strong charge-transfer character, no relevant difference in the electronic transition is observed. The rigidification effect due to the bulkier substituents also affects the fluorescence QY and the excited state lifetime that rises, with respect to **1**, to QY = 0.65 and $\tau = 7.7$ ns in **2**.

On the contrary, the substitution of each of the three phenyl rings with three strong electron donor methoxy groups to give **3** produces a large hypsochromic shift both of the absorption band, $\lambda = 524$ nm ($\varepsilon = 26{,}200\ M^{-1}cm^{-1}$) and of the fluorescence maximum $\lambda_{em} = 555$ nm, corresponding to a decrease of the

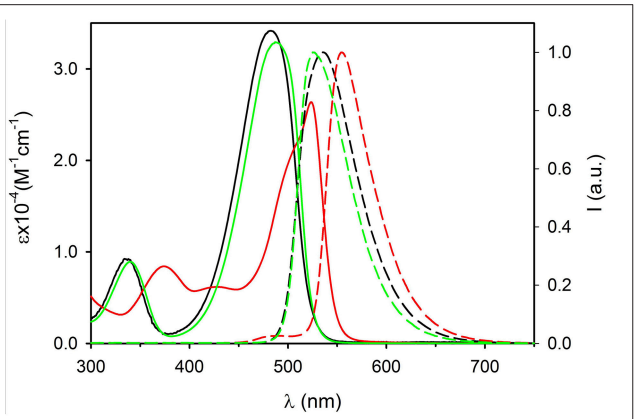

FIGURE 2 | Absorption (continuous lines) and fluorescence spectra (dashed lines) of molecules 1 (black, $\lambda_{exc} = 450$ nm) 2 (green, $\lambda_{exc} = 450$ nm) and 3 (red, $\lambda_{exc} = 490$ nm) in dichloromethane (concentration 5×10^{-5} M).

energy of the transition to 2.30 eV. The further increase of the hindrance of the phosphazene substituents in **3** with respect to **2** leads to a decrease of the Stokes shift to 0.13 eV. On the other hand the presence of the electron rich trimethoxyphenyl group causes a decrease of the fluorescence QY to 0.09 and of the excited state lifetime to $\tau = 4.2$ ns

Preparation and Characterization of the NPs

Dye molecules **1**, **2**, and **3** are water insoluble and nanoparticles (NPs) were prepared by nanoprecipitation (Reisch and Klymchenko, 2016). A small volume (10 μL) of a THF solution of **1**, **2** or **3** (2 mg/ml) and the surfactant Pluronic F127 (20 mg/mL) was rapidly injected into 2.5 mL of Millipore water under vigorous stirring. The reaction vial was kept open to atmospheric air in order to allow complete evaporation of the organic solvent. After 2 h of stirring, a precipitate was formed in the case of compound **1** while transparent, colored suspensions were obtained for samples containing **2** and **3**.

The formation of the NP constituted by **2** and **3** was demonstrated by dynamic light scattering (DLS), transmission electron microscopy (TEM) and fluorescence microscopy (FM). In particular, DLS measurements showed the presence of a quite monodisperse single population of NPs both in the sample containing **2** (**2NP**, d = 128 nm, PdI = 0.11) and **3** (**3NP**, d = 140, PdI = 0.06). The size distribution of the two samples is shown in **Figures 3a,b**, respectively. DLS measurements were performed after dilution of the NPs suspension in phosphate-buffered saline (PBS) solution (1:50, vol:vol). After such a dilution, the concentration of the surfactant Pluronic F127 was 0.13 μM, hence more than three order of magnitude below the critical micelles concentration (cmc = 0.3 mM at r.t.) (Rampazzo et al., 2011). In order to exclude the formation of NPs constituted by the surfactant (micelles that, on the other hand, have been reported to show size of tens of nm), a blank sample was prepared following the same procedure used for **2NP** and **3NP**. No relevant scattering signal was detected in the case of the blank samples, confirming the absence of NPs.

The size distribution of **2NP** and **3NP** was also investigated by TEM: representative images of the two samples are shown in **Figures 3c,d,** respectively while the histogram obtained by measuring the size of the NP in the images with the software Image J are shown in **Figures 3e,f**. Fitting the data with a Gaussian model, we obtained the NP size: 91 ± 13 and 54 ± 9 for **2NP** and **3NP**, respectively. While the diameter measured for **2NP** by TEM was consistent with the hydrodynamic diameter measured by DLS, a significant difference was observed in the case of **3NP**. The larger hydrodynamic diameter measured by DLS for this latter sample revealed a partial aggregation of **3NP** in water.

The photophysical characterization of **2NP** and **3NP** was performed in PBS, results are summarized in **Table 1**. Since it was not possible to compare the properties of **2NP** and **3NP** with the molecular components **2** and **3** in aqueous medium because of their insolubility, we compared them to the parent compound diethylamino-NBD (**4**), as shown in **Table 1**.

The UV vis absorption spectra of **2NP** and **3NP** are shown in **Figures 4**, **5**, respectively. The molar absorption coefficient (ε) was calculated for the molecules **2** and **3** in the NP considering their average concentration. **Figures 4**, **5** clearly show that the aggregation in the NP has only a minor effect on the absorption properties of the dye molecules that undergo only a modest hypsochromic shift and a moderate decrease of ε.

On the contrary, NP formation had a very different effect on the fluorescence properties of **2** and **3**. In particular, **2** maintains in the NPs an acceptable quantum yield (QY = 0.31) while **3** undergoes strong aggregation induced quenching (QY = 0.01). This observation suggests that the introduction of methyl on the bulky tri(phenyl)phosphazene group is suitable to decrease the intermolecular electronic interactions in the NPs by reducing the overlap of the molecular orbitals of the fluorescent NBD units. Nevertheless, the presence of electron donating tri-methoxyphenyl groups is known to cause fluorescence quenching because of the formation of charge-transfer non-fluorescent excited states (Shukla and Wan, 1993). Fluorescence anisotropy measurements demonstrated that the quenching effect is enhanced by excitation energy migration inside the NPs (Bonacchi et al., 2008; Jiang and McNeill, 2017). Both **2** and **3** in fact showed in a high viscosity medium like propylene glycol, quite a high value of fluorescence anisotropy r ($r = 0.21$ for **2** and $r = 0.23$ for **3** at r.t.). On the contrary, the two fluorophore immobilized in the NPs showed a fluorescence anisotropy which is zero both for **2NP** and **3NP**. The complete depolarization observed in the NP is in contrast with the lack of rotational freedom of the fluorophores in the nanostructures and can be explained only by considering a fast depolarization involving the homo-energy transfer processes (Genovese et al., 2013).

Time resolved fluorescence measurements (time correlated single photon counting, TCSPC) showed that the spectral changes observed upon NP formation were due to the presence, in the NPs, of populations of fluorophores experiencing different environments. Tri-exponential decays were observed both in the case of **2NP** ($\tau_1 = 0.46$ ns, $B_1 = 3{,}196$, $\tau_2 = 1.45$, $B_2 = 1{,}085$, $\tau_3 = 6.16$, $B_3 = 44$) and **3NP** ($\tau_1 = 0.62$ ns, $B_1 = 4{,}132$, $\tau_2 = 2.44$, $B_2 = 3{,}724$, $\tau_3 = 7.81$, $B_3 = 1{,}559$). From these data the average excited

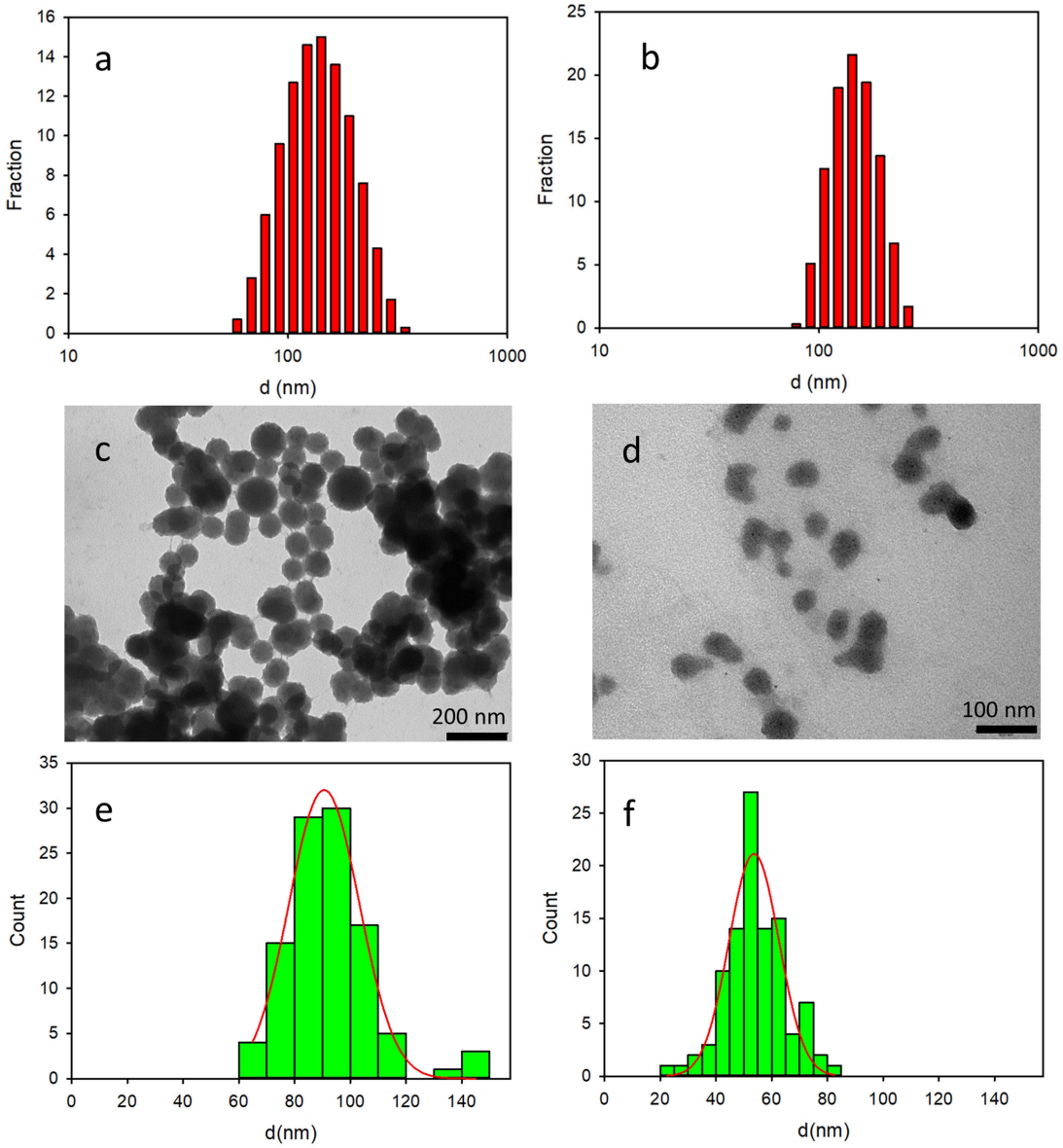

FIGURE 3 | Top: size distribution obtained by DLS analysis of 2NP **(a)** and 3NP **(b)**. Center: representative TEM images of 2NP **(c)** and 3NP **(d)**. Bottom: size distribution resulting from the analysis of the TEM images of 2NP **(e)** and 3NP **(f)**.

lifetime was calculated to be $< \tau > = 2.53$ ns and $< \tau > = 0.77$ ns for **2NP** and **3NP**, respectively. This result is in agreement with the low fluorescence QY measured for **3NP**.

In order to evaluate the order of magnitude of the fluorescence brightness of **2NP** and **3NP,** the number of molecules per particles was estimated as reported in **Table 1**. This number was calculated considering the molar volume of **2** and **3** (molecular volume of **1**, **2**, and **3** were calculated to be 338.0, 380.9, and 533.6 Å^3, respectively) and the hydrodynamic diameter of the NPs.[1]

$$V = \frac{\pi}{6} d^3 N \quad (1)$$

[1]http://www.scfbio-iitd.res.in/software/drugdesign/VolumeCalculator.jsp.

Molar volume for **2NP** and **3NP** were 2.4×10^5 and 5.0×10^4 L mol^{-1} while molar volume for **2** and **3** were 0.23 Lmol^{-1} and 0.32 L mol^{-1}, respectively. Hence **2NP** and **3NP** contain about 1.1×10^6 molecules and 1.6×10^5 dye molecules, respectively. Considering these values, the brightness of **2NP** results to be as high as $\sim 10^{10}$M^{-1}cm^{-1} while **3NP** show a brightness which is almost two orders of magnitude lower than **2NP**.

Size Characterization of 2NP by Fluorescence Optical Tracking

Thanks to their outstanding brightness, **2NP** could be detected, in suspension, as single bright spots in a conventional fluorescence microscope. Using an acquisition time as short as 10 ms, the

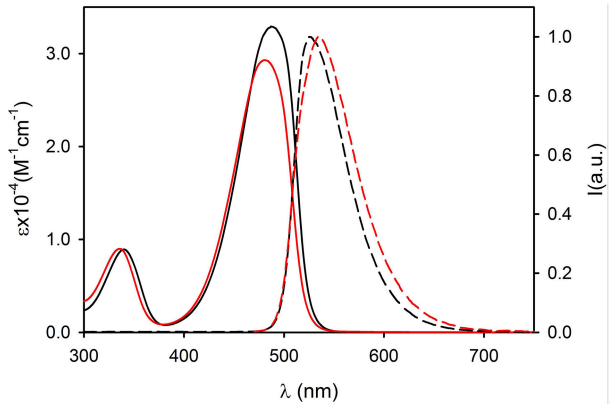

FIGURE 4 | Absorption (continuous lines) and fluorescence spectra (dashed lines, $\lambda_{exc} = 450$ nm) of compound 2 (black, dichloromethane) and of 2NP (red, PBS).

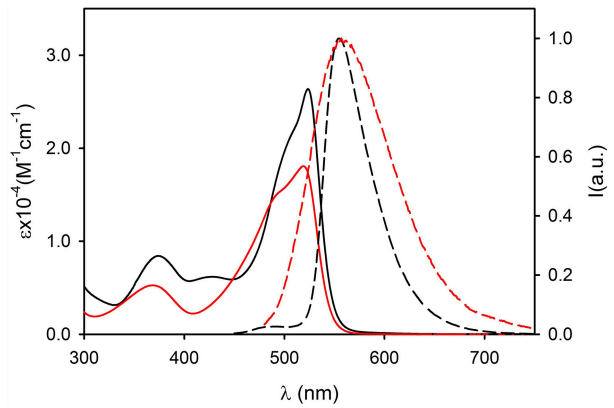

FIGURE 5 | Absorption (continuous lines) and fluorescence spectra (dashed lines, $\lambda_{exc} = 490$ nm) of compound 3 (black, dichloromethane) and of 3NP (red, PBS).

NP appeared motionless as shown in **Figure 6** (inset). Thermal motions of the NP were clearly observed by time lapsed acquisition (4,000 frames). The resulting movies were analyzed to measure the linear displacements of the NPs using the plugin MOSAIC for Image J (Sbalzarini and Koumoutsakos, 2005; Chenouard et al., 2014). The displacements were then plotted in a histogram as shown in **Figure 6**. We would like to stress that an analogous experiment was performed for a **3NP** sample and no emissive spots attributable to NP diffusion could be observed. This demonstrated that these NPs were not bright enough to be detectable as individual objects by fluorescence microscopy. Moreover, by comparing two samples of **2NP** and **3NP** with the same concentration (8 μg/ml), the average intensity measured within a frame in the case of **2NP** was more than 2 orders of magnitude higher than the one measured for **3NP**.

The diffusion coefficient of **2NP** was calculated by tracking the fluorescent NP via fluorescence microscopy considering the

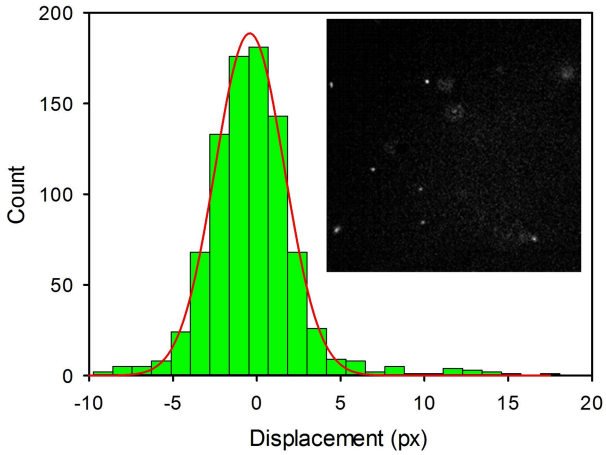

FIGURE 6 | Histogram of the linear displacements measured for 2NP in PBS by fluorescence microscopy for a time interval $\Delta t = 10$ ms. Images were acquired in time-lapse mode (4,000 frames) with an EMCCD Camera and processed with Image J (Plug-in MOSAIC). Each pixel corresponds to 0.16 μm. A representative image of the NP (bright white spots) is shown in the inset.

following equations:

$$P(x,t) = \frac{1}{\sqrt{4\pi Dt}} \exp\left(-\frac{(x-x_0)^2}{4Dt}\right) \quad (2)$$

Where P is the probability of observing a displacement of an NP from the position x_0 to the position $\times$ after a time delay t and D is the diffusion coefficient of the NP that, in a spherical approximation, is dependent on the diameter of the NP according to the Stokes-Einstein equation:

$$D = \frac{kT}{3\pi\eta d} \quad (3)$$

Where k is the Boltzmann constant, T the temperature and η is the viscosity of the medium. Image sequences were processed to acquire the positions of the NP in each frame and to identify individual NP movements. The trajectories of the NPs were used to get the displacement (in pixels, where a pixel corresponds to 0.16 μm) of the NP in the frame acquisition time interval ($t = 1.0 \times 10^{-2}$ s). Data represented in the histogram were fitted with a Gaussian model, as shown in **Figure 6**, to obtain the diffusion coefficient $D = 2.65 \times 10^{-12}$ m^2s^{-1}; a value that corresponds to NPs with an average diameter of 160 nm in good agreement with the DLS analysis.

Biological Experiments

To demonstrate their efficacy as a fluorescent probe, **2NP** and **3NP** were incubated with HeLa cells at the relatively low dose of 80 ng/ml at 37°C. After confocal microscopy analysis of 20 h, cells (**Figure 7**) revealed an intense structured **2NP** signal within the cell cytoplasm, suggesting endosomal NP internalization, although cytoplasmatic internalization cannot be completely

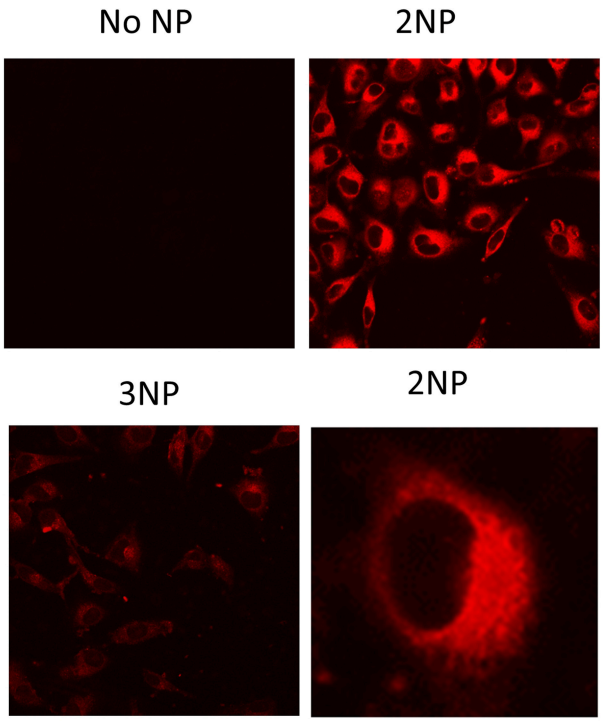

FIGURE 7 | Fluorescence signal of NPs in cells. HeLa cells grown on glass cover-slips were incubated for 20 h with no NPs (medium alone), 2NP or 3NP, as indicated and analyzed by fluorescence confocal microscopy with the same instrumental setting for comparison. Representative images are shown. In the case of 2NP cell signal distribution details are shown at higher magnification. Bars are the standard deviations of the means.

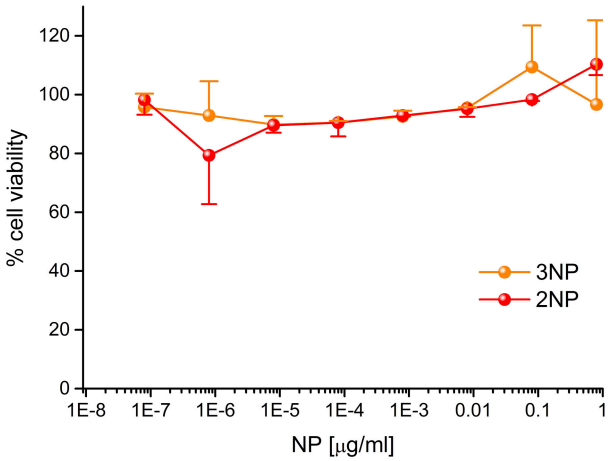

FIGURE 8 | Cytotoxicity of 2NPs and 3NPs. HeLa cells were incubated for 20 h with the indicated doses of NPs in DMEM at 37°C and subjected to MTS assay. Data, expressed as % of control (no NP) samples, are mean ± SE (N=3).

ruled out. As expected, based on their weak intrinsic fluorescence, **3NP** cellular signal was much weaker. MTS assays showed that both **2NP** and **3NP** are devoid of the toxic effects on HeLa cells of up to 1 μg/ml (**Figure 8**).

CONCLUSIONS

Summarizing the results so far discussed, we found that molecule **1** does not form stable NP upon nanoprecipitation in our experimental conditions. On the contrary, nanoprecipitation of molecules **2** and **3** leads to NP formation. However, the quantum yield of molecule **3,** which is already low in the non-aggregated form, further decreases upon assembly in the NP. As a result, the brightness of **3NP** is about two orders of magnitude lower than the one of **2NP**. Such a difference is so relevant that while **2NP** can be clearly tracked at the single NP level in solution at very low concentration by fluorescence microscopy, **3NP** cannot be observed with the same technique. Most interestingly, the brightness of **2NP** could be estimated to be about six orders of magnitude higher than an NBD water soluble derivative used as reference. These results demonstrate that rational design of the molecular precursor is fundamental for producing stable and strongly bright nanoparticles by self-assembly. Cellular experiments proved that **2NPs** are suitable to be used as fluorescent contrast agents for bioimaging, also thanks to their good biocompatibility. We believe that our approach can be extended to other molecules and surfactants in order to tune the excitation/emission wavelength as well as the NP size.

EXPERIMENTAL SECTION

General: Solvents were purified by standard methods. All the reagents used were purchased by Sigma-Aldrich and used as received.

TLC analyses were performed using Merck 60 F254 precoated silica gel glass plates. Column chromatography was carried out on Macherey-Nagel silica gel 60 (70–230 mesh).

NMR spectra were recorded using a Bruker AV 500 spectrometer operating at 500 MHz for 1H, 125.8 MHz for 13C. Chemical shifts are reported relative to internal Me4Si. Multiplicity is given as follow: s = singlet, d = doublet, t = triplet, q = quartet, qn = quintet, m = multiplet, br = broad peak.

ESI-MS mass spectra were obtained with an Agilent Technologies LC/MSD Trap SL mass spectrometer. EI/MS spectra were obtained with an Agilent Technologies 6850-5973 GS/MS.

Synthesis of 4-Azido-7-Nitrobenzofurazan (NBD-N_3)

Into a flask, covered with an aluminum foil and containing NaN_3 (0.350 g, 5.39 mM) dissolved in a EtOH/H_2O mixture (1:1 v/v, 20 mL), a solution of NBD-Cl (0.5 g, 2.505 mM) in EtOH (40 mL) was added dropwise within a 1 h period. The reaction was left stirring for 6 h at RT. Subsequently, the solvent was removed under reduced pressure and crude was purified via column chromatography on silica gel using petroleum ether/AcOEt 4:6 as eluent. The product **1** was obtained as an orange solid in 90% yield.

^{1}H NMR (300 MHz, d_6-DMSO), δ: 8.70 (d, J =5.3 Hz, 1H), 6.40 (d, J = 5.3 Hz, 1H).

ESI/MS, m/z: 207.8 (15%, M+H$^+$), 178.8 (100%, M-N_2+H$^+$).

EI/MS, m/z: 207 (100%, M$^+$), 180, 150, 133, 120, 104, 92, 77, 64, 52.

Synthesis of 4-Triarylphosphazo-7-Nitrobenzofurazan (1-3)

Into a flask, covered with aluminum foil and containing **1** (0.1 g, 0.485 mM) and the desired phosphine (3 eq.) dissolved in THF (8 mL), H_2O (2.6 mL, 145.553 mM) was added at once and left to react overnight under stirring. Subsequently, the formed solid was filtered-off, washed with cold THF and dried giving the final product as an orange solid with quantitative yield.

4-Triphenylphosphazo-7-Nitrobenzofurazan (1)

^{1}H NMR (300 MHz, $CDCl_3$) δ 8.19 (d, J = 8.3 Hz, 1H), 7.74 (m, J = 13.0, 10.7, 4.7 Hz, 6H), 7.65–7.56 (m, 3H), 7.54–7.37 (m, 7H), 6.56 (d, J = 8.5 Hz, 1H).

^{31}P NMR (202 MHz, $CDCl_3$) δ 14.01.

^{13}C NMR (126 MHz, $CDCl_3$) δ 137.04, 134.06, 134.02, 133.06, 132.92, 130.21, 130.04, 126.84, 125.51, 40.86, 40.58, 40.30, 40.02, 39.74, 39.47, 39.19.

ESI-MS, m/z: 425.2 (100%, M+H$^+$).

4-Tri-(2-Methylphenyl)Phosphazo-7-Nitrobenzofurazan (2)

^{1}H NMR (500 MHz, DMSO-d_6) δ 8.20 (d, J = 8.8 Hz, 1H), 7.71 (t, J = 7.4 Hz, 3H), 7.58–7.46 (m, 10H), 5.50 (d, J = 8.9 Hz, 1H), 2.20 (s, 9H).

^{31}P NMR (202 MHz, DMSO-d_6) δ 21.31.

^{13}C NMR (126 MHz, DMSO-d6) δ 154.93, 150.91, 143.15, 143.08, 137.24, 134.40, 134.32, 134.09, 133.98, 133.49, 133.40, 127.61, 127.51, 123.92, 123.15, 121.57, 117.25, 109.16, 109.06, 31.16, 30.06.

ESI-MS, m/z: 483.2 (100%, M+H$^+$), 505.1 (10%, M+Na$^+$).

4-Tri-(2,4,6-Triemthoxyphenyl)Phosphazo-7-Nitrobenzofurazan (3)

^{1}H NMR (500 MHz, Acetone-d6) δ 8.54 (d, J = 8.6 Hz, 1H), 8.05 (d, J = 9.4 Hz, 1H), 7.90 (s, 1H), 6.25 (d, J = 4.7 Hz, 6H), 5.83 (d, J = 8.4 Hz, 1H), 3.88 (s, 10H), 3.60 (s, 27H).

^{31}P NMR (202 MHz, Acetone-d_6) δ 3.03.

^{13}C NMR (126 MHz, Acetone-d_6) δ 167.49, 163.92, 142.36, 140.66, 140.53, 135.71, 129.25, 125.86, 118.39, 96.10, 56.14, 55.65.

ESI-MS, m/z: 711.2 (100%, M+H$^+$).

Absorption and Fluorescence Spectra

UV-VIS absorption spectra were recorded at 25°C by means of Cary 300 UV-Vis spectrophotometer (Agilent Technologies).

Steady State Fluorescence Spectra

The fluorescence spectra were recorded with a Horiba Fluoromax-4 spectrofluorimeter and with an Edinburgh FLS920 fluorimeter equipped with a photomultiplier Hamamatsu R928P. Quartz cuvettes with optical path length of 1 cm were used for both absorbance and emission measurements.

Excited State Lifetimes

Excited state lifetime was measured with an Edinburgh FLS920 fluorimeter equipped with an electronic card for time correlated single photon counting TCSPC900. The kinetic tracks were fitted with a tri-exponential model: $I(t) = A + B_1e^{-t/\tau_1} + B_2e^{-t/\tau_2} + B_3e^{-t/\tau_3}$ with the software package FAST.

Fluorescence Anisotropy Spectra

All fluorescence anisotropy measurements were performed on an Edinburgh FLS920 equipped with Glan-Thompson polarizers. Anisotropy measurements were collected using an L-format configuration, and all data were corrected for polarization bias using the G-factor.

In particular four different spectra were acquired for each sample combining different orientations of the excitation and emission polarizers: I_{VV}, I_{VH}, I_{HH}, I_{HV} (where V stands for vertical and H for horizontal with respect to the plane including the excitation beam and the detection direction; and the first subscript refers to the excitation and the second subscript refers to the emission). The spectra were used to calculate the G-factor and the anisotropy r: $G = I_{HV}/I_{HH}$ and $r = I_{VV} - GI_{VH}/I_{VV} + 2GI_{VH}$.

Epifluorescence Microscopy

The fluorescence images were obtained with an inverted microscope (Olympus IX71) equipped with a Xenon lamp for excitation. Excitation, dichroic and emission filters were purchased from Chroma and Thorlabs. Excitation filter: 475 ± 17.5 nm; emission filter: 530 ± 21.5 nm; dichroic Reflection/Transmission): 470–490/508–675 nm. Fluorescence images were acquired with an Electron Multiplying Charge Coupled Device EMCCD Camera (Princeton Instruments, Photon Max 512). Acquisition time was 30 ms per frame at the maximum amplification gain using a 100x oil immersion objective for fluorescence (Olympus UPLFLN100XO2).

Particle Tracking

Trajectories were tracked by analyzing sequences of images acquired with an integration time τ of 10 ms per frame. The particles were localized and tracked by using the plug-in MOSAIC for the software ImageJ (Sbalzarini and Koumoutsakos, 2005; Chenouard et al., 2014). The displacement distribution was processed with the software Sigmaplot to obtain histograms that were fitted with Gaussian peaks. The Stokes-Einstein equation was used to obtain the particle diameter d.

Dynamic Light Scattering

Light Scattering measurements were performed using a Malvern Nano ZS instrument equipped with a 633 nm laser diode. Samples were housed in disposable polystyrene cuvettes of 1 cm optical path length. DLS measurements were performed after dilution of the NPs suspension in phosphate-buffered saline (PBS) solution (1:50, vol:vol).

Transmission Electron Microscopy

A Philips CM 100 transmission electron microscope operating at 80 kV was used. For TEM investigations, a 3.05 mm copper grid (400 mesh) covered by a Formvar support film was dried up under vacuum after deposition of a drop of nanoparticles solution.

Cellular Experiments

HeLa cells were maintained in a DMEM medium (Gibco) supplemented with 10% FCS (Euroclone) and antibiotics (penicillin and streptomycin, Invitrogen) at 37°C in a humidified atmosphere containing 5% (v/v) CO_2; cells were split every 2–3 days. For MTS cytotoxicity assay, cells (1×10^4 cells) were plated onto a 96-well culture plate the day before the experiment. Cells were then incubated for 20 h with NPs at different concentrations in DMEM, added with 10% FCS. Cellular mitochondrial activity (indicator of cellular viability) was evaluated by MTS assay (Promega) according to the instruction manual. For the MTS test $N = 3$ independent experiments were run in triplicate. *t* test (significativity $p < 0,05$) were performed, but differences compared to control (no particles) were always not significant ($p > 0,05$). For the assessment of intracellular distribution of NPs, cells (1×10^5) were seeded on cover glasses and after 24 h they were incubated for 20 h at 37°C with NPs, washed with PBS and directly analyzed by confocal microscopy (Leica SP2). Images were processed using ImageJ software.

DATA AVAILABILITY

All datasets generated for this study are included in the manuscript and/or the supplementary files.

AUTHOR CONTRIBUTIONS

MM designed the synthesis of the NPs and supervised their preparation and characterization. FM and JT synthesized molecules 1, 2, and 3. VC prepared and characterized the NP. AC performed the photophysical characterization of molecules. RT and EP performed the cellular experiments.

ACKNOWLEDGMENTS

We gratefully acknowledge financial support from the European Research Council (ERC) (MOSAIC Starting Grant 259014) and the US Army Research Office (US-ARO) project W911NF-16-1-0324.

REFERENCES

Antaris, A. L., Chen, H., Cheng, K., Sun, Y., Hong, G. S., Qu, C. R., et al. (2016). A small-molecule dye for NIR-II imaging. *Nat. Mater.* 15, 235–242. doi: 10.1038/nmat4476

Battistini, G., Cozzi, P. G., Jalkanen, J. P., Montalti, M., Prodi, L., Zaccheroni, N., et al. (2008). The erratic emission of pyrene on gold nanoparticles. *ACS Nano* 2, 77–84. doi: 10.1021/nn700241w

Bodige, S. G., Méndez-Rojas, M. A., and Watson, W. H. (1999). Structure and properties of N-phenylmaleimide derivatives. *J. Chem. Crystallograph.* 29, 57–66. doi: 10.1023/a:1009571214760

Bonacchi, S., Cantelli, A., Battistelli, G., Guidetti, G., Calvaresi, M., Manzi, J., et al. (2016). Photoswitchable NIR-emitting gold nanoparticles. *Angew. Chem. Int. Ed.* 55, 11064–11068. doi: 10.1002/anie.201604290

Bonacchi, S., Rampazzo, E., Montalti, M., Prodi, L., Zaccheroni, N., Mancin, F., et al. (2008). Amplified fluorescence response of chemosensors grafted onto silica nanoparticles. *Langmuir* 24, 8387–8392. doi: 10.1021/la800753f

Boucard, J., Linot, C., Blondy, T., Nedellec, S., Hulin, P., Blanquart, C., et al. (2018). Small molecule-based fluorescent organic nanoassemblies with strong hydrogen bonding networks for fine tuning and monitoring drug delivery in cancer cells. *Small* 14:e1802307. doi: 10.1002/smll.201802307

Cauzzi, D., Pattacini, R., Delferro, M., Dini, F., Di Natale, C., Paolesse, R., et al. (2012). Temperature-dependent fluorescence of Cu5 metal clusters: a molecular thermometer. *Angew. Chem. Int. Ed.* 51, 9662–9665. doi: 10.1002/anie.201204052

Chen, J., Zeng, F., Wu, S., Su, J., and Tong, Z. (2009). Photoreversible fluorescent modulation of nanoparticles via one-step miniemulsion polymerization. *Small* 5, 970–978. doi: 10.1002/smll.200801067

Chen, K. H., Boettiger, A. N., Moffitt, J. R., Wang, S. Y., and Zhuang, X. W. (2015). RNA imaging. Spatially resolved, highly multiplexed RNA profiling in single cells. *Science* 348:aaa6090. doi: 10.1126/science.aaa6090

Chenouard, N., Smal, I., de Chaumont, F., Maška, M., Sbalzarini, I. F., Gong, Y., et al. (2014). Objective comparison of particle tracking methods. *Nat. Methods* 11, 281–289. doi: 10.1038/nmeth.2808

Cho, E. B., Volkov, D. O., and Sokolov, I. (2011). Ultrabright fluorescent silica mesoporous silica nanoparticles: control of particle size and dye loading. *Adv. Funct. Mater.* 21, 3129–3135. doi: 10.1002/adfm.201100311

Faucon, A., Benhelli-Mokrani, H., Fleury, F., Dutertre, S., Tramier, M., Boucard, J., et al. (2017). Bioconjugated fluorescent organic nanoparticles targeting EGFR-overexpressing cancer cells. *Nanoscale* 9, 18094–18106. doi: 10.1039/c7nr06533g

Fery-Forgues, S., Fayet, J.-P., and Lopez, A. (1993). Drastic changes in the fluorescence properties of NBD probes with the polarity of the medium: involvement of a TICT state? *J. Photochem. Photobiol. A Chem.* 70, 229–243. doi: 10.1016/1010-6030(93)85048-D

Genin, E., Gao, Z. H., Varela, J. A., Daniel, J., Bsaibess, T., Gosse, I., et al. (2014). "Hyper-bright" near-infrared emitting fluorescent organic nanoparticles for single particle tracking. *Adv. Mater.* 26, 2258–2261. doi: 10.1002/adma.201304602

Genovese, D., Bonacchi, S., Juris, R., Montalti, M., Prodi, L., Rampazzo, E., et al. (2013). Prevention of self-quenching in fluorescent silica nanoparticles by efficient energy transfer. *Angew. Chem. Int. Ed.* 52, 5965–5968. doi: 10.1002/anie.201301155

Grimm, J. B., English, B. P., Chen, J. J., Slaughter, J. P., Zhang, Z. J., Revyakin, A., et al. (2015). A general method to improve fluorophores for live-cell and single-molecule microscopy. *Nat. Methods* 12, 244–250. doi: 10.1038/nmeth.3256

Jiang, K., Sun, S., Zhang, L., Lu, Y., Wu, A. G., Cai, C. Z., et al. (2015). Red, green, and blue luminescence by carbon dots: full-color emission tuning and multicolor cellular imaging. *Angew. Chem. Int. Ed.* 54, 5360–5363. doi: 10.1002/anie.201501193

Jiang, Y. F., and McNeill, J. (2017). Light-harvesting and amplified energy transfer in conjugated polymer nanoparticles. *Chem. Rev.* 117, 838–859. doi: 10.1021/acs.chemrev.6b00419

Joshi, S., Kumari, S., Bhattacharjee, R., Sakhuja, R., and Pant, D. D. (2014). Estimation of ground and excited state dipole moments of synthesized coumarin derivative [N-(2-oxo-2H-chromen-4-yl)imino]triphenyl-phosphorane. *J. Mol. Liquids* 200, 115–119. doi: 10.1016/j.molliq.2014.09.054

Lee, M. H., Kim, J. S., and Sessler, J. L. (2015). Small molecule-based ratiometric fluorescence probes for cations, anions, and biomolecules. *Chem. Soc. Rev.* 44, 4185–4191. doi: 10.1039/C4CS00280F

Ma, K., Mendoza, C., Hanson, M., Werner-Zwanziger, U., Zwanziger, J., and Wiesner, U. (2015). Control of ultrasmall sub-10 nm ligand-functionalized fluorescent core–shell silica nanoparticle growth in water. *Chem. Mater.* 27, 4119–4133. doi: 10.1021/acs.chemmater.5b01222

Mak, C. C., Pomeranc, D., Montalti, M., Prodi, L., and Sanders, J. K. M. (1999). A versatile synthetic strategy for construction of large oligomers: binding and photophysical properties of a nine-porphyrin array. *Chem. Commun.* 1083–1084. doi: 10.1039/a900513g

Mei, J., Leung, N. L. C., Kwok, R. T. K., Lam, J. W. Y., and Tang, B. Z. (2015). Aggregation-induced emission: together we shine, united we soar! *Chem. Rev.* 115, 11718–11940. doi: 10.1021/acs.chemrev.5b00263

Melnychuk, N., and Klymchenko, A. S. (2018). DNA-functionalized dye-loaded polymeric nanoparticles: ultrabright FRET platform for amplified detection of nucleic acids. *J. Am. Chem. Soc.* 140, 10856–10865. doi: 10.1021/jacs.8b05840

Montalti, M., Battistelli, G., Cantelli, A., and Genovese, D. (2014). Photo-tunable multicolour fluorescence imaging based on self-assembled fluorogenic nanoparticles. *Chem. Commun.* 50:5326. doi: 10.1039/c3cc48464e

Mukherjee, S., Chattopadhyay, A., Samanta, A., and Soujanya, T. (1994). Dipole moment change of NBD group upon excitation studied using solvatochromic and quantum chemical approaches: implications in membrane research. *J. Phys. Chem.* 98, 2809–2812. doi: 10.1021/j100062a014

Muller, B. J., Zhdanov, A. V., Borisov, S. M., Foley, T., Okkelman, I. A., Tsytsarev, V., et al. (2018). Nanoparticle-based fluoroionophore for analysis of potassium ion dynamics in 3D tissue models and *in vivo*. *Adv. Funct. Mater.* 28:1704598. doi: 10.1002/adfm.201704598

Nifant'ev, E. E., Belov, S. P., Komlev, I. V., Petukhov, V. A., Semenov, M. A., Mezentseva, G. A., et al. (2008). Synthesis and investigation of new organophosphorus dyes of green and red luminescence. *Russian J. Gen. Chem.* 78, 383–391. doi: 10.1134/s1070363208030080

Ow, H., Larson, D. R., Srivastava, M., Baird, B. A., Webb, W. W., and Wiesner, U. (2005). Bright and stable core-shell fluorescent silica nanoparticles. *Nano Lett.* 5, 113–117. doi: 10.1021/nl0482478

Pitto-Barry, A., and Barry, N. P. E. (2014). Pluronic® block-copolymers in medicine: from chemical and biological versatility to rationalisation and clinical advances. *Polymer Chem.* 5, 3291–3297. doi: 10.1039/C4PY00039K

Proetto, M. T., Anderton, C. R., Hu, D. H., Szymanski, C. J., Zhu, Z. H., Patterson, J. P., et al. (2016). Cellular delivery of nanoparticles revealed with combined optical and isotopic nanoscopy. *ACS Nano* 10, 4046–4054. doi: 10.1021/acsnano.5b06477

Pyo, K., Thanthirige, V. D., Kwak, K., Pandurangan, P., Ramakrishna, G., and Lee, D. (2015). Ultrabright luminescence from gold nanoclusters: rigidifying the Au(I)–thiolate shell. *J. Am. Chem. Soc.* 137, 8244–8250. doi: 10.1021/jacs.5b04210

Ragab, S. S., Thapaliya, E. R., Zhang, Y., Tang, S., McMahan, J. B., Syed, S., et al. (2016). Synthesis in living cells with the assistance of supramolecular nanocarriers. *RSC Adv.* 6, 32441–32445. doi: 10.1039/C6RA04335F

Rampazzo, E., Bonacchi, S., Genovese, D., Juris, R., Sgarzi, M., Montalti, M., et al. (2011). A versatile strategy for signal amplification based on core/shell silica nanoparticles. *Chem. Eur. J.* 17, 13429–13432. doi: 10.1002/chem.201101851

Reisch, A., and Klymchenko, A. S. (2016). Fluorescent polymer nanoparticles based on dyes: seeking brighter tools for bioimaging. *Small* 12, 1968–1992. doi: 10.1002/smll.201503396

Rio-Echevarria, I. M., Selvestrel, F., Segat, D., Guarino, G., Tavano, R., Causin, V., et al. (2010). Highly PEGylated silica nanoparticles: "ready to use" stealth functional nanocarriers. *J. Mater. Chem.* 20:2780. doi: 10.1039/b921735e

Rio-Echevarria, I. M., Tavano, R., Causin, V., Papini, E., Mancin, F., and Moretto, A. (2011). Water-soluble peptide-coated nanoparticles: control of the helix structure and enhanced differential binding to immune cells. *J. Am. Chem. Soc.* 133, 8–11. doi: 10.1021/ja107588q

Sbalzarini, I. F., and Koumoutsakos, P. (2005). Feature point tracking and trajectory analysis for video imaging in cell biology. *J. Struct. Biol.* 151, 182–195. doi: 10.1016/j.jsb.2005.06.002

Selvestrel, F., Moret, F., Segat, D., Woodhams, J. H., Fracasso, G., Echevarria, I. M. R., et al. (2013). Targeted delivery of photosensitizers: efficacy and selectivity issues revealed by multifunctional ORMOSIL nanovectors in cellular systems. *Nanoscale* 5:6106. doi: 10.1039/c3nr00402c

Shukla, D., and Wan, P. (1993). Product studies of electron transfer from dimethoxybenzene and trimethoxybenzene to photoexcited xanthenium cations in S1 in aqueous acid solution. *J. Photochem. Photobiol. A Chem.* 76, 47-53. doi: 10.1016/1010-6030(93)80172-6

Sun, G. R., Berezin, M. Y., Fan, J. D., Lee, H., Ma, J., Zhang, K., et al. (2010). Bright fluorescent nanoparticles for developing potential optical imaging contrast agents. *Nanoscale* 2:548. doi: 10.1039/b9nr00304e

Tang, Y. H., Lee, D. Y., Wang, J. L., Li, G. H., Yu, J. H., Lin, W. Y., et al. (2015). Development of fluorescent probes based on protection–deprotection of the key functional groups for biological imaging. *Chem. Soc. Rev.* 44, 5003–5015. doi: 10.1039/C5CS00103J

Trofymchuk, K., Reisch, A., Didier, P., Fras, F., Gilliot, P., Mely, Y., et al. (2017). Giant light-harvesting nanoantenna for single-molecule detection in ambient light. *Nat. Photonics* 11, 657–663. doi: 10.1038/s41566-017-0001-7

Volkov, D. O., Cho, E. B., and Sokolov, I. (2011). Synthesis of ultrabright nanoporous fluorescent silica discoids using an inorganic silica precursor. *Nanoscale* 3:2036. doi: 10.1039/c0nr01015d

Wolfbeis, O. S. (2015). An overview of nanoparticles commonly used in fluorescent bioimaging. *Chem. Soc. Rev.* 44, 4743–4768. doi: 10.1039/C4CS00392F

Wu, C. F., Szymanski, C., and McNeill, J. (2006). Preparation and encapsulation of highly fluorescent conjugated polymer nanoparticles. *Langmuir* 22, 2956–2960. doi: 10.1021/la060188l

Xu, S. D., Fang, C. H., Tian, G. X., Chen, Y., Dou, Y. H., Kou, J. F., et al. (2015). Reduction of 4-azidonaphthalimide with different phosphine ligands and exploration of their spectroscopic properties. *J. Mol. Struct.* 1102, 197–202. doi: 10.1016/j.molstruc.2015.08.056

Xu, W., Zeng, Z. B., Jiang, J. H., Chang, Y. T., and Yuan, L. (2016). Discerning the chemistry in individual organelles with small-molecule fluorescent probes. *Angew. Chem. Int. Ed.* 55, 13658–13699. doi: 10.1002/anie.201510721

Conflict of Interest Statement: The authors declare that the research was conducted in the absence of any commercial or financial relationships that could be construed as a potential conflict of interest.

frontiers in Chemistry

ORIGINAL RESEARCH
published: 03 December 2018
doi: 10.3389/fchem.2018.00593

Growth of CNT Forests on Titanium Based Layers, Detailed Study of Catalysts

*Anna Szabó[1], Pavao Andričević[2], Zsuzsanna Pápa[3], Tamás Gyulavári[1], Krisztián Németh[1], Endre Horvath[2], László Forró[2] and Klara Hernadi[2]**

[1] Department of Applied and Environmental Chemistry, University of Szeged, Szeged, Hungary, [2] Laboratory of Physics of Complex Matter (LPMC), Ecole Polytechnique Federale de Lausanne, Lausanne, Switzerland, [3] Department of Optics and Quantum Electronics, University of Szeged, Szeged, Hungary

For better electrical contacts of potential devices, growth of vertically aligned carbon nanotubes (CNT forests) directly onto conductive substrates is an emerging challenge. Here, we report a systematic study on the CCVD synthesis of carbon nanotube forests on titanium based substrates. As a crucial issue, the effect of the presence of an insulating layer (alumina) on the growing forest was investigated. Other important parameters, such as the influence of water vapor or the Fe-Co catalyst ratio, were also studied during the synthesis. As-prepared CNT forests were characterized by various techniques: scanning and transmission electron microscopies, Raman spectroscopy, spectroscopic ellipsometry. CNT forests grown directly onto the conductive substrate were also tested as electrodes in hybrid halide perovskite photodetectors and found to be effective in detecting light of intensity as low as 3 nW.

Keywords: CNT forests, conductive substrate, CCVD synthesis, titanium substrate, Fe-Co catalyst, hybrid perovskite photodetectors

OPEN ACCESS

Edited by:
Carlos Lodeiro, Universidade Nova de Lisboa, Portugal

Reviewed by:
Maria Vittoria Diamanti, Politecnico di Milano, Italy
Ayaskanta Sahu, New York University, United States

****Correspondence:***
Klara Hernadi
hernadi@chem.u-szeged.hu

Specialty section:
This article was submitted to Nanoscience, a section of the journal Frontiers in Chemistry

Received: *20 September 2018*
Accepted: *13 November 2018*
Published: *03 December 2018*

Citation:
Szabó A, Andričević P, Pápa Z, Gyulavári T, Németh K, Horvath E, Forró L and Hernadi K (2018) Growth of CNT Forests on Titanium Based Layers, Detailed Study of Catalysts. Front. Chem. 6:593. doi: 10.3389/fchem.2018.00593

1. INTRODUCTION

Vertically aligned carbon nanotubes (VACNT) which are often referred to as carbon nanotube forests in the literature (CNT forest), were synthesized for the first time in 1996 (Li et al., 1996). Since then, this invention has served as a novel architectural design to integrate into various devices in the field of nanotechnology. The most conventional way to produce CNT forests is *via* catalytic chemical vapor deposition (CCVD). During the CVD method, the most commonly used catalysts are transition metals, which can be Fe, Co, Ni, while SiO_2, Al_2O_3, or MgO are often used as oxide support (Noda et al., 2007; Halonen et al., 2008; Mattevi et al., 2008; Sakurai et al., 2011; Robertson et al., 2012). In the research field of CNT forests an important breakthrough was made in 2004, when Hata et al. (2004) introduced a small amount of water into the CVD synthesis chamber, which drastically influenced the growth rate the ultimate height and quality of VACNT. Although, there is a growing understanding about the molecular-level mechanism of this so called "super-growth" method, still studying the influence of the synthesis conditions on the physicochemical properties of CNTs is still crucial, in order to reveal and tune the parameter space of the properties such as the orientation, the height, the density, and degree of graphitization.

The catalyst layer can be deposited in various ways. For example, wet-chemical methods as dip-coating, spray coating, or high vacuum techniques as thermal evaporation, magnetron sputtering, and pulsed laser deposition (PLD) (Mauron et al., 2002; Murakami et al., 2003; Fejes et al., 2015). In 2007, Noda et al. studied the effect of the presence of aluminum oxide on

silicon substrate in relation to the synthesis of carbon nanotube forests. They have found that the intermediate oxide support on the silicon substrate was crucial to provide a strong interaction between the oxide layer and the catalyst layer.

Besides silicon, many other materials, such as SiO_2, stainless steel, copper, aluminum, and titanium could serve as a support for VACNT synthesis (Santhanagopalan et al., 2009; Atthipalli et al., 2011; Dörfler et al., 2013; Zhu et al., 2013; Silva et al., 2014). Potential use of VACNTs in electronics and optoelectronics aims for the elimination of the insulating oxide layer and necessitates the growth of carbon nanotubes directly on conductive substrates to provide better electrical contact. Only few publications are addressing this topic, where the synthesis of the carbon nanotube forests was achieved directly on metallic aluminum or stainless steel. The aim of these papers was mainly to investigate the conductivity properties of the products (Matthews et al., 2006; Masarapu and Wei, 2007; Pattinson et al., 2015).

Regarding the synthesis of carbon nanotube forests, the formation of the catalyst layer is a significant parameter, hence it strongly affects the growth of the carbon nanotubes. Several publications have dealt with the effect of catalyst ratios, the most commonly used transitional metals were such as Fe, Co, and Ni (Dresselhaus et al., 2005; Antunes et al., 2006). In the literature, Fe:Co = 1:1 is most often used (Shokry et al., 2014), nevertheless FeO also has contributed to the growth of carbon nanotube forests, where iron oxide clusters were formed on the substrate (Mauron et al., 2002). However, thorough research was carried out in this topic, where other ratios have been studied and such an observation could be made that similar results can be achieved using other catalyst ratios (Seo et al., 2003; Magrez et al., 2011; Szabó et al., 2017).

Here, we investigate the effect of aluminum oxide support on the growth of carbon nanotube forests over metallic titanium substrates. The as prepared VACNTs have been combined with organic inorganic lead halide perovskite single crystals to prepare heterojunction interfaces by applying simple mechanical pressure and point-contact electrodes. We have found that the VACNTs without alumina layer could serve as an excellent electrode material for lead halide perovskite photodetectors. The elimination of the alumina deposition step might reduce the degree of complications, ultimately the price in the photodetector fabrication process.

2. MATERIALS AND METHODS

2.1. Materials

In the experimental part Titanium sheets were used, manufactured by WRS Materials Company. The catalyst layers were evolved using aluminum-oxide (WRS Materials Company), iron (III)-oxide (99.998%, Sigma-Aldrich), and cobalt (II)-oxide (99.99%, Sigma-Aldrich) were used as pellets. During CCVD synthesis ethylene, hydrogen, and nitrogen were used, all manufactured by Messer Hungary.

2.2. Catalyst Layer Production

Catalyst layers and oxide were prepared by PLD following the same deposition conditions as in our previous work (Pápa et al., 2018). Catalyst and oxide target were made of metal oxides' powder (Fe_2O_3, CoO and Al_2O_3) with a total weight of 1 g shaped into a 1 cm diameter pellet. The mechanical resistance was improved by heat treatment, which in this case lasted 4 h at 500°C in air. In order to provide reproducible adhering conditions onto the substrate, the titanium substrate was sequentially washed with distilled water, absolute ethanol, and acetone prior to catalyst layer deposition. The cleaned titanium substrate was placed into a vacuum chamber. For the layer deposition, laser pulses of a LLG TWINAMP ArF excimer laser (λ = 193 nm, pulse length: 18 ns, repetition rate: 10 Hz) with average fluence of 13 J/cm^2 were focused on the target pellets placed in front of the titanium substrate where the layer was formed. The target-substrate distance was 3 cm. The catalyst layer thickness could be tuned with the number of lasers shots. According to a previous thickness optimization, the catalyst layer thickness was set to be 5 nm proven by spectroscopic ellipsometry measurements (Woollam M-2000F) (Fejes et al., 2015; Pápa et al., 2018).

2.3. CCVD Synthesis

For the carbon nanotube forest production, the CCVD synthesis method was used. The titanium sheets including the catalyst layers were cut into 4 × 4 mm small sheets, in order to fit the quartz boat, (diameter 20 mm). The experiments were carried out at 700°C and the reaction time was 30 min. During the synthesis, the carrier gas was nitrogen with a flow rate of 50 cm^3/min, the carbon source was ethylene with a flow rate of 70 cm^3/min, the reducing agent was hydrogen with a flow rate of 50 cm^3/min, while the system contained water vapor with a flow rate of 30 cm^3/min, which contributed to the growth of carbon nanotube forests.

In the first step of the synthesis, the reactor was purged with nitrogen to exclude oxygen from the system (2 min). Then hydrogen gas was introduced into the reactor, to reduce the catalysts (5 min). Subsequently, ethylene and water vapor were added to the synthesis. When the reaction was finished, all gas flows were closed, except nitrogen gas, which remained in the system for an additional 5 min. After the reactor was removed from the oven, and it was cooled to room temperature; in the final step as-synthesized samples were removed from the reactor. "Blank" synthesis was also carried out with the elimination of carbon source ethylene.

2.4. Microscopic and Spectroscopic Characterization of CNT Samples

The orientation of the CNT forests was investigated by the means of Scanning Electron Microscopy (SEM), which type was Hitachi S-4700 Type II FE-SEM (5–15 keV). For the careful measurement of CNTs, the sample holder was tilted at a 35° angle within the SEM device, making possible their examination from all directions. The SEM results were evaluated with ImageJ software. During determination of the height of CNT forests this condition has to be taken into account, thus the measured height was divided by sin 35° based on geometric considerations to obtain the actual height.

The diameters of the carbon nanotubes were examined by Transmission Electron Microscopy (TEM, Philips CM 10, 100

keV). In order to prepare the TEM grids, small amount of CNT forests were scraped off the Ti foil with a spatula and was suspended in 1.25 cm^3 absolute ethanol. Two to three drops of the suspension were applied on the holey carbon grid (Lacey, CF 200).

The graphitic properties of CNT were analyzed by Raman Spectroscopy (Thermo Scientific DXR Raman microscope, excitation wavelength 532 nm).

2.5. Fabrication of Hybrid Perovskite Photodetectors

2.5.1. Crystal Growth

Crystals of the methylammonium lead tribromide were synthesized by solution growth. The 3.3 mmol lead (II) acetate trihydrate ($Pb(ac)_2 \times 3H_2O$, > 99.9%) was reacted with 6 ml saturated HBr solution (48 wt% HBr in H_2O). The formed $PbBr_2$ precipitate is stable in the acidic solution. The respective amount (3.30 mmol) of methylamine (CH_3NH_2) solution (40 wt% in H_2O) was pipetted into the 5 °C ice cooled solution of $PbBr_2$. The cold solution avoids the evaporation of methylamine during the exothermic reaction. Orange colored microcrystallites of $CH_3NH_3PbBr_3$ were formed. The $MAPbBr_3$ crystals were recrystallized in a temperature gradient of 15°C in the acidic media to get transparent, high purity crystals.

2.5.2. Optoelectronic Characterization

All the performances measurements of the devices were done in ambient conditions at room temperature. The junction characteristics have been determined by two points resistivity measurements, tungsten needles as electrical leads. One of the contacts is positioned directly on the perovskite single crystal, whereas the second one touches the Ti foil as the back electrode. A Keithley 2400 source meter allowed us to measure the current with <0.1 nA resolution, while tuning the applied bias voltage, in dark and under visible light illumination. Current-Voltage measurements were performed by sweeping the voltage from 0 to +2 V/-2 V and back, with a scan speed of 0.2 V/s. Photocurrent measurements at low light intensities were done by choosing 550 nm wavelength, within the spectral response of our device, enabling also to achieve high enough intensities of light that can be detected. The wavelength was set with a monochromator (Horiba Micro HR), while light intensity was adjusted by closing and opening slits in the light path.

3. RESULTS

3.1. The Effect of the Oxide Layers on the Titanium-Based Support

Firstly, the presence of the oxide layer on the surface of the substrate was investigated regarding its influence on the quality of the CNT forests. During the synthesis two possibilities were inspected: applying an Al_2O_3 layer between the catalyst layer and the substrate, and in the other case, without any oxide layer present. All synthesis parameters were kept identical, including the thickness of the catalyst layer of 5 nm.

In literature, oxide layers are often used on the substrate, as they may influence the CNT forests quality significantly *via* promoting the separation of catalytic particles. The interface created between the Al_2O_3 and the catalyst particles was proved to play an essential role on the growth of CNTs. Furthermore, the hydrocarbon adsorption onto the aluminum oxide, and the surface diffusion from the aluminum oxide to the Fe nanoparticles was found to be very important (Noda et al., 2007). Nevertheless, CNT forests grown directly on metals might allow immediate junction with the conductive substrate, which can result in reduced contact resistance providing increased conductivity of the sample (Zhao and Kang, 2011). The effect of oxide supports on the CNT forest was first characterized by SEM images (**Figure 1**).

Neverthless, the CNT forests can clearly grow on a conductive support without an aluminum oxide layer, as seen in the SEM image (**Figure 1b**). However, it could be observed that the height of CNT forests was influenced significantly by the oxide support. While the height of the CNT forests over the alumina support was 108 μm (**Figure 1a**), the height of the CNT forests over metallic titanium support was only 32 μm (**Figure 1b**). However, besides the disparity in height no considerable difference in the quality was detected according to the SEM micrographs. However, water vapor might oxidize the metallic substrates *in-situ* during the nanotube growth.

Therefore, to exclude potential artifacts, the possibility of growing carbon nanotube vertically aligned structures on metallic titanium substrate without water vapor was tested. Samples with and without the intermediate alumina layer were prepared. The synthesis conditions were kept constant, as before, with the addition of absolutely excluding water vapor from the feed to prove whether the oxidative property of water vapor was indispensable during the synthesis.

Again, it is clearly visible from SEM images that carbon nanotube forests are formed on both types of Ti substrates (**Figure 2**) Interestingly, nevertheless the height of the forest on the titanium substrate having the alumina intermediate layer is in the same range (**Figure 2**) as that one synthesized with water vapor. Unlike the catalyst having the alumina layer, those without alumina showed significantly reduced height as compared their counterparts prepared in the presence of water vapor. While the height of carbon nanotube forest was 32 μm in the presence water vapor, this value dropped down 4.62 μm in the absence of water vapor. The role of ethylene in the gas feed is to provide carbon source for the growth of CNT forest, however, the hydrocarbon simultaneously deactivates the catalytic particles via reduction. To lessen this disadvantageous effect, water vapor is added to the system, too, which is able to oxidize thus regenerate the catalyst particles continuously. Nevertheless, water vapor can react with the forming CNT forest reducing their height (CNT walls are very stable if well-graphitized so they can be more easily attacked from the ends) (Hernadi et al., 2001). Without water vapor not only the height of the CNTs was very low, but also the structural quality, probably because of the healing capacity of water vapor. It seems to be a reasonable explanation, nevertheless, in the literature of CCVD methods such interpretation occurs only in few cases (Sugime et al., 2018).

The catalyst morphology, of a sample with a layer thickness of 5 nm, was investigated right after the heat treatment. During

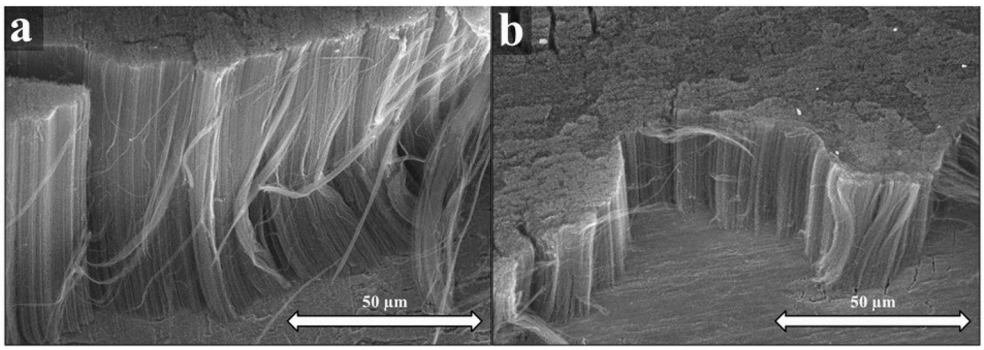

FIGURE 1 | SEM images of CNT forests synthesized with Al_2O_3 oxide support **(a)**, SEM images of CNT forests synthesized without Al_2O_3 oxide support **(b)**.

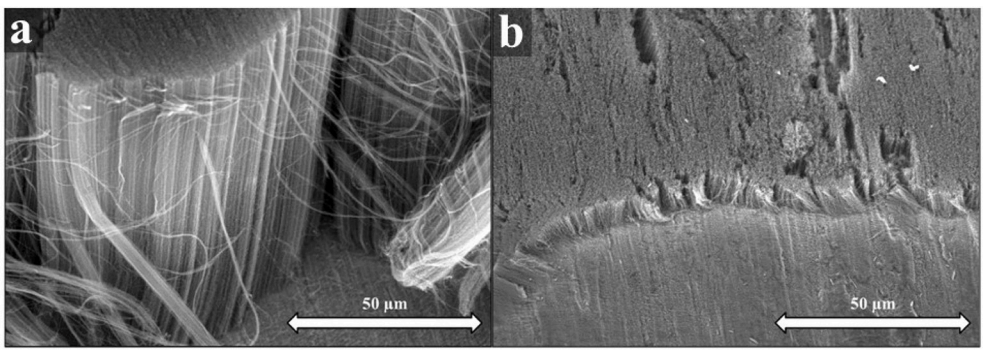

FIGURE 2 | SEM images of CNT forests synthesized with **(a)** and without **(b)** Al_2O_3 oxide support with no water vapor in the gas feed.

this blank synthesis, the carbon source was not allowed into the system. SEM images of the samples and a histogram of the particle size distribution can be seen in **Figure 3**. It can be concluded, that the supporting oxide layer has a significant influence on the distribution of catalyst particles on the surface of the substrate.

From the SEM images (**Figure 3a**), it can be observed, that the catalyst particles are separated when the oxide layer is deposited in advance onto the surface of the substrate and their average diameter is 27.5 ± 5.7 nm (**Figure 3c**). However, when there was no aluminum oxide layer on the substrate, the catalyst particles were aggregated probably as a result of the different wetting properties of the oxide and the metal (see **Figure 3b**) and their average diameter was 50.4 ± 11.6 nm (**Figure 3c**).

As in other metallic substrates, titanium can form special diphase type of alloys (α + β) with various metals and allows the formation of Ti_xMe_y precipitates especially on the surface (Frommeyer, 2007). In this way, the essential condition of separated catalytic particles for seeding carbon nanotube growth at the very beginning of the CCVD reaction is ensured.

Further structural analyses were performed on the CNT forests. TEM analysis was carried out to verify the quality of individual carbon nanotubes (**Figures 4a,b**). An observable difference was found between the graphitic properties of carbon nanotubes prepared with and without the oxide layer on the substrate. In accordance with Raman spectroscopy results, TEM investigations revealed that fewer defects can be detected in the CNT walls when an oxide layer is also deposited on the titanium substrate. HR-TEM images revealed that the CNTs were typically consisted of 8–9 walls in average (**Figure 4c**). The CNT with and increased number of walls showed much less graphitic features (**Figure 4d**). Furthermore, catalyst particles were predominantly not observed, which demonstrates that the carbon nanotube forest growth can be explained by the root mechanisms (Sugime et al., 2013; Yang et al., 2015). However, rarely particles were found at the end of the tube, (**Figure 4d**) not entirely excluding the tip growth mechanism. Analyzing the histogram it was concluded that the outer diameter of carbon nanotubes was between 12–13 nm for both samples (**Figure 4e**).

Raman Spectroscopy was used to determine the Raman shifts in the case of both samples. Based on the Raman spectra, only a small difference was observed, however, in the presence of Al_2O_3 the value of the I_G/I_D peaks fraction was: I_G/I_D = 1.18, while in the absence of Al_2O_3 it was I_G/I_D = 1.33 (**Figure 4f**). According to literature data, samples with an oxide support exhibit higher-levels of graphitic properties.

3.2. The Effect of Catalyst Ratio on the CNT Forests

Secondly, the effect of the Fe:Co ratio of the catalyst was investigated regarding the CNT forest growth. As previously,

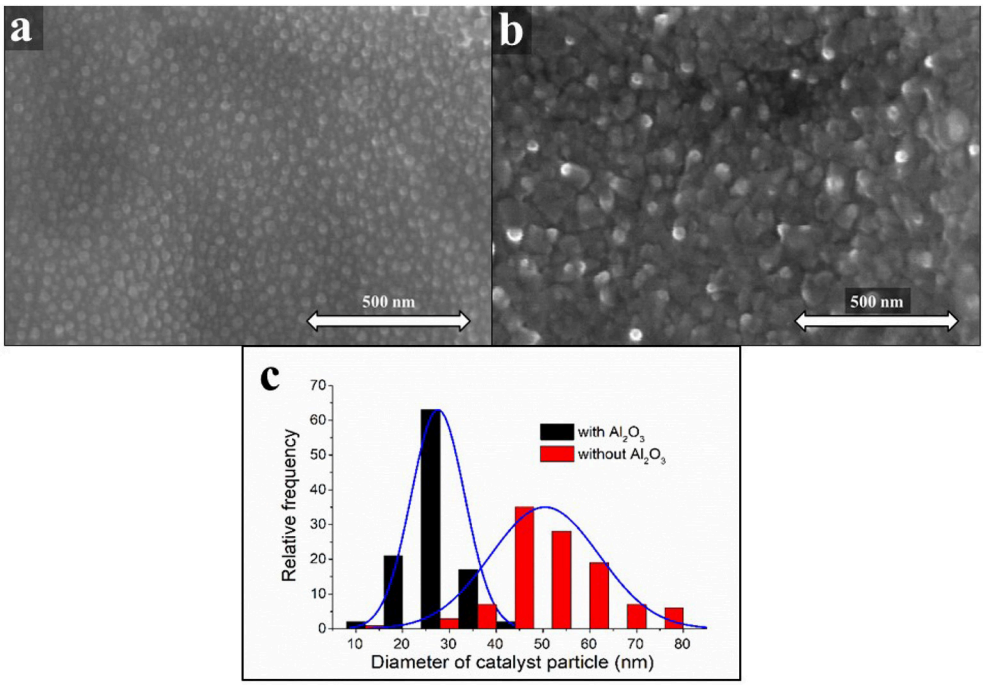

FIGURE 3 | SEM images of CNT forests pre-synthesized with **(a)** and without Al_2O_3 oxide support **(b)**. Distribution of catalyst particle size with and without Al_2O_3 oxide support **(c)**.

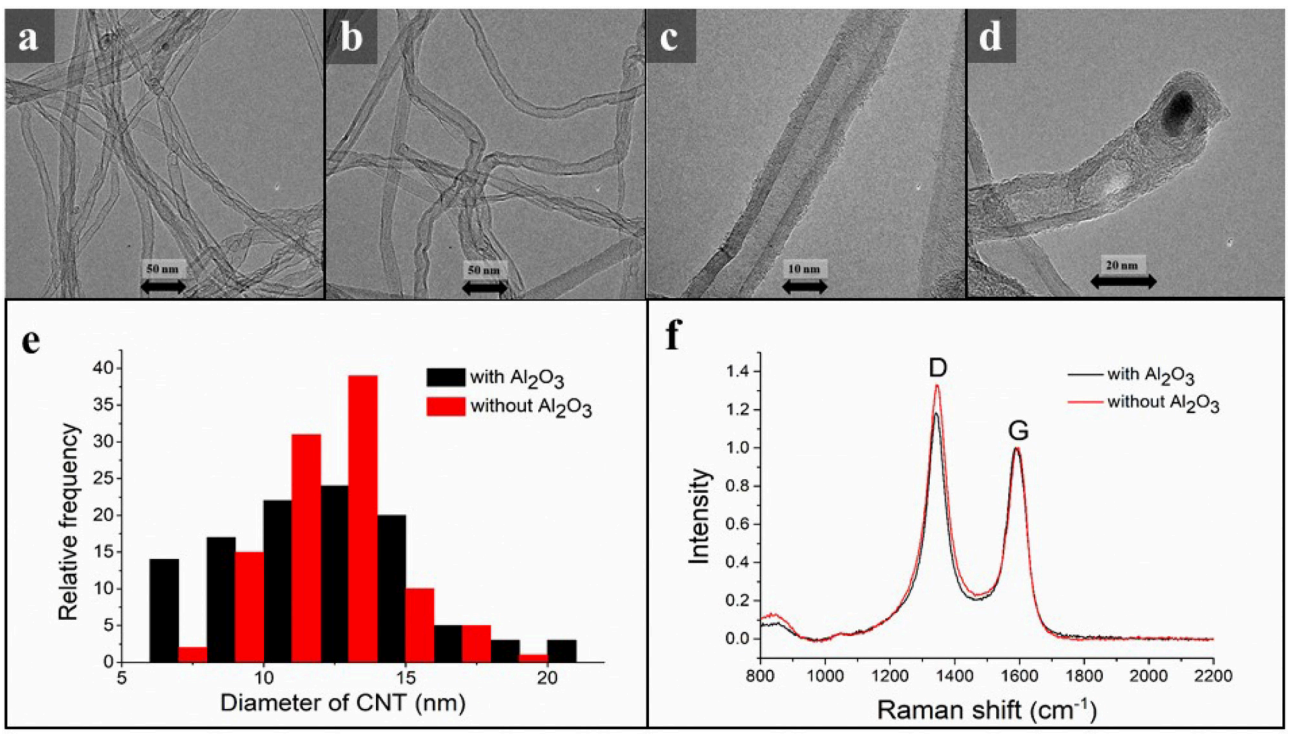

FIGURE 4 | TEM images of carbon nanotubes synthesized with **(a)** and without Al_2O_3 oxide support **(b)**, with higher magnification **(c)**, of a catalyst particle at the end of a CNT **(d)**; the diameter distribution of carbon nanotubes grown in the presence or the absence of alumina layer **(e)**; Raman spectra of CNT forests synthesized with and without Al_2O_3 oxide support **(f)**.

samples were synthesized with and without the Al_2O_3 layer on the substrate, dividing the samples in two groups. Consequently, the catalyst ratios were changed as follows: Fe:Co = 1:3, 2:3, 1:1, 3:2, and 3:1.

The Al_2O_3 oxide layer proved to facilitate the growth of the CNT forests as it created a thin layer on the substrate, which suppressed diffusion and aggregation of the catalyst nanoparticles. It was found that the growth of CNT forests was dependent from the presence of the oxide layer, so we suppose that alumina may affect the deposition of the catalyst particles on the surface, as well as the formation of an Al-Fe alloy (Magrez et al., 2011).

Based on literature data it is well known, that Ti has excellent wetting and thermal properties, along with being one of the best thermal interface materials. Therefore, it was feasible to deposit catalytic particles on its surface, ensuring the possibility to grow CNT forests directly on metal surfaces (Li et al., 2009). Accordingly, the effect of the Fe:Co ratio of the catalyst on the CNT forest growth was investigated *via* SEM (**Figure 5**).

From the SEM images (**Figure 5**), it was observed that the composition of the catalyst affects the heights of the carbon nanotube forests. However, at the same time, the orientation of the CNT forests was not changed significantly. The highest CNT forests 110 μm were attained with a 1:1 ratio. Surprisingly, this is in contrast with our former observations with an aluminum support (Szabó et al., 2017). It was believed that the height of the CNT forests grown with a 1:1 ratio is very similar to that of a 1:3 ratio. However, from the results in **Figure 5** it is clear that with a 3:1 ratio, the minimum CNT forests height is obtained, namely 10 μm.

Same series of CNT growth, varying the catalyst ratio, were performed now employing titanium supports without the alumina layer. SEM images revealed (**Figure 6**), that different catalyst ratio have also affected the growth of carbon nanotube forests, but to a much less extent. While the height of the first four samples (1:3, 2:3, 1:1, and 3:2) was around 20 μm with small differences. The catalyst ratio Fe:Co = 3:1, enable the growth of a much higher CNT forest (62 μm). In contrast with former literature observations, the frequently used 1:1 ratio resulted in a much lower CNT forest, up to three times lower CNT forests than its 3:1 ratio counterpart.

Summarizing the results from the two series, it was observed that in the presence of an insulating oxide layer on the surface of titanium substrate higher CNT forests were obtained. Interestingly, when the catalyst ratio was 2:3 or 3:2, the height of the CNT forests was relatively close in both cases, independently of the presence of the alumina layer. In the literature it can be found, that the oxide support has an advantageous effect on the substrate as the oxide layer can prevent the diffusion and aggregation of the catalyst nanoparticles, thus the dissolution of the reduced catalytic metal in the substrate can be prevented, as a result, on the oxide support separated nanoparticles on the substrate can act as catalyst. In our case when there was Al_2O_3 oxide support on the substrate, the highest CNT forest grew over the layers with 1:1 and 1:3 ratio as shown in the **Figure 7**. In the literature the most commonly used Fe:Co ratio is the 1:1 (Kaneko et al., 2012), however, in our system the 1:3 ratio produced similar height, probably due to the stronger interaction of cobalt oxide and alumina layer, keeping separated catalyst nanoparticles on the surface. In the second case when the substrate was applied without Al_2O_3 oxide layer, the maximum height of carbon nanotube forests was observed at the ratio of 3:1 as shown in the **Figure 7** and practically the height increases linearly with iron content. Beside the above-mentioned Ti_xMe_y precipitates, another occurrence might affect the growth mechanism of CNT growth, namely, increasing iron content in titanium substrate can enhance hydride formation (Dalebrook et al., 2013), which might promote carbon nanotube formation.

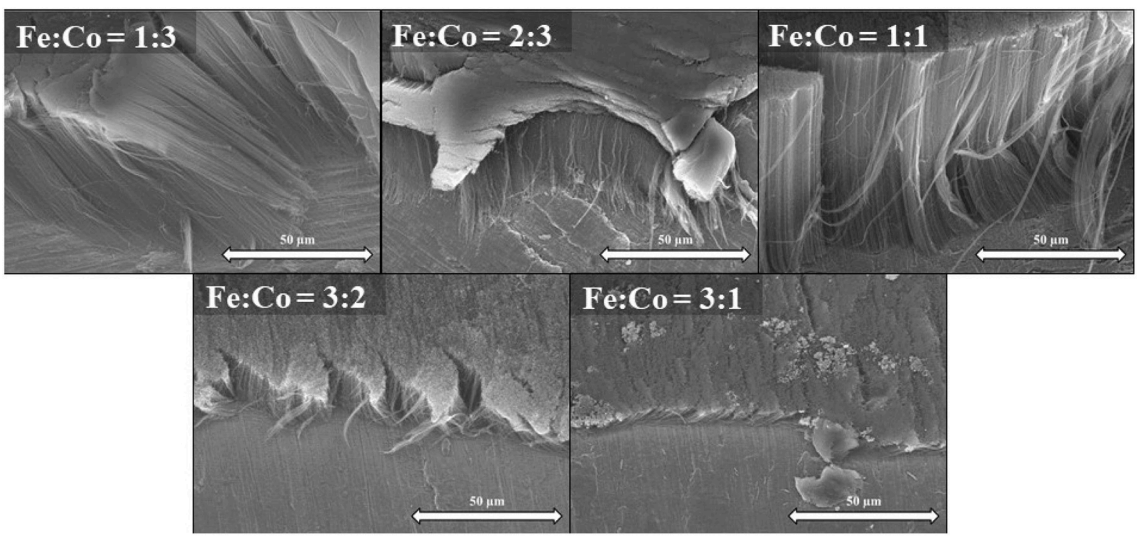

FIGURE 5 | SEM images of CNT forests synthesized at various catalyst ratios with Al_2O_3 oxide layer on titanium support.

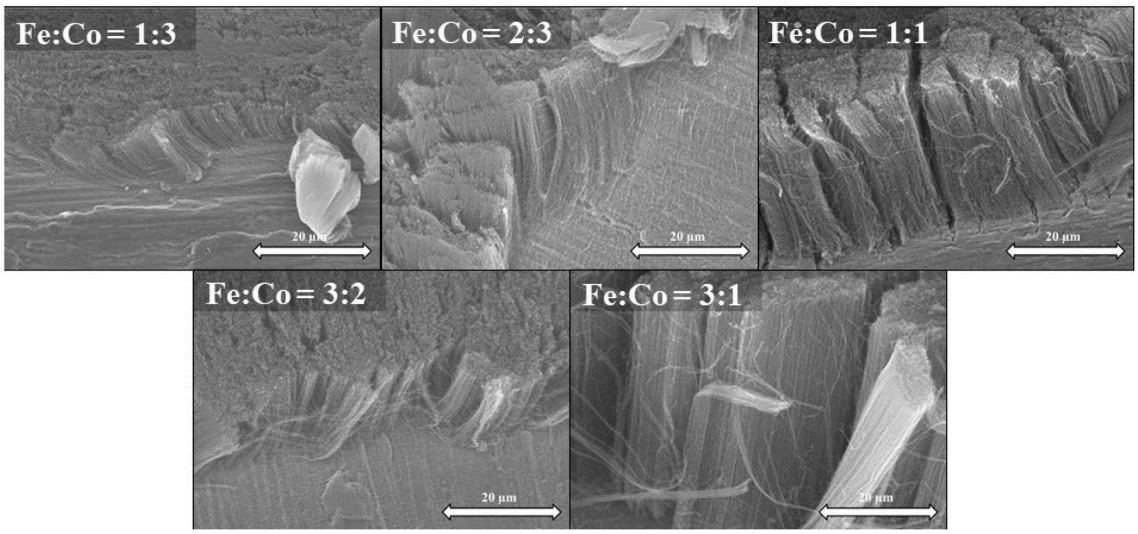

FIGURE 6 | SEM images of CNT forests synthesized at various catalyst ratios without Al_2O_3 oxide layer on titanium support.

3.3. The Effect of the Oxide Supports on Performances of Organic-Inorganic Halide Perovskite Photodetectors Employing Vertically Aligned CNT Forests as Electrodes

Recently, CNT forests have been introduced as electrodes in sensitive hybrid perovskite photodetectors, able to detect visible light of nW intensities (Andričević et al., 2017). Therefore, light detector devices were fabricated using the aforementioned CNT forests and methylammonium lead tribromide ($MAPbBr_3$) single crystals to study the effect of the presence of oxide layers on the detection properties. A heterojunction was fabricated by dry pressing a 5 mm $MAPbBr_3$ single crystal on the top of CNT forests.

In order to measure the photodiode performance, tungsten needles, which served as electrical leads, were pressed on top of the surface of the perovskite single crystal and onto the Ti foil back electrode, respectively (**Figure 8a**). Current-Voltage (I–V) characteristics were measured for both samples in the dark and under white fluorescent light source with an intensity of 1.02 mW/cm^2 (**Figure 8b**). Both devices exhibit diode-like characteristics. The presence of the aluminum oxide support does not differ the photocurrent of the forward bias region and the On-Off measurement significantly (**Figure 8c**). However, the photocurrent in reverse bias is smaller for the device without Al_2O_3, resulting in a higher diode ideality factor than its counterpart with the presence of an oxide layer. The photodetectors have been tested at low light intensities to determine the responsivity, a typical figure of merit for light sensing devices. On-Off measurements were performed under 550 nm green light for intensities ranging from 250 to 3 nW. The photocurrent increases with increasing light intensity for both devices with and without the oxide layer as seen in **Figures 8d,e**, respectively. Importantly, both devices detect light in the lowest intensity range of 3 nW, achieving reasonably high responsivities up to 1 A/W (**Figure 8f**).

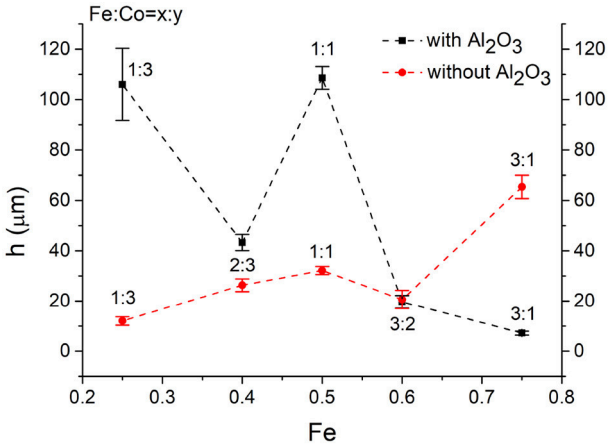

FIGURE 7 | Heights of CNT forests with Al_2O_3 oxide support and without Al_2O_3 oxide support.

CONCLUSION

In conclusion, certain parameters during both catalyst preparation procedure and CCVD synthesis can strongly affect the growth of vertically aligned carbon nanotubes. Applying titanium plates as a substrate it was found that the presence of an alumina layer on the surface significantly modifies the morphology of the catalyst layer (before reaction), thus influencing the CNT forest growth. One could expect that titanium as a metallic substrate dissolves reduced Fe-Co nanoparticles during preliminary hydrogenation and in this way

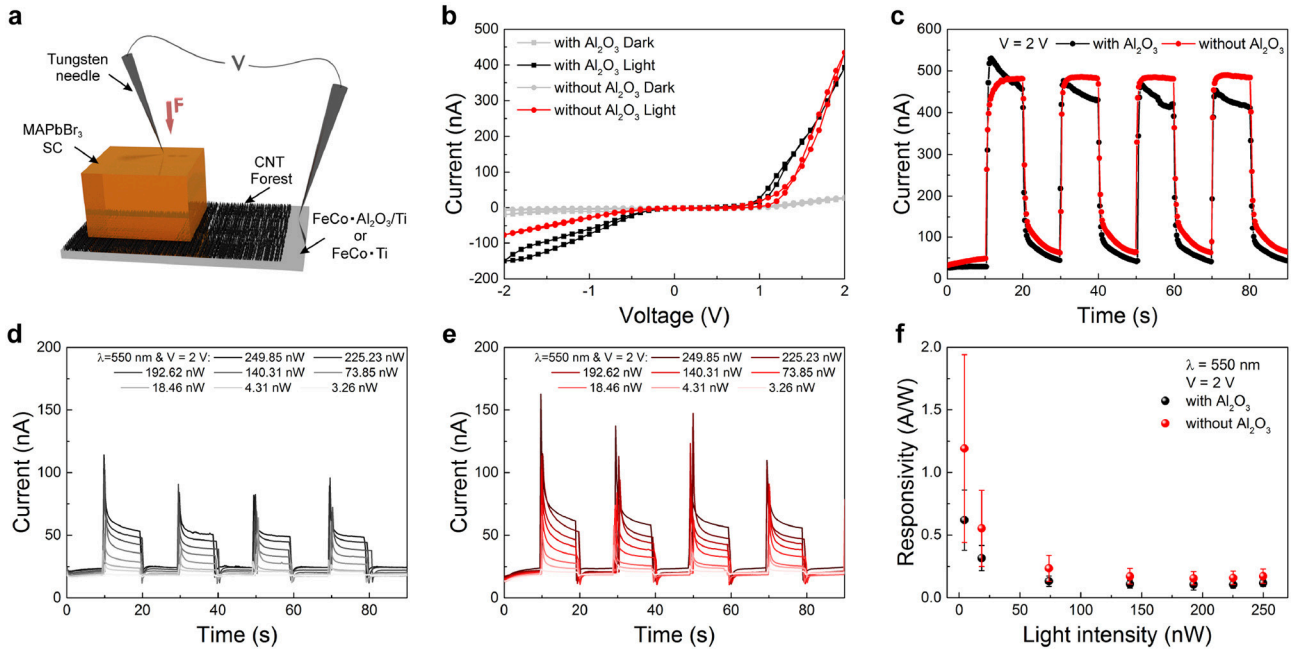

FIGURE 8 | (a) Schematic illustration of the measurement setup. **(b)** Current-Voltage measurements in the dark and under visible light of intensity 1.02 mW/cm^2. The voltage was swept from 0 to +2 V/-2 V and back. **(c)** Transient photoresponse on-off characteristics of the two devices under visible light illumination and a bias voltage of 2 V. **(d,e)** On-off characteristics of the photodetector with **(d)** and without **(e)** alumina layer under illumination with 550 nm light at different light intensities at a bias voltage of 2 V. **(f)** Responsivity of the photodetectors with (black) and without (red) alumina layer.

completely inhibits carbon deposition. However, in this study, titanium proved to show a different feature. Consequently, the formation of $Ti_xFe\text{-}Co_y$ precipitates on the surface provided seeding for the CNT growth. Nevertheless, it was attested that the insulating layer plays a significant role in CNT forest formation: both the height and the quality of CNT forest depended on the initial structure of the catalyst layer. It was also pointed out that water vapor in the gas feed during CCVD considerably affects the same parameters of the final product. Structural characterization revealed important differences in CNT forests grown with or without alumina layer. However, these variances did not affect drastically the performance of photodetector devices employing these CNT forests as electrodes. These minor differences can be a result of many parameters such as graphitization of the CNTs, presence of alumina layer, density of CNT forest, fabrication conditions, etc. Therefore, we could postulate that the alumina layer does not play an important role as a current blocking layer. By eliminating the alumina deposition step, one might reduce the degree of complications, ultimately reducing the price of the optoelectronic device fabrication process.

AUTHOR CONTRIBUTIONS

All the authors contributed to the discussion of the results and writing the manuscript. AS designed and performed the experiments, wrote the manuscript and contributed by taking the TEM images of CNT forests. PA and EH contributed by performing halide perovskite photodetectors of CNT forests. TG contributed by taking SEM images of CNT forests. KN contributed by Raman measurements of CNT forests. ZP contributed to the PLD technic of the catalyst layer. KH and LF conceived and designed the experiments.

ACKNOWLEDGMENTS

This work was supported by the OTKA NN114463. The authors are also very grateful to the financial support provided by the Swiss National Science Foundation (No. 160169) and the ERC advanced grant PICOPROP (Grant 670918). KH acknowledges the financial support of the GINOP-2.3.2-15-2016-00013 project.

REFERENCES

Andričević, P., Kollár, M., Mettan, X., Náfrádi, B., Sienkiewicz, A., Fejes, D., et al. (2017). Three-dimensionally enlarged photoelectrodes by a protogenetic inclusion of vertically aligned carbon nanotubes into CHNHPbBr single crystals. *J. Phys. Chem. C* 121, 13549–13556. doi: 10.1021/acs.jpcc.7b03421

Antunes, E. F., Lobo, A. O., Corat, E. J., Trava-Airoldi, V. J., Martin, A. A., and Veríssimo, C. (2006). Comparative study of first- and second-order Raman spectra of MWCNT at visible and infrared laser excitation. *Carbon* 44, 2202–2211. doi: 10.1016/j.carbon.2006.03.003

Atthipalli, G., Tang, Y., Star, A., and Gray, J. L. (2011). Electrochemical characterization of carbon nanotube forests grown on copper foil

using transition metal catalysts. *Thin Solid Films* 520, 1651–1655. doi: 10.1016/j.tsf.2011.08.105

Dalebrook, A. F., Gan, W., Grasemann, M., Moret, S., and Laurenczy, G. (2013). Hydrogen storage: beyond conventional methods. *Chem. Commun.* 49, 8735–8751. doi: 10.1039/c3cc43836h

Dörfler, S., Felhösi, I., Marek, T., Thieme, S., Althues, H., Nyikos, L., et al. (2013). High power supercap electrodes based on vertical aligned carbon nanotubes on aluminum. *J. Power Sour.* 227, 218–228. doi: 10.1016/j.jpowsour.2012.11.068

Dresselhaus, M. S., Dresselhaus, G., Saito, R., and Jorio, A. (2005). Raman spectroscopy of carbon nanotubes. *Phys. Rep.* 409, 47–99. doi: 10.1016/j.physrep.2004.10.006

Fejes, D., Pápa, Z., Kecsenovity, E., Réti, B., Toth, Z., and Hernadi, K. (2015). Super growth of vertically aligned carbon nanotubes on pulsed laser deposited catalytic thin films. *Appl. Phys. A Mater. Sci. Process.* 118, 855–861. doi: 10.1007/s00339-014-8965-3

Frommeyer, G. (2007). "Mechanical properties and structural superplasticity in ultrafine-grained α-titanium/tixmey-intermetallic ti-8fe-4al, ti-10co-4al and ti-10ni-4al alloys," in *Innovations in Titanium Technology*, eds N. G. Mehmet, I. M. Ashraf, and F. H. Sam (Orlando, FL: TMS Annual Meeting & Exhibition), 219–222.

Halonen, N., Kordás, K., Tóth, G., Mustonen, T., Mäklin, J., Vähäkangas, J., et al. (2008). Controlled CCVD synthesis of robust multiwalled carbon nanotube films. *J. Phys. Chem. C* 112, 6723–6728. doi: 10.1021/jp7110617

Hata, K., Futaba, D. N., Mizuno, K., Namai, T., Yumura, M., and Iijima, S. (2004). Water-assisted highly efficient synthesis of impurity-free single-walled carbon nanotubes. *Science* 306, 1362–1364. doi: 10.1126/science.1104962

Hernadi, K., Siska, A., Thiên-Nga, L., Forró, L., and Kiricsi, I. (2001). Reactivity of different kinds of carbon during oxidative purification of catalytically prepared carbon nanotubes. *Solid State Ionics* 141–142, 203–209. doi: 10.1016/S0167-2738(01)00789-5

Kaneko, A., Yamada, K., Kumahara, R., Kato, H., and Homma, Y. (2012). Comparative study of catalytic activity of iron and cobalt for growing carbon nanotubes on alumina and silicon oxide. *J. Phys. Chem. C* 116, 26060–26065. doi: 10.1021/jp309232w

Li, G., Chakrabarti, S., Schulz, M., and Shanov, V. (2009). Growth of aligned multiwalled carbon nanotubes on bulk copper substrates by chemical vapor deposition. *J. Mater. Res.* 24, 2813–2820. doi: 10.1557/jmr.2009.0339

Li, W. Z., Xie, S. S., Qian, L. X., Chang, B. H., Zou, B. S., Zhou, W. Y., et al. (1996). Large-scale synthesis of aligned carbon nanotubes. *Science* 274, 1701–1703. doi: 10.1126/science.274.5293.1701

Magrez, A., Smajda, R., Seo, J. W., Horvath, E., Ribic, P. R., Andresen, J. C., et al. (2011). Striking influence of the catalyst support and its acid-base properties: new insight into the growth mechanism of carbon nanotubes. *ACS Nano* 5, 3428–3437. doi: 10.1021/nn200012z

Masarapu, C., and Wei, B. Q. (2007). Direct growth of aligned multiwalled carbon nanotubes on treated stainless steel substrates. *Langmuir* 23, 9046–9049. doi: 10.1021/la7012232

Mattevi, C., Wirth, C. T., Hofmann, S., Blume, R., Cantoro, M., Ducati, C., et al. (2008). *In-situ* X-ray photoelectron spectroscopy study of catalyst- support interactions and growth of carbon nanotube forests. *J. Phys. Chem. C* 112, 12207–12213. doi: 10.1021/jp802474g

Matthews, K. D., Lemaitre, M. G., Kim, T., Chen, H., Shim, M., and Zuo, J. M. (2006). Growth modes of carbon nanotubes on metal substrates. *J. Appl. Phys.* 100:044309. doi: 10.1063/1.2219000

Mauron, P., Emmenegger, C., Zuttel, A., Nutzenadel, C., and Schlapbach, L. (2002). Synthesis of oriented nanotube films by chemical vapor deposition. *Carbon Nanotubes* 40, 1339–1344. doi: 10.1016/S0008-6223(01)00295-0

Murakami, Y., Miyauchi, Y., Chiashi, S., and Maruyama, S. (2003). Direct synthesis of high-quality single-walled carbon nanotubes on silicon and quartz substrates. *Chem. Phys. Lett.* 377, 49–54. doi: 10.1016/S0009-2614(03)01094-7

Noda, S., Hasegawa, K., Sugime, H., Kakehi, K., Zhang, Z., Maruyama, S., et al. (2007). Millimeter-thick single-walled carbon nanotube forests: hidden role of catalyst support. *Jpn. J. Appl. Phys. Part 2 Lett.* 46:3. doi: 10.1143/JJAP.46.L399

Pápa, Z., Kecsenovity, E., Fejes, D., Budai, J., Toth, Z., and Hernadi, K. (2018). Height and diameter dependence of carbon nanotube forests on the porosity and thickness of catalytic layers. *Appl. Surface Sci.* 428, 885–894. doi: 10.1016/j.apsusc.2017.09.206

Pattinson, S. W., Viswanath, B., Zakharov, D. N., Li, J., Stach, E. A., and Hart, A. J. (2015). Mechanism and enhanced yield of carbon nanotube growth on stainless steel by oxygen-induced surface reconstruction. *Chem. Mater.* 27, 932–937. doi: 10.1021/cm504209u

Robertson, J., Zhong, G., Esconjauregui, C. S., Bayer, B. C., Zhang, C., Fouquet, M., et al. (2012). Applications of carbon nanotubes grown by chemical vapor deposition. *Jpn. J. Appl. Phys.* 51:01AH01. doi: 10.1143/JJAP.51.01AH01

Sakurai, S., Nishino, H., Futaba, D. N., Yasuda, S., Maigne, A., Matsuo, Y., et al. (2011). Role of subsurface diffusion and ostwald ripening in catalyst formation for SWNT forest growth. *J. Am. Chem. Soc.* 134, 2148–2153. doi: 10.1021/ja208706c

Santhanagopalan, S., Teng, F., and Meng, D. D. (2009). "IC-compatible deposition of vertically-aligned CNT forests for micro-supercapacitors," in *PowerMEMS 2009* (Washington, DC).

Seo, J. W., Couteau, E., Umek, P., Hernadi, K., Marcoux, P., Lukic, B., et al. (2003). Synthesis and manipulation of carbon nanotubes. *N. J. Phys.* 5, 120.1–120.22. doi: 10.1088/1367-2630/5/1/120

Shokry, S. A., El Morsi, A. K., Sabaa, M. S., Mohamed, R. R., and El Sorogy, H. E. (2014). Study of the productivity of MWCNT over Fe and FeCo catalysts supported on SiO_2, Al_2O_3 and MgO. *Egypt. J. Petrol.* 23, 183–189. doi: 10.1016/j.ejpe.2014.05.005

Silva, T. A., Zanin, H., Saito, E., Medeiros, R. A., Vicentini, F. C., Corat, E. J., et al. (2014). Electrochemical behaviour of vertically aligned carbon nanotubes and graphene oxide nanocomposite as electrode material. *Electrochim. Acta* 119, 114–119. doi: 10.1016/j.electacta.2013.12.024

Sugime, H., Esconjauregui, S., Yang, J., D'Arsie, L., Oliver, R, A., Bhardwaj, S., et al. (2013). Low temperature growth of ultra-high mass density carbon nanotube forests on conductive supports. *Appl. Phys. Lett.* 103:073116. doi: 10.1063/1.4818619

Sugime, H., Ushiyama, T., Nishimura, K., Ohno, Y., and Noda, S. (2018). An interdigitated electrode with dense carbon nanotube forests on conductive supports for electrochemical biosensors. *Analyst* 143, 3635–3642. doi: 10.1039/C8AN00528A

Szabó, A., Kecsenovity, E., Pápa, Z., Gyulavári, T., Németh, K., Horvath, E., et al. (2017). Influence of synthesis parameters on CCVD growth of vertically aligned carbon nanotubes over aluminum substrate. *Sci. Rep.* 7:9557. doi: 10.1038/s41598-017-10055-0

Yang, J., Esconjauregui, S., Robertson, A. W., Guo, Y., Hallam, T., Sugime, H., et al. (2015). Growth of high-density carbon nanotube forests on conductive TiSiN supports. *Appl. Phys. Lett.* 106:083108. doi: 10.1063/1.4913762

Zhao, N., and Kang, J. (2011). "Direct growth of carbon nanotubes on metal supports by chemical vapor deposition," *Carbon Nanotubes Synthesis, Characterization, Applications*, ed K. K. Kar (London, UK: IntechOpen), 99–120.

Zhu, Z. G., Garcia-Gancedo, L., Chen, C., Zhu, X. R., Xie, H. Q., Flewitt, A. J., et al. (2013). Enzyme-free glucose biosensor based on low density CNT forest grown directly on a Si/SiO_2 substrate. *Sens. Actuators B Chem.* 178, 586–592. doi: 10.1016/j.snb.2012.12.112

Conflict of Interest Statement: The authors declare that the research was conducted in the absence of any commercial or financial relationships that could be construed as a potential conflict of interest.

frontiers in Chemistry

ORIGINAL RESEARCH
published: 13 March 2019
doi: 10.3389/fchem.2019.00116

Boron Doped Graphene Quantum Structure and MoS_2 Nanohybrid as Anode Materials for Highly Reversible Lithium Storage

Riyanto[1], *Imam Sahroni*[1], *Kartick Bindumadhavan*[2], *Pei-Yi Chang*[2] *and Ruey-an Doong*[2,3]*

[1] Department of Chemistry, Faculty of Mathematics and Natural Science, Islamic University of Indonesia, Yogyakarta, Indonesia, [2] Institute of Environmental Engineering, National Chiao Tung University, Hsinchu, Taiwan, [3] Department of Biomedical Engineering and Environmental Sciences, National Tsing Hua University, Hsinchu, Taiwan

Herein, the boron-doped graphene quantum structure (BGQS), which contains both the advantages of 0-D graphene quantum dot and 2-D reduced graphene oxide, has been fabricated by top-down hydrothermal method and then mixed with molybdenum sulfide (MoS_2) to serve as an active electrode material for the enhanced electrochemical performance of lithium ion battery. Results show that 30 wt% of BGQS/MoS_2 nanohybrid delivers the superior electrochemical performance in comparison with other BGQS/MoS_2 and bare components. A highly reversible capacity of 3,055 mAh g^{-1} at a current density of 50 mA g^{-1} is achieved for the initial discharge and a high reversible capacity of 1,041 mAh g^{-1} is obtained at 100 mA g^{-1} after 50 cycles. The improved electrochemical performance in BGQS/MoS_2 nanohybrid is attributed to the well exfoliated MoS_2 structures and the presence of BGQS, which can provide the vitally nano-dimensional contact for the enhanced electrochemical performance. Results obtained in this study clearly demonstrate that BGQS/MoS_2 is a promising material for lithium ion battery and can open a pathway to fabricate novel 2-D nanosheeted nanocomposites for highly reversible Li storage application.

Keywords: boron-doped graphene quantum structures (BGQS), MoS_2, anode materials, reversible capacity, cycling stability

OPEN ACCESS

Edited by:
Carlos Lodeiro, Universidade Nova de Lisboa, Portugal

Reviewed by:
Arshad Saleem Bhatti, COMSATS Institute of Information Technology, Pakistan
Christos Dimitrakopoulos, University of Massachusetts Amherst, United States

***Correspondence:**
Ruey-an Doong
radoong@mx.nthu.edu.tw

Specialty section:
This article was submitted to Nanoscience, a section of the journal Frontiers in Chemistry

Received: *18 August 2018*
Accepted: *14 February 2019*
Published: *13 March 2019*

Citation:
Riyanto, Sahroni I, Bindumadhavan K, Chang P-Y and Doong R (2019) Boron Doped Graphene Quantum Structure and MoS_2 Nanohybrid as Anode Materials for Highly Reversible Lithium Storage. Front. Chem. 7:116. doi: 10.3389/fchem.2019.00116

INTRODUCTION

The rapid technological development and miniaturization of electronic devices need reliably portable and highly efficient energy supply systems. In response to such increasing demands, the present decade has witnessed a thriving interest in development of high performance lithium ion batteries (LIBs). The choice of LIBs is based on their high reliability, user friendliness, safety, and, commendable shelf life for long term usage (Cheng et al., 2017). Since the performance of LIBs are influenced by the electrochemical property of electrodes among many other parameters, there still exists a fast progress on development of superior anode materials (Eftekhari, 2017).

The transition metal dichalcogenides (TMDs) are one of the first families of compound to serve as anode materials in secondary battery because of their gallery-type structure (Whittingham, 1976). The layered structure in such compounds is held by van der Waals force of interaction which acts as the host for intercalation and deintercalation of foreign ions and molecules. Among

the TMDs used, molybdenum disulfide (MoS_2) and its nanocomposites have been used as anode materials for LIBs (Hwang et al., 2011; Cao et al., 2013; Stephenson et al., 2014; Li et al., 2015; Jiang et al., 2016; Teng et al., 2016). The theoretical specific capacity of MoS_2 is 670 mAh g^{-1} and can be improved by tailoring the number of layers, particle size and morphology during synthesis (Hwang et al., 2011). However, the stacking behavior and the formation of polymeric intermediate decrease the specific capacity and performance of MoS_2 during the electrochemical cycling, and thereby pose a major challenge in real time application.

More recently, the incorporation of graphene-based nanomaterials such as reduced graphene oxide (rGO), graphene aerogel and graphene nanoflower with MoS_2 as the anode has been reported to provide an extra volume for Li^+ ion uptake during charge/discharge, and results in the improved electrochemical performance in comparison with bare MoS_2 (Cao et al., 2013; Li et al., 2015; Jiang et al., 2016; Teng et al., 2016). The graphitic backbone of graphene family also acts as mechanically buffering matrix to maintain the mechanical integrity of MoS_2-graphitic carbon nanocomposites during the extended cycle life of LIBs. Teng et al. (2016) have fabricated the vertical MoS_2 nanosheets over the graphene sheets by hydrothermal treatment and a reversible capacity of 1,077 mAh g^{-1} at 100 mA g^{-1} after 150 cycles was observed. The fabrication of MoS_2-graphene nanoflower has delivered the reversible capacity of 1,150 and 890 mAh g^{-1} at current density of 0.1 and 1 A g^{-1}, respectively (Li et al., 2015). Such a high electrochemical property is mainly attributed to the fact that graphene-based materials prevent the restacking of MoS_2 and also enable the fast electron kinetics because of their highly conductive and diffusive features (Jiang et al., 2016; Teng et al., 2016). More recently, several studies have used boron-doped rGO for the improvement on the electrochemical performance of LIB as well as the dechlorination of priority pollutants (Bindumadhavan et al., 2017; Sahu et al., 2017). Doping with boron atoms substantially decreases the internal resistance of anode material and increases the defect sites of graphitic structure, which leads to the enhanced electrochemical performance of lithium ion intercalation/deintercalation. Our previous study has shown that the Ag/B-rGO anode material exhibits superior reversible capacity of 1,484 mAh g^{-1} at a current density of 50 mA g^{-1} initially and can retain stably reversible capacity of 430 mAh g^{-1} at 1,000 mA h^{-1} (Bindumadhavan et al., 2017), showing that B-rGO is a promising graphitic-based material for LIBs. However, the combination of B-rGO with MoS_2 as the anode material for LIB application has received less attention.

In addition to 2-D graphene and 3-D graphene aerogel, the reduction in nanomaterial size is also advantageous on property enhancement. Graphene quantum dots (GQDs), the newly developed 0-D graphene family, have been under limelight because of their exciting surface and electrochemical properties. Currently, various morphologies of carbon based nanomaterials including ordered mesoporous carbons, rGO and GQDs are invariably under the investigation for the development of sensors, supercapacitors, and drug delivery systems (Dutta Chowdhury and Doong, 2016; Liu et al., 2016; Anh et al., 2017; Ganganboina et al., 2017, 2018). The decoration of nitrogen doped-GQDs over the 3-D MoS_2-rGO nanohybrid has improved the onset potential of oxygen reduction reaction to +0.81 V vs. reversible hydrogen electrode (RHE) (Vinoth et al., 2016). The coral-type MoS_2/GQD catalyst showed excellent performance with a small onset overpotential of 95 mV and a low Tafel slope for long-term electrocatalytic stability (Guo et al., 2017). Moreover, the GQDs have been used as a component of anode for application in LIB. Guo et al. (2016) have recently investigated the electrochemical performance of MoS_2/GQD nanocomposites as the anode for LIBs and found that an initial reversible capacity of 1,394 mAh g^{-1} was obtained. However, there remains a large scope to investigate the effect of boron-doped graphene quantum structure (BGQS), which contains both B-GQDs and B-rGO, on the electrochemical performance when combined with MoS_2 as the anode materials.

Herein, the BGQS/MoS_2 with various loadings of BGQS were fabricated to serve as anode materials for LIB application. BGQS, which possesses the advantages of both 0-D B-GQDs and 2-D B-rGO, was first synthesized by top-down hydrothermal method and then 10–70 wt% BGQS were mixed with MoS_2 as the anode materials for enhanced electrochemical performance of LIBs. As shown in **Scheme 1**, the fabrication of BGQS involves a single step fragmentation with size reduction under hydrothermal conditions to generate novel B-GQDs embedded onto B-rGO nano-sheeted structures. The *in situ* reduction of molybdate precursor in the presence of BGQS in subsequent hydrothermal reaction at 180°C leads to the formation of BGQS/MoS_2 nanohybrids. The BGQS/MoS_2 exhibits excellent electrochemical performance in comparison with bare MoS_2 and BGQS and the 30 wt% BGQS/MoS_2 shows superior initial reversible capacity of 3,055 mA g^{-1} at 50 mA g^{-1} with excellent rate capability and cycling stability after 50 cycles. The synergistic effect between BGQS and MoS_2 improves the electrochemical performance of nanohybrids by reducing the internal resistance as well as acting as nano-dimensional contact points for fast charge transport. Moreover, the BGQS component also serves as a buffering matrix to maintain the mechanical integrity of the anode during charge/discharge processes.

MATERIALS AND METHODS

Preparation of Graphite Oxide

The graphite oxide was prepared by modified Hummers' method by oxidizing pristine graphite with a hard oxidation mixture. In a typical procedure, 100 mg of graphite was mixed with 50 mg $NaNO_3$ and 4 mL of concentrated H_2SO_4 in an ice bath with stirring. After 30 min of stirring, the mixture was moved to room temperature and 300 mg of potassium permanganate was added gradually, which would result in the change in color from black to deep purple. The stirring was further continued for 1 h to get a thick purple slurry. The above mixture was then diluted by addition of 1 L distilled deionized water (DI water) (18.2 MΩ cm) and allowed to settle. After sedimentation for 48 h, the supernatant was discarded and the remaining yellow solid particles were washed with hot DI water several times,

centrifuged, freeze dried, and then stored in desiccator for further analysis.

Preparation of B-rGO and BGQS

The BGQS was prepared originally from the 2-D rGO. Initially B-rGO was prepared by thermal degradation of 100 mg graphite oxide with 30 wt% boric acid in a quartz tube furnace at 700°C for 4 h under nitrogen atmosphere (Bindumadhavan et al., 2017). The tube furnace was allowed to cool to ambient temperature to form B-rGO. In order to obtain the quantum structures of BGQS by top down approach, B-rGO was again oxidized with a mixture of H_2SO_4/HNO_3 (3/1, v/v) for 24 h. After the treatment, the mixture was centrifuged after repeatedly washed with hot DI water and finally freeze dried. The dry black powder was dispersed in DMSO and hydrothermally heated in Teflon vessel at 180°C for 24 h. The mixture was filtered and washed with DI water after hydrothermal reaction. The BGQS was then obtained as a fine black powder after drying and were then retained for further analysis.

Fabrication of BGQS/MoS_2 Nanohybrids

The as-prepared MoS_2 and BGQS/MoS_2 nanohybrids were prepared by hydrothermal reaction involving the reduction of ammonium thiomolybdate with thiourea. Aqueous solutions of ammonium thiomolybdate and thiourea were mixed in a molar ratio of 1:2 and at pH 6.5. The mixture was then transferred into a Teflon vessel and the hydrothermal reaction was performed at 180°C for 24 h. Subsequently, the dark gray solid was dried and further calcined under argon gas at 400°C for 2 h, and 250 mg of MoS_2 was retained after calcination. Moreover, the BGQS/MoS_2 hybrids were prepared by adding 10, 30, 50, and 70 wt% of BGQS to the identical aqueous solutions of ammonium thiomolybdate and thiourea, which were used in preparation of bare MoS_2. The obtained hybrids were denoted as BGQS-X/MoS_2 where X is the loading amount of BGQS.

Characterization

The structure and morphology of BGQS and BGQS/MoS_2 nanohybrids were characterized using JEOL JEM-ARM200F transmission electron microscope (TEM) and JEOL JEM-2,010 high-resolution transmission electron microscope (HR-TEM) at an accelerating voltage of 15 and 300 kV, respectively. The morphological images of GQD were also identified using Tecnai G2 F30 S-twin scanning transmission electron microscope (STEM). X-ray photoelectron spectroscopy (XPS) was performed with an ESCA Ulvac-PHI 1,600 photoelectron spectrometer from Physical Electronics using Al Kα radiation photon energy at 1,486.6 ± 0.2 eV. The X-ray diffraction (XRD) patterns were recorded on Bruker D8 X-ray diffractometer with Ni filtered Cu-Kα radiation (λ = 1.5406 Å). Raman spectra of nanomaterials including bare BGQS, MoS_2 and BGQS/MoS_2 nanohybrids were recorded with Bruker Senterra micro-Raman spectrometer equipped with an Olympus BX 51 microscope and DU420-OE CCD camera. The thermogravimetric analysis of MoS_2, BGQS and BGQS/MoS_2 at various BGQS loadings was determined by thermogravimetric analysis (TGA) using Mettler Toledo DSC/TGA 3+ Stare system in air.

Electrochemical Measurement

The electrochemical measurement of half cells were performed by mixing 70 wt% of BGQS/MoS_2 nanohybrids with 20 wt% carbon black and 10 wt% polyvinylidene fluoride in 0.3 mL of *N*-methylpyrrolidone, and then well-mixed in a mortar until a homogeneous slurry was obtained. The slurry was then spread onto a copper foil current collector and dried in vacuum at 60°C for 6 h. The 2,032 type coin cells were assembled in an argon-filled glove box using the coated copper foil as the working electrode, Li metal foil as the counter electrode, and 1.15 M solution of $LiPF_6$ in a 1:1:1 (v/v/v) mixture of ethylene carbonate, ethyl methyl carbonate and dimethyl carbonate as the electrolyte. The cells were charged and discharged galvanostatically under the current density range of 50–1,000 mA g^{-1} by a Maccro Model 4,300 battery testing system at room temperature. In addition, cyclic voltammogram (CV) was obtained at a scan rate of 0.1 mV s^{-1} in a fixed voltage window of 0.01–3 V (vs. Li^+/Li). The electrochemical impedance spectra (EIS) were carried out by an Autolab PGSTAT 302N electrochemical test system (Metrohm Autolab B.V., Netherlands) in a two-electrode system with a sine wave of 10 mV amplitude over a frequency range of 100 kHz to 0.01 Hz.

RESULTS AND DISCUSSION

Surface Characterization of BGQS/MoS_2 Nanohybrids

The BGQS was fabricated by *in-situ* top-down method from 2-D B-rGO nanosheets and then the morphology of as-synthesized BGQS was first examined by TEM and STEM to elucidate the evolvement of quantum structure. The TEM image of BGQS in the left inset of **Figure 1a** clearly shows the well-dispersed B-GQDs embedded within the large rGO-based matrix, confirming the formation of twin structures during the fragmentation of B-rGO. The formation of such low dimensional contact points is a result of extensive oxidation during pretreatment and fragmentation under hydrothermal reaction. The developed region of B-GQDs can serve as the attachment center of Li ions to enhance the intercalation/deintercalation capacity for LIB application. In addition, the large domain of B-rGO plays a vital role in acting as a buffering matrix for the enhancement of conductivity and longevity of anodes during the electrochemical charge/discharge cycles. Moreover, the HRTEM image of BGQS (**Figure 1**) clearly shows the formation of B-GQDs (white circle in **Figure 1**) after hydrothermal treatment and the fringes of B-GQDs can be well-matched with the (002) diffraction plane of graphene with an interlayer spacing of 0.34 nm, indicating the purity in the crystalline region of as-prepared BGQS. In addition, the particle sizes of B-GQDs are in the range of 1–4 nm with mean particle size of 2.5 nm (right inset of **Figure 1**), which is in good agreement with the reported data of GQDs (Dutta Chowdhury and Doong, 2016; Ganganboina et al., 2017, 2018).

The TEM images of bare MoS_2 and BGQS/MoS_2 nanohybrids with various BGQS loadings of 10–70 wt% were further recorded to assess the change in morphology after inclusion of BGQS. As illustrated in **Figure 1b**. The as-prepared MoS_2 appears as the well-exfoliated few layered structures, which are transparent and

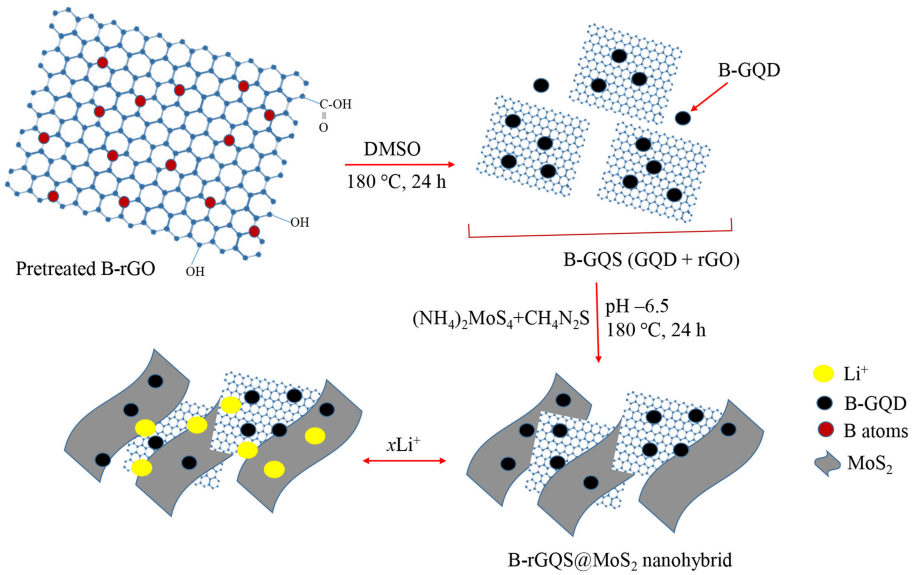

SCHEME 1 | Schematic illustration of preparation of BGQS/MoS_2 nanohybrids and the application for Li^+ ion intercalation/deintercalation.

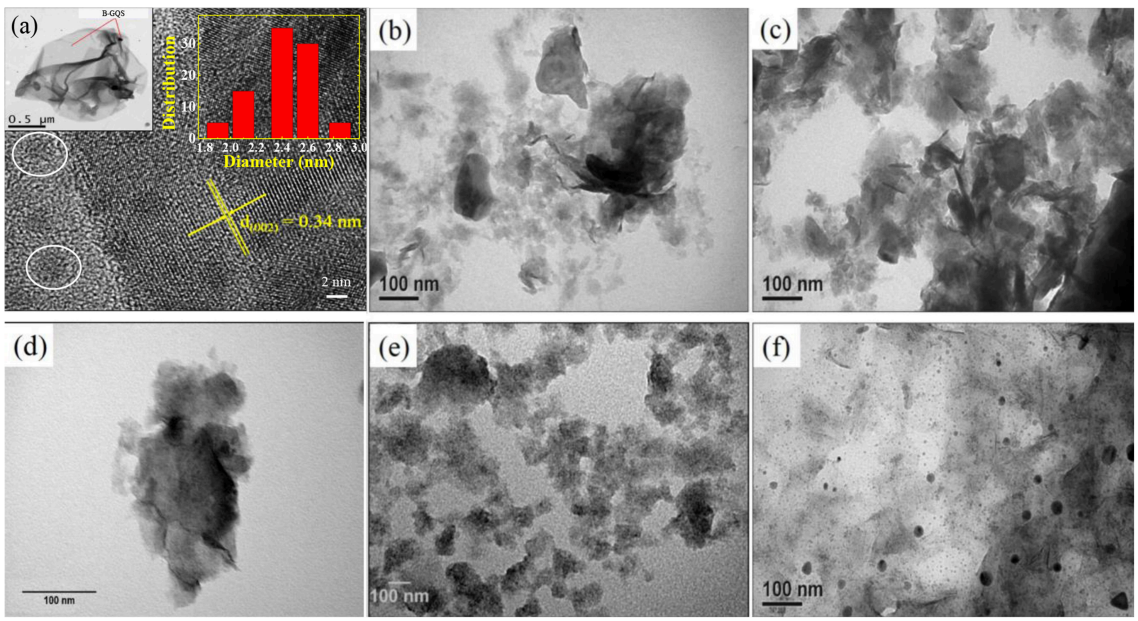

FIGURE 1 | (a) STEM images of boron doped graphene quantum structures (BGQS) and TEM images of **(b)** as-prepared MoS_2, **(c)** BGQS-10/MoS_2, **(d)** BGQS-30/MoS_2, **(e)** BGQS-50/MoS_2, and **(f)** BGQS-70/MoS_2. Insets of this figure are TEM image (left) and histogram (right) of BGQS. The white circle indicates the particle size of B-GQDs.

stable to the electron beam irradiation. After loading with 10 and 30 wt% BGQS, the TEM images show the co-dispersion of both BGQS and MoS_2 (**Figures 1c,d**) and 30 wt% BGQS can be clearly attached onto the surface of layered MoS_2. It is important to note that a severe aggregation of MoS_2 occurs when 50 wt% of BGQS is mixed with MoS_2 (BGQS-50/MoS_2) (**Figure 1e**), which is a result of excessive interaction from large proportion of BGQS and may result in the loss of electrochemical properties. The TEM image of 70 wt% BGQS/MoS_2 (BGQS-70/MoS_2) shows the complete phase separation of BGQS structures as they exist as the individual entity and inhomogenously spread over the thin platelets of MoS_2 (**Figure 1f**).

Figure 2A shows the HRTEM image of BGQS-30/MoS_2. The irregularly shaped BGQS can be embedded into the lattice of

MoS_2, which confirms the homogeneous co-dispersion of 30 wt% BGQS in nanohybrids. From the STEM image shown in **Figure 2B**, the clear fringes of BGQS structures (0.34 nm) and MoS_2 (0.67 nm) pertain to their characteristic (002) diffraction planes, which indicates the purity of BGQS/MoS_2 nanohybrids. Such a co-existence of the components is necessary to enhance the charge and electron transport kinetics in the electrochemical application and the homogeneity in BGQS-30/MoS_2 structure can improve the anodic behavior of MoS_2-based material for LIB application.

XPS is an effective technique to identify the chemical species of elements in nanomaterials (Chang and Doong, 2004), which was used to determine the chemical environments and the presence of boron element in BGQS/MoS_2. The 30 wt% BGQS/MoS_2 was used as the model material because the XPS spectra of various loadings of BGQS/MoS_2 nanohybrids are similar. As shown in **Figure 3A**, the survey scan shows the presence of C 1 s, Mo 3 d and S 2 p peaks at 284.5, 232.5, and 169.8 eV, respectively. In addition, a low intensity peak corresponding to B 1 s at 188.9 eV is observed, clearly showing the successful doping of B atoms into BGQS/MoS_2 nanohybrids. The deconvoluted S peak shows the contribution from S $2p_{1/2}$ and S $2p_{3/2}$ centered at 163.7 and 162.6 eV, respectively (**Figure 3B**). The deconvoluted C 1s peak exhibits C-O, C=O and C=C functionality at 285.9, 288.3, and 284.7 eV, respectively, indicating the presence of oxygenated groups in BGQS structures (**Figure 3C**). The two deconvoluted B 1s peaks at 190.5 and 192.8 eV are mainly contributed from the chemical bonds of BC_2O and BCO_2, respectively (**Figure 3D**), which confirm the existence of partial bonding between B and sp^2 hybridized C atoms in the BGQS (Lin et al., 2011). A large peak at 187.8 eV is attributed to the presence of elemental B in BGQS/MoS_2 nanohybrids. Moreover, the Mo 3d peak after deconvulation shows a doublet of Mo $3d_{3/2}$ and Mo $3d_{5/2}$ at 232.4 and 229.3 eV, respectively (**Figure 3E**), which can be assigned as the characteristic peaks of Mo^{4+} in MoS_2 (Dong et al., 2015; Wang et al., 2017).

Figure 4 shows the microstructural analysis of MoS_2, BGQS and their nanohybrids including crystallinity, thermal property and structural fingerprint. The XRD patterns of as-prepared MoS_2 shows peaks at $2\theta = 14.1^\circ$, 33.9°, 37.1°, 60.4°, and 66.7°, which correspond to (002), (100), (103), (008), and (200) reflection planes, respectively (JCPDS = 77–1716). An additional peak at 53.6° 2θ belongs to the (108) plane of 3R phase of MoS_2 (Wei et al., 2016). After addition of various weight ratios of BGQS, the intensity of (002) plane of 2H-MoS_2 diminishes with the increase in BGQS content, presumably attributed to the loss of layer stacking and formation of small crystallites of MoS_2. In addition, the (002) reflection peak of MoS_2 in BGQS-30/MoS_2 and BGQS-50/MoS_2 shows a slight shift from 14.1° to 13.9° 2θ, indicating that the addition of 30–50 wt% BGQS particles enhance the layer distortions in 2H-MoS_2 (Bindumadhavan et al., 2013). Such layer distortion and exfoliation may enhance the intercalation/deintercalation kinetics of Li^+ ions and molecules during the charge/discharge reactions. However, the (002) reflection of MoS_2 in BGQS-70/MoS_2 reappears at 14.06° 2θ along with the increase in strong reflection from (004) plane, depicting the re-stacking of MoS_2 again at high BGQS loading of 70 wt%. Moreover, the MoS_2 with 70 wt% BGQS exhibits the phase separation due to the inhomogeneous co-dispersion. It is noteworthy that low peak intensity of (002) plane of BGQS also appears at 26.2° 2θ in all BGQS/MoS_2 nanohybrids, clearly indicating the presence of graphitic backbone structures of graphene family.

The key change in the structures of BGQS/MoS_2 after the addition of various ratios of BGQS can be identified by Raman spectra. The as-prepared MoS_2 shows the presence of two peaks centered at 375.9 and 403.3 cm^{-1} arising from the E_{2g} and A_{1g} vibration modes, respectively (**Figure 4B**). The opposite vibration of two S atoms with respect to the Mo atoms gives rise to the E_{2g} mode, while A_{1g} mode is attributed to the out-of-plane vibration of only S atoms in opposite direction (Li et al., 2012). The change in E_{2g} and A_{1g} peak intensity also indicates the variation in stacking and layer arrangement in MoS_2 after the inclusion of BGQS. It is interesting to note that both the E_{2g} and A_{1g} peaks of all nanohybrids appear distinguishably and their peak intensities vary with the change in BGQS contents. The BGQS-30/MoS_2 nanohybrid shows the maximum enhancement in E_{2g} intensity in comparison with A_{1g} peak, which can be attributed to the formation of less stacked structure (Lee et al., 2010). Moreover, BGQS-30/MoS_2 exhibits the similar spectral feature to the reported result of layered MoS_2 (Li et al., 2012) and the E_{2g} and A_{1g} peaks show red and blue shifts, respectively, which occur as a result of optimal exfoliation and few layer stacking. The shift in peaks is highly related to the defects and electronic interactions of MoS_2 with BGQS entity. The presence of few layered structure of BGQS can be beneficial in improving the intercalation properties of BGQS-30/MoS_2 nanohybrids for LIB application. The further increase in BGQS loading to 50–70 wt%, however, results in the aggregation of MoS_2, and subsequent decreases the peak intensity of E_{2g} and A_{1g} by stiffening the vibration modes in opposite direction (Lee et al., 2010). This result supports the fact that 30 wt% BGQS can be exfoliated into few layers with distinct co-dispersion of fine particles, which can lead to superior conductivity of nanohybrids to improve their performance as anode in LIBs.

The thermal stability of MoS_2 and BGQS/MoS_2 nanohybrids was evaluated by performing TGA under air atmosphere. As displayed in **Figure 4C**, the thermogram of MoS_2 shows the weight loss when temperature >400°C, which is attributed to the oxidation of MoS_2 to molybdenum oxide (MoO_2) and sulfur dioxide (SO_2) (Yang et al., 2016). A total weight loss of 15% for MoS_2 is observed, showing the high thermal stability of MoS_2. In contrast, the bare BGQS exhibits the typical thermal behavior of a graphitic material, wherein the weight loss continues from 100 to 700 °C. The slight weight loss at 50–200°C is mainly from the loss of water molecules and then the subsequent decrease in weight at 200–450°C is attributed to the pyrolysis of thermally labile oxygenated functional groups. A nearly complete weight loss in the temperature range of 500–700°C is the exothermal removal of remaining oxygenated moiety and the complete degradation of graphitic carbon backbone (Hsiao et al., 2013). It is noteworthy that the residual weight of 7 wt% for bare BGQS after 900 °C is the doped amount of B atoms in BGQS.

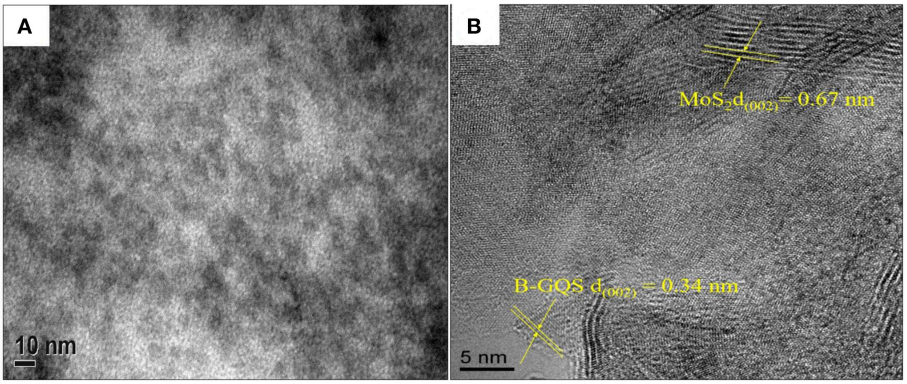

FIGURE 2 | (A) HRTEM and **(B)** STEM images of the BGQS-30/MoS_2 nanohybrid with the corresponding lattice indications of MoS_2 and BGQS.

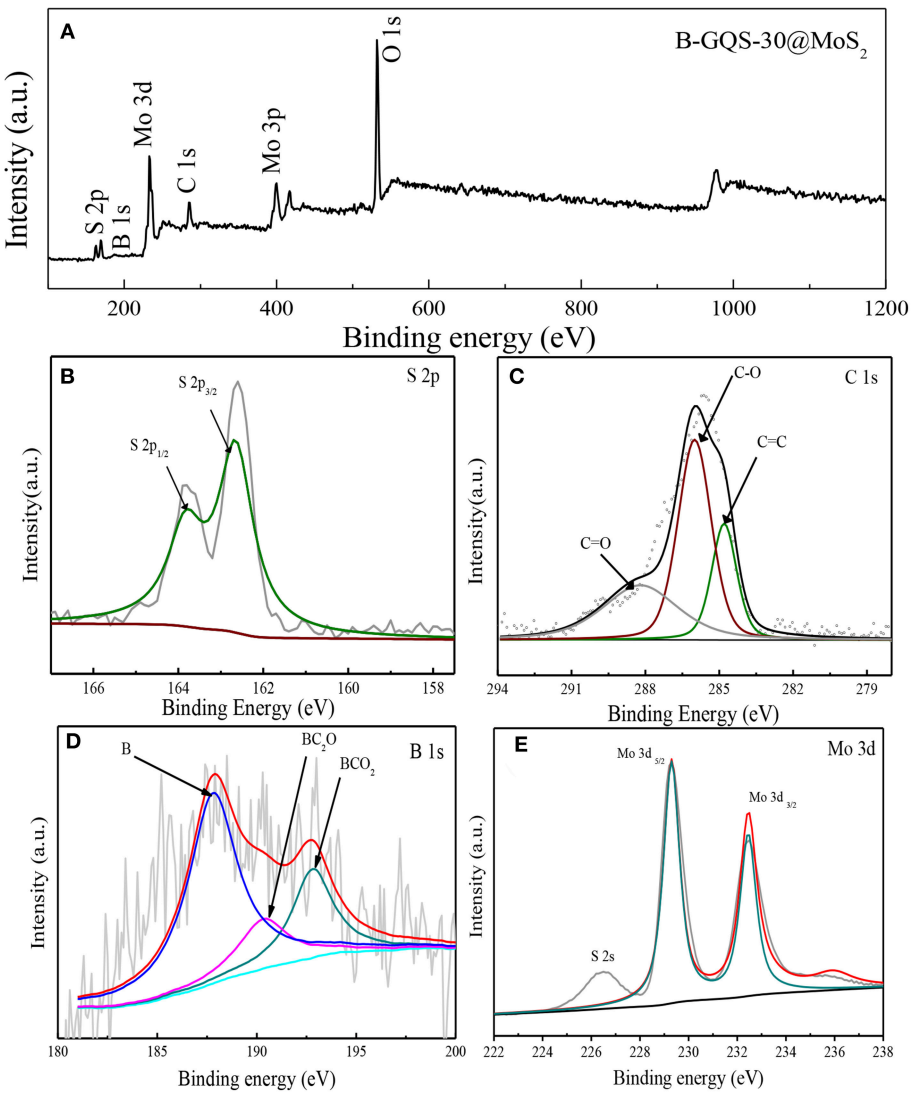

FIGURE 3 | (A) XPS survey spectra of BGQS-30/MoS_2 and the deconvoluted spectra of **(B)** S 2p, **(C)** C 1s, **(D)** B 1s, and **(E)** Mo 3d peaks.

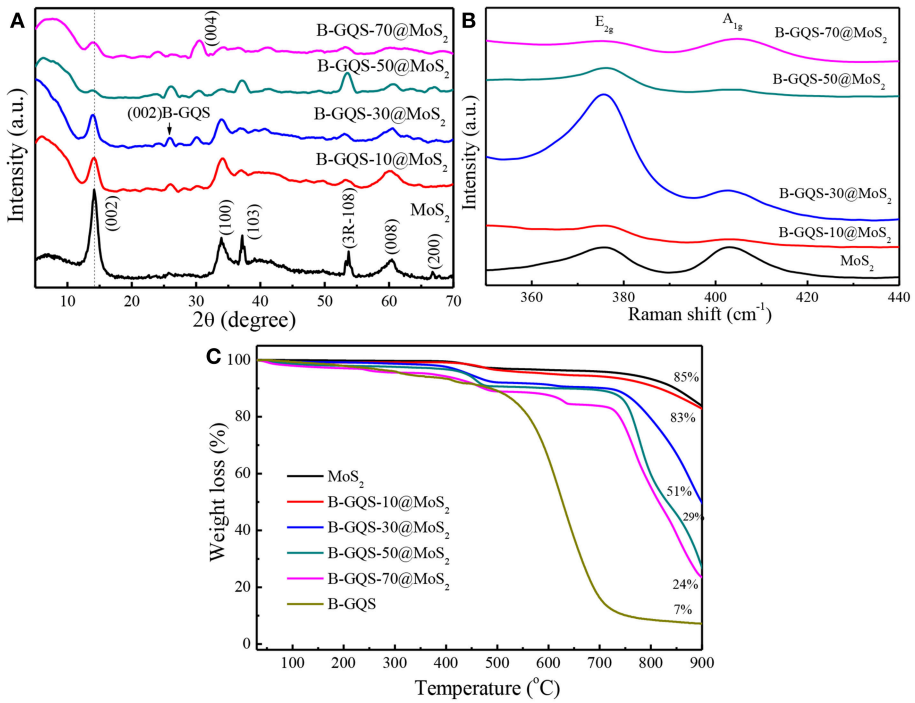

FIGURE 4 | (A) XRD patterns, **(B)** Raman spectra, and **(C)** thermograms of MoS_2 and BGQS/MoS2 nanohybrids with various BGQS loading of 10–70 wt%.

For BGQS/MoS_2 nanohybrids, the thermal stability reduces with the increase in mass loading of BGQS and a two-stage decomposition is observed for BGQS-10/MoS_2. In the first stage of thermal degradation, small amount of the physisorbed water molecules as well as oxygenated functional groups are lost up to 400°C, and then follows the oxidation of MoS_2 and final breakdown of BGQS backbone, which is similar to that of bare MoS_2. However, a distinct three-stage decomposition can be noted when the loading amount of BGQS is in the range of 30–70 wt%. The slight weight loss at 50–400°C is mainly from loss of physisorbed water molecules and oxygenated functional groups of carbon materials. The second stage of weight loss between 400 and 750°C can be attributed to the oxidation of MoS_2 and BGQS structures. Moreover, the obvious weight loss at temperature >750°C is the degradation of residual graphitic backbone structures inhibited by MoS_2 to provide any further thermal stability (Thangappan et al., 2016).

Electrochemical Performance of BGQS/MoS_2

The electrochemical properties of BGQS/MoS_2 with respect to lithium ion intercalation-deintercalation were first evaluated by the CV curve for five cycles at a scan rate of 0.1 mV s^{-1} in the potential window of 0.01 to 3.0 V. The CV curves of few layered MoS_2 exhibit several well-defined characteristic peaks, which match well with the finding of reported MoS_2 (Xiao et al., 2011; Wang et al., 2014). As shown in **Figure 5A**, two prominent peaks at 0.97 and 0.4 V are observed during the first cathodic cycle. The peak at 0.97 V is the insertion reaction of Li ions to MoS_2 (Equation 1), leading to the formation of Li_xMoS_2 along with the phase transformation of MoS_2 from trigonal prismatic (2H) to octahedral (1T) lithiated MoS_2 (Wang et al., 2014). It is noteworthy that the peak appeared at 0.4 V is intensive in the first cycle but decreases dramatically in the subsequent cathodic curves of 2–5 cycles, which indicates the irreversible intercalation reaction of Li_xMoS_2 and Li ions to form Li_2S and Mo (Equation 2). Moreover, the formation of metallic Mo (Equation 2) can significantly enhance the conductivity of the whole electrode (Xiao et al., 2011), and subsequently enhances the electrochemical performance of B-QGS/MoS_2 nanohybrids.

$$MoS_2 + x\,Li^+ + x\,e^- \rightarrow Li_xMoS_2 \quad (1)$$

$$Li_xMoS_2 + (4-x)Li^+ + (4-x)e^- \rightarrow 2Li_2S + Mo \quad (2)$$

In the subsequent cathodic cycles, less intense peak at 1.93 V is observed, indicating the generation of Li_2S from MoS_2, while another peak at 1.10 V is the continuous reaction of Mo with Li. During the anodic scans of 1st−5th cycles, the strong peak at 2.33 V is mainly attributed to the delithiation of Li_2S during the charging process (Wang et al., 2013). Moreover, a dormant peak at 1.69 V can be assigned to the oxidation of metallic Mo. The highly overlapped CV curves of 2nd−5th cycles mean the good reversibility of BGQS/MoS_2 for intercalation/deintercalation of Li^+ ions.

The CV curves of bare BGQS were also recorded in order to elucidate its contribution to lithium uptake. As presented in **Figure 5B**, the anode composed of bare BGQS shows a steady

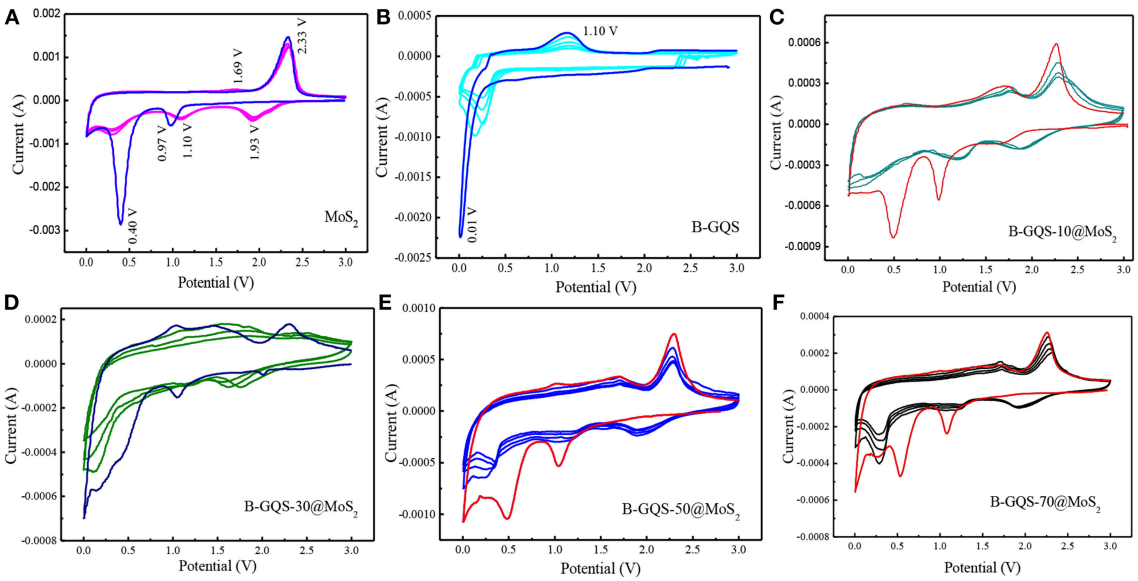

FIGURE 5 | Cyclic voltammograms of MoS_2, BGQS and BGQS/MoS_2 nanohybrids with various BGQS loadings of 10-70 wt%. **(A)** Pure MoS2, **(B)** pure BGQS, **(C)** 10 wt%, **(D)** 30 wt%, **(E)** 50 wt%, and **(F)** 70 wt%.

trough in the first cathodic cycle between 0.9 and 0.5 V, which can be attributed to the formation of solid electrolyte interface (SEI) layer produced from the reaction between BGQS and electrolyte. A strong peak arising from the reaction and uptake of Li ions by the basal planes of BGQS is observed at 0.01 V. It is important to note that this peak shifts to 0.16–0.26 V with the significant decrease in peak intensity in the subsequent 2nd−5th cathodic cycles, indicating the occurrence of an irreversible Li ions uptake. In the first anodic cycle, the appearance of peak at 1.10 V is the delithiation of Li ions from BGQS structures to form LiC_6 structures (Bindumadhavan et al., 2017). However, the decrease in peak intensity at 1.10 V in the 2nd−5th anodic cycle is the irreversible uptake of Li ions by bare BGQS. After incorporation of various amounts of BGQS with MoS_2, the CV curves of all the BGQS/MoS_2 nanohybrids resemble the features of bare MoS_2 (**Figures 5C–F**). In addition, the nanohybrids with BGQS loading of >30 wt% show the contribution from BGQS component in the potential window of 0.01–0.3 V, depicting that both MoS_2 and BGQS can exhibit good electrochemical performance in nanohybrids.

Figure 6 shows the first three cycles of galvanostatic charge-discharge curves (GCD) of BGQS/MoS_2 nanohybrids at a current density of 50 mA g^{-1} in the potential window of 0.01–3.0 V. The bare MoS_2 shows the plateaus located at 1.13 and 0.67 V in the first discharge curve (**Figure 6A**). The plateau appeared at high potential is ascribed to the lithium ion intercalation into the MoS_2 lattices, resulting in the formation of Li_xMoS_2. Furthermore, the conversion reaction of Li_xMoS_2 to Mo particles embedded in Li_2S is characterized by the plateau at 0.67 V (Ma et al., 2014). The slope continues to decrease below 0.5 V, which indicates the formation of SEI layers along with the electrochemical degradation of electrolyte and lithium storage at the interfaces of Li_2S and Mo phases (Huang et al., 2013). The obvious change in the GCD curves during the 2nd and 3rd cycles is also observed in the discharge curves where the plateau occurs in the potential range of 2.1–1.9 V and 1.3–1.1V, respectively, which is in good agreement with the CV curves. Similar to the discharge curve, the plateau at 2.1–2.3 V in the initial charge curve is attributed to the deintercalation of Li ions and incomplete oxidation of Mo (Huang et al., 2013). It is noteworthy that the bare MoS_2 exhibits a highly reversible capacity of 2,106 mAh g^{-1} in the first discharge, and a corresponding charge capacity of 1,621 mAh g^{-1} is obtained. The loss in coulombic efficiency of 23% in the first cycle can be attributed to the irreversible lithium uptake and the formation of SEI layers. From the second cycle onwards, a 96–99% of columbic efficiency is observed, indicating the good cycling characteristics of bare MoS_2.

The charge-discharge curves of BGQS were also recorded to investigate its lithium uptake characteristic with respect to applied potential. As shown in **Figure 6B**, the first discharge curve of BGQS is similar to the profile of typically mesoporous carbon materials reported elsewhere (Vinoth et al., 2016), wherein the gradual slope up to 0.5 V is attributed to the Li ion uptake majorly by the basal planes and defect sites over the structures of BGQS. The reversible capacity of BGQS in the voltage range of 0.5–0.3 V is the direct intercalation of Li ions to the BGQS layer interfaces and the extended slope beyond 0.2 V is ascribed to the additional storage capacity of lithium ions in the basal planes of BGQS. It is also noted that the slight decrease in slope at the potential of <0.5 V is attributed to the formation of SEI layer, leading to the irreversible capacity (Chang and Chen, 2011). In contrast, a plateau due to the delithiation reaction is noted at 1.1 V in

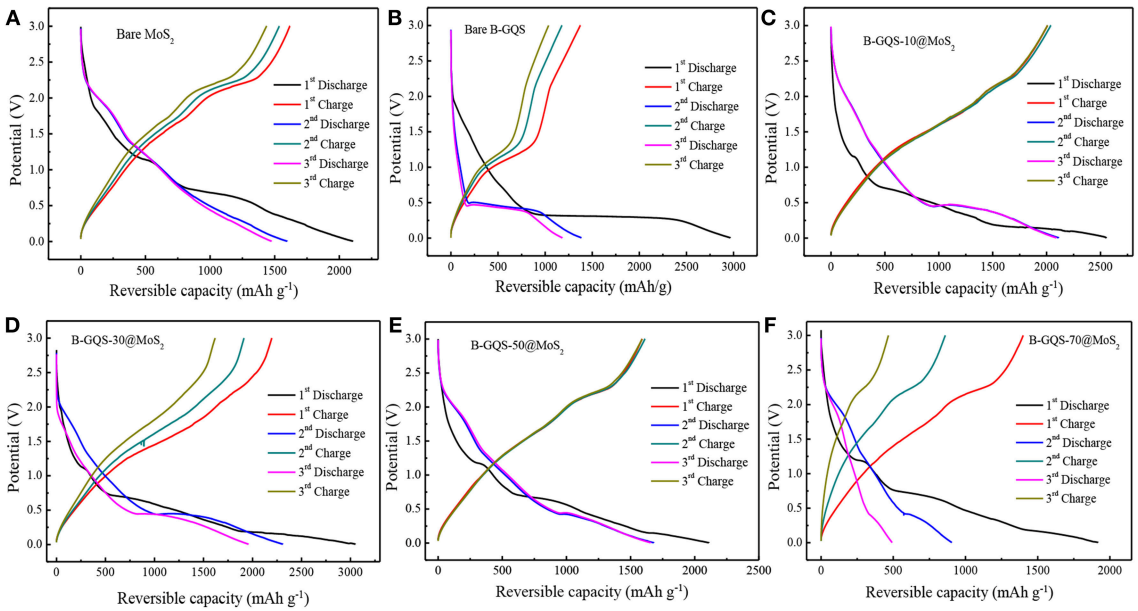

FIGURE 6 | The glvanostatic discharge-charge curves of **(A)** bare MoS2, **(B)** bare BGQS **(C)** BGQS-10/MoS2, **(D)** BGQS-30/MoS2, **(E)** BGQS-50/MoS2, and **(F)** BGQS-70/MoS2 nanohybrids at a current density of 50 mA/g in the potential window of 0.01–3.0 V.

the first discharge curve. The first discharge capacity of bare BGQS is 2,996 mAh g^{-1} with a columbic efficiency of 46%. This low columbic efficiency of bare BGQS in the first cycle can be attributed to the formation of large proportion of SEI layers. Furthermore, the BGQS also shows obvious capacity loss in the subsequent charge-discharge cycles, possibly due to the fact that the presence of 0-D GQD particles is unable to retain their structural stability during volume expansion in charge-discharge reaction.

Figures 6C–F show the GCD curves of all the BGQS/MoS_2 nanohybrids with various BGQS loadings of 10–70 wt%. The combination of MoS_2 with 10–30 wt% BGQS exhibits a synergistic effect on the electrochemical performance. The initial discharge capacity of BGQS/MoS_2 increases from 2,554 mAh g^{-1} for BGQS-10/MoS_2 to 3,061 mAh g^{-1} for BGQS-30/MoS_2. However, the increase in BGQS loading to 50–70 wt% decreases the reversible capacity to 1,917–2,110 mAh g^{-1}. It is important to note that the first discharge profiles of all the nanohybrids are similar to the characteristic curve of bare MoS_2, which the plateaus located at 1.13 and 0.67 V are clearly observed. However, a slight difference in the first charge profile of BGQS-30/MoS_2 is noted where the plateau at 2.1–2.3 V is unclear. This indicates the formation of small MoS_2 particles. Moreover, the well-dispersed BGQS in 30 wt% BGQS/MoS_2 nanohybrids makes the conversion reaction more reversible in comparison with the bare MoS_2. The initial discharge capacity of 3,061 mAh g^{-1} with a corresponding charge capacity of 2,203 mAh g^{-1} for BGQS-30/MoS_2 is delivered, implicating a 72% of columbic efficiency for the initial capacity. However, the BGQS-30/MoS_2 nanohybrid shows a high retention in columbic efficiency after 2nd discharge-charge cycles, depicting the superior electrochemical properties. In addition, the decreased reversible capacity of BGQS/MoS_2 at 50–70 wt% BGQS is attributed to the phase separation of the components due to aggregation of BGQS and MoS_2, resulting in the inefficient electrochemical reaction with Li ions.

Figure 7 displays the rate capability of BGQS/MoS_2 nanohybrids fabricated with 10–70 wt% BGQS at various current densities ranging from 50 to 1,000 mA g^{-1}. In addition, the reversible capacity of BGQS/MoS_2 is compared with those of as-prepared MoS_2 and BGQS. The bare MoS_2 exhibits a high Li^+ ion uptake capacity with initial reversible discharge capacity of 2,966 mAh g^{-1} at a current density of 50 mA g^{-1}. The high reversible capacity of MoS_2 at low current density is probably due to the well-exfoliated and few-layered MoS_2 obtained in this study, which has been shown in TEM image. However, the reversible capacity of MoS_2 fades dramatically with the increase in the first 10 cycles at 50 mA g^{-1} and only 387 mAh g^{-1} is obtained after 10 cycles, which is mainly attributed to the decomposition of electrolytes. The reversible capacity continues to decrease when the current density increases and only 187 mAh g^{-1} is obtained at 1,000 mA g^{-1} because of the low mechanical strength and structural integrity of bare MoS_2.

Moreover, the reversible capacity of bare MoS_2 does not recover to its original capacity when the current density is back to 50 mA g^{-1}. At the end of 50 cycles, only reversible capacity of 187 mAh g^{-1} is obtained, which is 48% of the original discharge capacity after 10 cycle at 50 mA g^{-1}. The poor performance can be attributed to the serious aggregation of MoS_2 layers and the formation of SEI layers between the 2-D porous structures, making the kinetics of lithium uptake sluggish. Similarly, the initial reversible capacity of BGQS is 2,766 mAh g^{-1} at 50 mA g^{-1} and then fades dramatically after

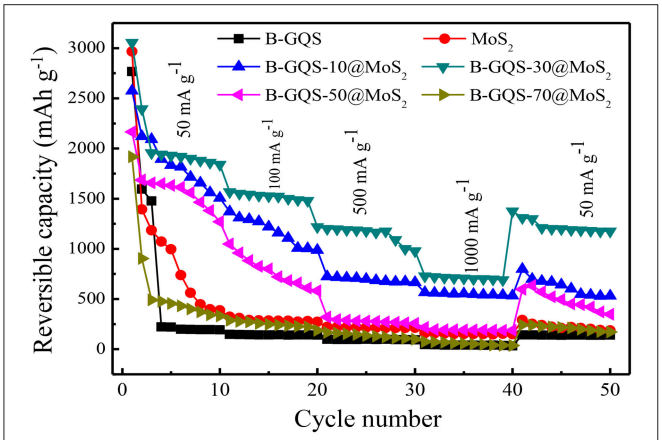

FIGURE 7 | Rate capability of MoS_2, BGQS and BGQS/MoS_2 nanohybrids at various current densities ranging from 50 to 1,000 mA g^{-1}.

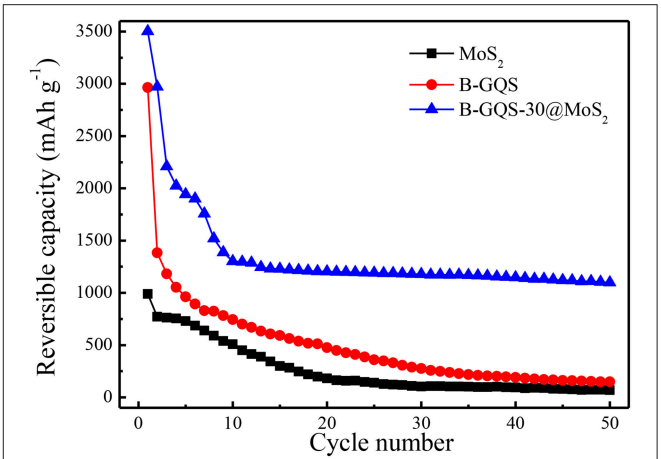

FIGURE 8 | Cycling stability performance of MoS_2, BGQS and BGQS-30/MoS_2 at 100 mA g^{-1}.

the first 5 cycles, possibly due to the formation of SEI layers and irreversible reaction between Li^+ and BGQS. The capacity of BGQS is 220 mAh g^{-1} during the subsequent cycles at 50 mA g^{-1} and further decreases upon increasing the current density. At a high current density of 1,000 mA g^{-1}, BGQS exhibit a reversible capacity of merely 36 mAh g^{-1}, suggesting that the BGQS structure as an individual component is not a suitable anode material for retaining a high amount of Li ions during intercalation.

The combination of MoS_2 with BGQS improves the stability of rate capacity at high current density. The BGQS-10/MoS_2 nanohybrid shows an exceedingly improved rate performance compared to its individual components at all current densities of 50–1,000 mA g^{-1} and maintains a relatively high reversible capacity of 575 mAh g^{-1} at 1,000 mA g^{-1}. Among all the nanohybrids prepared in the present study, the BGQS-30/MoS_2 nanohybrid exhibits superior rate capability to other BGQS/MoS_2 nanohybrids. The BGQS-30/MoS_2 delivers an excellent initial discharge capacity of 3,055 mAh g^{-1} at a current density of 50 mA g^{-1} and retains the reversible capacity of 1,523 mAh g^{-1} at 100 mAh g^{-1}. When the current density further increases to 500 and 1,000 mA g^{-1}, the reversible capacity is noted to be 1,175 and 715 mAh g^{-1}, respectively. Apart from the high reversible capacity at various current densities, the BGQS-30/MoS_2 also exhibits an excellent electrochemical performance in capacity when the current density is returned to 50 mA g^{-1} and the reversible capacity is recovered to 1,374 mAh g^{-1} at the 40th cycle. At the end of 50th cycle, a high reversible capacity of 1,175 mAh g^{-1} is retained, exhibiting its superior electrochemical performance compared to those individual components (bare MoS_2 and BGQS) and other nanohybrids.

The robust electrochemical performance of BGQS-30/MoS_2 is attributed to the optimal co-dispersion among the components, resulting in a synergistic effect on electrochemical performance. The HRTEM image of BGQS-30/MoS_2 (**Figure 2**) clearly shows the homogenous embedment of BGQS onto the MoS_2 layers. The presence of BGQS provides additional intercalation sites for lithium ions, which is also evident from the CV curves. It is also important to note that the presence of 0-D GQD structures embedded in 2-D rGO and/or MoS_2 provides active sites for strong attachment of lithium ions during discharge, which can improve their uptake capacity. In addition, the quantum structures act as nano-dimensional contact points for fast electron and charge transport during the electrochemical cycling (Guo et al., 2016). The graphitic backbones also act as the volume buffering matrix, which significantly improve the mechanical stability of anode materials during the continuous expansion and contraction of MoS_2 layers during charge-discharge cycles (Chang and Chen, 2011).

The further increase in weight percent of BGQS to 50–70 wt% decreases the electrochemical performance on rate capacity at various current densities. The reversible capacity of BGQS-70/MoS_2 at all current densities lies between those of bare MoS_2 and BGQS. Such a loss in capacity retention at high weight loading of BGQS is mainly attributed to the phase separation of BGQS and MoS_2, and subsequently lowers the uptake capacity of Li ions. In addition, the MoS_2 layers tend to restack at high BGQS content, resulting in the loss of mechanical stability as well as the decrease in availability on transport pathways for the intercalation and deintercalation of lithium ions and molecules. This sluggish kinetics leads to the loss in stable reversibility of lithium charge/discharge rates at high BGQS loading.

In order to examine the improvement on the long-term performance for application, the electrochemical cycling stability of BGQS-30/MoS_2 was performed. **Figure 8** shows the electrochemical performance of BGQS-30/MoS_2 nanohybrids at a current density of 100 mA g^{-1} for 50 cycles. The bare MoS_2 and BGQS show a high reversible capacity of 1,015 and 2,964 mAh g^{-1}, respectively, at the initial cycle. However, the reversible capacity of both bare 2-D nanomaterials decreases significantly during the subsequent cycles and only 10–15% of their initial capacity is retained at the end of 50 cycles. The BGQS-30/MoS_2 nanohybrid exhibits the synergistic effect on the enhancement of the long-term electrochemical performance,

and an initial reversible capacity of 3,491 mAh g^{-1} is obtained. Although the capacity of BGQS-30/MoS_2 decreases during the first 10 cycles because of the formation of SEI layers and side reactions, the reversible capacity reach a stable condition and a reversible capacity of 1,041 mAh g^{-1} is maintained after 50 cycles. Wang et al. fabricated the single layered MoS_2-graphene nanosheet nanocomposites for LIB application and a capacity of 571 mAh g^{-1} at 1,000 mA g^{-1} was obtained (Wang et al., 2013). A previous study combined GQDs with MoS_2 and an initial discharge capacity of 1,394 mAh g^{-1} at a current density of 100 mA g^{-1} was reported (Guo et al., 2016). These results clearly indicate that the electrochemical performance of BGQS-30/MoS_2 is exceedingly superior in comparison with the individual bare MoS_2 and BGQS and other reported data (Wang et al., 2013; Li et al., 2015; Guo et al., 2016; Jiang et al., 2016; Teng et al., 2016; Bindumadhavan et al., 2017). The significant enhancement in cycling stability can be attributed to the optimal deposition loading of BGQS with few layered MoS_2 sheets to restrict the agglomeration of MoS_2 species and maintain the capacity retention for a long cycle life. The presence of BGQS can act as buffering sites during the extended cycling and provide required volume for absorption of mechanical stress developed during the intercalation/deintercalation (Chang and Chen, 2011; Huang et al., 2013).

CONCLUSIONS

In this study, we have demonstrated the superiority of BGQS/MoS_2 as the high-performance anode material for LIB application. The top-down strategy can successfully prepare BGQS by embedding 0-D GQD onto a large 2-D rGO fragment. The morphological and structural characterization confirm the formation of well-dispersed few layered BGQS onto MoS_2 nanohybrids to improve the conductivity as well as to provide nano-dimensional contact points for the enhanced uptake capacity of Li ions. BGQS-30/MoS_2 is an excellent anode material for highly reversible Li storage and stable rate capability. An excellent initial discharge capacity of 3,055 mAh g^{-1} is achieved by BGQS-30/MoS_2 nanohybrid at a current density of 50 mA g^{-1}. The BGQS-30/MoS_2 nanohybrid also exhibits the superior rate capability and a highly reversible capacity of 715 mAh g^{-1} at a current density of 1,000 mA g^{-1} is obtained. In addition, the reversible capacity of 1,041 mAh g^{-1} at 100 mA g^{-1} after 50 cycles is retained, clearly indicating the excellent long cycle life because the presence of BGQS can serve as the buffering matrix to adsorb the mechanical stress during intercalation/deintercalation processes. Results obtained in this study clearly demonstrate that BGQS/MoS_2 is a promising anode material which can open an avenue to fabricate novel B-doped GQS/MoS_2 nanocomposites for highly reversible Li storage application.

AUTHOR CONTRIBUTIONS

All authors listed have made a substantial, direct and intellectual contribution to the work, and approved it for publication.

ACKNOWLEDGMENTS

We authors thank the Ministry of Science and Technology (MOST), Taiwan and Ministry of Research Technology and Higher Education, Indonesia for financial support under grant Nos. MOST 105-2113-M-009-023-MY3, 107-2221-E-007-113-MY3 and 123.6/D2.3/KP/2018 (World Class Professor Program).

REFERENCES

Anh, N. T. N., Dutta Chowdhury, A., and Doong, R. A. (2017). Highly sensitive and selective detection of mercury ions using N, S-codoped graphene quantum dots and its paper strip based sensing application in wastewater. *Sens. Actuat. B Chem.* 252, 1169–1178. doi: 10.1016/j.snb.2017.07.177

Bindumadhavan, K., Chang, P. Y., and Doong, R. A. (2017). Silver nanoparticles embedded boron-doped reduced graphene oxide as anode material for high performance lithium ion battery. *Electrochim. Acta* 243, 282–290. doi: 10.1016/j.electacta.2017.05.063

Bindumadhavan, K., Srivastava, S. K., and Mahanty, S. (2013). MoS_2-MWCNT hybrids as a superior anode in lithium-ion batteries. *Chem. Commun.* 49, 1823–1825. doi: 10.1039/c3cc38598a

Cao, X., Shi, Y., Shi, W., Rui, X., Yan, Q., and Kong, J., et al. (2013). Preparation of MoS_2-coated three-dimensional graphene networks for high-performance anode material in lithium-ion batteries. *Small* 9, 3433–3438. doi: 10.1002/smll.201202697

Chang, K., and Chen, W. (2011). *In situ* synthesis of MoS_2/graphene nanosheet composites with extraordinarily high electrochemical performance for lithium ion batteries. *Chem. Commun.* 47, 4252–4254. doi: 10.1039/c1cc10631g

Chang, S. M., and Doong, R. A. (2004). The effect of chemical states of dopants on the microstructures and band gaps of metal-doped ZrO_2 thin films at different temperatures. *J. Chem. Phys. B* 108, 18098–18103. doi: 10.1021/jp047440n

Cheng, X. B., Zhang, R., Zhao, C. Z., and Zhang, Q. (2017). Toward safe lithium metal anode in rechargeable batteries: a review. *Chem. Rev.* 117, 10403–10473. doi: 10.1021/acs.chemrev.7b00115

Dong, H., Liu, C., Ye, H., Hu, L., Fugetsu, B., Dai, W., et al. (2015). Three-dimensional nitrogen-doped graphene supported molybdenum disulfide nanoparticles as an advanced catalyst for hydrogen evolution reaction. *Sci. Rep.* 5:17542. doi: 10.1038/srep17542

Dutta Chowdhury, A., and Doong, R. A. (2016). Highly sensitive and selective detection of nanomolar ferric ions using dopamine functionalized graphene quantum dots. *ACS Appl. Mater. Interfaces* 8, 21002–21010. doi: 10.1021/acsami.6b06266

Eftekhari, A. (2017). Lithium-ion batteries with high rate capabilities. *ACS Sustain. Chem. Eng.* 5, 2799–2816. doi: 10.1021/acssuschemeng.7b00046

Ganganboina, A. B., Dutta Chowdhury, A., and Doong, R. A. (2017). New avenue for appendage of graphene quantum dots on halloysite nanotubes as anode materials for high performance supercapacitors. *ACS Sustain. Chem. Eng.* 5, 4930–4940. doi: 10.1021/acssuschemeng.7b00329

Ganganboina, A. B., Dutta Chowdhury, A., and Doong, R. A. (2018). N-doped graphene quantum dots decorated V_2O_5 nanosheet for fluorescence turn off-on detection of cysteine. *ACS Appl. Mater. Interfaces* 10, 614–624. doi: 10.1021/acsami.7b15120

Guo, B., Yu, K., Li, H., Qi, R., Zhang, Y., and Song, H., et al. (2017). Coral-shaped MoS_2 decorated with graphene quantum dots performing as a highly active electrocatalyst for hydrogen evolution reaction. *ACS Appl. Mater. Interfaces* 9, 3653–3660. doi: 10.1021/acsami.6b14035

Guo, J., Zhu, H., Sun, Y., Tang, L., and Zhang, X. (2016). Boosting the lithium storage performance of MoS_2 with graphene quantum dots. *J. Mater. Chem. A* 4, 4783–4789. doi: 10.1039/C6TA00592F

Hsiao, M. C., Ma, C. C., Chiang, J. C., Ho, K. K., Chou, T. Y., and Xie, X., et al. (2013). Thermally conductive and electrically insulating epoxy nanocomposites with thermally reduced graphene oxide–silica hybrid nanosheets. *Nanoscale* 5, 5863–5871. doi: 10.1039/c3nr01471a

Huang, G., Chen, T., Chen, W., Wang, Z., Chang, K., Ma, L., et al. (2013). Graphene like MoS_2/Graphene composites: cationic surfactant-assisted hydrothermal synthesis and electrochemical reversible storage of lithium. *Small*. 9, 3693–3703. doi: 10.1002/smll.201300415

Hwang, H., Kim, H., and Cho, J. (2011). MoS_2 nanoplates consisting of disordered graphene-like layers for high rate lithium battery anode materials. *Nano Lett*. 11, 4826–4830. doi: 10.1021/nl202675f

Jiang, L., Lin, B., Li, X., Song, X., Xia, H., and Li, L., et al. (2016). Monolayer MoS_2-graphene hybrid aerogels with controllable porosity for lithium-ion batteries with high reversible capacity. *Appl. Mater. Interfaces* 8, 2680–2687. doi: 10.1021/acsami.5b10692

Lee, C., Yan, H., Brus, L. E., Heinz, T. F., Hone, J., and Ryu, S. (2010). Anomalous lattice vibrations of single-and few-layer MoS_2. *ACS Nano* 4, 2695–2700. doi: 10.1021/nn1003937

Li, H., Yu, K., Fu, H., Guo, B., Lei, X., and Zhu, Z. (2015). MoS_2/graphene hybrid nanoflowers with enhanced electrochemical performances as anode for lithium-ion batteries. *J. Phys. Chem. C* 119, 7959–7968. doi: 10.1021/acs.jpcc.5b00890

Li, H., Zhang, Q., Yap, C. C. R., Tay, B. K., Edwin, T. H. T., and Olivier, A. (2012). From bulk to monolayer MoS_2: evolution of Raman scattering. *Adv. Funct. Mater*. 22, 1385–1390. doi: 10.1002/adfm.201102111

Lin, T., Huang, F., Liang, J., and Wang, Y. (2011). A facile preparation route for boron-doped graphene, and its CdTe solar cell application. *Energy Environ. Sci*. 4, 862–865. doi: 10.1039/C0EE00512F

Liu, J., Zheng, M., Shi, X., Zeng, H., and Xia, H. (2016). Amorphous FeOOH quantum dots assembled mesoporous film anchored on graphene nanosheets with superior electrochemical performance for supercapacitors. *Adv. Funct. Mater*. 26, 919–930. doi: 10.1002/adfm.201504019

Ma, L., Huang, G., Chen, W., Wang, Z., Ye, J., and Li, H., et al. (2014). Cationic surfactant-assisted hydrothermal synthesis of few-layer molybdenum disulfide/graphene composites: microstructure and electrochemical lithium storage. *J. Power Sources* 264, 262–271. doi: 10.1016/j.jpowsour.2014.04.084

Sahu, R. S., Bindumadhavan, K., and Doong, R. A. (2017). Boron-doped reduced graphene oxide-based bimetallic Ni/Fe nanohybrids for the rapid dechlorination of trichloroethylene. *Environ. Sci. Nano*. 4, 565–576. doi: 10.1039/C6EN00575F

Stephenson, T., Li, Z., Olsen, B., and Mitlin, D. (2014). Lithium ion battery applications of molybdenum disulfide (MoS_2) nanocomposites. *Energy Environ. Sci*. 7, 209–231. doi: 10.1039/C3EE42591F

Teng, Y., Zhao, H., Zhang, Z., Li, Z., Xia, Q., and Zhang, Y., et al. (2016). MoS_2 nanosheets vertically grown on graphene sheets for lithium-ion battery anodes. *ACS Nano* 10, 8526–8535. doi: 10.1021/acsnano.6b03683

Thangappan, R., Kalaiselvam, S., Elayaperumal, A., Jayavel, R., Arivanandhan, M., and Karthikey, R., et al. (2016). Graphene decorated with MoS_2 nanosheets: a synergetic energy storage composite electrode for supercapacitor applications. *Dalton Trans*. 45, 2637–2646. doi: 10.1039/C5DT04832J

Vinoth, R., Patil, I. M., Pandikumar, A., Kakade, B. A., Huang, N. M., and Dionysios, D. D. (2016). Synergistically enhanced electrocatalytic performance of an N-doped graphene quantum dot-decorated 3D MoS_2-graphene nanohybrid for oxygen reduction reaction. *ACS Omega* 1, 971–980. doi: 10.1021/acsomega.6b00275

Wang, R., Gao, S., Wang, K., Zhou, M., Cheng, S., and Jiang, K. (2017). MoS_2/rGO nanoflakes as high performance anode materials in sodium ion batteries. *Sci. Rep*. 7:7963. doi: 10.1038/s41598-017-08341-y

Wang, R., Xu, C., Sunn, J., Liu, Y., Gao, L., Yao, H., et al. (2014). Heat-induced formation of porous and free-standing MoS_2/GS hybrid electrodes for binder-free and ultralong-life lithium ion batteries. *Nano Energy* 8, 183–195. doi: 10.1016/j.nanoen.2014.05.009

Wang, Z., Chen, T., Chen, W., Chang, K., Ma, L., Huang, G., et al. (2013). CTAB-assisted synthesis of single-layer MoS_2-graphene composites as anode materials of Li-ion batteries. *J. Mater. Chem. A* 1, 2202–2210. doi: 10.1039/C2TA00598K

Wei, W., Sun, K., and Hu, Y. H. (2016). An efficient counter electrode material for dye-sensitized solar cells – flower-structured 1T metallic phase MoS_2. *J. Mater. Chem. A* 4, 12398–12401. doi: 10.1039/C6TA04743B

Whittingham, M. S. (1976). Electrical energy storage and intercalation chemistry. *Science* 192, 1126–1127. doi: 10.1126/science.192.4244.1126

Xiao, J., Wang, X. J., Yang, X. Q., Xun, S. D., Liu, G., Koech, P. K., et al. (2011). Electrochemically induced high capacity displacement reaction of PEO/MoS_2/graphene nanocomposites with lithium. *Adv. Funct. Mater*. 21, 2840–2846. doi: 10.1002/adfm.201002752

Yang, X., Niu, H., Jiang, H., Wang, Q., and Qu, F. A. (2016). A high energy density all-solid-state asymmetric supercapacitor based on MoS_2/graphene nanosheets and MnO_2/graphene hybrid electrodes. *J. Mater. Chem. A* 4, 11264–11275. doi: 10.1039/C6TA03474H

Conflict of Interest Statement: The authors declare that the research was conducted in the absence of any commercial or financial relationships that could be construed as a potential conflict of interest.

Advantages of publishing in Frontiers

OPEN ACCESS
Articles are free to read for greatest visibility and readership

FAST PUBLICATION
Around 90 days from submission to decision

HIGH QUALITY PEER-REVIEW
Rigorous, collaborative, and constructive peer-review

TRANSPARENT PEER-REVIEW
Editors and reviewers acknowledged by name on published articles

Frontiers
Avenue du Tribunal-Fédéral 34
1005 Lausanne | Switzerland

Visit us: www.frontiersin.org
Contact us: info@frontiersin.org | +41 21 510 17 00

REPRODUCIBILITY OF RESEARCH
Support open data and methods to enhance research reproducibility

DIGITAL PUBLISHING
Articles designed for optimal readership across devices

FOLLOW US
@frontiersin

IMPACT METRICS
Advanced article metrics track visibility across digital media

EXTENSIVE PROMOTION
Marketing and promotion of impactful research

LOOP RESEARCH NETWORK
Our network increases your article's readership